Cosmology Large Angular Scale Surveyor (CLASS): Integration and Testing of CLASS at 40 GHz

by

Zhilei Xu

A dissertation submitted to The Johns Hopkins University in conformity with the requirements for the degree of Doctor of Philosophy.

Baltimore, Maryland

August, 2017

Abstract

The Cosmology Large Angular Scale Surveyor (CLASS) is an array of telescopes to observe Cosmic Microwave Background (CMB) polarization in Chile. CLASS will make large angular scale CMB polarization measurements in frequency bands at 40 GHz, 90 GHz, 150 GHz, and 220 GHz. The CLASS survey (started from 2016) will constrain the tensor-to-scalar ratio from the first moments of the universe and also provide critical data on cosmic reionization, the sum of neutrino masses, and the Galactic interstellar medium. In this thesis, the CLASS strategy and design are introduced. The optical filter system is described in details along with two testing devices, including a Fourier Transform Spectrometer (FTS) and an optics test cryostat. For the telescope mount system, a bottom-up introduction is provided focusing on individual components. Preliminary data analysis from the first observing season with the 40 GHz telescope is also described.

Primary Reader: Charles L. Bennett

Secondary Reader: Tobias A. Marriage

ABSTRACT

Acknowledgments

I would like to thank my advisor, Professor Charles L. Bennett. Without his generous support, my graduate studies would have been much less productive and enjoyable. Professor Bennett is much more than an academic mentor to me; he has been a true advisor to me in all aspects of life. I would also like to thank Professor Tobias Marriage. He not only instructed me in the ways of experimental physics, but he also treated me as a friend, which I especially appreciated while being so far away from my home. His advice, support, and companionship made the last six years scientifically and emotionally fulfilling. I would also like to thank everyone else I worked with on the CLASS experiment. I was deeply impressed with everyone's dedication to science and exquisite ability to solve problems. More importantly, the friendly environment made the whole group feel like a second home to me.

Beyond the CLASS group, I definitely owe a huge "thank you" to my fellow students in the department. They made my Ph.D. life so positive and memorable. In graduate school, we were classmates; after graduation, we will be life-long friends. I would also like to thank the administrative staff. Without their guidance, I would

never have been able to progress through my studies so smoothly. I would like to thank the staff of the IDG and the machine shop. Thank you so much for your valuable suggestions, hard work, and generous help. It would have been impossible for me to complete my projects without your support.

Finally, I would like to thank my father, who passed away during my first year of graduate school. It was his vision and guidance that led me to pursue my dream of a career in physics. One of my great regrets is that he could not see me reach this stage, but I hope that he would have been proud. I would also like to thank my mother, who has been amazingly supportive and mentally strong even through our most difficult times. She sacrificed so much to provide me a stable environment to finish my degree. I would also like to thank my extended family in China. Without their help, my mother and I could not have recovered. It was because of their help that I was able to stay in the US and finish my degree. What made my graduate school experience even more special is that I met my fiancée, Jing Zhang. She is a doctoral student at the University of Pennsylvania, where I will be joining her as I start my post-doctoral position in September. When I was hesitant about possible careers after graduate school, it was her consistent encouragement that guided me to put aside my doubts and pursue my dream.

Special thanks to Duncan Watts, Matthew Petroff, and Rachael Alexandroff, who generously instructed me on the finer points of English grammar in the writing of this thesis (including this sentence).

ACKNOWLEDGMENTS

Dedication

For my parents and my fiancée

Contents

List of Tables

List of Figures

LIST OF FIGURES

Chapter 1

Cosmology

Although scientists have been seeking to understand our universe for thousands of years, it was not until the 20th century that cosmology started to evolve into a robust science. It was not until the last decades that different theories could be tested by scientific experiments. We are living in an exciting era when our understanding of the universe is rapidly improving.

1.1 Hubble's Law

Astronomical observations have shown that at large scales (> 20 Mpc) the universe is homogeneous and isotropic. This is called the cosmological principle. It is also observed that the universe is expanding uniformly. Given these two observational facts, we can introduce a scale factor $a(t)$, which is only a function of time t.

The scale factor is defined to be a dimensionless parameter to scale the physical distance between two far-away objects (say two galaxies in the following context) in an expanding universe. This implies that we can assign "co-moving" coordinates that do not change with time. These coordinates are fixed to the galaxies, in which the distance between the galaxies at any given time is the coordinate difference $\Delta x = |x_1 - x_2|$ multiplied by the scale factor:

$$D = a(t) \times |x_1 - x_2| = a(t)\Delta x. \tag{1.1}$$

We set the scale factor at the current time, t_0, to unity, $a(t_0) = 1$. The relative velocity between the two galaxies is the time derivative of the distance, $\dot{D}$. According to our previous definitions, only $a(t)$ is a function of time. So we have the relative velocity:

$$V = \dot{D} = \dot{a}(t)\Delta x. \tag{1.2}$$

Then combining Equation 1.1 and 1.2, we can eliminate the variable Δx and have the relative velocity expression as $V = (\dot{a}/a)\ D$. If we define $\dot{a}/a$ as $H(t)$, we will have:

$$V(t_0) = H(t)D(t_0),$$

where $H(t)$ is the Hubble parameter, which describes the expansion rate of the universe at large scales (> 20 Mpc). Its current value, H_0, is called the Hubble constant.

Using the Hubble constant, the previous equation becomes Hubble's Law:

$$V = H_0 D. \tag{1.3}$$

Hubble's Law was discovered by Edwin Hubble in 1929.[24] This relation applies to all locations in the universe. At large scales, any two galaxies are moving away from each other; the relative speed is proportional to the distance between them. This large scale receding motion of all the objects solely from the expansion is called the Hubble flow. Because the scale factor $a(t)$ describes the expansion of the universe and also defines the Hubble parameter, it is a key to understanding the dynamical evolution of the universe.

1.2 Friedmann Equations

Applying Einstein's field equations to a homogeneous and isotropic universe, the time-time component gives us an equation

$$\left(\frac{\dot{a}}{a}\right)^2 + \frac{kc^2}{a^2} = \frac{8\pi G}{3}\frac{\varepsilon}{c^2}, \tag{1.4}$$

where c is the speed of light in vacuum, G is Newton's gravitational constant, ε is the energy density, k is a constant associated with the curvature of the universe. The scale factor a and the energy density ε are functions of time. This is the first

Friedmann equation, derived by Alexander Friedmann in 1922.[17]

The parameter k can be defined as

$$k = \frac{K}{{R_0}^2},$$

where R_0 is the radius of curvature, the constant K describes the curvature of the universe. $K = +1$ implies the universe is closed with positive curvature; $K = -1$ implies the universe is open with negative curvature. Between the open and the closed universe, there is a boundary when the universe is neither open nor closed. On that boundary, the universe is flat, Euclidean, with $K = 0$. Current observations support that the universe is flat,[22] to within measurement uncertainties.

With $K = 0$, the first Friedmann equation can be re-written as

$$H^2 = \left(\frac{\dot{a}}{a}\right)^2 = \frac{8\pi G}{3}\frac{\varepsilon}{c^2}.$$

This equation provides the density for a flat universe, which is called the critical density ε_c:

$$\varepsilon_c = \frac{3H^2c^2}{8\pi G}. \tag{1.5}$$

The energy density contains different components in the universe, including radiation (and relativistic matter) and non-relativistic matter.

The first Friedmann equation (Equation 1.4) relates curvature k, dynamics $a(t)$

and the energy components of the universe $\varepsilon(t)$. The energy density $\varepsilon(t)$ and the scale factor $a(t)$ are both functions of time. We need to find a relation between ε and a before we can proceed to solve for $a(t)$.

If we consider one component in the universe within the volume of V, the second law of thermodynamics can be written as

$$dQ = pdV + d(\varepsilon V), \tag{1.6}$$

where p is the pressure from this component, and Q is the heat transferred into this component. The CMB temperature uniformity across the super-horizon scale implies no net energy exchange,[22] meaning $dQ = 0$. Then Equation 1.6 can be rearranged as

$$Vd\varepsilon = -pdV - \varepsilon dV. \tag{1.7}$$

The volume V must be proportional to a^3, which gives us the relation $dV/V = 3da/a$. Then the time-derivative of Equation 1.7 can be rearranged as

$$\dot{\varepsilon} + 3\frac{\dot{a}}{a}(\varepsilon + p) = 0. \tag{1.8}$$

This is called the fluid equation. Now let's multiply the first Friedmann equation

(Equation 1.4 with zero curvature) by a^2 and then take the time derivative

$$2\dot{a}\ddot{a} = \frac{8\pi G}{3c^2}(\dot{\varepsilon}a^2 + 2a\dot{a}\varepsilon).$$

Dividing the above equation by $2a\dot{a}$

$$\frac{\ddot{a}}{a} = \frac{4\pi G}{3c^2}(\frac{a}{\dot{a}}\dot{\varepsilon} + 2\varepsilon)$$

and substituting $\dot{\varepsilon}$ with the fluid equation 1.8, we have the second Friedmann equation, also know as the acceleration equation.

$$\frac{\ddot{a}}{a} = -\frac{4\pi G}{3c^2}(\varepsilon + 3p) \tag{1.9}$$

This equation describes the acceleration of the expansion. The expansion of the universe accelerates when $\ddot{a} > 0$; while the expansion decelerates when $\ddot{a} < 0$.

1.3 Equation of State

The fluid equation (Equation 1.8) provides a promising way to solve ε as a function of a. But there is still one quantity we need to know, the pressure p. The pressure is closely connected to the energy density, as described by the equation of state,

$$p = w\varepsilon, \tag{1.10}$$

where the quantity w is the equation of state parameter.

With Equation 1.8 and 1.10, we obtain $ad\varepsilon = -3\varepsilon(1+w)da$. And solving this equation gives us,

$$\varepsilon = \varepsilon_0 a^{-3(1+w)}, \tag{1.11}$$

where ε_0 is the current energy density for $a = 1$. The result shows that the energy density follows a power law of the scale factor with the index determined by the equation of state parameter w. For example, $\rho = \rho_0 a^{-3}$ if $w = 0$.

If we combine the equation of state (Equation 1.10) and the acceleration equation (Equation 1.9), we get

$$\frac{\ddot{a}}{a} = -\frac{4\pi G}{3}(1+3w)\rho.$$

This equation gives us the criterion that governs the acceleration of the universe. It shows:

$$\begin{aligned} w > -\frac{\mathbf{1}}{\mathbf{3}} &\Rightarrow \ddot{a} < 0 \Rightarrow \textit{Decelerating universe}, \\ w < -\frac{\mathbf{1}}{\mathbf{3}} &\Rightarrow \ddot{a} > 0 \Rightarrow \textit{Accelerating universe}. \end{aligned} \tag{1.12}$$

Now let's take a look at the values of w for different components in the universe. In thermodynamics, we know that pressure can be expressed as $P = nk_BT$ for an ideal gas, where n is the number density of the particle, k_B is the Boltzmann constant and T is the temperature of thermal motion. If we assume the particles have mass of μ, the mean square speed for non-relativistic massive particles can be estimated as,

according to the equipartition theorem,

$$\frac{3}{2}k_B T \approx \frac{1}{2}\mu\langle v^2\rangle.$$

With this relation, pressure from this component can be estimated as:

$$P = nk_B T \approx \frac{\varepsilon}{\mu c^2}k_B T = \frac{\langle v^2\rangle}{3c^2}\rho$$

where we can have an estimation of $w = \langle v^2\rangle/3c^2$. The mean square velocity $\langle v^2\rangle$ for non-relativistic particles is much smaller than c^2, so that $w \approx 0$; while $\langle v^2\rangle \approx c^2$ for relativistic particles, where $w \approx 1/3$.

This is not hard to understand qualitatively. Pressure comes from particles hitting an imaginary surface. For non-relativistic particles, nearly all of the energy is stored in the particle's rest mass. The thermal motion of the particles, for the temperatures and masses assumed here, only takes a negligible amount of the energy density; therefore, the pressure from the thermal motion is negligible. On the other hand, relativistic particles contain nearly all of their energy in their thermal motion. This amount of thermal motion should contribute to a significant amount of pressure, which provides a non-zero w.

In our current universe, the non-relativistic particles consist of baryons, dark matter particles, and non-relativistic neutrinos with $w = 0$; while the relativistic particles, made up of photons, act as radiation, with $w = 1/3$. As Equation 1.12

shows, both of those components contribute towards a decelerating universe.

The universe was believed to be decelerating until acceleration was discovered in 1998.[34] The fact that the universe is accelerating is rather counter-intuitive. The components we previously knew all exert a gravitational attraction force. Although the universe is currently expanding, gravity is decelerating the expansion. However, the accelerating expansion implies that there must be one (or more) component that is pushing the universe apart. Furthermore, this component must dominate; it not only compensates for the gravitational matter attraction in the universe, but accelerates the expansion of the universe. A name is assigned to this component: dark energy. From Equation 1.12, we know that the equation of state parameter for the dark energy must be less than $-1/3$ to accelerate the universe. Current observations prefer $w \approx -1$,[22] which favors the dark energy being a cosmological constant Λ, originally introduced by Einstein in 1917.[12] For now we assume the dark energy is the cosmological constant (implying no time evolution). A summary is presented in Table 1.1.

Table 1.1: Equation of State Parameter for Different Components

Component	w	$\varepsilon(a)$	Acc/Dec
Radiation	$1/3$	a^{-4}	Dec
Matter	0	a^{-3}	Dec
Cosmological Constant	-1	*constant*	Acc

1.4 Evolution of the Universe

Now we have the function of $\varepsilon(a)$ as shown in Equation 1.11. If we assume there is only one component in the universe (e.g. radiation, matter, and cosmological constant), the Friedmann equation (Equation 1.4) can be written as

$$\left(\frac{\dot{a}}{a}\right)^2 + \frac{k}{a^2} = \frac{8\pi G}{3c^2}\varepsilon_0 a^{-3(1+w)}. \tag{1.13}$$

We set $k = 0$ according to current observations.[22] Then the equation above can be simplified:

$$\left(\frac{\dot{a}}{a}\right)^2 = \frac{8\pi G}{3c^2}\varepsilon_0 a^{-3(1+w)} = H_0^2 a^{-3(1+w)}. \tag{1.14}$$

This equation can be solved analytically for each single component with an equation of state parameter w, which gives us the scale factor $a(t)$ as a function of time for a flat universe:

$$a(t) = \left(\frac{3(1+w)H_0}{2}\right)^{\frac{2}{3(1+w)}} \times t^{\frac{2}{3(1+w)}}, \qquad \text{when } w \neq -1, \tag{1.15}$$

$$a(t) = constant \times e^{H_0 t}, \qquad \text{when } w = -1, \tag{1.16}$$

or

$$a(t) \propto t^{\frac{2}{3(1+w)}}, \qquad \text{when } w \neq -1, \tag{1.17}$$

$$a(t) \propto e^{H_0 t}, \qquad \text{when } w = -1. \tag{1.18}$$

These are solutions for a single component with w. From Section 1.1, we calculated w for different components as shown in Table 1.1. Then we have:

$$\text{Radiation-dominated}, \qquad w = \frac{1}{3}, \qquad a(t) \propto t^{\frac{1}{2}}, \tag{1.19}$$

$$\text{Matter-dominated}, \qquad w = 0, \qquad a(t) \propto t^{\frac{2}{3}}, \tag{1.20}$$

$$\text{Cosmological Constant-dominated}, \qquad w = -1, \qquad a(t) \propto e^{H_0 t}. \tag{1.21}$$

1.5 Our Current Understanding

In fact, our universe simultaneously contains the three components (radiation r, matter m, and dark energy). Assuming the cosmological constant Λ is the dark energy, Equation 1.14 can be re-written as:

$$\left(\frac{\dot{a}}{a}\right)^2 = \frac{8\pi G}{3c^2}(\varepsilon_{r,0}\ a^{-4} + \varepsilon_{m,0}\ a^{-3} + \varepsilon_{\Lambda,0}) \tag{1.22}$$

where $\varepsilon_{r,0},\ \varepsilon_{m,0},\ \varepsilon_{\Lambda,0}$ are the current energy density for each component. Given the current critical density as $\varepsilon_{c,0}$, the ratios of each energy density to the critical density

$\varepsilon_{c,0}$ (Equation 1.5) are defined as $\Omega_{r,0},\ \Omega_{m,0},\ \Omega_{\Lambda,0}$. Then Equation 1.22 can be written as:

$$\left(\frac{\dot{a}}{a}\right)^2 = \frac{8\pi G}{3c^2}\varepsilon_{c,0}(\Omega_{r,0}\ a^{-4} + \Omega_{m,0}\ a^{-3} + \Omega_{\Lambda,0}). \tag{1.23}$$

Using Equation 1.5 and the relation $H = \dot{a}/a$, the above equation can be simplified:

$$1 = \Omega_{r,0}\ a^{-4} + \Omega_{m,0}\ a^{-3} + \Omega_{\Lambda,0}.$$

Solving this equation will give us the expansion history of our universe. However, it cannot be solved analytically without approximations (it could be solved numerically). Instead, we can solve it in pieces. The components evolve differently with the scale factor a. For most values of a, there will be only one dominant component. If we only consider the dominating component, Equation 1.23 can be solved as Equation 1.14 piecewisely. So far, we have been assuming each component stays as the same kind through the entire history of the universe, which is a valid assumption for most of the constituents except for neutrinos. Their small but non-zero masses make them relativistic in early universe while non-relativistic in late universe. Therefore, the sum of neutrino masses affects the evolution of the universe which makes cosmological observation a powerful probe to constrain the masses. For latter discussions, neutrinos are treated as radiation during both the early and late universe for consistency.

Observations[22] constrain the current density fractions $\Omega_{r,0},\ \Omega_{m,0},\ \Omega_{\Lambda,0}$:

$$\Omega_{r,0} = 8.4 \times 10^{-5},\ \Omega_{m,0} = 0.3,\ \Omega_{\Lambda,0} = 0.7 \tag{1.24}$$

whose evolution is shown in Figure 1.1.

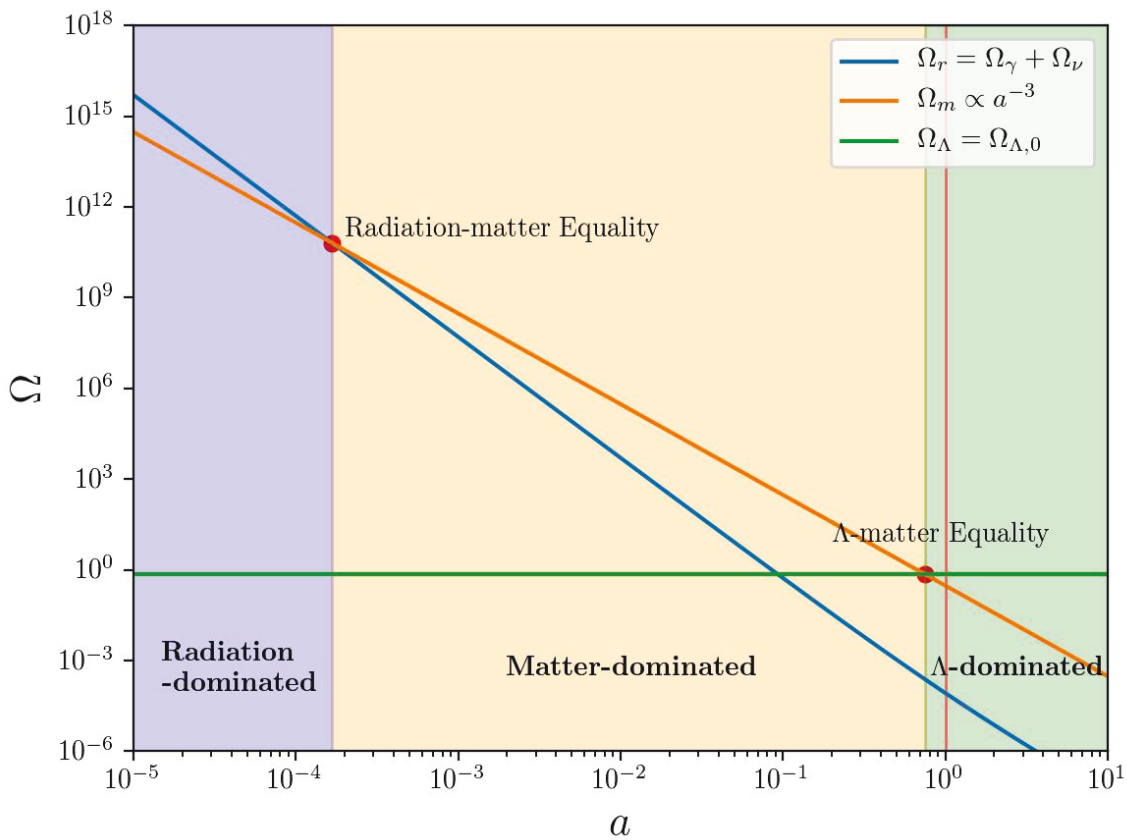

Figure 1.1: Energy density evolution. The plot shows the universe went through radiation-dominated (blue-shaded region), matter-dominated (yellow-shaded region) and dark energy-dominated (green-shaded region). The red vertical line shows where we are right now. The slope of Ω_r (including photon energy density Ω_γ and neutrino energy density Ω_ν) changes because the neutrinos turned from relativistic to non-relativistic during the evolution of the universe, assuming the sum of neutrino masses of 60 meV.

In the very early times, the universe was radiation-dominated until the radiation-matter energy density equality point. After the radiation-matter equality, the universe became matter-dominated for a long time. Around the age of 8 billion years ($a \approx 0.75$), the universe passed the cosmological constant (Λ)-matter equality and became Λ-dominated. Treating different eras separately, the evolution of the universe can be described as:

- $t_{\text{inflation}} < t < 47,000$ yr, radiation-dominated, $a(t) \propto t^{\frac{1}{2}}$
- $47,000$ yr $< t <$ 9.8 Gyr, matter-dominated, $a(t) \propto t^{\frac{2}{3}}$
- 9.8 Gyr $< t <$ now ($\approx$ 13.8 Gyr), dark energy-dominated, $a(t) \propto e^{H_0 t}$.

1.6 Cosmic Microwave Background

As the universe expands, its temperature decreased inversely with the scale factor,

$$T \propto \frac{1}{a}.$$

When the universe was young and the scale factor a was small, the temperature of the universe was high. Before the age $\sim 350,000$ years, the universe was hotter than 3000 K. Above this temperature, energetic photons were abundant enough to ionize all the hydrogen atoms in the universe. The ionized hydrogen atoms constituted $\sim 90\%$ of the baryons in the universe. Photons were strongly coupled to baryons

through Thomson Scattering. These couplings established the photons in equilibrium with the baryons in a photon-baryon fluid. As time went on, when the temperature dropped, the electrons and protons combined into electrically-neutral hydrogen atoms, which were only loosely coupled with photons. The photons were released from the baryons at $t \approx 350,000$ yr. This event is called "decoupling." After decoupling, this thermal distribution of photons free-streamed across the universe, observed today as the Cosmic Microwave Background (CMB).

The CMB is the most powerful probe of our universe. It provides information about the universe in its infancy. Because the CMB photons were in equilibrium with the baryons before decoupling and free-streamed afterward, they provide direct information about the early universe. Meanwhile, when the CMB was decoupled, the whole universe was almost homogeneous with relatively simple physical processes at ~ 3000 K. These processes can be understood by well-established physics, which enables the CMB to serve as a powerful probe of the early universe.

The CMB was predicted by Alpher, Bethe and Gamow in 1948[3] and discovered by Penzias and Wilson in 1965.[31] In 1991, the CMB blackbody spectrum ($2.726 \pm 0.001K$) was confirmed by the COBE satellite.[28] A blackbody spectrum results from matter in thermal equilibrium with radiation. It is consistent only with an expanding universe, where the early universe was once hot and dense.

Although the CMB was measured to be almost isotropic, small anisotropy ($\sim 10^{-4}$) was discovered across the sky by the COBE satellite.[6] The anisotropy across

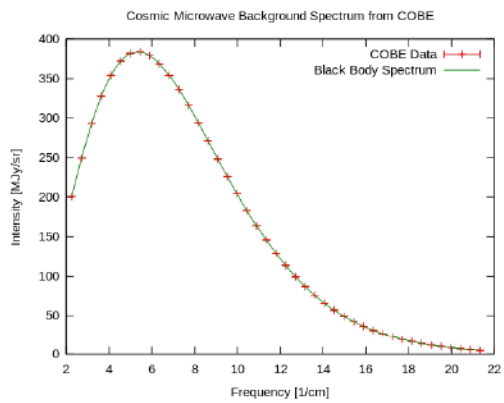

Figure 1.2: The CMB spectrum as measured by the COBE satellite.[16] The spectrum is well-fit by a blackbody spectrum at 2.723 K.

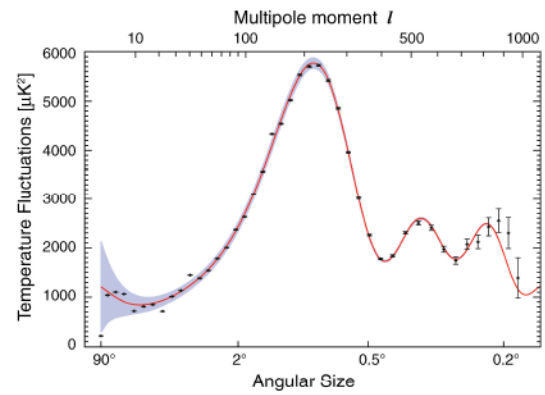

Figure 1.3: The CMB anisotropy power spectrum measured by the WMAP satellite.[21] Features in the power spectrum contain rich information about the universe.

the sky can be decomposed into spherical harmonics:

$$\frac{\Delta T}{T} = \sum_{l=0}^{\infty} \sum_{m=-l}^{l} a_{lm} Y_{lm}(\theta, \phi) \tag{1.25}$$

with the coefficients a_{lm} calculated by:

$$a_{lm} = \int_{4\pi} \frac{\Delta T}{T}(\theta, \phi) Y^*_{lm} \, \mathrm{d}\Omega.$$

The power spectrum C_l is then defined as the average of the a^2_{lm} under the same l value:

$$C_l = \langle |a_{lm}|^2 \rangle \simeq \frac{1}{2l+1} \sum_m a^*_{lm} a_{lm}.$$

An example of the CMB anisotropy power spectrum is presented in Figure 1.3 from the WMAP satellite. This power spectrum contains rich information about the

universe. The data in Figure 1.2 and 1.3, when combined with one or more other measurements (such as the Hubble Constant and the optical depth to reionization), can determine all of the fundamental parameters of the early universe. From the CMB temperature measurement $T \approx 2.7K$ in Figure 1.2, the radiation energy density is calculated as $\Omega_{r,0} \approx 8 \times 10^{-5}$, including 5×10^{-5} from CMB photons and 3×10^{-5} from neutrinos. From CMB anisotropy measurement in Figure 1.3, position of the first peak measures the curvature of the universe, now preferring a flat universe, $k = 0$ in the Friedmann equation (Equation 1.4). The underlying amplitude and tilt of the power spectrum measures the primordial fluctuation level A_s and the spectral index n_s. The heights of the collection of acoustic peaks determines the matter energy density $\Omega_{m,0} \approx 0.3$, while the height of the odd peaks vs even peaks gives the baryon density $\Omega_{b,0}$. Then the dark energy Λ density is calculated as $\Omega_{\Lambda,0} \approx 1 - \Omega_{m,0} - \Omega_{r,0} \approx 0.7$ in a flat universe.

Beyond the temperature power spectrum, the CMB polarization ones contain additional information to further constrain the fundamental parameters. Excitingly, they could also tell us how the universe began.

1.7 Inflation

Although modern cosmology has achieved great triumphs, there are still questions to be answered:

- Horizon Problem. The CMB observations show homogeneity across the entire sky. However, the universe should not have been able to reach any equilibrium beyond the causal horizon at decoupling, which corresponds ~ 2 degrees separation on the sky.

- Flatness Problem. The current universe is measured to be flat within a fraction of a percent, which would be unexpected as the universe would evolve away from flatness if there was any curvature at the very beginning. The fine tuning needed at earlier times of the universe would be extraordinary and unnatural.

- Cosmic Defect Problem. Cosmic defects (including magnetic monopole, cosmic string, and domain walls) are predicted to be observed within our observable universe, whereas none of them have been observed.

- Initial Fluctuations. The anisotropy from the CMB reflects the initial fluctuations . The origin of these fluctuations remains to be explained.

In 1980s, the inflation paradigm was proposed to answer these questions.[19] The inflation paradigm suggests the existence of a scalar quantum field (similar to the recently discovered Higgs field) in the very early universe. We call it the inflaton field ϕ. The field has its corresponding effective potential $V(\phi)$, which can reach the Grand Unified Theory (GUT) energy level. The pressure and the total energy (kinetic and

potential energy) of the field can be written as:

$$p(\phi) = \frac{1}{2}\dot{\phi}^2/\hbar c^3 - V(\phi), \tag{1.26}$$

$$\varepsilon(\phi) = \frac{1}{2}\dot{\phi}^2/\hbar c^3 + V(\phi). \tag{1.27}$$

From the equation of state $p = w\varepsilon$ (Equation 1.10), w for this inflation field is:

$$w = \frac{p(\phi)}{\varepsilon(\phi)} = \frac{\frac{1}{2}\dot{\phi}^2/\hbar c^3 - V(\phi)}{\frac{1}{2}\dot{\phi}^2/\hbar c^3 + V(\phi)}. \tag{1.28}$$

If the kinetic energy is much smaller than the potential energy, the so-called "Slow Roll" model,

$$\dot{\phi}^2 \ll \hbar c^3 V(\phi),$$

Equation 1.28 becomes

$$w \approx -1.$$

This is the same as that of a cosmological constant (Section 1.4), where we calculated that the universe expands exponentially when $w = -1$. This inflation model, which assumes a small kinetic energy, is called slow-roll inflation.[27,1] Slow-roll inflation describes a universe that went through an exponential expansion within the first 10^{-32} seconds, dramatically expanding the universe.

The period of dramatic expansion blew up causally-connected regions beyond the size of our observable universe, which solves the horizon problem. The expansion also

smooths any curvature to produce a nearly flat universe, which solves the flatness problem. The expansion also dilutes the density of cosmic defects to less than one in our observable universe, thereby explaining why these have not been observed. Finally, the expansion stretches the inevitable quantum fluctuations of the inflaton field to cosmic scales, explaining the origins of the observed CMB anisotropy. The anisotropy became the density fluctuations that seed large scale structure.

The inflation paradigm seems to be a promising theory, since all the questions above were naturally answered. In addition, the scalar fluctuation spectral index n_s is measured be to slightly smaller than unity,[22] just as inflation would predict. However, inflation has not yet been convincingly verified. Verifying inflation is one fundamental goal in cosmology. Further, inflation is a general idea. Only specific models of $V(\phi)$ make specific predictions. Inflation can even be extended to invoking multiple fields. We need to know not just if the inflation paradigm is right, but what kind of inflation happened in our universe.

If the inflation paradigm is right, it should have generated cosmic-scale gravitational waves. The gravitational waves would have imprinted a divergence-free polarization pattern on the CMB through Thomson scattering. The pattern is divergence-free, know as B-mode analogous to the magnetic field. Measuring this inflationary B-mode polarization is the most powerful remaining test of the inflation paradigm. It is the only way to determine the amplitude of $V(\phi)$, which may be the first time a GUT-energy-level phenomenon is observed.

Chapter 2

The CLASS Project

The Cosmology Large Angular Scale Surveyor (CLASS) is designed to make measurements of large angular scale CMB polarization to measure the inflationary Cosmic Microwave Background (CMB) B-mode polarization at large angular scales and also to constrain the optical depth to reionization τ. To observe nearly the full sky and minimize atmospheric loading, the CLASS telescopes are located in the Atacama Desert, close to the equator at an altitude of 5,200 meter. To recover large angular scales on the sky, CLASS employs a novel polarization modulation device, the variable-delay polarization modulator (VPM). To remove the galactic foreground, the CLASS telescopes observe in four frequency bands: 40 GHz, 90 GHz, 150 GHz, and 220 GHz. To achieve high sensitivity, the CLASS telescopes employ polarization-sensitive high-efficiency transition-edge-sensor (TES) bolometers. The CLASS telescopes are optimized to measure the CMB polarization signals at large angular scales

with state-of-art technology.

2.1 Scientific Objective

The CLASS experiment is optimized to measure the large-angular-scale polarization signal with high sensitivity. The results will help us understand cosmology, fundamental physics, and our own galaxy. The primary scientific goals for CLASS are to test the inflation paradigm, characterize inflation, determine the optical depth to reionization τ, and constrain the sum of neutrino masses Σm_ν.

2.1.1 Inflation

If inflation happened, quantum fluctuations of the inflaton field would have generated scalar perturbations, while quantum fluctuations of the gravitational field would have generated tensor perturbations. Perturbations polarize CMB photons through Thomson scattering as shown in Figure 2.1 on the left. The polarization field can be decomposed into curl-free and divergence-free components as E-mode polarization and B-mode polarization, shown in Figure 2.1 on the right.

The B-mode polarization at the largest angular scales could only come from inflationary tensor perturbations. Therefore, measuring the large-angle B-mode polarization is a powerful tool for testing and characterizing the inflation paradigm.

The amplitude of the CMB B-mode polarization anisotropy is represented by the

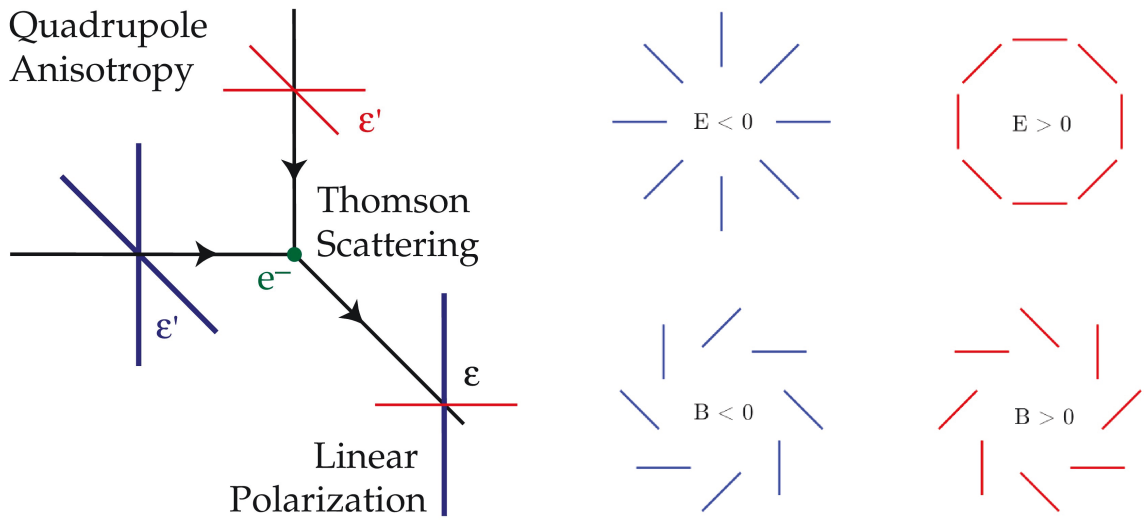

Figure 2.1: CMB Polarization from Thomson Scattering and E/B-mode. On the left, the Thomson scattering is shown.[23] If an electron sits at the center of a quadrupole perturbation, photons coming from different directions have different temperatures. Assuming that the horizontal photons (shown in blue) have higher temperature than the vertical photons (shown in red), the electron scatters more power vertically than horizontally if observed perpendicularly to the paper; equivalently, a net vertical polarization signal is generated. On the right, E-mode and B-mode in the CMB polarization field are shown.[25] The left part of this figure shows one local polarization signal with one certain direction. If we zoom out to the whole sky, polarization will form a vector field on the sky. Analogous to the electromagnetic field, this vector field can be decomposed into curl-free and divergence-free components similar to the electric field (E-mode) and the magnetic field (B-mode)

tensor perturbation amplitude A_t. It is often expressed in terms of the ratio to the scalar perturbation amplitude A_s, whose value is measured from the CMB temperature anisotropy. The scalar perturbation amplitude A_s depends on scale, $A_s = A_s(k)$ using wavenumber k to describe scale. If the tensor perturbation amplitude also depends on scale, the ratio r is defined as

$$r_k = \frac{A_t(k)}{A_s(k)},$$

with the current upper limit as $r < 0.12$ at $k = 0.05$ Mpc^{-1} with 95% confidence.[7]

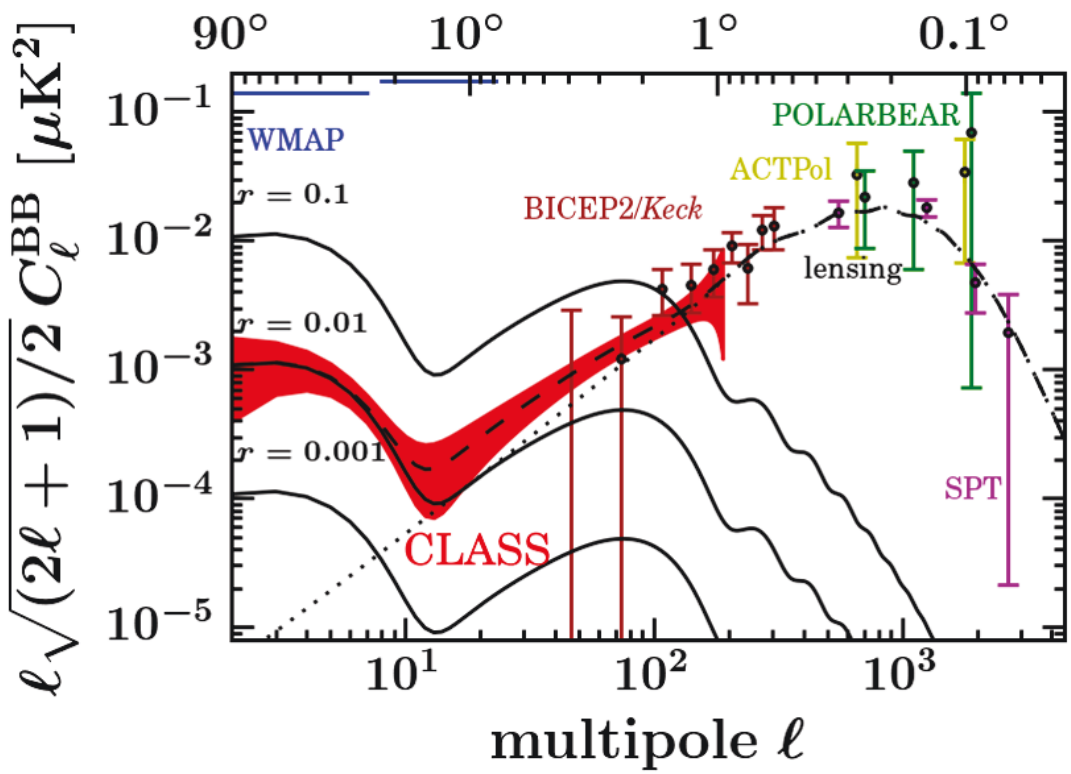

Figure 2.2: CMB B-mode Polarization Power Spectrum. The solid lines show the inflationary B-mode power spectrum at different r values; as the r value decreases from 0.1 to 0.001, the amplitude of the power spectrum decreases accordingly. The dotted line shows the B-mode power leaked from the E-mode through gravitational lensing. The dashed line shows the combination of the two components with $r = 0.01$ for the inflationary B-mode. Measurements from other experiments are also shown in this figure. The red band shows the projected sensitivity per mode from CLASS. Figure credits: Duncan Watts.

B-mode power spectra are shown in Figure 2.2 along with available measurements and the projected CLASS sensitivity. There are two extragalactic sources that generate B-mode power: one is the tensor perturbations from inflation; the other one is gravitational lensing. The gravitational lensing transforms E-modes into B-

modes. Because E-mode power is orders of magnitude larger than B-mode power, E-to-B leakage could be significant. The inflationary B-mode power may dominate at small l (large-scale) as shown in Figure 2.2. Lensing B-modes dominate at small angular scales. As the inflationary B-mode power decreases, the cross-over from lensed B-modes to inflationary B-modes moves to larger angular scales. Therefore, the large angular scale CMB polarization should be measured for the inflationary B-mode power. With the help from large-angular-scale observation, the details of the inflationary B-mode power spectrum will be characterized to further understand the very beginning of the universe.

As shown in Figure 2.2, the WMAP satellite was able to measure large angular scales but it could only provide upper limits given its sensitivity. To measure the inflationary B-mode polarization signal, high sensitivity is required for the experiment.

The CLASS design is optimized to measure the large-angular-scale CMB polarization signal with high sensitivity. The projected sensitivity per mode in Figure 2.2 is shown by the red band. The CLASS project aims at recovering the largest scale signals over most of the sky, with the sensitivity that is able to constrain the inflationary B-mode power at the $r \sim 0.01$ level.[37]

2.1.2 Reionization & Neutrino Masses

The epoch of reionization is a process (at redshift $6 < z < 20$) when first-generation stars and galaxies were ignited, after which the entire universe was ionized.

Understanding the epoch of reionization is critical to understanding the formation of first stars, first galaxies and eventually the details of the cosmic evolution. Currently, the study of the epoch of reionization is still in its early stages. The CMB photons, traveled from the early universe, were scattered and thus picked up information from the epoch of reionization. The most basic information is summarized as the optical depth to reionization τ, the attenuation of the CMB anisotropy since the surface of last scattering. This optical depth helps us to understand the epoch of reionization.

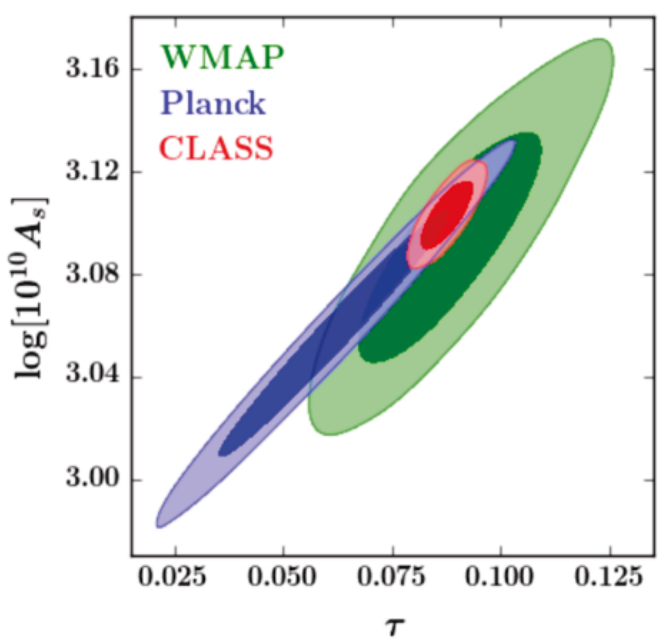

Figure 2.3: Primordial scalar perturbation A_s and optical depth τ posterior distributions.[20] The CMB temperature power spectrum measures $A_s e^{-2\tau}$ as a whole, resulting in a degeneracy between A_s and τ. From WMAP 9-year[22] to Planck 2015,[32] although the sensitivity and resolution on the CMB temperature measurement have improved, constraints on τ and A_s have not improved much due to the degeneracy. With the large angular CMB polarization measurements from CLASS, the degeneracy will be broken, and the measurement on both τ and A_s will be significantly improved. Figure credits: Duncan Watts.

The primordial scalar perturbation amplitude A_s combines with the optical depth τ in the form $A_s e^{-2\tau}$ to determine the amplitude of the measured CMB temperature power spectrum, leading to a degeneracy between the two quantities, as shown in Figure 2.3. However, the large angular scale CMB polarization can measure τ independently. CLASS is designed to measure the τ value with a sensitivity at the cosmic variance limit, which is the intrinsic variance because we only have one universe to observe. So the CLASS polarization measurement at large angular scales will be the best measurement possible short of making a full-sky measurement. Figure 2.3 shows the constraining power at a cosmic-variance-limited level measurement from CLASS. The τ and A_s degeneracy is broken. With a better measurement on τ, we can improve the measured value of the primordial scalar perturbation A_s. This, in turn, will help us to constrain the sum of neutrino masses.

The value of A_s is estimated from CMB large-scale ($> 2°$) anisotropy measurements. In practice, it is derived from a fit to the whole power spectrum, representing the underlying level of initial perturbations. This perturbation can be regarded as an initial state. After billions of years evolution, the perturbation amplitude has evolved into a final state that can be observed by complementary observations, including CMB lensing and galaxy cluster etc.. As we pin down the initial and final states, the evolution of the universe during that period can be better understood. Accordingly, the components governing the evolution can be constrained, including neutrinos. Neutrinos have tiny but non-zero masses, they were relativistic in early

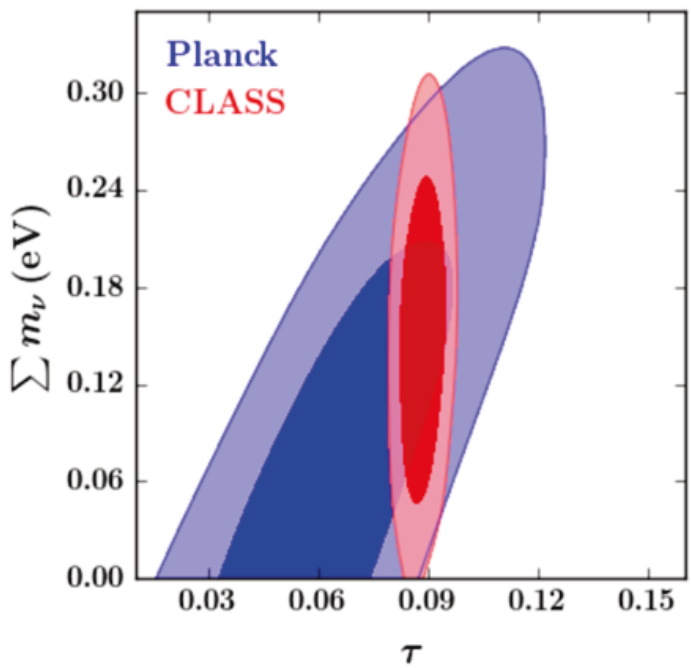

Figure 2.4: Sum of neutrino masses Σm_ν and optical depth τ posterior distributions.[20] This plot shows that an improved measurement on τ constrains the sum of neutrino masses Σm_ν. The blue contour is generated from Planck 2015 Monte-Carlo chain,[32] which weakly constrains the sum of neutrino mass. The polarization measurement from CLASS, cosmic-variance limited, significantly improves the constraints on Σm_ν. Figure credits: Duncan Watts.

universe and became non-relativistic in late universe. As we discussed in Section 1.4, relativistic and non-relativistic matters determine the evolution of the universe differently. The fraction of time when neutrinos were relativistic affected the evolution of the universe, which eventually depends on neutrino masses. Therefore, the sum of neutrino masses can be constrained by the evolution of the universe. Investigations have been made to study the power of CMB in combination with next generation CMB lensing and galaxy cluster studies.[2] With a cosmic-variance-limited large scale E-mode measurement, the constraint is forecast to be $\sigma(\Sigma m_\nu) = 15$ meV (compared

with 103 meV without CMB polarization measurements).[2]

2.1.3 Galactic Sciences

CLASS is able to provide nearly all sky polarization maps over different frequency bands with unprecedented sensitivity. Those maps will also provide valuable information to study our own Galaxy. For example, the 40 GHz signal, containing synchrotron radiation aside from CMB, is a probe of the large scale structure of the Galaxy. With the sensitivity of CLASS, synchrotron emission will be mapped out across the entire Galaxy. This will shed more light on the WMAP haze,[5,15] Fermi bubble[35] and the E/B power imbalance.[33,9] More generally, the deep maps at multiple frequencies will provide more information to understand the structure and dynamics of the Galaxy and the interstellar materials.

2.2 The CLASS Design

To achieve the scientific goals mentioned in section 2.1, the CLASS telescopes are optimized to observe the CMB polarization signal at large angular scales with high sensitivity.

2.2.1 Site & Scan Strategy

Locations at different latitudes on the Earth provide different sky coverages. Assuming scan elevations greater than 45°, 70.7% of the sky is observable on the equator, while only 14.6% of the sky is observable at the South and North poles. Therefore, CLASS should locate near the equator. Besides maximizing sky coverage, the atmospheric transparency and loading also drives the site selection. The ideal site would have minimum in-band atmospheric emission and atmospheric loading, especially in the CLASS observing frequency bands.

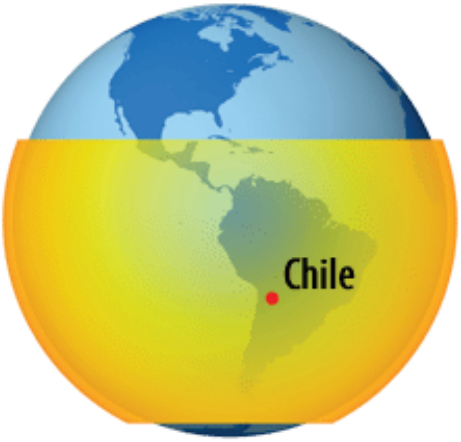

Figure 2.5: The CLASS site is located at the Atacama Desert, Chile. At an observing elevation of 45°, 65% of the sky is observable everyday at this low latitude location. This figure first appeared in the Johns Hopkins University Summer 2014 issue of Arts & Sciences Magazine†.

Combining these two factors, the CLASS site was selected to be in the Atacama Desert, Chile, as shown in Figure 2.5. With a latitude of -23°, 65% of the sky is observable at an observing elevation of 45°. With an elevation of 5200 meters, the

†website: http://krieger.jhu.edu/magazine/v11n2/a-class-by-itself/

site stands above the thickest 5 km of the atmosphere. In a desert, the site is dry with low precipitable water vapor (PWV). These two facts lead to reduced in-band atmospheric emission (as shown in Figure 2.6) and reduced atmospheric loading.

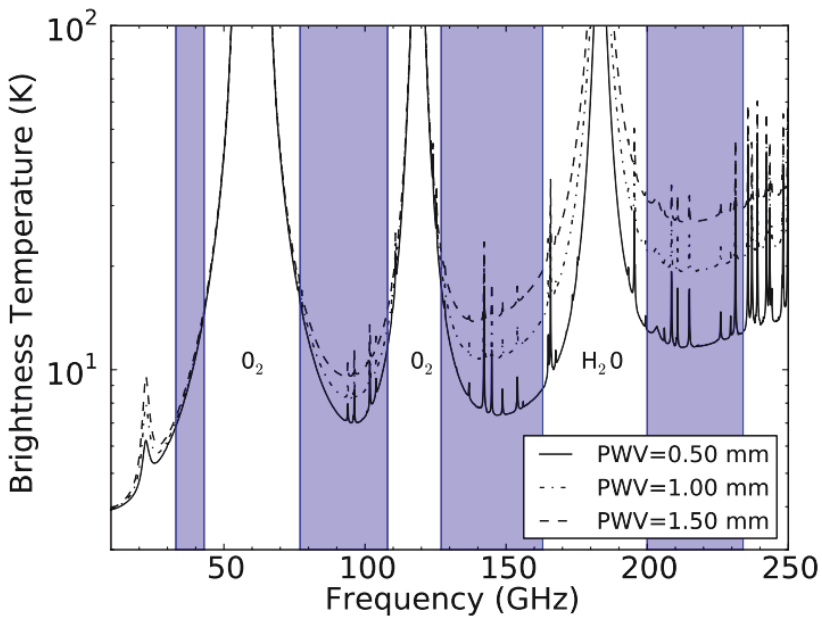

Figure 2.6: Estimated atmospheric brightness temperature spectra from precipitable water vapor (PWV) levels at 0.50 mm, 1.00 mm and 1.50 mm. Atmospheric emission only leaves several windows for microwave observations. Blue bands in the plot are the four CLASS frequency bands, designed to avoid oxygen and water emission lines. Even within those bands, PWV loading increases significantly as PWV rises, especially at high frequency bands. Median PWV at CLASS site is around 1.3 mm[§]. Figure credits: Thomas Essinger-Hileman.[11]

The scan strategy must be designed to recover the largest angular scales on the sky. The CLASS telescopes point to the sky at 45° elevation angle and scan the sky only with azimuthal rotation. The azimuthal rotation (spanning up to 720°) measures a 90° diameter circle on the sky in less than 10 minutes, a timescale on which the

[§]APEX weather monitor, website: www.apex-telescope.org/weather

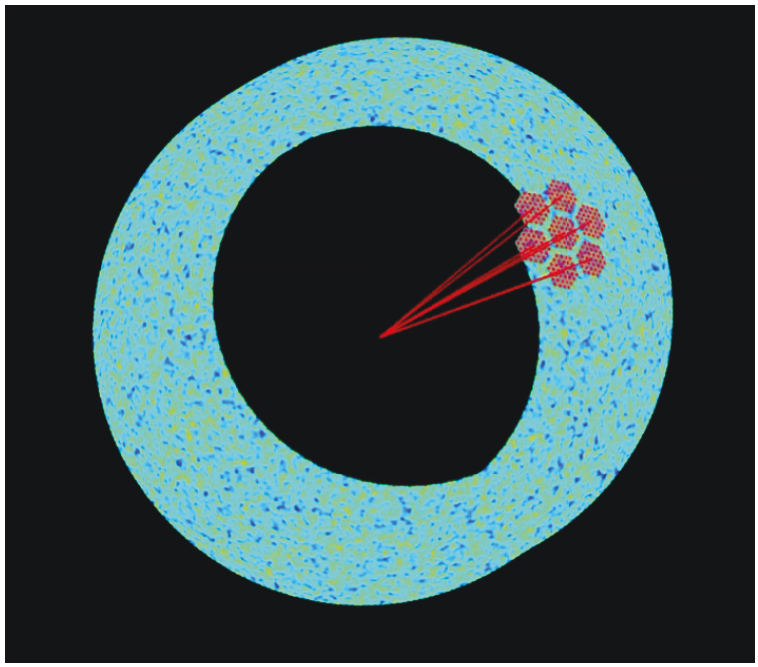

Figure 2.7: The CLASS scan strategy. CLASS telescopes stay at 45° elevation angle and scan the sky with azimuthal rotation. The seven hexagons represent one 90 GHz focal plane projected onto the sky. As the telescope scans azimuthally, the focal plane scans the sky in a circle. The Earth spin moves the circle slowly on the sky. As the Earth spins, the telescopes scan nearly two full rotations in one day. Daily sky coverage is shown in the yellow band in Figure 2.5. Figure credits: David Larson.

CLASS measurement is designed to remain stable (Subsection 2.2.2). As the Earth spins, the azimuthal circle moves across the sky as shown in Figure 2.7. As the Earth spins one round everyday, the telescopes cover the entire survey area (the yellow band in Figure 2.5) with nearly two full rotations. The resulting maps have cross-linked scan circles to allow reconstruction of CMB polarization on the largest angular scales.

This scan strategy enables CLASS telescopes to observe 65% of the sky twice every day. With thousands of detectors, each point on the sky is visited by multiple detectors. To recover full polarization information and check systematic effects, CLASS

telescopes have a boresight axis, which enables daily change of the instrument-sky polarization angle. Finally, the entire survey will have data for each point on the sky measured by thousands of detectors, hundreds of times each, with different polarization angles. Averaging over these data mitigates systematic effects associated with different detectors and variations in responsivity at different times and with different polarization angles.

2.2.2 Fast, Front-end Modulation

Although the CLASS site and scan strategy are optimized to observe large angular scales, atmospheric loading drift and instrumental instability would hinder recovering the extremely faint large-angular-scale structures from CMB polarization. Because of the challenges, CLASS pioneers to be the first and only ground-based nearly all-sky CMB polarization experiment, implementing a novel fast front-end modulation technology.

The idea of modulation is shown in Figure 2.8. Although the atmospheric loading drift can be orders of magnitude higher than the polarized signal, it is unpolarized. If we can modulate only the polarized part, we can recover the polarized incoming signal through the modulation frequency. If the modulation frequency is much higher than the drift frequency, the polarized signal can be recovered with high-fidelity. If the atmosphere is polarized, as long as it changes over time scales slower than the modulation time scale it will not survive synchronously demodulated output averaged

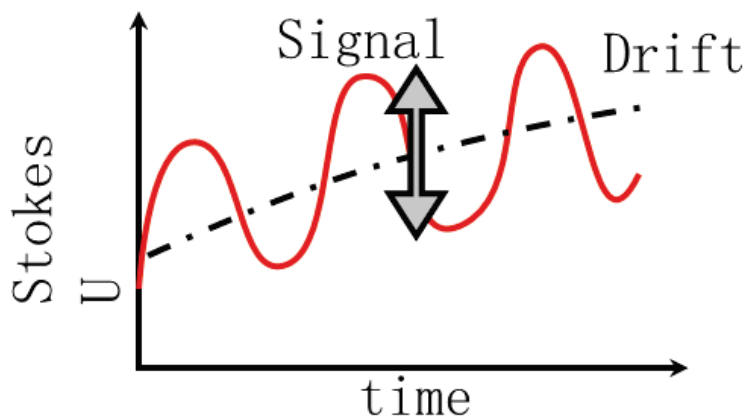

Figure 2.8: The idea of modulation. The modulated data (red) combine a fast-modulated signal and a long-time-scale drift. The signal is "locked" in the amplitude at the modulation frequency. If the modulation is fast enough so that its frequency is much higher than the drift frequency, the signal can be recovered with high-fidelity regardless of the drift. Figure credits: Toby Marriage.

over time to the permanent sky signal.

CLASS uses an instrument called the variable-delay polarization modulator (VPM) to modulate the incoming signal. The VPM has a stationary wire grid in front, backed by a movable mirror. Because the wire grid reflects one linear polarization and transmits the orthogonal one, the transmitted polarization is reflected back by the mirror to merge back with the other polarization but with a phase delay as shown in Figure 2.9. An optical path difference Δ is added during this process:

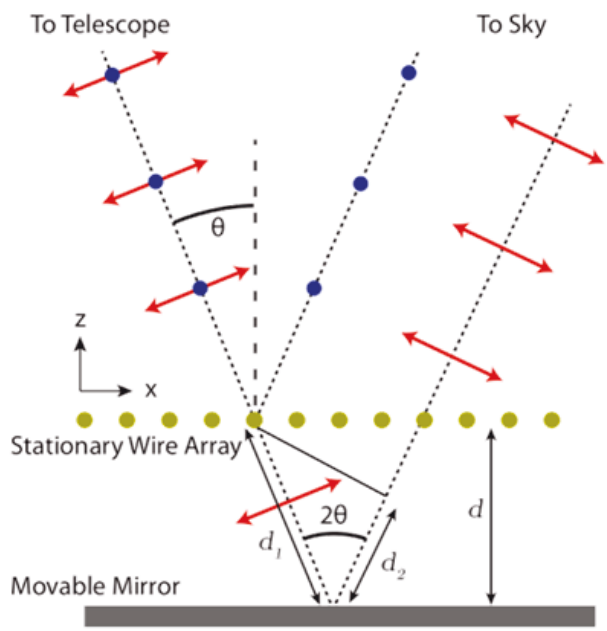

Figure 2.9: The VPM schematic diagram.[10] The VPM consists of a stationary wire array and a movable mirror. The wire array reflects the polarization along the wires while transmitting the orthogonal polarization. The transmitted polarization is reflected by the movable mirror and recombines with the orthogonal polarization. This process adds an additional phase delay between the two orthogonal polarization directions; the amplitude is proportional to the distance between the stationary wire array and the movable mirror. The polarization state therefore changes as the mirror moves. Figure credits: Joseph Eimer.

$$
\begin{aligned}
\Delta &= d_1 + d_2 \\
&= \frac{d}{\cos(\theta)} + \frac{d\ \cos(2\theta)}{\cos(\theta)} \\
&= \frac{1 + [\cos^2(\theta) - \sin^2(\theta)]}{\cos(\theta)} d \\
&= \frac{2\cos^2(\theta)}{\cos(\theta)} d \\
&= 2d\cos(\theta)
\end{aligned}
\tag{2.1}
$$

where d_1, d_2, θ, d are defined in Figure 2.9. Equation 2.2.2 shows that the optical path difference depends on the grid-mirror distance d and the incident angle θ. Once θ is fixed, changing d (which is equivalent to moving the mirror) changes the polarization state at the same frequency. With polarization sensitive detectors to measure the change, the idea of modulation shown in Figure 2.8 is realized.

The VPM is the first optical element in the CLASS telescopes, performing front-end modulation. The front-end modulation guarantees that only the polarization signal from the sky is modulated. Instrumental polarization from optical components is rejected because it is introduced after the modulator and thus is not modulated. This again enables CLASS to constrain the systematic effects from the instrument to provide a high-sensitivity measurement.

Comparing to other modulation technology, such as a rotating half-wave plate (HWP), the VPM is unique in several key ways. The VPM technology uses only reflective elements. This allows it to be used in ambient temperature as the front-end modulator. HWP modulators are made of lossy dielectric materials, which emits excess loading in ambient temperature. Further, front-end modulators need to be large enough to achieve degree-scale resolution. At frequencies below 90 GHz, this translates into meter-sized apertures. Apertures also grow with the size of the focal plane (number of detectors). Further, the VPM design is scalable because all the components are manufacturable to the required meter scale and perhaps beyond,

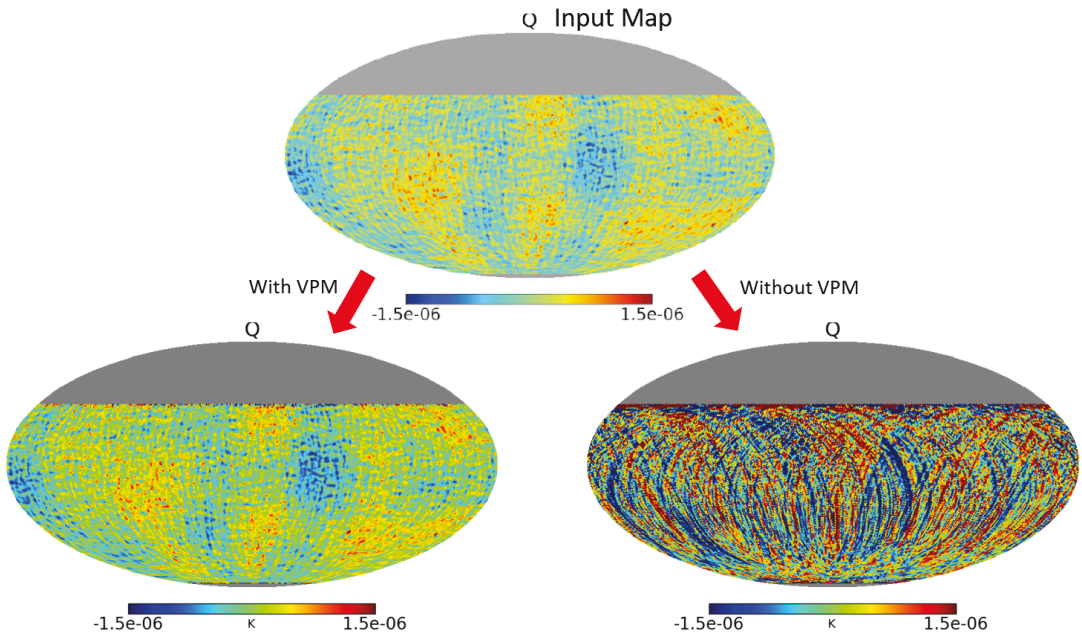

Figure 2.10: Simulations on the VPM performance.[29] The top map is the input map for Stokes Q with some large angular scale structures. On the bottom, the left(right) map represents the recovered map with(without) the VPM. With the VPM, the input large-angular-scale structures are retained; without the VPM, the map is entirely dominated by noise.

which makes the VPM technology a possible solution for next-generation experiments.

End-to-end simulations with realistic systematics were carried out to study the VPM performance on the sky.[29] Figure 2.10 shows that the input large-angular-scale structures are recovered with the VPM, while the recovered map is dominated by noise without the VPM. This study demonstrates that the VPM (or an equivalent fast modulation scheme) is both effective and necessary to recover the large-angular-scale CMB polarization structures on the sky.

2.2.3 Multi-frequency Observation

Polarized galactic emission has proven to be a major contaminant for CMB polarization observations.[7] Galactic emission has a different frequency spectrum than the CMB anisotropy. Therefore, CLASS requires multi-frequency channels to separate the CMB from galactic signals. CLASS was designed to remove the polarized galactic emission by the use of multi-frequency observations, at 40 GHz, 90 GHz, 150 GHz, and 220 GHz; the polarized galactic emission consists of polarized synchrotron radiation and polarized thermal dust emission, whose spectra can be described as a power law as $S \propto \nu^{\alpha}$. At low frequency, the galactic emission is mainly from the polarized synchrotron radiation with a negative spectral index α; at high frequency, it is mainly from the polarized dust emission with a positive spectral index α. As shown in Figure 2.11, the addition of the two components reaches its minimum at around 70 GHz, but it is still higher in amplitude than the inflationary B-mode polarization power. The polarized galactic emission needs to be removed before the inflationary B-mode power could emerge. Templates for polarized synchrotron and dust emission can be established through low (40 GHz) and high (220 GHz) frequency maps respectively. Those templates would, in return, be used to subtract the polarized galactic emission to recover the inflationary B-mode polarization signal. Alternatively, all four CLASS channels could be simultaneously fit for three components: CMB, synchrotron emission, and dust emission.

As noted earlier, although polarized galactic emission is a contaminant for CMB

polarization studies, this radiation contains rich information for various Galactic studies (See Subsection 2.1.3).

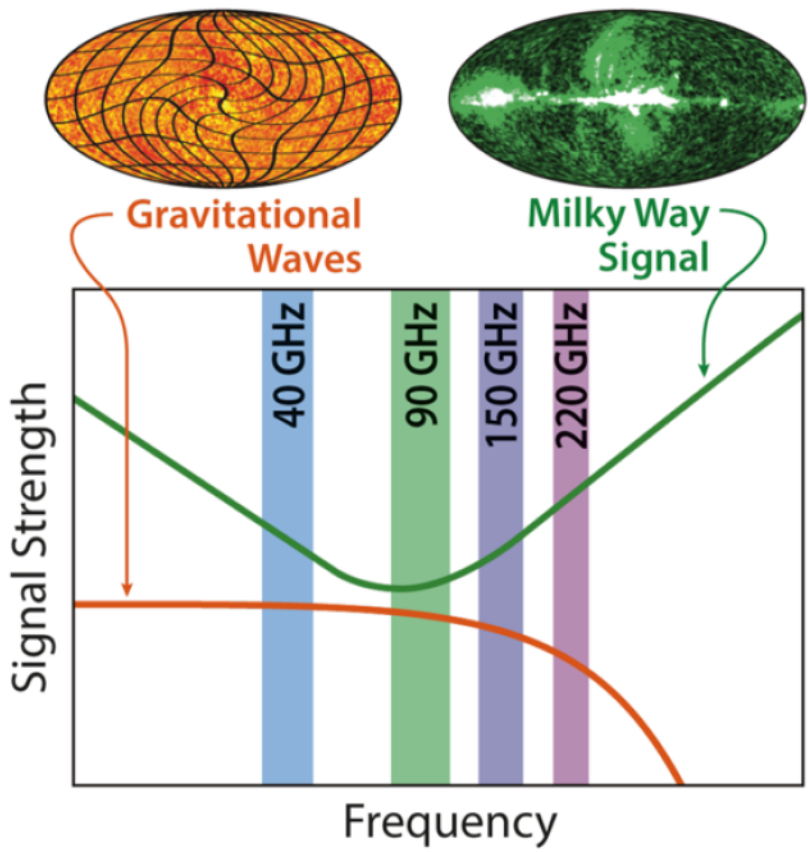

Figure 2.11: CLASS multi-frequency observations. The plot shows the spectra for the CMB B-mode polarization from inflationary gravitational waves (orange) and the Galactic emission (green). The four vertical bands represent the four CLASS frequency bands: 40 GHz, 90 GHz, 150 GHz, and 220 GHz. The 40 GHz map can be used to make a polarized synchrotron template, while 220 GHz map can be used for a polarized dust template. Together, these templates will be used to subtract the galactic emission in the final CMB polarization maps. This figure first appeared in the Johns Hopkins University Summer 2014 issue of Arts & Sciences Magazine[‖].

[‖]website: http://krieger.jhu.edu/magazine/v11n2/a-class-by-itself/

2.3 The CLASS Telescopes

The CLASS experiment consists of four telescopes: one observes at 40 GHz, two observe at 90 GHz, and one dichroic telescope covers 150 GHz and 220 GHz. This design optimizes the sensitivity for a final CMB polarization map after subtracting foreground components from 40 GHz and 220 GHz bands. Mechanically, two telescopes share one mount pointing to the same direction on the sky. Overall, the observatory has two mounts supporting four telescopes observing the sky at four frequency bands, as shown in Figure 2.12.

The four CLASS telescopes share a common optical design as shown in Figure 2.13. Incoming light encounters the VPM first at the front end. The modulated light is then reflected by the primary mirror and the secondary mirror before it enters the cryogenic receiver.

Details of the cryogenic receiver are shown in Figure 2.14. After the incoming light is modulated and focused by the warm optics, it enters the cryogenic receiver through a 46 cm-diameter ultra-high-molecular-weight polyethylene (UHMWPE) window. The window must maintain the vacuum while being transparent to microwave. In the receiver, the radiation first passes through stages of optical filters, which either reflect or absorb the infrared thermal loading before it enters a colder stage. The radiation is then focused by two high-density polyethylene (HDPE) lenses before it reaches the feedhorns on the focal plane.

CLASS implements feedhorn-coupled detectors to control beam systematics, with

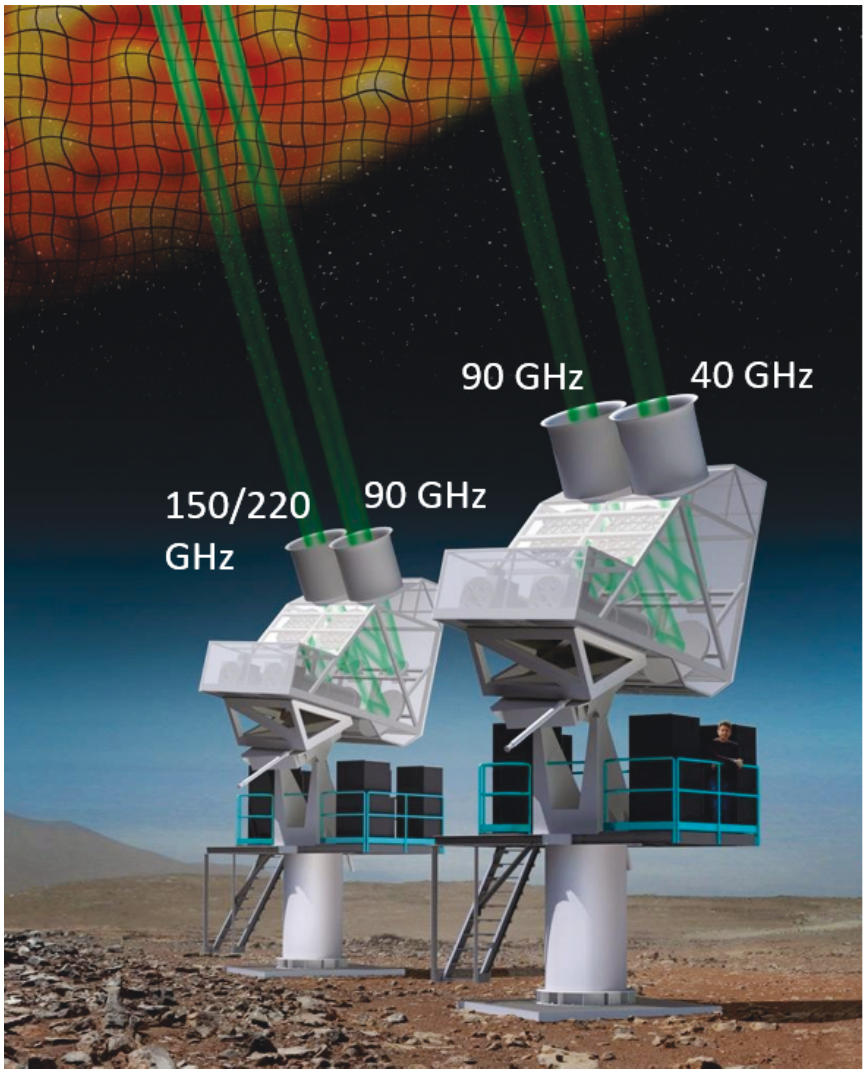

Figure 2.12: CLASS telescopes. CLASS is designed to have four telescopes: one observes at 40 GHz frequency band, two observe at 90 GHz frequency band, and one dichroic telescope observers at 150 GHz and 220 GHz frequency bands. Two telescopes share one mount with co-pointing. This figure first appeared in the Johns Hopkins University Summer 2014 issue of Arts & Sciences Magazine[††].

easily-machined smooth-walled feedhorns developed.[38] The feedhorns couple the radiation to high-efficiency polarization-sensitive detectors.[4,36] The radiation collected by one feedhorn is sampled on one detector chip, as shown in the top photographs

[††]website: http://krieger.jhu.edu/magazine/v11n2/a-class-by-itself/

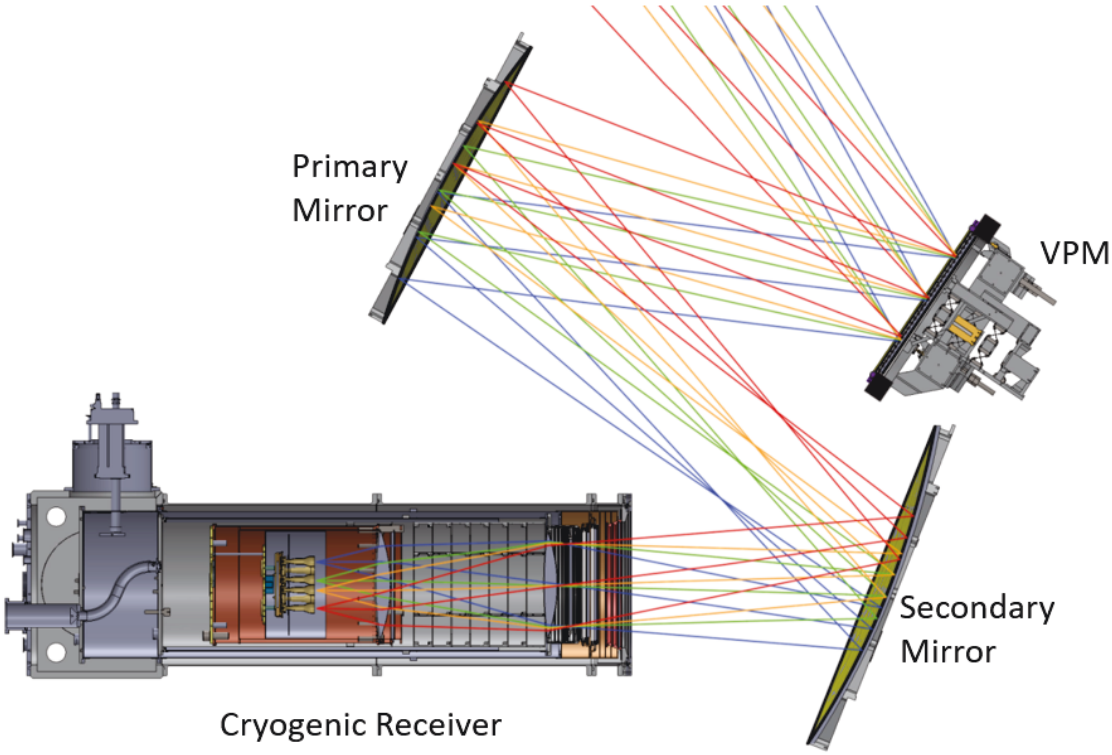

Figure 2.13: CLASS 40 GHz telescope design. The 40 GHz telescope components are shown in this figure, including the VPM, the primary mirror, the secondary mirror, and the cryogenic receiver. Colored lines represent light rays converging onto four feedhorns on the focal plane. The optics and receiver models are made by Joseph Eimer.

in Figure 2.14. The two orthogonal sets of antennas separate the two orthogonal polarization signals and directs each through a microstrip. After being guided by the microstrip, the energy is dissipated on a TES island. The TES is maintained on its super-conducting transition curve, so any change in temperature leads to a significant change in resistance. Operating the detectors at low temperature ($\sim$150 mK) significantly reduces the noise. This cutting-edge detector technology enables CLASS to measure the CMB polarization with high-sensitivity.

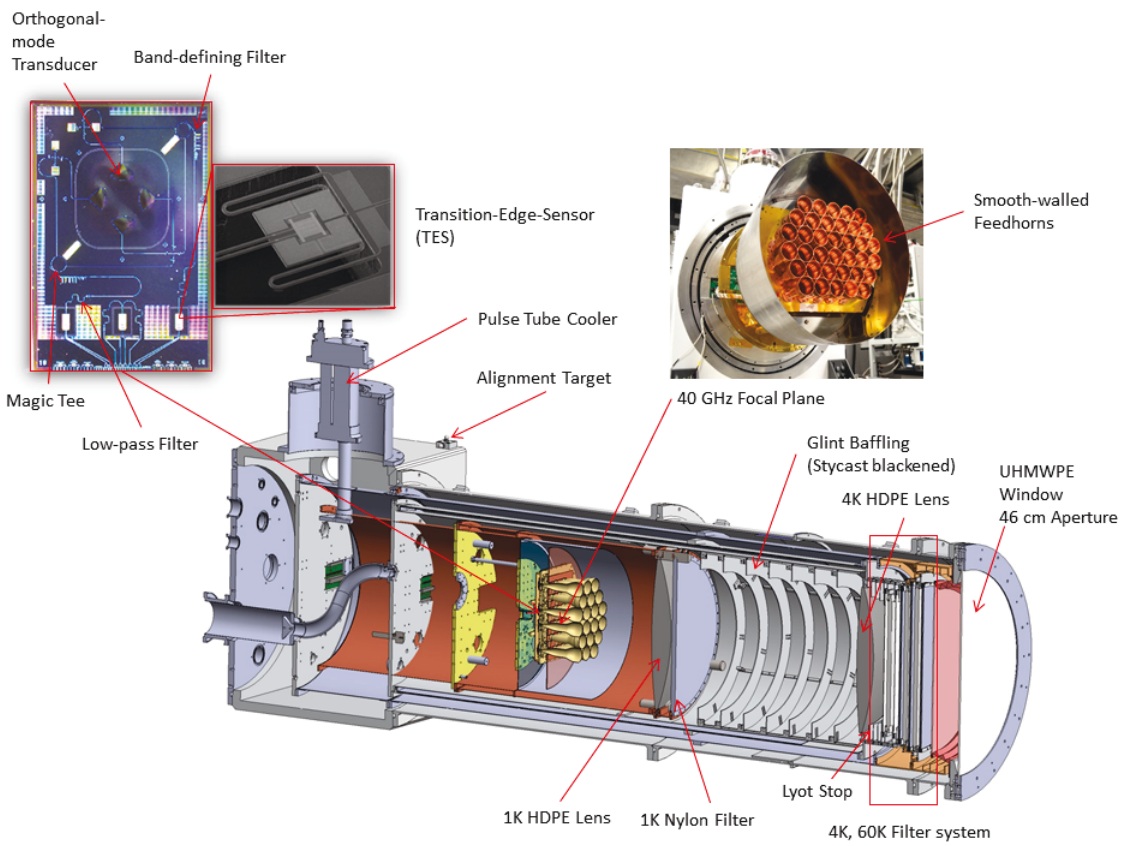

Figure 2.14: CLASS 40 GHz receiver design. The 40 GHz receiver is presented in a cross-section view. Critical optical components are pointed out. The top right photograph shows the focal plane assembly. The top left one shows a detector chip with a scanning-electron-microscope image of the Transition Edge Sensor (TES). Photo credits: Dave Chuss, Kevin Denis, and David Larson.

Chapter 3

Optical Components

To implement the CLASS design, a suite of new optical components needed to be developed and tested. A Fourier Transform spectrometer (FTS) and a Large Aperture Bolometer were first developed for characterizing the optical properties of CLASS components. Then I developed and tested an optical filter system and a cryogenic window using these two instruments.

3.1 Fourier Transform Spectrometer (FTS)

A Fourier Transform Spectrometer (FTS) is an instrument developed to measure spectral information for optical components (including the CLASS cryogenic window, filter system components, and detectors) or an entire system. The FTS covers the frequency range from 25 GHz to 1 THz. This frequency range covers the CLASS

frequency bands and beyond, which enables us to check in-band and out-of-band optical properties. It also measures spectra up to 1 THz, which helps characterize thermal heating and loading on the focal plane. The FTS is designed to have an aperture similar to the CLASS optical components (around 40 cm), which enables the components to be tested in full scale.

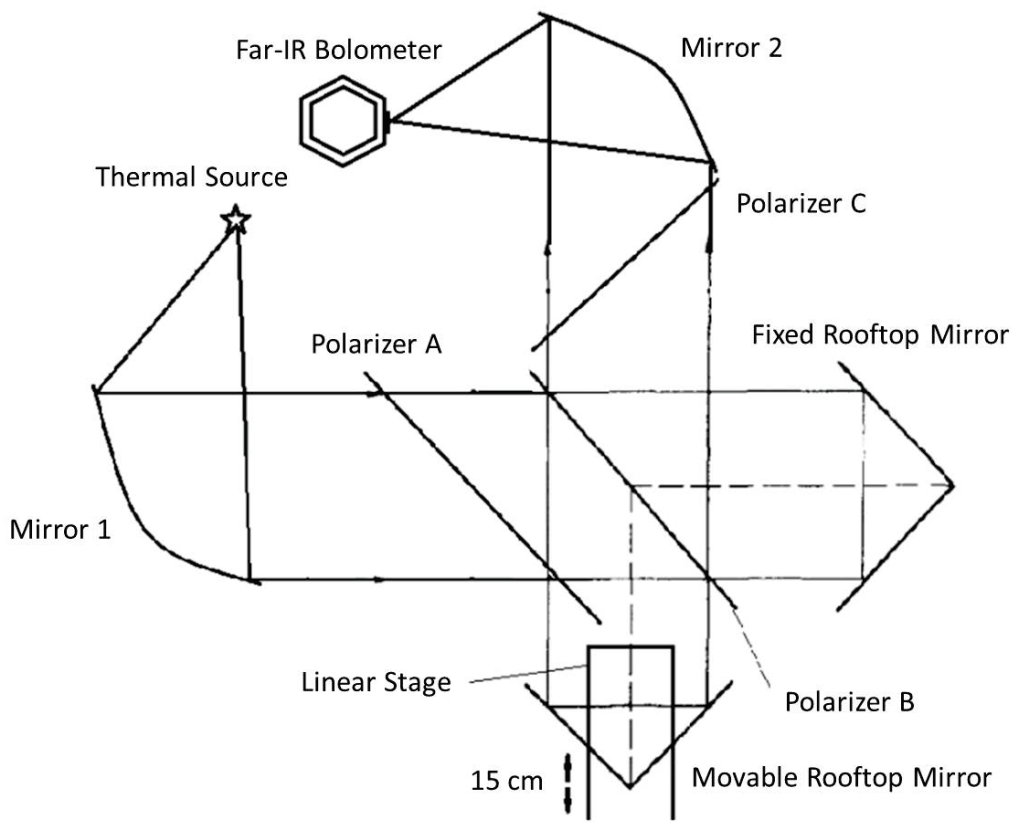

Figure 3.1: Schematic diagram of the Fourier Transform Spectrometer (FTS). The FTS contains two reflective mirrors, three polarizers, one fix rooftop mirror, and one movable rooftop mirror. This figure was originally made by Tiffany Wei.

The schematic diagram of the FTS is shown in Figure 3.1 (Tiffany Wei, Senior Thesis, Johns Hopkins University, 2012). Diverging radiation coming out of a thermal source is first collimated by a parabolic reflective mirror (Mirror 1). Then the

unpolarized radiation passes through a horizontal linear polarizer (Polarizer A). After the horizontal polarization is selected, the radiation encounters another polarizer (Polarizer B) whose polarization direction orients 45° from horizontal. This polarizer acts as a beam splitter. The incoming horizontally-polarized beam is split (reflected/transmitted) evenly. The split two beams propagate towards two separate rooftop mirrors. One of the rooftop mirrors is fixed, while the other one is movable. After reflection by the rooftop mirror, the two beams merge back at the beam splitter (Polarizer B). The movable rooftop mirror can change the optical path difference between the two arms. When reflected by the rooftop mirrors, the polarization is flipped about the rooftop mirror vertical spine, so that the arm that was initially reflected is transmitted after the reflection, and vice versa. The merged beam then continues in the other direction, with the polarization as a superposition of two orthogonal linear polarizations with a phase difference. Then the final polarizer (Polarizer C) selects the projection of the horizontal polarization again. When the two beams are in phase, the merged beam after Polarizer B is horizontally polarized, and the power after Polarizer C reaches the maximum. When the beams are exactly out of phase, the radiation after Polarizer B is vertically polarized, the power after Polarizer C is minimized. Finally, the collimated beam is focused by another reflective mirror (Mirror 2) onto the detector.

The two parabolic mirrors and two rooftop mirrors were designed with the software

Zemax* and sent to a shop for manufacturing. The polarizers are based on Mylar sheets†. A layer of aluminum (300 $\sim$ 500 Å) was first sputtered on a $2' \times 2'$ Mylar sheet (6.2 μm thick). The aluminum layer was then etched into polarizing grids, which are 50 μm-wide lines with 50 μm gaps between them, i.e. 100 μm grid spacing. The aluminum polarizing grids reflect the linear polarization along their direction and transmit the orthogonal one, so they can be used as polarizers at sub-mm wavelengths. The fabrication was done by Tech-Etch‡. Finally, the linear stage (Aerotech PRO115-HS-150)§ controls the motion of the movable rooftop mirror. It provides position accuracy of 10 μm across a range of 150 mm. The parallelism is constrained within 0.5 mm across 150 mm ($\sim$ 0.2 degrees).

The source and detector have two combinations. One is a broadband configuration with a 700 K thermal source and a far-IR 1.6 K bolometer system from IR-lab¶. This configuration provides spectral information from 100 GHz to 1 THz, limited by the bolometer frequency range. In this configuration, intensity data are taken as a function of the linear stage position before further analysis. The other configuration is a narrow band configuration with coherent sources and detectors that, taken together, cover the in-band frequencies. One set covers a frequency range from 32 GHz to 44 GHz, while the other covers from 80 GHz to 100 GHz. Millitech‖ and Hittite**

*Zemax L.L.C., website: http://www.zemax.com/
†Mylar Sheet description, website: http://www.grafixplastics.com/
‡Tech-Etch Photo Etching, website http://www.tech-etch.com/
§Aerotech Inc., website: https://www.aerotech.com/
¶Infrared Laboratories, website: http://www.infraredlaboratories.com/Bolometers.html
‖Millitech, website: http://www.millitech.com/
**Hittite Microwave, website: http://www.analog.com/en/index.html

provide the coherent microwave parts. In the coherent configuration, the narrow source sweeps the frequency range much faster than the measurement integration time, so the measurement is over a bandwidth covered by the frequency sweep. The rest is similar to the broadband configuration.

The instrument measures intensity I from the detector with corresponding linear stage position x, this gives us the intensity I as a function of x:

$$I = I(x).$$

Its Fourier transformation provides the power at wavenumber k space $g(k)$:

$$g(k) = \int_{-L/2}^{L/2} I(x) e^{ik\,2x} dx,$$

where L is the distance range covered by the linear stage (150 mm), k is the light wavenumber. The phase delay is $2kx$, where x is the position of the movable mirror. The factor two results from the light ray in that arm transversing the distance twice. The radiation frequency can then be calculated as:

$$\nu = \frac{k}{2\pi} c,$$

where c is the speed of light in vacuum. The final spectrum is given by:

$$f(\nu) = g(\frac{2\pi\nu}{c}) = \int_{-L/2}^{L/2} I(x) e^{i\frac{2\pi\nu}{c}2x} dx.$$

Spatial information is transformed into frequency information. The spatial range determines the spectral resolution while the spatial resolution determines the spectral range. This FTS is designed to cover the frequency range from 10 GHz to 1000 GHz with spectral resolution at 1 GHz level. This requires spatial information to cover a range of 75 mm with position accuracy of 150 μm, which is well within the specifications of the linear stage.

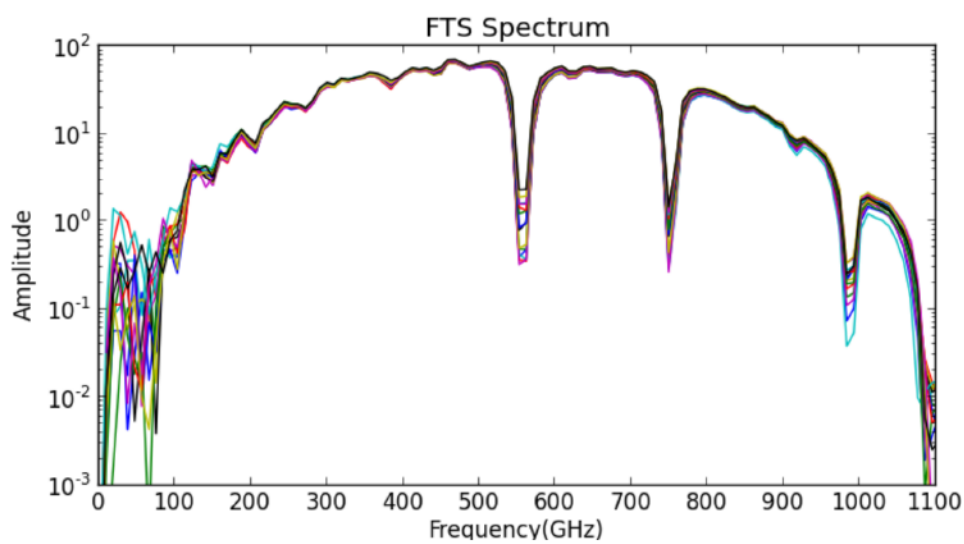

Figure 3.2: FTS intrinsic spectra from the broad band configuration. Fifteen independent measurements are presented in this figure. The consistency shows the repeatability of the instrument from 100 GHz to 1 THz. The limits are constrained by the bolometer. The prominent absorption lines are from atmospheric gas molecules.

Before performing a discrete Fast Fourier Transform (FFT) on the data, I apodized

the data to avoid the hard boundary at two ends ($x = 0$ and $x = 150$ mm). Details can be seen in Appendix A. The broad-band and narrow-band configurations provide similar results except they cover different frequency ranges. Figure 3.2 shows the intrinsic spectra for the broad-band configuration. Fifteen independent measurements are presented in this figure. The consistency between 100 GHz to 1 THz proves the ability of the instrument to measure spectral properties within this region reliably in the broad-band configuration.

With this instrument, different materials were tested at their full size (Section 3.3), which provides invaluable information for implementing the CLASS optical design. Finally, the FTS was used to calibrate the system spectral response during integration tests.

3.2 Optics Test Cryostat

To test the 300 K and 60 K optics more conveniently, we built a reduced version of the CLASS receiver. It has the same diameter with a truncated length and is cooled down by a wet dewar with liquid nitrogen. The reduced cryostat is mainly used for two purposes: the optical filters bolometric performance test and the large-aperture (46 cm) vacuum window structural test.

The cryostat is around one meter tall and 60 cm in diameter. It has a chamber half of its size within as a wet dewar. After the cryostat is pumped under vacuum,

liquid nitrogen is transferred into the coolant chamber. The coolant chamber has a cold plate as its top, which can reach temperature of 77 K when it is filled with liquid nitrogen. The lid of the cryostat is 40 cm above the cold plate. The lid is used to install the vacuum window. Therefore, beneath the vacuum window, the 300 K and 60 K filters can be placed on the cold plate. This setup mimics the configuration in actual CLASS receivers.

The filters along with the vacuum window are designed to block infrared radiation, since excessive infrared loading impedes cryostat cool down. The optical components are also to be tested in their full sizes (around 40 cm in diameter). Thus, a special large aperture bolometer was developed.

The incoming radiation loading is estimated around 75 W, while the residual loading must be less than 1 W after 300K and 60K filter systems. So the bolometer should measure a loading range from 0.1 W to 100 W.

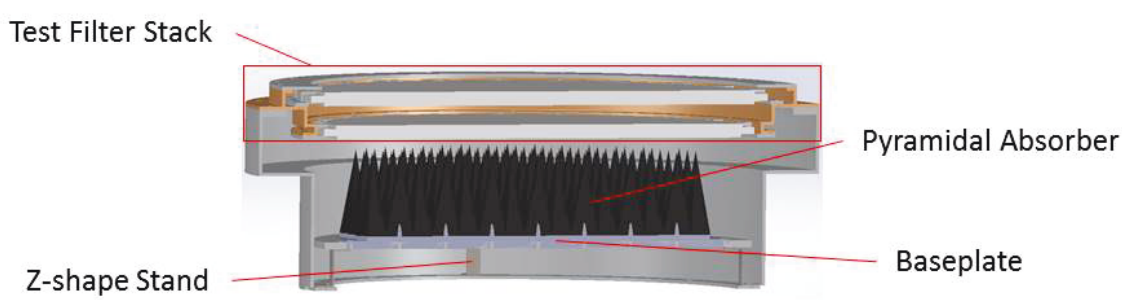

Figure 3.3: The large aperture bolometer with a test filter stack. This assembly sits within the test cryostat on the cold plate. The large aperture bolometer (consisting of pyramidal absorber, baseplate, and Z-shape stands) is thermally coupled to the cold plate. The filter stack is supported by an aluminum structure with good thermal conduction to the cold plate.

The design starts from a 40 cm diameter aluminum baseplate with good thermal conductivity. The temperature difference across it is uniform to within 3 K during operation. On the baseplate, pyramidal absorber tiles (Tessellating TeraHertz RAM from Terahertz*) are epoxied on with high-thermal-conductivity Emerson & Cuming Stycast 2850†. Far-infrared reflection from the pyramidal absorbers is < -35 dB.

The thermal baseplate is thermally coupled to the cold plate by four 'Z' shape stands. To cover the required power range from 0.1 W to 100 W, two sets of Z stands were built, one of aluminum and the other one of stainless steel. The aluminum one has higher thermal conductivity and is used for a high power range (2 - 100 W), while the stainless steel one, with its lower thermal conductivity, is used for a lower power range (0.1 - 5 W).

Once the absorptive plate is in thermal equilibrium, the thermal energy flow relation can be written as

$$P_{\text{incident}} = P_{\text{radiation}} + P_{\text{conduction}}, \tag{3.1}$$

where P_{incident} is the incident radiation power, $P_{\text{radiation}}$ is the power that the absorber radiates out, and $P_{\text{conduction}}$ is the power conducted down to the cold plate via the Z stands.

*Terahertz, website: http://www.terahertz.co.uk/

†Emerson&Cuming Adhesive, website: https://www.ellsworth.com/manufacturers/emerson-cuming/

Fifteen silicon diode* thermometers monitor the temperature at different positions. The temperature data not only reveal the temperature gradient but also help estimate the powers in Equation 3.1. Using the temperature of the pyramidal absorbers, $P_{\text{radiation}}$ is estimated assuming blackbody radiation. Using the temperature of the baseplate and the cold plate, $P_{\text{conduction}}$ can be estimated after calibration. Then according to equation 3.1, the incident power P_{incident} can be estimated. P_{incident} is an upper limit to loading incident on the bolometer from the outside, since loading from the walls of the aluminum support structure also contributes to it.

The test filter stack in Figure 3.3 can be left open or replaced by any filter or a combination of filters. The large aperture bolometer measures the loading, which provides another piece of valuable information for optical filter design.

3.3 Optical Filters

The CLASS detectors require a base temperature < 100 mK to operate. It is this low-temperature operation that guarantees CLASS high-sensitivity. However, this low-temperature operation sets a strict criterion on thermal loading, given the limited dilution refrigerator's cooling power. According to this requirement, optical loading on the focal plane should be limited to less than 100 μW. The large aperture of CLASS receivers accepts around 75 W of power at the vacuum window. The

*Lake Shore UT-670 Silicon Diode, website: http://www.lakeshore.com/products/Cryogenic-Temperature-Sensors/Silicon-Diodes/DT-670/Pages/Overview.aspx

majority of the power is carried by $\sim 100\,\mu$m far-infrared radiation instead of our in-band frequencies. So starting from the window to the focal plane, the optical loading should be reduced from 75 W to 100 μW, almost six orders of magnitude. Meanwhile, the in-band radiation should be transmitted with high efficiency.

With the FTS and the large aperture bolometer, spectral and bolometric properties of individual materials were tested. The information was used to design the CLASS filter system. Finally, the spectral and bolometric properties of the assembled filter system design were characterized in the same fashion.

3.3.1 Metal Mesh Filter

A metal mesh filter is a low-pass optical filter with tunable cutoff frequency. It is reflective with minimal emission, so that it can be used at high temperature stages. CLASS metal mesh filters are 45 cm in diameter. The filter film is made by Tech-Etch and PhotoMachining* and assembled on tensioning rings at Johns Hopkins University.

As shown in Figure 3.4, CLASS metal mesh filters are thin plastic substrates with two-dimensional grid aluminum squares on them. The square pattern has spatial period g ($g = 200\ \mu m$ in Figure 3.4 left). This pattern strongly reflects radiation with wavelength shorter than g; while it is transparent to radiation with wavelength longer than g through diffraction according to Huygens's Principle. The FTS (described in Section 3.1) and the large aperture bolometer were used to measure the spectral

*PhotoMachining Inc., website: http://www.photomachining.com/

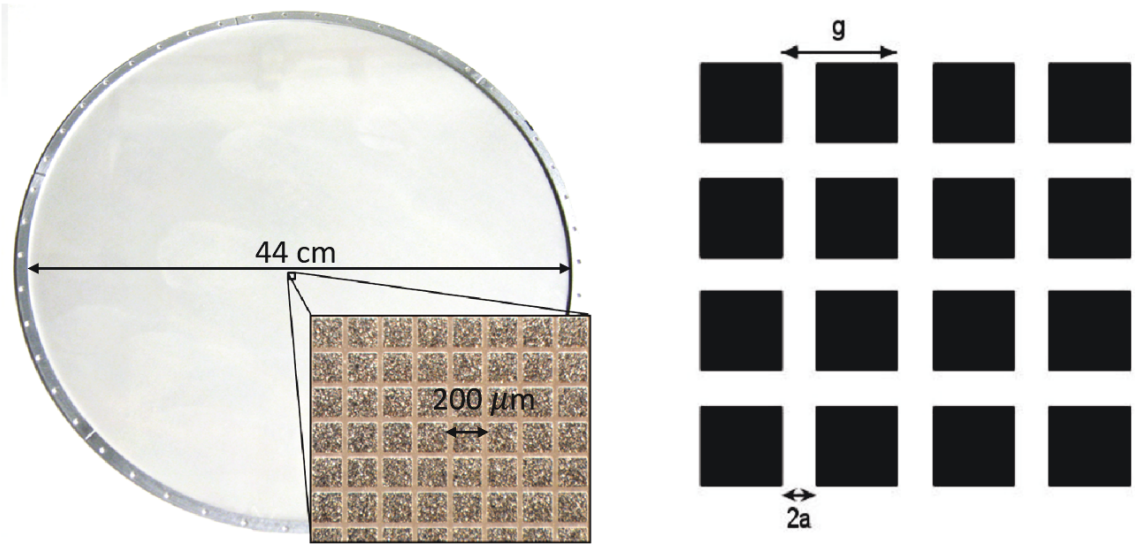

Figure 3.4: A CLASS metal mesh filter is shown on the left with a microscopic photograph of the grid structure. On the right, a cartoon of the grid pattern is presented with the spacial period g and grid spacing $2a$ marked. Figure on the right is made by Thomas Essinger-Hileman.

and bolometric properties of these filters. High in-band transmission was characterized (Figure 3.5), and Figure 3.6 shows the residual transmitted power after a given number of filters. After two layers, only marginal improvement was achieved by increasing the number of filters. This can be understood qualitatively. Because metal mesh filters are purely reflective, increasing layers increases the chance to trap radiation between layers, leading to resonant transmission and reflection, which results in marginal improvement in reflecting short wavelength radiation.

After full-size spectral and bolometric characterization, metal mesh filters were selected to be used in CLASS 40 GHz filter system at different stages (see Section 3.5 for the entire optical filter system). At each stage, the metal mesh filters were only stacked to the number of two..

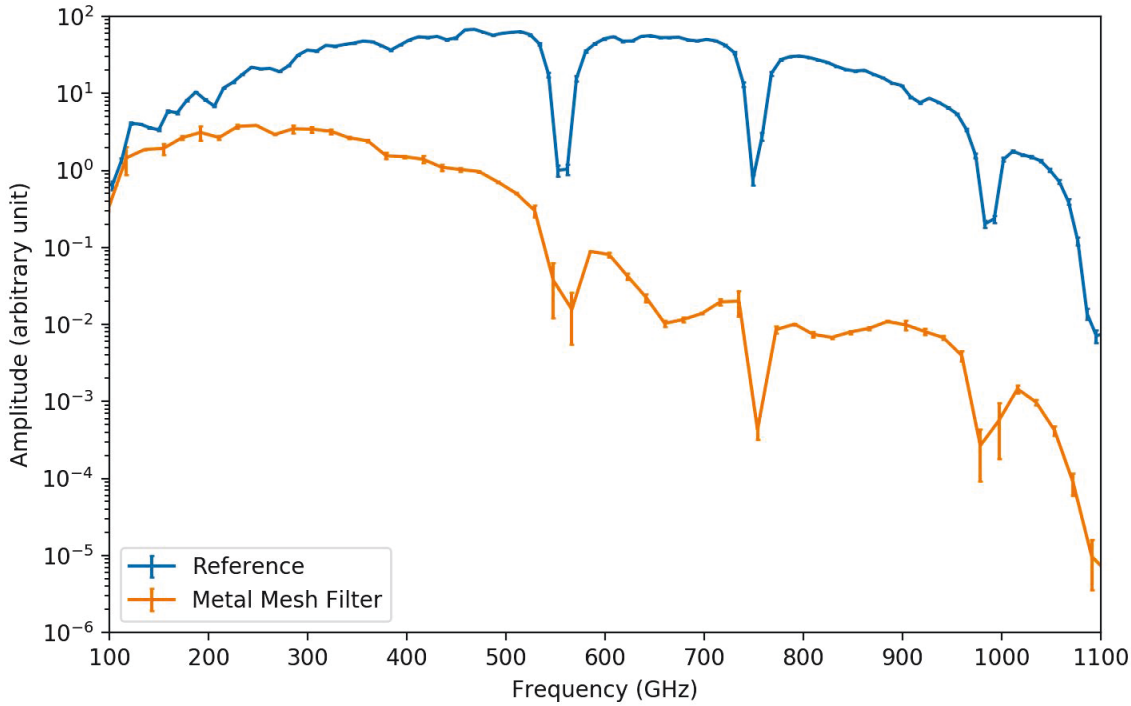

Figure 3.5: Metal mesh filter transmission spectrum measured by the FTS broad band configuration. From 100 GHz to 1000 GHz, the metal mesh filter transmission spectrum deviates further away from the reference, meaning it is cutting off higher frequency signal while maintaining high in-band pass. Error bars were generated among multiple measurements.

3.3.2 Polytetrafluoroethylene (PTFE) Filter

As shown in Figure 3.6, because metal mesh filters rely completely on reflection, stacking more than two only gives marginal improvement. However, if infrared absorptive filters are placed within the "cavities", together their performance can be significantly improved. After spectral and bolometric characterization, the absorptive filter material for CLASS 40 GHz telescope has selected as Polytetrafluoroethylene (PTFE). It absorbs infrared radiation above one terahertz with high in-band microwave transmission.

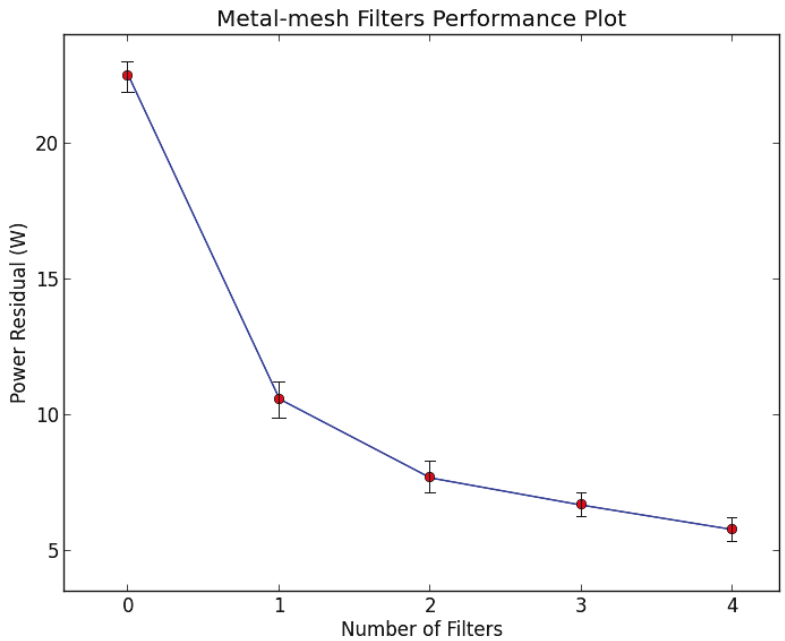

Figure 3.6: Metal Mesh Filter Stacking Performance. The plot shows the transmitted thermal loading after certain number of metal mesh filters. This measurement is made with the large aperture bolometer described in Section 3.2.

Anti-reflective (AR) coating was also placed on the absorptive filter surfaces. Ideal AR-coating requires two parameters to be controlled, the index of refraction n and the coating thickness d:[8]

$$n = \sqrt{n_1 n_2}, \tag{3.2}$$

$$d = \frac{\lambda}{4n}, \tag{3.3}$$

where n_1 and n_2 are the index of refraction for the two associated media and λ is the AR-coating wavelength in vacuum. CLASS 40 GHz telescope filters use simulated dielectric AR-coating. To make simulated dielectrics, a pattern of sub-wavelength

holes is drilled into the dielectric surface. This lowers the effective density and hence the dielectric constant, so it equivalently lowers the index of refraction. The index of refraction is then tunable by controlling the pattern and drill size, while the thickness of the AR-coating is controlled by the drill depth. This work was done by Katie Harrington and Sumit Dahal.

The PTFE filters together with metal mesh filter pairs (see Subsection 3.3.1 for details) form the basic filter assembly. Unlike the reflective metal mesh filters, absorptive filters also have intrinsic emission, which adds extra in-band loading. The loading is proportional to the temperature, so only low-temperature absorptive filters are allowed to be directly visible at lower-temperature stages.

The solution is that we use the basic filter assembly (containing metal mesh filters pair and a PTFE filter) at different temperature stages to bring the incoming loading down step by step. Different configurations were tested in the test cryostat with the large aperture bolometer measuring the loading. The design finally settled on having two basic filter assemblies (metal mesh filter pairs and a PTFE filter) at 60 K stage and one at 4 K stage. The PTFE filter temperature settle around 110 K, 60 K, and 10 K respectively . Lower temperature stages are directly exposed to only the 10 K stage. The 10 K stage also guards the lower-temperature stages from 110 K and 60 K filter emission.

3.3.3 Nylon Filter

Nylon 6,6 is an absorptive material with stronger absorption than PTFE, which was mentioned in Subsection 3.3.2. Its absorption increases steeply as frequency. Therefore, by changing its thickness, its cutoff frequency is tuned. This property gives it an advantage to cutoff the high-frequency power below 1 THz. However, nylon has a slightly higher in-band loss. Spectral measurements were made with samples at different thickness at 4 K, the measured optical properties of this material at millimeter-wave are consistent with literature values.[26]

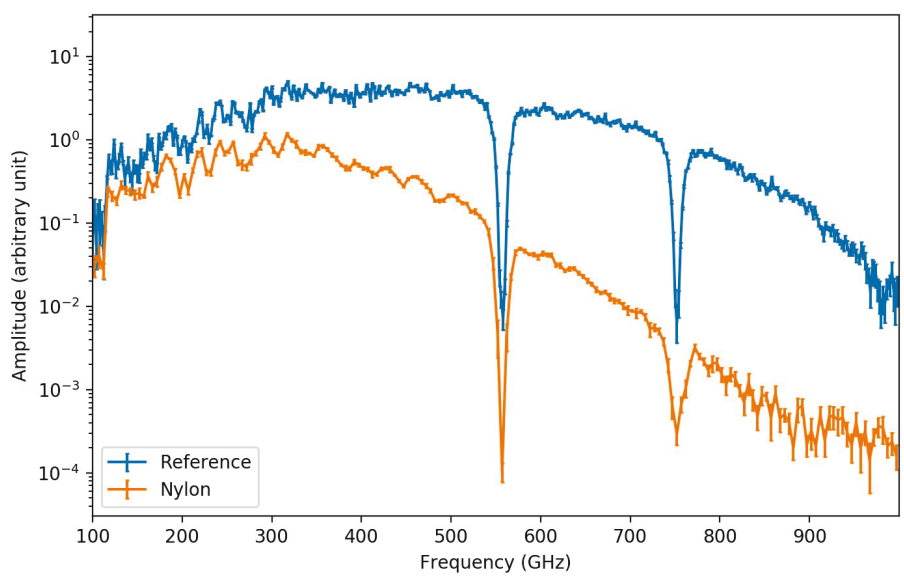

Figure 3.7: Nylon filter transmission spectrum measured by the FTS broad band configuration. Spectral information of the CLASS 40 GHz nylon filter is measured at ambient temperature, showing a cutoff frequency around 300 GHz. Error bars were generated among multiple measurements.

After comprehensive calculation and characterization, a nylon filter was designed to launch from 1 K stage to minimize its emission. The filter temperature settles

around 4 K during operation. Two-sided simulated dielectric anti-reflective coating was also machined on this filter. Its thickness is set to produce a cutoff frequency below 1 THz. The task of this final filter is to absorb extra loading below 1 THz. Figure 3.7 shows the spectral measurement from the FTS at ambient temperature.

3.3.4 Scattering Powder Filter

During the filter system development, many other kinds of filters were studied and characterized. One of the most promising filters was scattering powder filters.

This kind of filter is designed to replace the PTFE absorptive filters. The idea is to have silicon powder particles at a certain size loaded in a microwave transparent medium. Radiation with wavelengths longer than the particle size would see an effective dielectric and transmit through the material, while radiation with wavelength shorter than that would be strongly scattered. The advantage is two-fold: the cutoff frequency can be tuned by selecting the size of the particle, instead of relying on the intrinsic property of PTFE; in-band transparency could also be increased by selecting a transparent carrier material.

Initially, a kind of plastic, polymethylpentene, was selected because of its high microwave transparency. A prototype scattering powder filter was fabricated using this plastic, whose transmission spectrum is shown in Figure 3.8. This material was not deployed in the first telescope because of immature AR-coating technology. Currently, another material, aerogel, is actively being tested. Because aerogel is

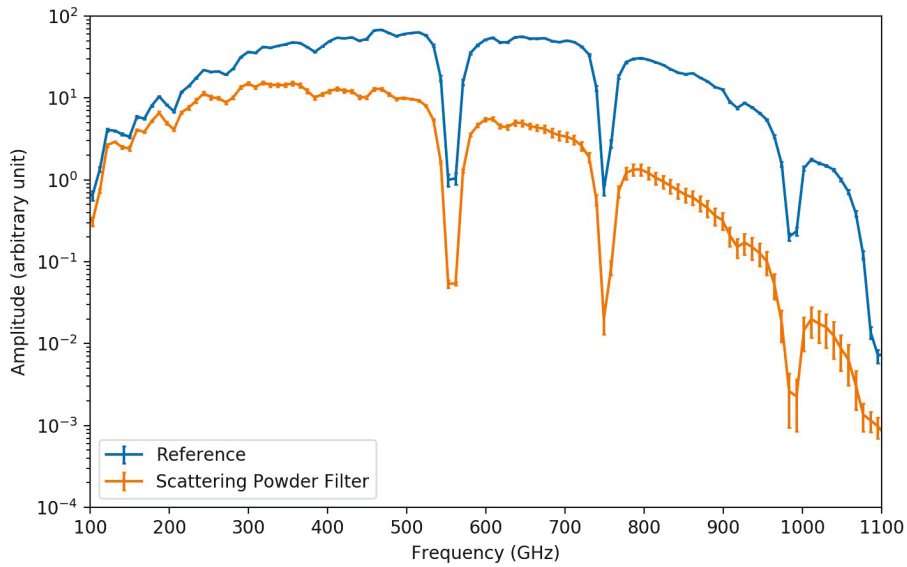

Figure 3.8: Scattering powder filter transmission spectrum measured by the FTS broad band configuration. Higher frequency signals are less transmitted because of scattering, while high in-band pass is maintained. Error bars were generated among multiple measurements.

mostly air with an index of refraction of almost one, AR-coating is not required. Further, in large parts of the far-IR aerogel is transparent so that the filter heats up far less. Even if the filter stays at a higher temperature, aerogel has such a low index of refraction that it doesn't significantly load the detectors. The aerogel based scattering powder filter is likely to be deployed in the coming CLASS telescopes.

3.4 Large Aperture Cryogenic Window

The CLASS optics design requires that the receiver have a window with an diameter of 46 cm. The CLASS receiver is pumped under vacuum during operation;

atmospheric force exerted on this area is:

$$F = P_{\text{atm}} A \approx 1.0 \times 10^5 \times \pi \times \left(\frac{0.46}{2}\right)^2 \text{N} \approx 17 \text{ kN},$$

where P_{atm} is atmospheric pressure and A is the window area. Supporting the almost two-ton force requires a strong mechanical structure, suggesting that it should be thick; meanwhile the window material has to have high in-band transparency to transmit in-band signals, suggesting that it should be thin. These two driving factors are in tension.

After testing different materials with various mounting structures, ultra high molecular weight polyethylene (UHMWPE) sheet was selected. It was selected, firstly, because it has a high in-band transmission. These properties were tested by the FTS described in Section 3.1. More importantly, the strengthened intermolecular interaction from long molecular chains provides extra strength compared to normal plastic materials.

Some calculations are involved in determining the thickness. The window is bolted down around the rim so that it can be treated as "an edge fixed circular flat plate";[30] the maximum tensile stress S and the maximum deformation d is given by:

$$S = \frac{0.24W}{t^2} = 0.24\pi P_{atm} \left(\frac{R}{t}\right)^2, \tag{3.4}$$

$$d = \frac{0.0543WR^2}{Et^3} = \frac{0.0543\pi P_{atm}}{E} \left(\frac{R}{t}\right)^3 R, \tag{3.5}$$

where W is the load on the plate, P_{atm} is atmospheric pressure, R is the radius, t is the thickness and E is the modulus of elasticity. The equations above are for simple elastic deformation. Equation 3.4 and Equation 3.5 inform us that the maximum tensile stress does not change as long as the radius to thickness ratio is fixed, but by self-similar scaling it does proportionally increase the deformation as the radius increases. Minimal thickness is preferred for optimal in-band transmission. Ideally the window should be just thick enough to support the atmosphere. In this regime, the window will certainly be driven beyond elastic deformation. The final determination of the thickness came from a full-size test using the test cryostat.

The Acatama B-mode Search (ABS) experiment utilized a UHMWPE window with a smaller aperture.[13] The successful result provides an anchor point to estimate the thickness at the CLASS aperture size by keeping the radius to thickness ratio fixed. After rounds of long duration test using the test cryostat, the thickness was selected to be 4.76 millimeter. A safety factor of more than a factor of two is guaranteed because the site atmospheric pressure is only half of that at sea level.

The UHMWPE window is also AR-coated with porous PTFE sheets, i.e. PTFE with pores in the material. Optically, its index of refraction n can be tuned by changing the volume fraction of the pores in the material, and the thickness d can be controlled by sheet thickness. The porous PTFE sheet is attached to the window by melting a low density polyethylene (LDPE) film. During this process, the window, the LDPE film and the porous PTFE sheet were pressed together and placed in a

vacuum oven. The oven was heated just above the melting point of LDPE, which is lower than that of both the window and AR-coating materials. The porous PTFE sheet was then attached to the window after cool down. Both sides of the UHMWPE window are AR-coated using this technique.

3.5 40 GHz Telescope Filter System

After introducing individual components in the filter system, the final system is presented in Figure 3.9. The system was tested multiple times in the lab before it was deployed to the field in 2016.

Figure 3.9 shows the layout of the fielded CLASS 40 GHz telescope filter system. The aperture of the receiver accepts 75 W loading from ambient temperature. The radiation first enters the cryogenic receiver through the 46 cm diameter AR-coated UHMWPE window (see Section 3.4), then a majority of the loading is reflected out by a pair of metal mesh filters (see Subsection 3.3.1) at 300 K. After the two 300 K stage elements, the power is cut down to around 15 W. The radiation then encounters the 110 K and 60 K stages sequentially. The two stages contain metal mesh filter pairs and AR-coated PTFE filters (see Subsection 3.3.2). After these stages, the loading is reduced to about 1.2 W and 0.1 W. To this stage, all the loading data were measured by the large aperture bolometer in our test cryostat. The radiation then passes through another stage at 10 K. This stage also contains a PTFE filter and a

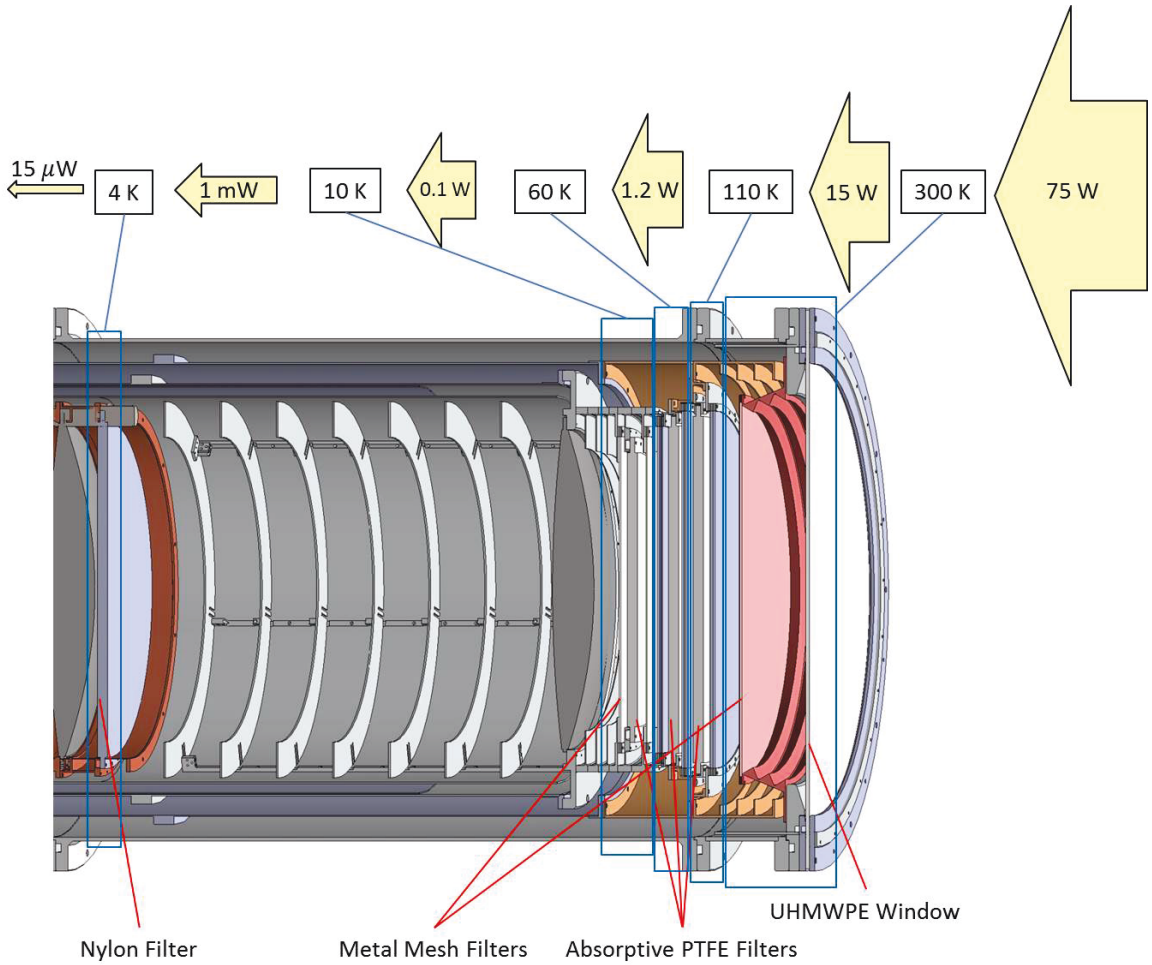

Figure 3.9: CLASS 40 GHz telescope optical filter system. The main part shows part of the CLASS 40 GHz receiver which houses the filter system from 300 K window to 4 K nylon filter. Different filters are pointed out at the bottom, and different temperature stages are pointed out on the top. Loadings entering and leaving each stages are also presented on the top.

metal mesh filter pair. The loading is estimated to be reduced to 1 mW. Finally, the radiation comes to the 4 K nylon filter, which was estimated to cut the power further down to around 15 μW.

The ultimate purpose of this optical filter system is to reduce thermal loading so that the cryostat successfully keeps the detectors cold, while keeping efficient in-band

transmission. Ultimate testing comes from the in-field performance. The CLASS 40 GHz telescope was deployed in 2016, and the telescope has been operating normally for over one year. The window held steady, which demonstrates that the 4.8 mm-thick UHMWPE window successfully supports atmospheric pressure over a long period of time. Meanwhile, the detector bath temperature continuously stayed below 40 mK, significantly lower than our goal of 100 mK. It is from this fact that we estimated the actually thermal loading at the focal plane is around 15 μW, also significantly lower than our goal 100 μW. More importantly, after initial calibration the efficiency of the entire telescope was found to match expectation. This is a sufficient proof of the high in-band transmission from all the optical components (including the window and the filters).

We can confidently state that goals for the filter system (including the window) were successfully accomplished.

Chapter 4

Mount System

According to the optical design introduced in Chapter 2, each CLASS telescope contains a variable-delay polarization modulator (VPM), a primary mirror, a secondary mirror, and a cryogenic receiver (containing two cryogenic lenses and the detectors). The cryogenic receiver also has associated cryogenic equipment, such as a mechanical pump, a turbo pump, a pulse-tube cryocooler system, and a dilution refrigerator system. In addition to these critical components, other auxiliary devices and instruments are also required for operation. All of them must be supported by a platform.

Further, an azimuth axis and an elevation axis are required for telescope pointing. Additionally, a boresight axis is needed to allow sampling the sky in detector angle more efficiently, which is important because the VPM only gives Stokes Q or U, but not both simultaneously. This means that we need the boresight rotation to efficiently

get both Q and U in a reasonable amount of time. The mount system must be able to rotate the entire telescope and instruments about the three axes.

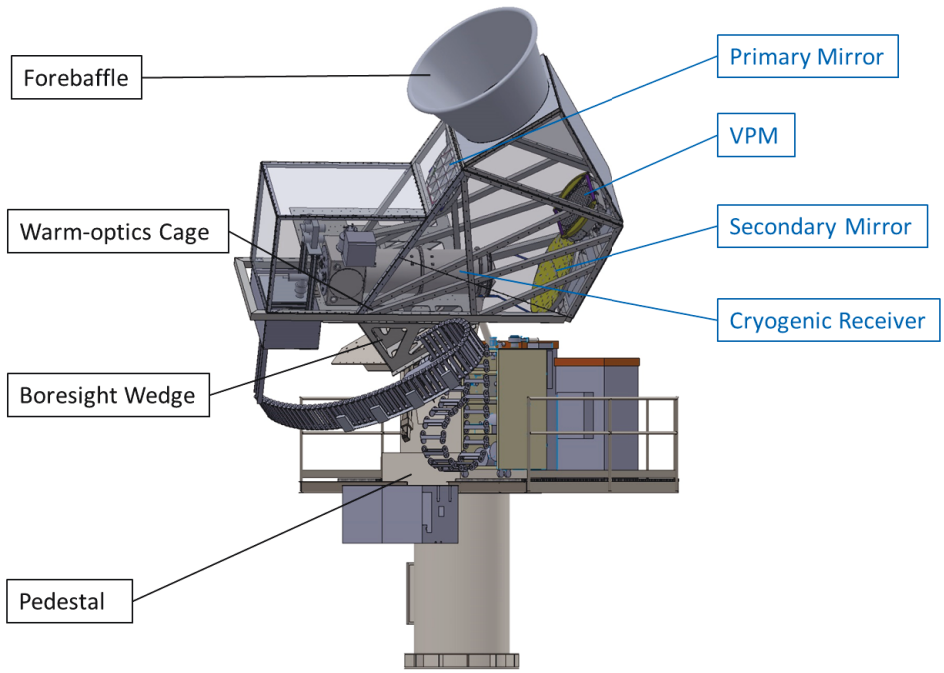

Figure 4.1: CLASS 40 GHz telescope on the first mount. This figure shows the CLASS 40 GHz telescope deployed in 2016 on the first mount. When the 90 GHz telescope is deployed, the first mount will be fully equipped with two telescopes. The telescope components (indicated in blue text) are supported by the mount system, which mainly contains a pedestal, a boresight wedge and a warm-optics cage (indicated in black text). As part of the mount system, a forebaffle is used to suppress the azimuth synchronized signal from the ground. The telescope is pointing at 45° elevation with 45° boresight angle in the picture.

The warm optical components, including the VPM and the two mirrors, must be accurately positioned within a required accuracy (1 mm for 40 GHz) to form a sharp image on the focal plane. As the telescope rotates about the three axes, the components would be rotated to different positions with various orientations. These

optical components weigh at least 50 kg individually, so the mount system must be rigid enough that the weight would only deform it within the required limit under all conditions. The azimuth synchronized signal from the ground must be minimized. For this purpose, a forebaffle along with its accessories was designed.

In the CLASS design, four telescopes share two mount systems. Each mount system provides a platform for two telescopes to operate. Figure 4.1 shows the first mount with the first-deployed 40 GHz telescope on-board. This chapter will introduce the mount system, including a pedestal, a wedge, a warm-optics cage (with its accessories) and a forebaffle. A mechanism and strategy to align the warm optical components will also be covered from both hardware and software perspectives.

4.1 Pedestal

Two pedestals were designed by Antedo Inc.* and manufactured by COSPAL†. After comprehensive modifications, the pedestals are being used to support CLASS telescopes. Figure 4.2 shows the first CLASS pedestal. The pedestal is attached to the ground by a bolt circle at the bottom of a foundation tube, which is the only structure that is static relative to the ground. On top of the foundation tube sits the azimuth platform. The azimuth platform carries all the other mount structures and the on-board equipment, rotating azimuthally. Cables run up through inside of

*Antedo Inc., `http://www.antedo.com/`
†COSPAL Composites, `http://www.cospal.com/index.html`

the foundation tube, where they are carefully wrapped to facilitate azimuth platform rotation. The azimuthal axis is indicated by a red dashed line in Figure 4.2. In the center of the azimuth platform, a "fork-shaped" structure supports the elevation platform by two pivot points. The elevation axis across the two pivot points is also represented by a dashed red line in Figure 4.2. On the back, an elevation actuator controls the orientation of the elevation platform by pulling or pushing. The two rotation axes provide an azimuthal range over 720° and an elevation range from 20° to 90°.

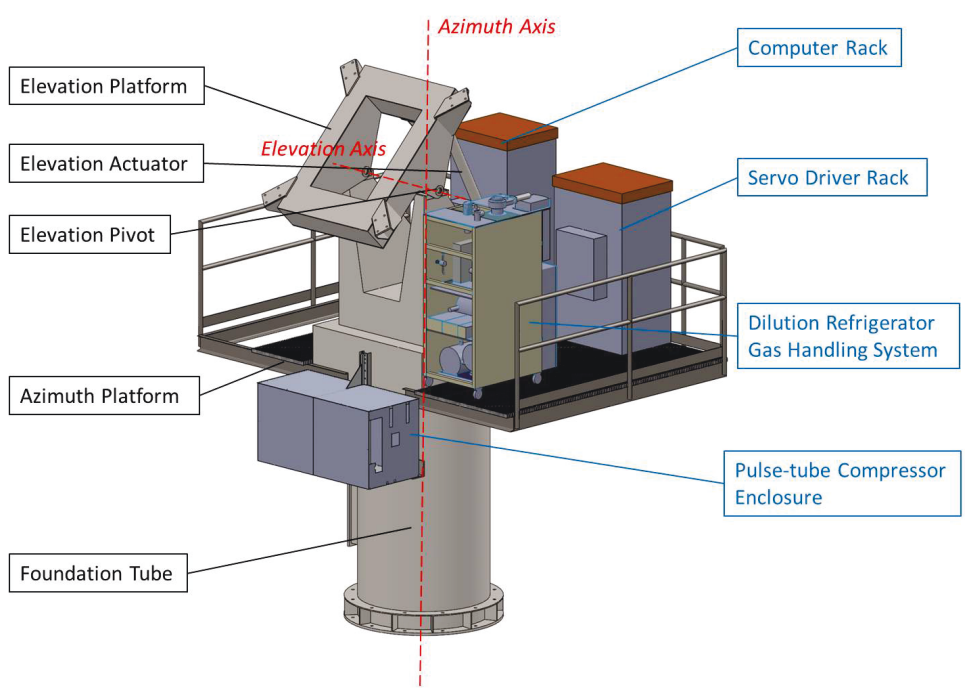

Figure 4.2: The pedestal and on-board equipment are shown in this figure. Structural components of the pedestal are pointed out in black text. The azimuth and elevation axis are presented in red. The on-board equipment is pointed out in blue text.

The azimuth platform carries multiple supporting equipment, indicated in blue

text in Figure 4.2. A pulse-tube compressor enclosure is suspending in front of the azimuth platform, which is designed to support two compressors, one for each of the two telescopes. On the azimuth platform, a dilution refrigerator gas handling system (GHS) is placed next to the main structure. The gas handling system is a system purchased from BlueFors Cryogenics* as one accessory of the dilution refrigerator. It directly connects to the cryogenic receiver via vacuum hoses, which cycle a He^4/He^3 mixture to cool the mixing chamber down. On the back, two racks are placed side by side. They are used to control the mount motion. The servo driver rack houses drivers for mount servos and other auxiliary electrical components, while the computer rack stores the computers that perform on-board calculations required for mount motion controls. The on-board equipment is placed close to the azimuth axis to minimize the azimuthal moment of inertia.

4.2 Boresight Wedge Assembly

The main telescope assembly starts above the elevation platform of the pedestal. Sitting directly on the elevation platform is the boresight wedge assembly which enables boresight rotation, as shown in Figure 4.3.

A boresight bearing plate, made of one-inch-thick steel, is installed directly on the elevation platform. A boresight bearing standoff and a boresight bearing are placed

*BlueFors Cryogenics, `http://www.bluefors.com/index.php/ld-series`

on the bearing plate, as shown in Figure 4.4. The boresight bearing* weighs 205 lbs and is $\sim$ 35 inch in diameter. With a dynamic weight capacity at 45,000 lbs, the boresight bearing supports a boresight wedge above and also provides the flexibility to rotate it. A boresight actuator is installed within the gap between the bearing plate and the boresight wedge. The actuator pushes or pulls the boresight wedge on the side to change the boresight angle. This mechanism covers boresight angles from -45° to 45°, assuming a 0° orientation when the boresight wedge is in the symmetric position, as shown in Figure 4.3.

The boresight wedge is a transition structure connecting the pedestal and the telescope parts above, which sets the foundation for the telescope mounting system. Structurally, its deformation at different orientations must be constrained to be smaller than the required accuracy (1 mm for 40 GHz), otherwise any deformations would be amplified through the upper structures. Furthermore, given the load capacity of the pedestal, the weight budget for the boresight wedge is limited to $<$ 500 kg. The material was then selected to be 1/2-inch thick aluminum with multiple inner structural ribs and struts to strengthen the structure. Individual plates were initially assembled by bolts and then welded together into a solid piece. The aluminum material was selected because its density is only 1/3 of that of steel. Additional material was cut out at non-structural regions of plates to further reduce the weight. Finite element analysis (FEA) was performed for various designs with various

*Kaydon Bearing Solutions, Part No.: KH-325E, website: `http://www.kaydonbearings.com/KH_turntable_bearings.htm`

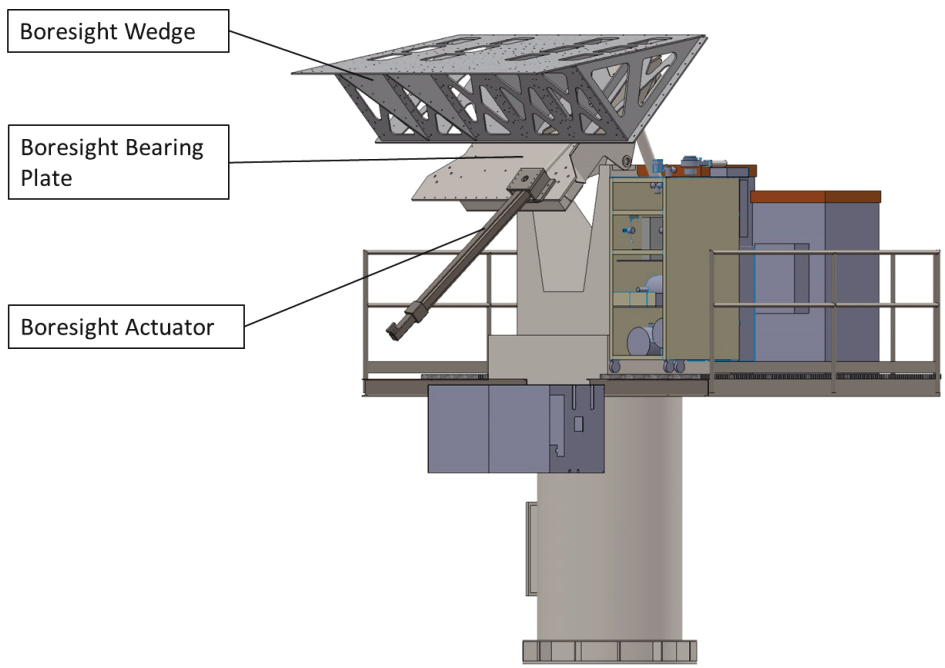

Figure 4.3: The boresight wedge assembly on the pedestal is presented in the figure. Some components visible from this perspective are pointed out in black text. The boresight bearing locates between the boresight wedge and the bearing plate (see Figure 4.4). The boresight wedge is at 0° boresight angle in this figure.

parameters (such as plate thickness, number of struts, size of cutouts etc.). Deniz Augusto Nunes Valle significantly contributed to the design of the boresight wedge. Finally, the optimized design, meeting both the structural and weight requirements, was manufactured by Bikle Manufacturing Inc*. Details can be found in Appendix B.

The boresight wedge serves more than a structural role. When the telescope rotates about the boresight axis, ideally it should not affect the telescope pointing.

*Bikle Manufacturing Inc., `http://www.biklemfg.com/`

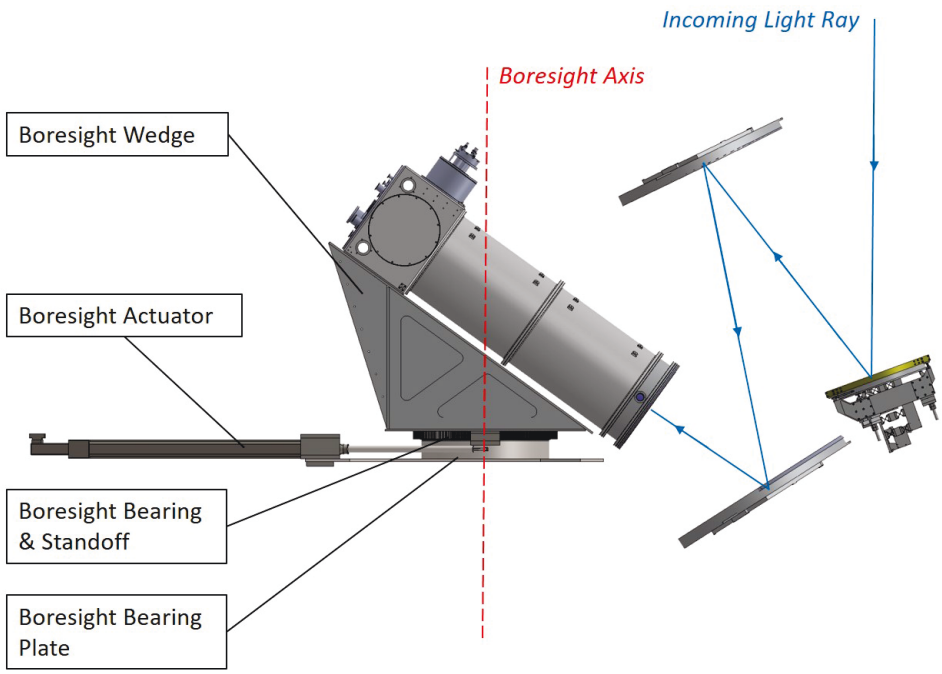

Figure 4.4: The boresight wedge optical role is presented in this figure. Components in the boresight wedge assembly are indicated in black text from another perspective. The boresight bearing and standoff are visible in this figure. The boresight axis and the outgoing light ray are also shown. They are designed to be parallel, which is realized by the boresight wedge. The telescope is pointing at 90-degree elevation with 0-degree boresight in this figure.

However, the CLASS optical design is not intrinsically convenient for this. The angle between the incoming light ray and the cryogenic receiver mounting plane is an arbitrary angle at $\sim 54.4°$ (Figure 4.4). Therefore, a structure is required to offset the cryogenic receiver so that the boresight axis and the incoming light ray are parallel. The boresight wedge angle is designed for this purpose, as shown in Figure 4.4. This design disentangled the telescope pointing from the boresight angle, which provides significant convenience for the telescope operation and further data analysis.

A natural question to ask about Figure 4.4 is that, since the warm optics (including the VPM and the two mirrors) are hanging far back in the figure, how are they mounted accurately at the designed locations with the right orientations? This brings us the the next two sections: warm-optics cage assembly and optical alignment.

4.3 Warm-optics Cage Assembly

Above the boresight wedge assembly, the warm optical components and other auxiliary equipment must be supported. A warm-optics cage assembly was designed and built accordingly.

The main structure in this assembly is the warm-optics cage, whose drawings can be found in Appendix C. The design of this structure is also constrained by two major factors: weight and deformation limitations. The weight budget for this 5-meter-long 3-meter-tall structure is 250 kg. With this 250 kg, it must support the three warm optical components with minimal deformations. When the telescope is at $+45°/\ -45°$ boresight angle (the boresight wedge rotates $+45°/-45°$ in Figure 4.4), a significant component of the gravity pulls sideways to the optical plane, toward opposite directions. Similarly, different pointings orient the telescope differently with respect to the gravity direction. However, deformation must be controlled < 1 mm. This requires the support structure to have adequate strength when gravity exerts from different directions.

Given the tight weight budget, aluminum square tubes were chosen as elements of the structure. Different designs were explored with extensive amount of finite element analysis (FEA) to assure that the maximum deformation is within the required value. But the structurally sound designs usually exceed the weight budget. To further reduce the weight, the stress on each square tube was carefully analyzed, which led to adaptively choosing the size of the square tubes. This enabled us to use a minimal amount of material without sacrificing the structural strength. Finally, a combination of 2-inch, 3-inch and 4-inch aluminum square tubes (with 1/4-inch-thick wall) were selected to form the entire structure. The structure was manufactured by KLK Welding* with full-penetration welding at all joints.

The warm-optics cage, carrying the warm optical components, is fixed to the top of the boresight wedge, as is the cryogenic receiver. The shaded area in Figure 4.5 is covered by aluminum honeycomb panels, manufactured by Pacific Panels†. These panels are hollow inside with honeycomb structures, which provide both light weight and high strength. The warm-optics cage assembly and the forebaffle interface (to be discussed in Section 4.5) are both enclosed by these panels. On the back of the cryogenic receiver (see Figure 4.5), a turbo station is mounted on the edge of the boresight wedge. The turbo station houses several pieces of cryogenic equipment, including a turbo pump, two pulse-tube chambers, and a pulse-tube motor. The turbo station also serves as a middle ground for hoses and cables going out of the

*KLK Welding Inc., `http://klkwelding.com/`
†Pacific Panels Inc., `http://www.pacificpanels.com/`

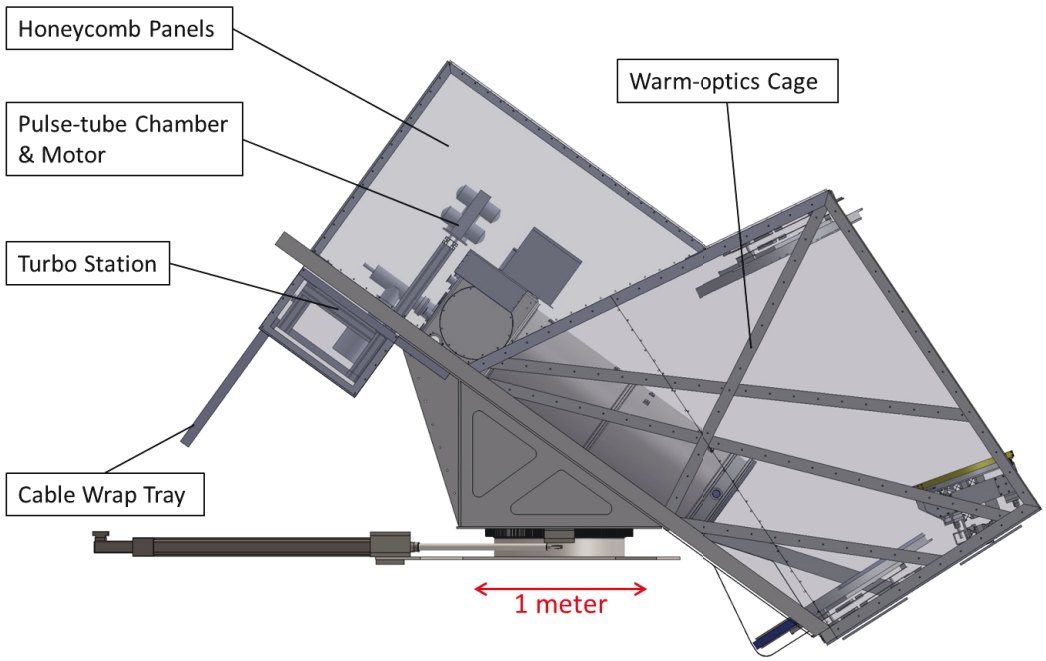

Figure 4.5: The warm-optics cage assembly on the boresight wedge. Starting from components presented in Figure 4.4, this figure shows structures fixed on top of the boresight wedge. These structures support the warm optical components and other accessories. The honeycomb panels were set to be transparent. A one-meter scale is provided for reference.

cryogenic receiver. A cable wrap tray is designed to send hoses and cables down to the cable wrap system. Details on the cable wrap system can be found in Appendix D.

4.4 Optical Alignment

The warm-optics cage manufacturing process can only achieve an accuracy around 1/4 inches (∼6 mm), which is much larger than the required accuracy ∼ 1 mm.

Thus, adjustment stages for the mirrors and the VPM were designed. A procedure to accurately measure their positions and adjust them to the desired positions was also developed.

4.4.1 Mirror Adjustment Stages

One rigid object has six degrees of freedom (DOF), in which five of them cannot be precisely positioned with the warm-optics cage (see Section 4.3) for the primary mirror and the secondary mirror. Therefore, the adjustment stages must be capable of adjusting the five DOF. This sets one of the requirements. Furthermore, the tolerance of the warm-optics cage is $< 1/4$ inch. The adjustment range must exceed this value. Multiplying it by a factor of two as a safety factor, the range was designed from -1/2 inches to 1/2 inches, which sets the other requirement. The two mirrors share similar designs, so the adjustment stages are similar. Therefore, only the primary mirror adjustment stage is introduced in detail.

The adjustment stage design for the primary mirror is shown in Figure 4.6. Three pairs of spring leaves (made of spring steel 1095) together with three ACME push screws adjust the longitudinal distances. As shown in Figure 4.6, each spring-leaf pair is fastened at the inner end and open at the other end. Two spring leaves in one pair are tensioned with > 100 kg (compared to the mirror weight ~ 50 kg) to provide rigid connections. The dimensions of the spring leaves are also designed to cover a > 1 inch range within its elastic limit. The front side of each pair is mounted to the

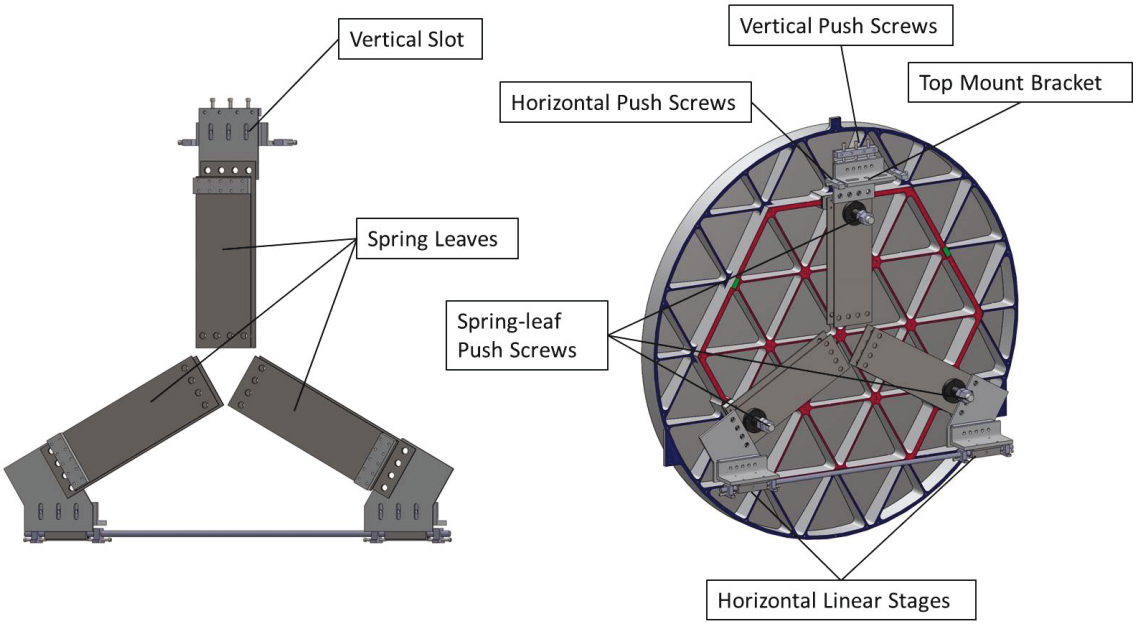

Figure 4.6: Primary mirror adjustment stage. The front of the stage is presented on the left, while the back is presented on the right with the primary mirror. The majority of the bolts are excluded in this figure. The mirror model was provided by Joseph Eimer.

mirror, while the back side connects to the rest of the adjustment stage. Adjusting three push screws changes the mirror's position and orientation. Three of the pairs together provide one translational DOF perpendicular to the mirror surface and the two rotational DOF within the mirror surface.

The vertical location is adjusted by three vertical push screws along with nine one-inch-long vertical slots. Bolts through the nine slots are first loosened; then the vertical push screws can be used to make the desired adjustments. The nine bolts are then tightened once the correct position is reached.

The adjustment stage is mounted on the cage by a top mount bracket and a linear stage, as shown in Figure 4.6. The top mount bracket has two one-inch-long horizontal

slots, and the linear stage allows the adjustment stage to move horizontally. When two bolts through the two slots are loose, the adjustment stage can be moved by horizontal push screws. The two bolts are then tightened back down once the correct position is found. Horizontal push screws are then tightened to lock the position.

This mirror adjustment stage meets the two requirements mentioned at the beginning by adjusting five degrees of freedom with a range of at least one inch. This design was used for both the primary mirror and the secondary mirror. Technical drawings on the adjustment stages are available in Appendix E.

4.4.2 VPM Adjustment Stages

Optically, the variable-delay polarization modulator (VPM) is equivalent to a flat mirror. Further, the illuminated area is smaller than the VPM size with a margin of more than 4 inches in diameter. This means at the level of 1/4 inches, the VPM transverse position (vertical and horizontal mentioned in Subsection 4.4.1) is not a sensitive factor to the telescope's optical performance. Therefore, only one translational DOF perpendicular to the VPM plane and the two rotational DOF within the VPM plane need to be adjusted. Similarly, the adjustment range should be 1 inch.

The VPM is mounted on the warm-optics cage via three mount brackets, as shown in Figure 4.7. The three mount brackets are installed on the warm-optics cage. Three ACME lead screws launch from the VPM and are clamped on to the mount brackets by two nuts. Positions of the mounting points can be adjusted by changing the

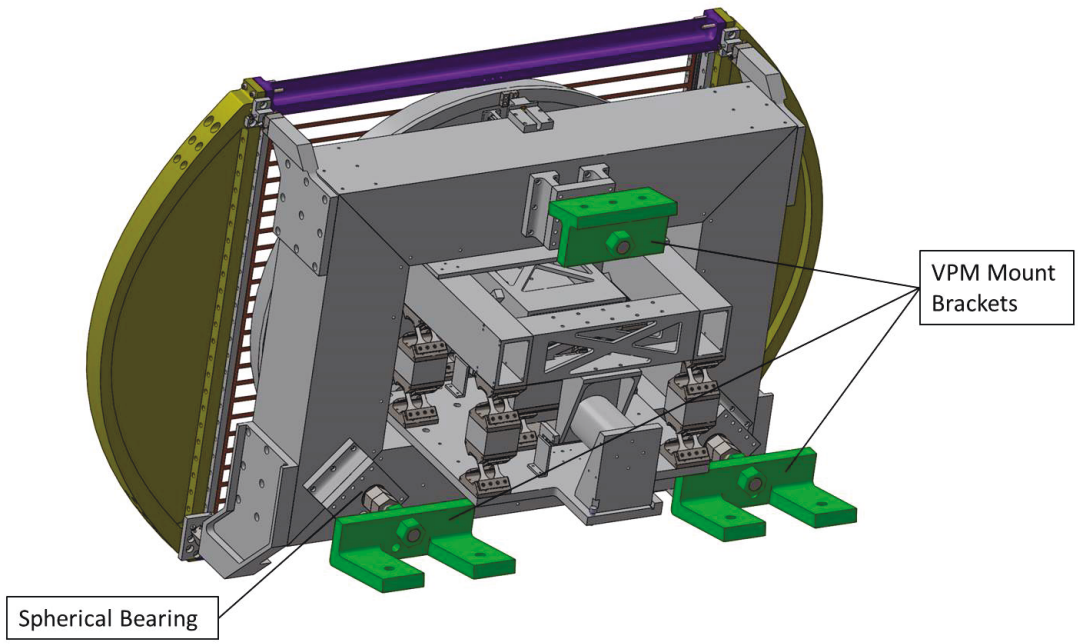

Figure 4.7: The VPM adjustment stage. The VPM structure is mounted by three brackets (green). One spherical bearing is also indicated. The VPM model was provided by Joseph Eimer and Katie Harrington.

clamping nuts positions on the lead screws. The lead screws are designed to be long enough to cover the one-inch adjustment range. The three lead screws can only move forward and backward simultaneously if their connections to the VPM are rigid. To avoid that, three spherical bearings are installed at the end of the lead screws. These bearings allow the VPM to be adjusted to different angles. Therefore, the VPM adjustment stage adjusts the three necessary DOF within the one inch range. Drawings on the adjustment stages are available in Appendix E.

4.4.3 Measurement & Adjustment

The adjustment stages provide a possibility to correctly align the warm optical components, but it is not sufficient. A strategy to accurately measure the positions of the components is also required. Furthermore, with the position information, correct operations on the adjustment stages need to be provided.

Our strategy is to use the cryogenic receiver, whose position is difficult to adjust, as an anchor, and then adjust other optical components with reference to it. This means we need to locate and adjust the secondary mirror, the primary mirror, and the VPM.

Assuming rigid bodies, each component needs at least three points (not in a line) to define its location. As shown in Figure 4.8, the cryogenic receiver has five measuring targets, the secondary mirror has three, the primary mirror has three and the VPM has four. Meanwhile, each components has six degrees of freedom (three translational ones, three rotational ones). Three components together have 18 degrees of freedom, implying at least 18 constraints are required to position them.

Constraints here can be any distances between two measuring targets from two different optical components. In our current target setup, there are 73 possible constraints. Theoretically, picking any 18 (or more) of them would be sufficient to locate the three optical components. However, considering measurement uncertainties, long baseline distances were preferred to minimize fractional uncertainties.

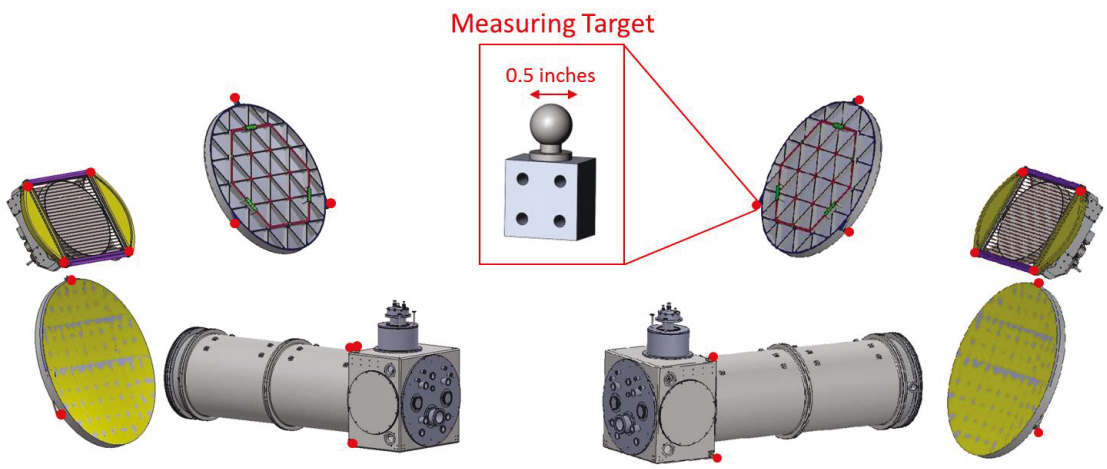

Figure 4.8: This figure provides two views of the CLASS telescope from two sides. Red dots represent measuring targets that are visible is each side view. The zoom-in figure shows the measuring target. Four holes on the block are used for mounting.

After setting up measuring targets, a Starrett inside micrometer* was used to measure the distances. Distances > 100 inch were measured with < 0.01 inch uncertainties.

Software was then developed to analyze the measured distance data. This software takes in the known optical components' geometric information along with the measured distances, and then outputs the coordinates of the center of mass along with three rotation angles for each optical components. Least-squares fitting was applied so that more than 18 constraints are not only allowed but preferred.

Additional software was also developed to take in the measured positions and

*Starrett 128BZ Inside Micrometer Set, `http://www.starrett.com/metrology/product-detail/metrology/metrology-products/precision-measuring-tools/micrometers/Inside-Micrometers/128BZ`

specify operations needed on each of the push screws to adjust the optical components to the designed positions. Details can be found in Appendix F.

The alignment procedure relies on both this software and the implemented hardware. After the cryogenic receiver and the warm optical components were installed, with all the adjustment stages locked in the middle of their range, more than 18 distances were measured with the inner micrometer. These measurements were then analyzed by the software that provided instructions of how to adjust each adjustment stage. After the operations were performed, the warm optical components were expected to be in the designed positions. An additional round of measurement was performed to check the results. The alignment procedure could be iterated until the next round of measurements gave the designed positions.

4.5 Forebaffle Assembly

The azimuth synchronous signal from the ground (ground pickup) is 300 K ground emission leaked into the telescope via either reflection or diffraction. Since the ground pickup naturally maps on to the sky via 360° telescope azimuthal motion, it can imprint the largest modes on the sky. Therefore, ground pickup is a major potential contaminant for the CLASS recovery of the largest modes.

A forebaffle was designed to mitigate ground pickup. A forebaffle interface was also designed to connect the forebaffle to the warm-optics cage. Between the forebaffle

and the interface, a closeout assembly was designed to house either a thin plastic film to seal the opening or a rotational wire-grid for polarization angle calibration.

4.5.1 Forebaffle & Interface

Before the forebaffle was designed, a light cone enclosing at least 99.9% of the in-beam power for every detector was generated according to the CLASS optical design by Joseph Eimer. Following the light cone, the base of the forebaffle was selected to be 184 cm away from the VPM wire-grid center. The bottom opening was then determined by the cross-section of the light cone. Launching from the baseplate, the forebaffle wall was designed with a half-angle greater than that from the light cone by a margin of 2°. This avoided the incoming radiation being parallel with the forebaffle wall, which may have led to light along the surface creating an unwanted diffracted signal. Finally, at the end of the forebaffle wall, a 3-inch diameter flare was designed to soften the boundary condition at the edge, minimizing diffraction. The forebaffle design is shown in Figure 4.9 on the left.

The forebaffle was designed to start from 184 cm away from the VPM wire-grid center. Therefore, a structure, called the forebaffle interface, was designed to support it. The interface sits on top of the warm-optics cage and locates the forebaffle into the correct position. Figure 4.9 shows the forebaffle interface along with the honeycomb panels to enclose it. Drawings on the forebaffle and its interface are presented in Appendix G.

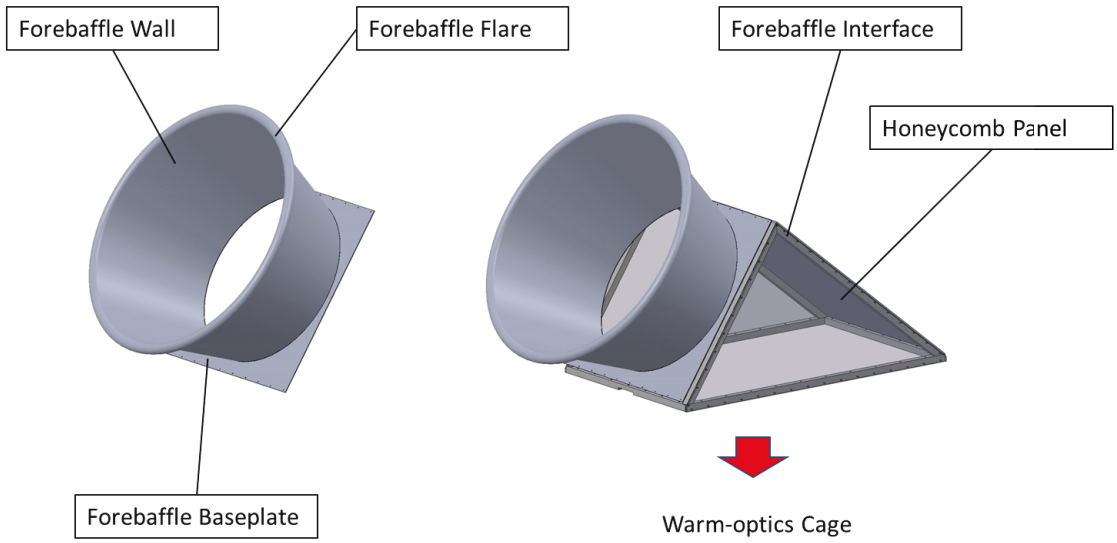

Figure 4.9: A forebaffle and its interface. On the left, the forebaffle is presented with the three components pointed out, including a baseplate, forebaffle wall and a flare. On the right, the forebaffle is installed on its interface to the warm-optics cage. An overall picture is shown in Figure 4.1. Honeycomb panels are also designed to enclose the interface. The forebaffle interface and one honeycomb panel are pointed out.

4.5.2 Closeout Assembly

Between the forebaffle and its interface, a closeout assembly was designed. The purpose of the assembly is twofold. During normal observation, the assembly has an insert with a thin plastic film at the forebaffle bottom. The thin plastic film environmentally seals the opening, protecting sensitive instruments inside from the elements. The assembly can also house an insert with a rotational wire-grid. The wire-grid emits linear polarization into the telescope so the telescope polarization angle can be calibrated.

The closeout assembly contains a closeout box and several inserts. The closeout box is a rectangular frame attached to the forebaffle on one side and to the interface

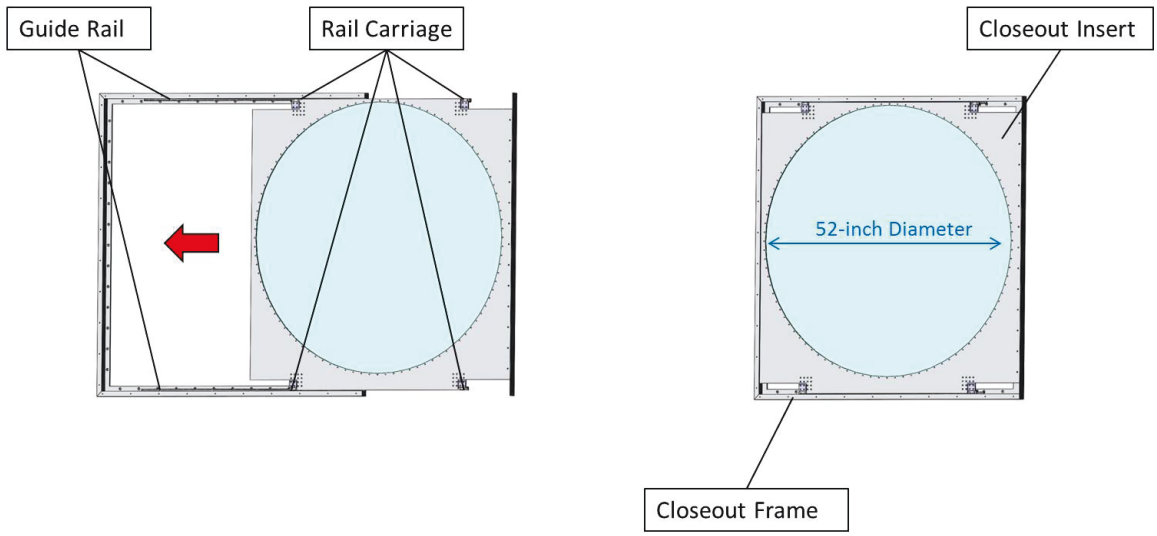

Figure 4.10: Forebaffle closeout assembly. On the left, one closeout insert being pushed into the closeout box is shown. On the right, the closeout assembly is presented in its normal operation status. Some parts are indicated, including an arrow indicating that the diameter of the opening is 52 inches.

on the other side. Two guide rails are installed for the rail carriages on the inserts, as shown in Figure 4.10. Different inserts can be swapped in easily in this design.

Two kinds of inserts are used, shown in Figure 4.11. One has a 0.0007-inch biaxially-oriented polypropylene (BOPP) film stretched across the opening. It basically closes out the opening to protect the inside instruments, and is therefore called the closeout insert. Two of them were built to have one in operation and the other one undergoing restoration.

The other is a wire-grid calibrator. Wires with 0.002-inch diameter are stretched across a ring with 0.5-inch spacing (the wires were changed to 0.005-inch diameter later). The wires emit linearly polarized signals along the wires, so the incoming signal for the telescope is linearly polarized at a known angle. The ring can be rotated by a

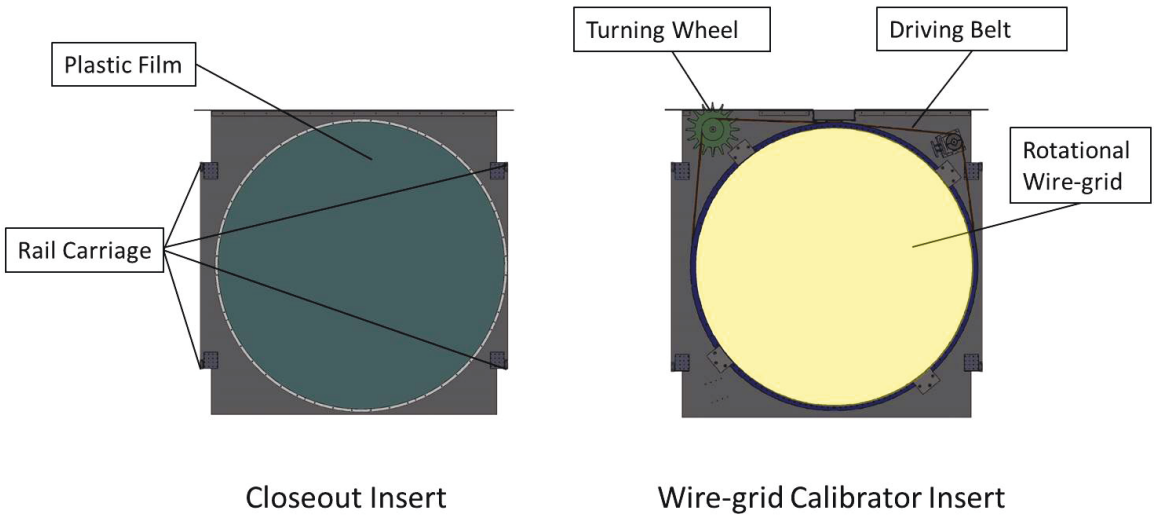

Figure 4.11: Two kinds of inserts are presented. The closeout insert is on the left with plastic film stretched across the opening. The calibration closeout is on the right with some of the parts pointed out. These inserts are designed by Thomas Essinger-Hileman.

driving belt, which is controlled by a turning wheel, shown in Figure 4.11 on the right. Once the calibrator insert is installed, rotating the turning wheel rotates the wire-grid, which eventually rotates the linear polarization angle. With the injected linear polarization direction known, the telescope polarization angle can be calibrated. The VPM response function to input linear polarization is also calibrated.

The forebaffle assembly is aligned similarly to the warm optical components. Four measuring targets were set around the forebaffle bottom ring to measure the forebaffle position. The entire assembly was adjusted on top of the warm-optics cage. Once the correct position was found, holes on the forebaffle interface were transferred onto the top of the warm-optics cage. The forebaffle assembly was then installed through these holes.

During the deployment of the 40 GHz telescope in 2016, the mount system was assembled as designed. Figure 4.12 shows the mount system with the on-board 40 GHz telescope. Over the past observing season, the mount system has been operating stably and successfully. More calibration results are available in Chapter 5.

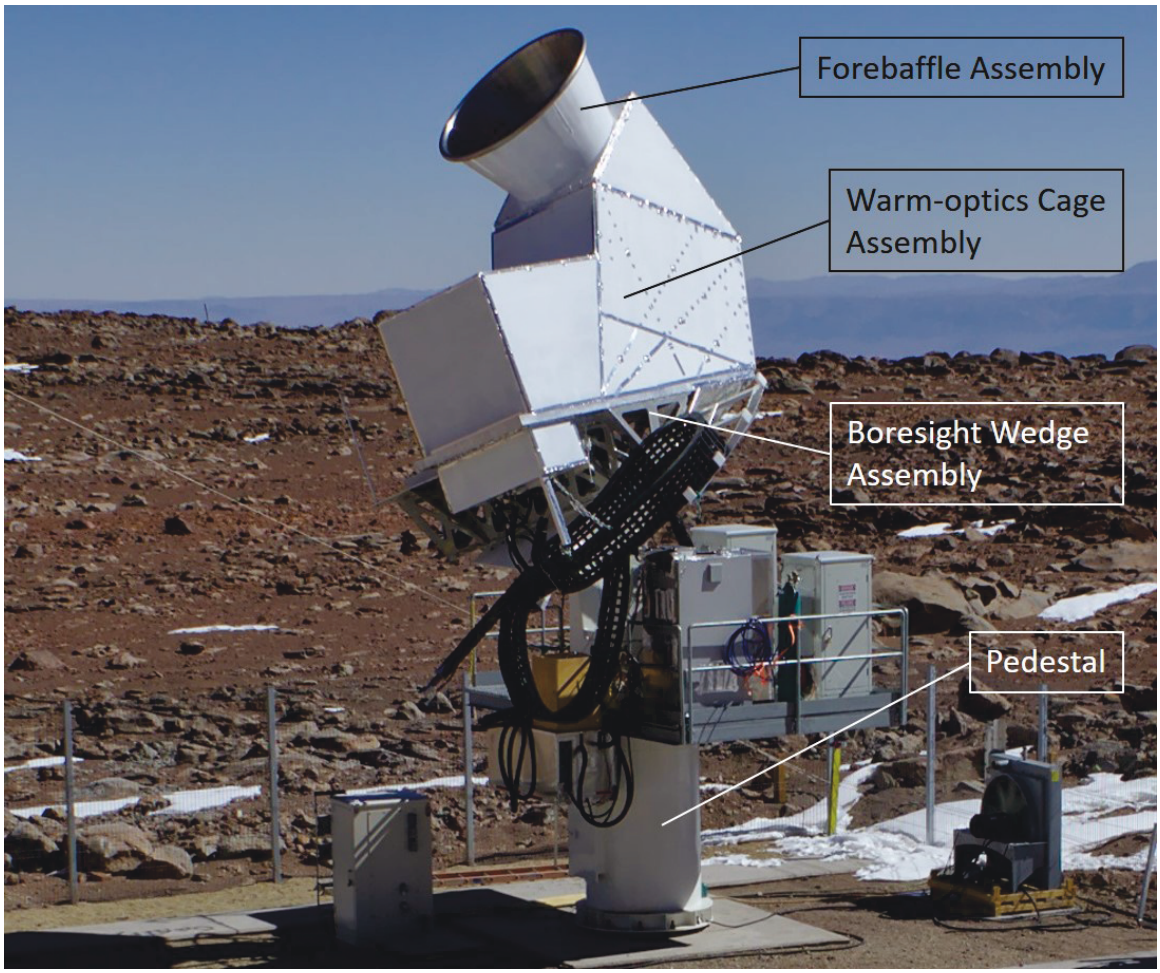

Figure 4.12: The mount system at the site. The mount system contains the pedestal, the boresight wedge assembly, the warm-optics cage assembly, and the forebaffle assembly introduced in this chapter. Photo credits: Matthew Petroff.

Chapter 5

Observations & Data Analysis

The 40 GHz telescope was deployed in 2016. After all the components were installed, an optical alignment was performed. After only one iteration, the warm optical components were adjusted to within the required accuracy. Meanwhile, the detectors started to function normally as the cryogenic receiver successfully cooled down to < 40 mK. Finally, the telescope was ready to observe the sky. First light of the 40 GHz telescope was in May of 2016. For cosmological observations, the CLASS telescope scans the sky azimuthally at a single elevation angle. See Subsection 2.2.1 for more information on the scan strategy for the cosmological survey. Because of the Earth's rotation, the survey area is observed with nearly two full rotation every day (minus a sun-avoidance region).

The Moon was observed for calibration of the telescope's pointing and beam patterns. Because we know the position and size of the Moon, these observations allow

us to calibrate both the pointing and the beam pattern (equivalent to the point spread function) of each detector. These calibrations are a critical check of the optical design(Chapter 3, Eimer et al 2012[11]), of the optical alignment (Section 4.4) and deformation in the telescope structure (Chapter 4). More generally, for cosmological studies, the pointing of each detector must be accurately calibrated for map making (the process by which time-ordered data form each detector is mapped to the celestial sphere). The CMB is processed by the telescope into the observed CMB map. Because the CLASS telescope is diffraction limited with a beam full width at half maximum (FWHM) of $\sim 1.5°$, the observed CMB map is smoothed on scales smaller than the beam. Therefore, to properly model the observed CMB map, a beam profile of each detector must be calibrated. Equivalently, the power spectrum of the observed CMB map is reduced at high-ℓ relative to the real CMB power spectrum by a window function, which is calibrated through the Moon observations.

To recover the largest angular modes in the CMB, we must estimate large-angle contamination arising from polarized emission from the ground, so-called "ground pickup." The ground pickup naturally maps onto the 360° of azimuth as the telescope scans the sky, and so it can imprint large-angular contaminating modes on the observed CMB map. To remove the ground pickup contamination, hardware (including the forebaffle assembly in Section 4.5) has been designed to suppress it, but the final test comes from field performance.

I led the effort to perform special observations for telescope pointing calibration

and beam calibration. I also comprehensively characterized the ground pickup signal. The work presented in this chapter is ongoing, and will be published in final, expanded form in a future paper characterizing the CLASS 40 GHz instrument.

5.1 Pointing Calibration

After first light, the array pointing was checked. The CLASS 40 GHz telescope has a beam size of around 1.5° (Full Width at Half Maximum, FWHM). The Moon, which spans 0.5° on the sky, is significantly smaller than the beam size. Therefore, the Moon was used for pointing calibration.

Designated Moon scans were organized, during which the telescope is fixed to 45° elevation angle, same as that of CMB scans. When the Moon rises or sets across the 45° elevation angle, the telescope scans ±13° in azimuth across the Moon field. The array field-of-view is 20° across so that these ±13° scans give at least a 3° radius observations even for the edge pixels.

The data analysis method is presented in Figure 5.1. The CLASS 40 GHz focal plane contains 72 detectors coupled to 36 feedhorns. They are distributed across a 20-degree field-of-view on the sky, shown in Figure 5.1. During Moon scans, as the Moon slowly rises or sets across the scan elevation, the telescope performs azimuthal scans (1 degree/s) at this elevation with a set boresight angle. In the sky coordinate system, both the Moon and the detectors are in motion. To simplify the problem,

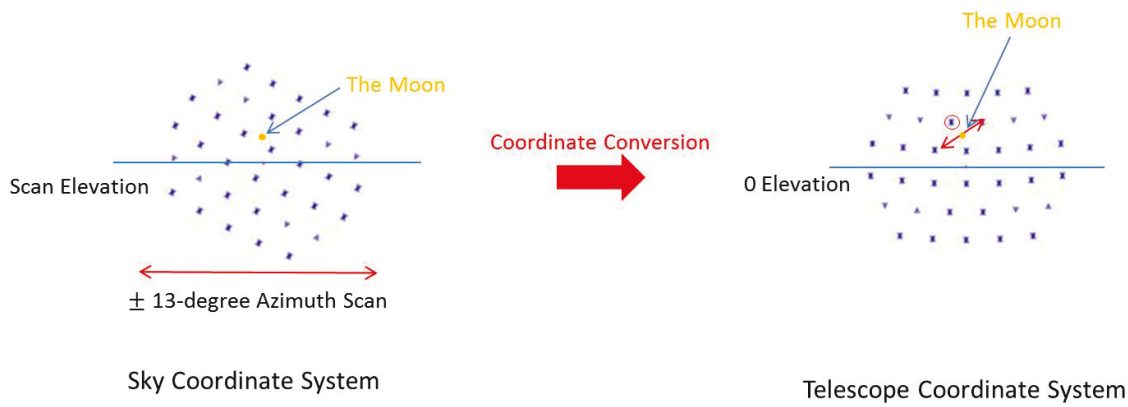

Figure 5.1: The Moon scan analysis method. On the left, the detector array is presented, centered at the scan elevation with a boresight rotation. The Moon slowly rises or sets as the telescope scans ±13° in azimuth. Both the Moon and the array center positions are described in the sky coordinate system. The Moon positions were converted into the telescope coordinate system, where the array center is at 0 elevation with 0 boresight angle. In the telescope coordinate system, every detector is fixed at a set azimuth and elevation angle while the Moon appears to zigzag across the array.

quaternion rotations (a useful tool to perform rotations) were applied to convert the Moon and the detectors into the telescope coordinate system, where the array center is at its origin. During this process, a quaternion that rotates the array center to the origin with 0 boresight angle was first generated; then this quaternion is used to rotate each detector from the sky, which gives their coordinates in the telescope coordinate system. In the telescope coordinate system, every detector is fixed at a certain azimuth and elevation angle while the Moon appears to zigzag across the array during each Moon scan. The telescope coordinate system is also the natural coordinate system to describe every detector's pointing and beam pattern, from which the pointing and beam pattern can be conveniently converted to the sky via coordinate

conversions.

In the telescope coordinate system, as the Moon travels across the array, beam maps for each detector are sampled. For one certain detector, e.g. the one circled in Figure 5.1, each position of the Moon relative to this detector has a corresponding readout from this detector. As the detector samples the Moon, the beam map for this detector is probed. Assuming a symmetric two-dimensional Gaussian beam, the peak position was estimated via the sampled points, which determines the pointing of this detector. The pointing direction of each detector is parametrized as X, and Y. They are both measured relative to the array center in the telescope coordinate system, with X along the azimuth direction and Y along the elevation direction.

Table 5.1: Moon Scan Numbers vs. Boresight Angles

Boresight Angle	Moon Scan Number
$-45°$	19
$-30°$	11
$-15°$	10
$0°$	22
$15°$	10
$30°$	10
$45°$	22

Around 100 Moon scans were performed at different boresight angles for the CLASS 40 GHz telescope from July to October in 2016, details can be found in Table 5.1. The pointing is consistent with the optical design, as shown in Figure 5.2. Each detector points at the designed position in the telescope coordinate system. Standard deviations, computed across the Moon scans, are within one arcmin. The

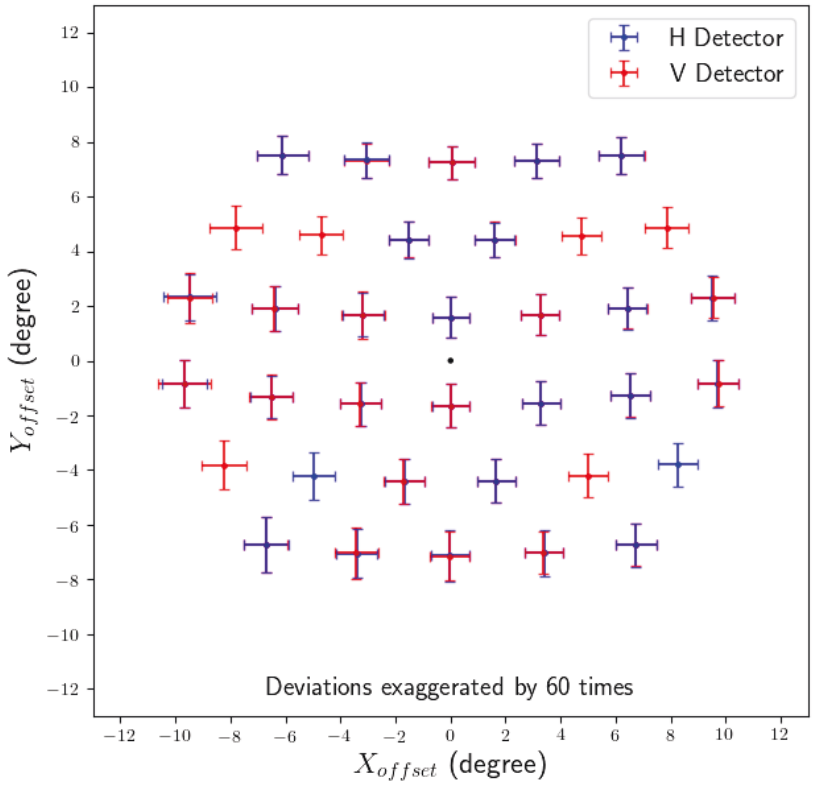

Figure 5.2: CLASS 40 GHz telescope array pointing overview. Detectors sensitive to horizontal (vertical) polarization are shown in blue (red) data points.. The displayed standard deviations for each detector's pointing are inflated by a factor of 60, i.e. one degree in the error bar is actually one arcmin. The array center is indicated by a black dot.

standard deviations shown in Figure 5.2 are inflated by a factor of 60. Given the beam size of 1.5° FWHM, one arcmin is around 1% of the beam size. Pointing differences between paired detectors under one feedhorn are plotted in Figure 5.2. The pair pointing differences are then exaggerated by 60 times and presented with the pointing standard errors from individual detectors in Figure 5.3. The pair pointing differences

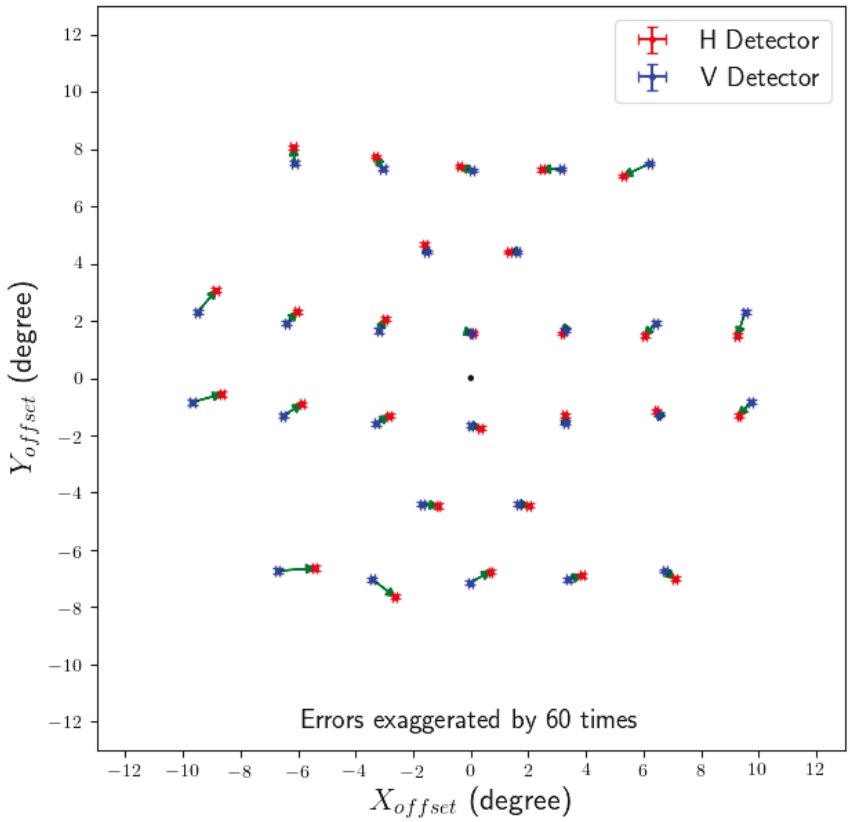

Figure 5.3: Detector pairs pointing differences. Pointing differences and pointing standard errors for individual detectors are exaggerated by 60 times. Eight pairs are missing since these detectors were not operational at the time these data were taken. The pointing differences are presented as vectors pointing from H detectors to V detectors. The magnitude of the pointing differences ($<$ 1 arcmin) are larger than pointing errors.

are larger than the detector pointing standard errors. The differences increase as the pairs are farther away from the center, but are still not significant compared to the beam FWHM.

Histograms on four pointing parameters (pointings X, Y and pair pointing differences Δ_X, Δ_Y) are presented in Figure 5.4. Standard deviations on X and Y are both within 1 arcmin, centered around 0.8 arcmin. The pair pointing differences on

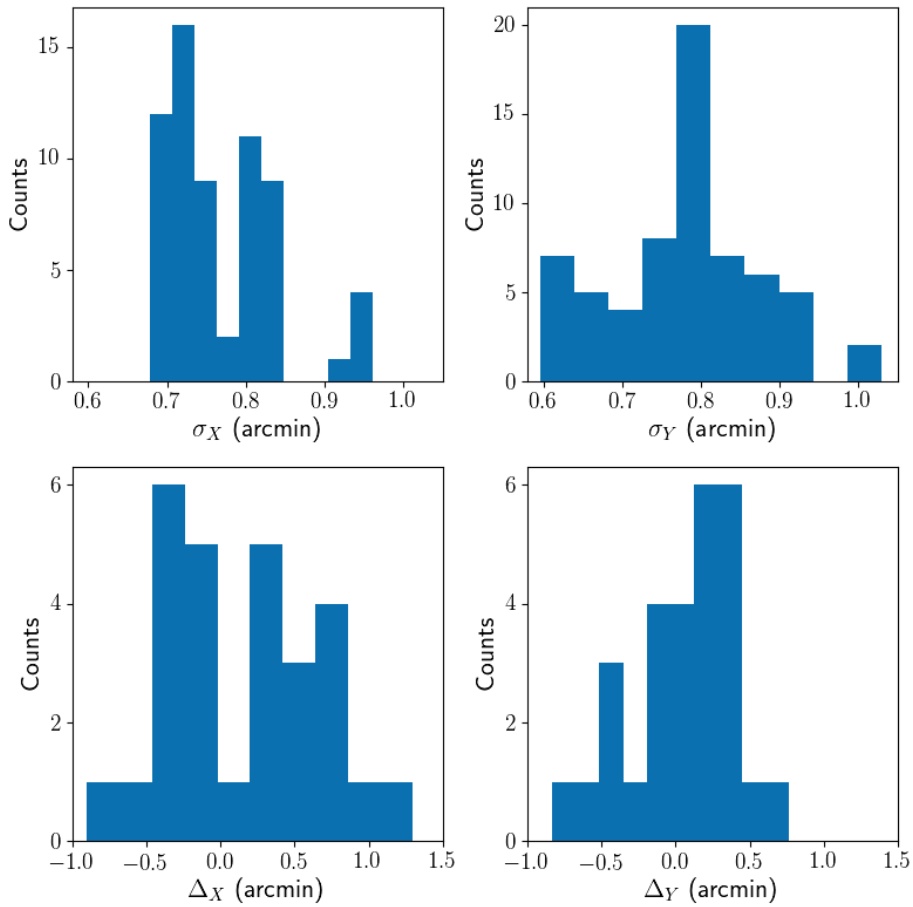

Figure 5.4: Pointing parameter histogram. Standard deviations (denoted as σ_X and σ_Y) are shown in top sub-figures, x scales of the two figures are the same. Pair pointing difference (denoted as Δ_X and Δ_Y) are shown in bottom sub-figures, x scales are also set to be the same.

X and Y are within 1.0 arcmin for most of the pair detectors, centering within 0.5 arcmin.

As noted in Section 4.3, the warm-optics cage reaches its maximum deformation at $\pm 45°$ boresight angle, which affects the positions of the optical components and eventually leads to pointing offsets. The warm-optics cage was designed to constrain the maximum deformation within 1 mm. From $-45°$ to $+45°$ boresight angles, the

X pointing offset should follow a continuous rising trend over ~ 1.2 arcmin; the Y pointing offset should follow a flat trend.

With Moon scans at different boresight angles, the pointing's dependence on boresight angles can be characterized. Figure 5.5 shows the trend and the amplitude are consistent with the estimation from the warm-optics mechanical design.

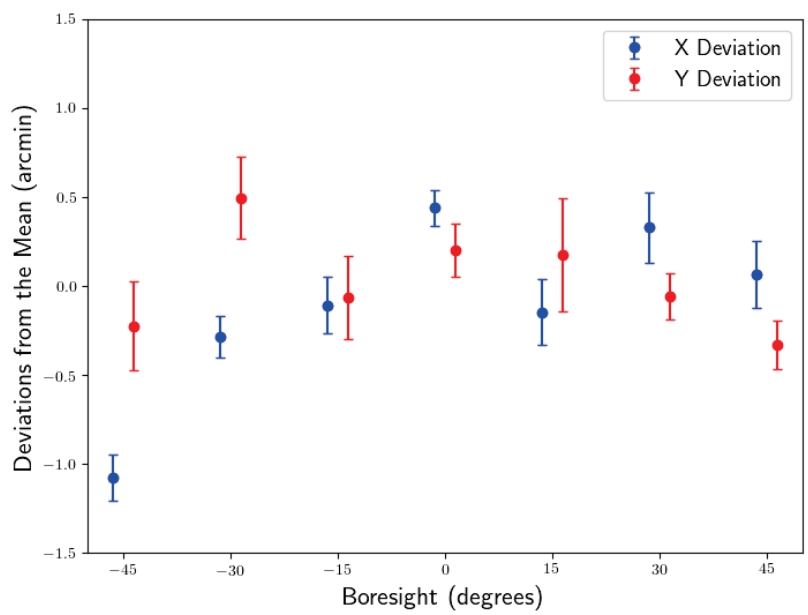

Figure 5.5: Pointing dependence on boresight angles for one detector. Blue (red) points show pointing deviation from the overall mean along the $X(Y)$ direction. The error bars are standard errors under the same boresight angles. The trend and amplitude (~ 1 arcmin) of the azimuth deviation is consistent the estimation from our mechanical design. The blue and red points are offset from the same boresight angles for clarity.

Shifting attention from this one detector to the whole array, the ensemble results are shown in Figure 5.6. The conclusions from Figure 5.5 hold across the array. The trend and the amplitude of the azimuth and elevation pointing deviation are

consistent with the design expectation. Now we can confidently say that the warm-optics cage meets the deformation limit requirement (< 1 mm) across all boresight angles.

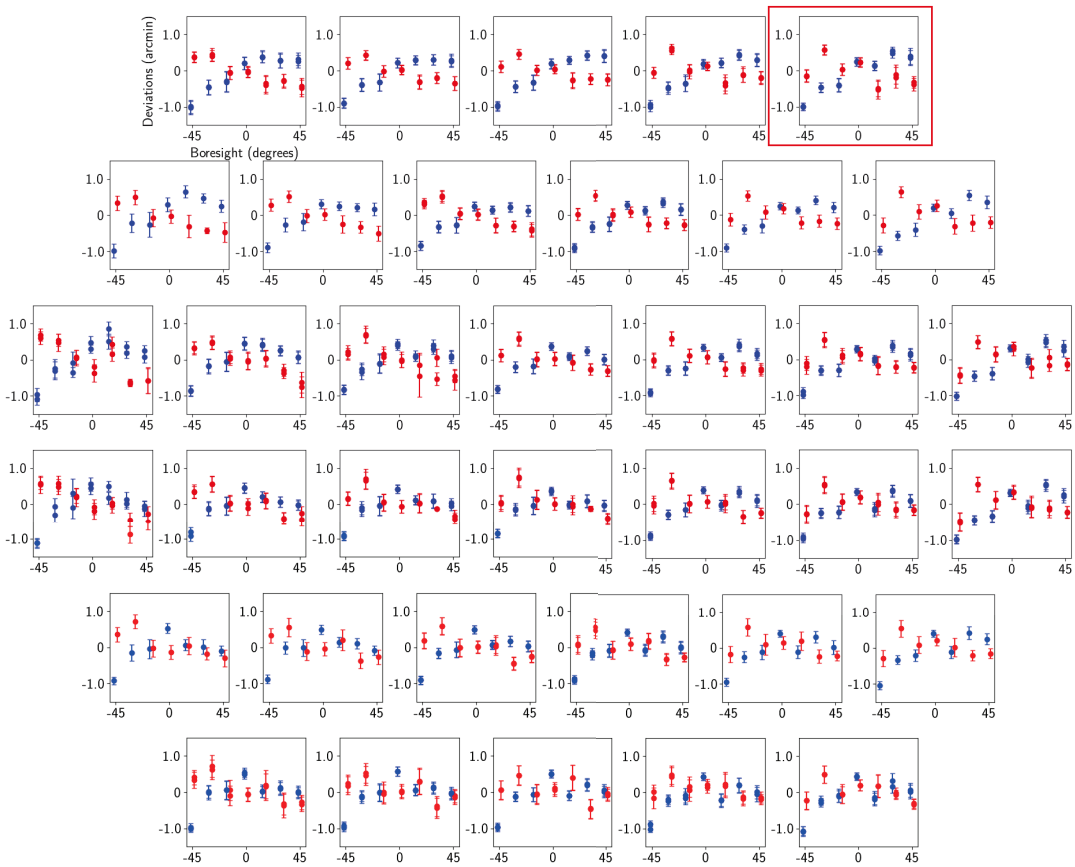

Figure 5.6: Pointing dependence on boresight angles for the array. Each sub-plot follows the same convention as in Figure 5.5. Plots for different detectors are organized according to their pointing on the sky. This array plot shows specific pointing information for each detector. The detector in Figure 5.5 is the one in the red box on top right.

Beyond the boresight angle dependence, there were also concerns about the warm-optics cage and the adjustment stages deforming with time. With Moon scans taken

at different times, pointing evolution was characterized in the same fashion.

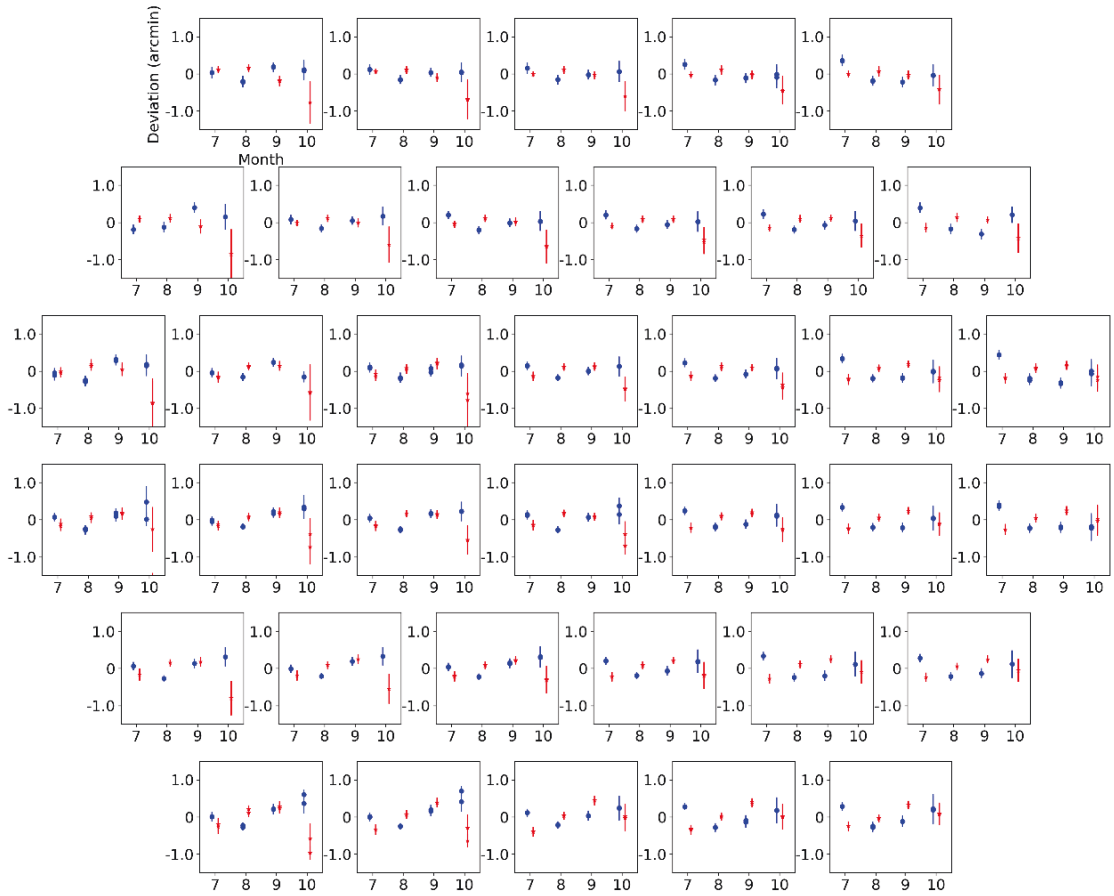

Figure 5.7: Pointing dependence on time. This array plot shows the pointing dependence on time for each detector. Azimuth and elevation deviations are shown by the blue and red points respectively. Y scales are kept the same as those in Figure 5.6 from -1.5 to 1.5 arcmin. X ticks represent months in 2016. Relatively large error bars in October are due to small number of Moon scans performed in that month.

Results are shown in Figure 5.7. Y scales are kept the same as in Figure 5.6 for comparison, which shows that deviations over time are smaller than those over boresight angle. No deviation beyond 1 arcmin was observed. This result proves that the warm-optics cage and the adjustment stages are stable over months.

5.2 Beam Calibration

During the Moon scans, beam maps are also measured. Since the Moon radiation is largely unpolarized, the unpolarized portion is used to characterize the overall beam shape; while the small fraction of polarization in the Moon radiation is used to characterize the instrument polarization response by making Moon polarization maps.

5.2.1 Intensity Beam

Temperature of the Moon is measured to be ~ 200 K.[40] The beam FHWM ($\sim 1.5°$) is three times the diameter of the Moon ($\sim 0.5°$). With the dilution factor estimated around 9, the beam-diluted signal is around ~ 22 K. The high signal from the Moon guarantees high signal-to-noise beam shape measurements, as shown in Figure 5.8 for V detectors and Figure 5.9 for H detectors. Each detector beam map is generated from stacking Moon scan data. Software was developed to reject bad Moon scans (due to bad weather, detector glitches etc.) for each detector; only the accepted Moon scans ($\sim$150 for each detector) were used to generate the stacked beam map. The accepted Moon scans were normalized to have a peak value of 1 before being stacked.

Additionally, because the telescope scans $\pm 13°$ during Moon scans, beam maps are measured to $10°$ for most detectors. Boresight rotation further rotates the detector

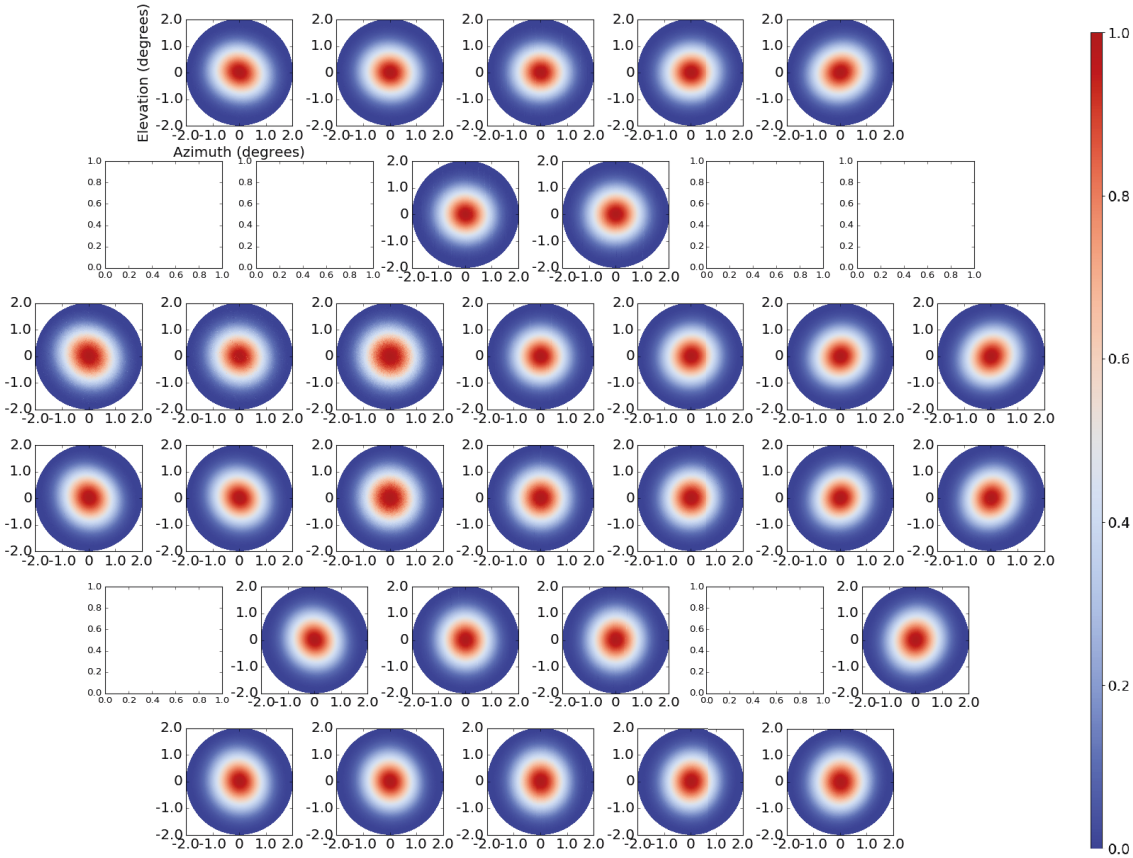

Figure 5.8: Intensity beam maps for V detectors. Intensity beam maps were obtained after stacking Moon scan data, which cover 2° in radius. The beam maps were normalized at their peaks.

array pattern on the sky, enabling detectors to sample the Moon at different angles. These together provide high signal-to-noise beam maps out to 10-degree for intensity, shown in Figure 5.10 for one detector. This beam map contains around four million data points (400,000 seconds) from $\sim$ 150 different Moon scans. The beam map color scale is set to be logarithmic from 10^{-1} to 10^{-4} (normalized at the peak); this color scale should reveal potential side lobes in this beam map. However, no unexpected side lobes are visible in the beam map. To measure radial profile, the data points were

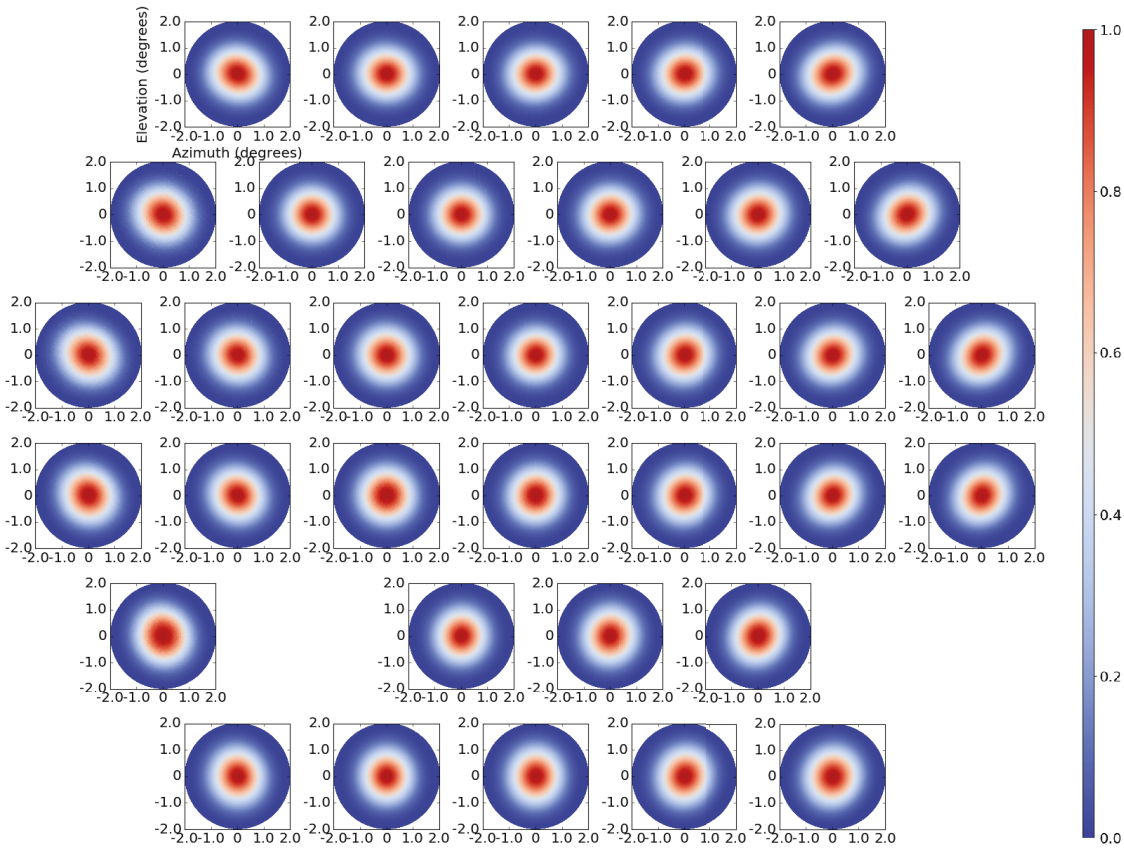

Figure 5.9: Intensity beam maps for H detectors. Intensity beam maps were obtained after stacking Moon scan data, which cover 2° in radius. The beam maps were normalized at peaks.

binned within annuli with 0.05° thickness. The profile is estimated from the medians within each annulus, with uncertainties estimated as the standard errors. The radial profile, along with its uncertainties, shows that the profile follows the optical model for signals > -30 dB and is signal dominated to $> 7°$. The noise level is at -50 dB level except for the central region for two reasons. First, the steepness of the profile in the central region leads to a significant gradient within a finite-thickness annulus; and second, the ellipticity of the beam leads to data points within a circular annulus

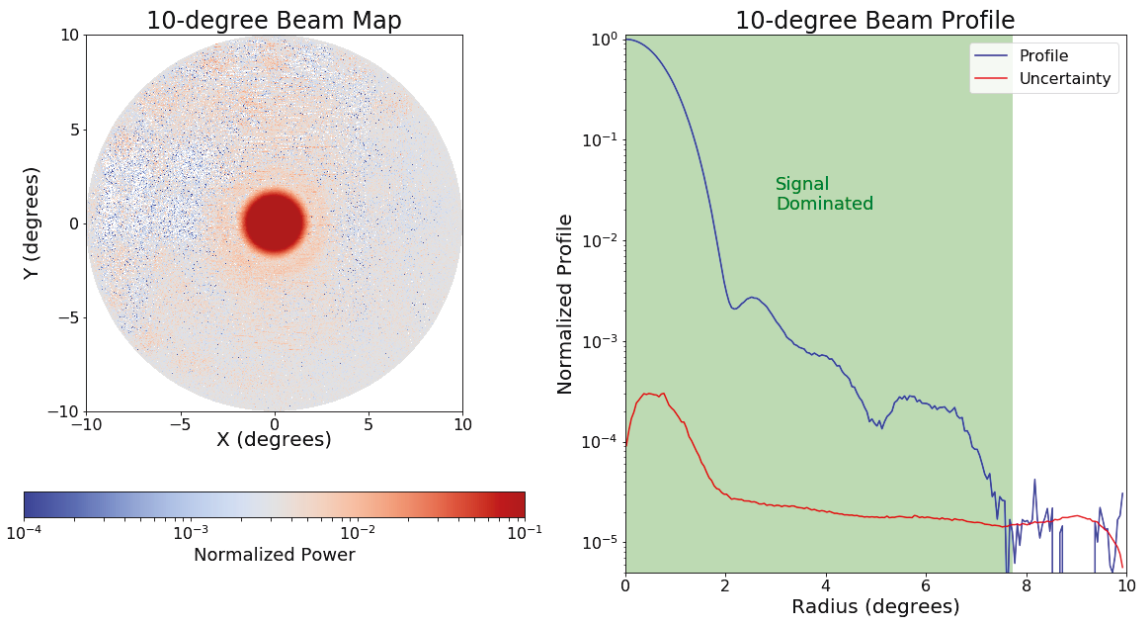

Figure 5.10: A beam map for one detector. A typical beam map is shown on the left. The color scale is logarithmic from 10^{-1} to 10^{-4} (normalized to the peak). This scale is selected to reveal any possible side lobes. On the right, the radial profile is measured in 0.05° annuli from the beam map, shown in blue curve. Uncertainties, shown in red curve, are estimated from the standard error of data points within each annulus. The green-shaded area shows the signal-dominated region within $> 7°$ radius.

having more scattered values. Once outside of the central region, the uncertainty is at -50 dB level, providing a 50 dB measurement of the intensity beam map.

Although one detector is discussed here, the same conclusions hold over all the detectors, which will not be discussed individually.

Once high-fidelity beam maps are available, characteristic parameters can be measured. Both the stacked beam maps and single-scan beam maps can be fit by a 2-D Gaussian profile. Full width at half maximum (FWHM) is then measured along the major-axis and minor-axis. Ellipticity is also calculated as $(a - b)/a$, where a and b are the semi-major axis and semi-minor axis. Since FWHM measurements were made

from many individual Moon scans, the precision of the combined FHWM estimate can be estimated as the standard error of the mean. The major-axis FWHM and the minor-axis FWHM are treated separately for each detector.

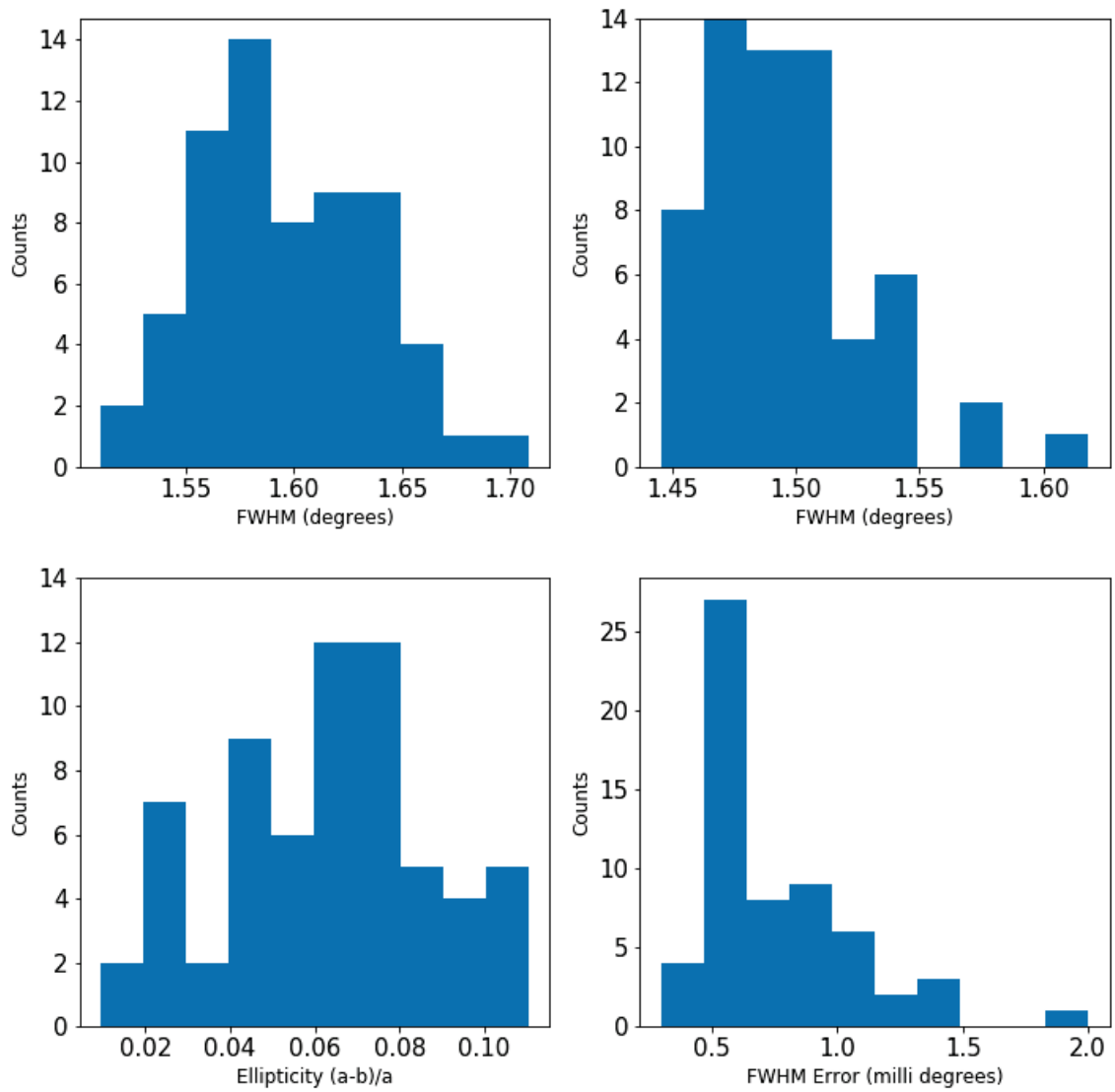

Figure 5.11: The histogram of beam parameters across all detectors. Histograms of the major-axis and the minor-axis FWHM are shown on the top. The ellipticity is shown on bottom left. Uncertainty of the FWHM measurement (calculated across different Moon scans) is shown on bottom right.

Figure 5.11 shows histograms of the major-axis FWHM, the minor-axis FWHM, the ellipticity, and the uncertainty on FWHM measurement. Both the major-axis and minor-axis FWHM are distributed within a 0.2° range, with the major-axis FWHM centering around 1.58° and the minor-axis FWHM centering around 1.48°. Since the beam maps are convolved with the Moon; the measured FWHM is enlarged by $\sim 0.03°$. Therefore, the FWHM measurements across different detectors can be summarized as 1.55° (major-axis) and 1.45° (minor-axis), with around 0.05° deviations across the array. The average of the two FWHMs is 1.5°, as expected from the optical design. The ellipticity is then shown to be within 0.1, centered at around 0.07. Although the FWHM across different detectors varies at the 0.1° level, the FWHM measurement for a single detector is accurate to the 0.001° level. Figure 5.11 on the bottom right shows the estimated uncertainties for different FWHM measurements. The majority have $< 0.001°$ error and the peak is at around 0.0005°. The fractional uncertainty on the ellipticity can then be easily be estimated as 0.08%, much smaller than the ellipticity value scattering.

For cosmological analyses, beams on the sky will be averaged across boresight angles. With even coverage across 90° boresight angles (rotating major axis to minor axis), ellipticity is removed from the averaged cosmological beams.

5.2.2 Moon Polarization Maps

The regolith of the Moon is a dielectric material. Emission from the regolith is refracted at the Moon surface and observed by the CLASS telescope. Using the Fresnel equations,[8] polarization of the refracted radiation is calculated assuming a uniform dielectric constant. No net polarization is emitted perpendicular to the regolith surface; a linear polarization is emitted to other directions, with the polarization direction parallel to the regolith surface normal direction. The polarization fraction increases as the angle to the normal direction increases. Therefore, the Moon's emission is unpolarized at the center, while its emission becomes increasingly polarized towards the limb. Polarization emission reaches a maximum near the limb. The polarization pattern has been measured at 1.4 GHz,[39] shown in Figure 5.12 on the left.

From the measured Moon properties[39] at 1.4 GHz, a simulation was performed to estimate the polarization signal observed by the CLASS 40 GHz telescope, assuming the polarization fraction at 40 GHz is the same. The Moon's polarization emission was simulated as a circularly symmetric annulus from 0.15° to 0.25° radius, with a radial pattern. The polarization amplitude was estimated as 20 K (half of the peak value $\sim$ 20% polarization fraction,[39] equivalent to $\sim$ 40 K from the measured Moon temperature[40]) in the annulus. The Stokes U map was then generated according to the polarization emission before it was convolved with a 1.5° FWHM Gaussian profile. The simulated Stokes U map is shown in Figure 5.12 on the right, with the U amplitude (reduced by beam dilution) around 8 mK. The polarization signal seen by

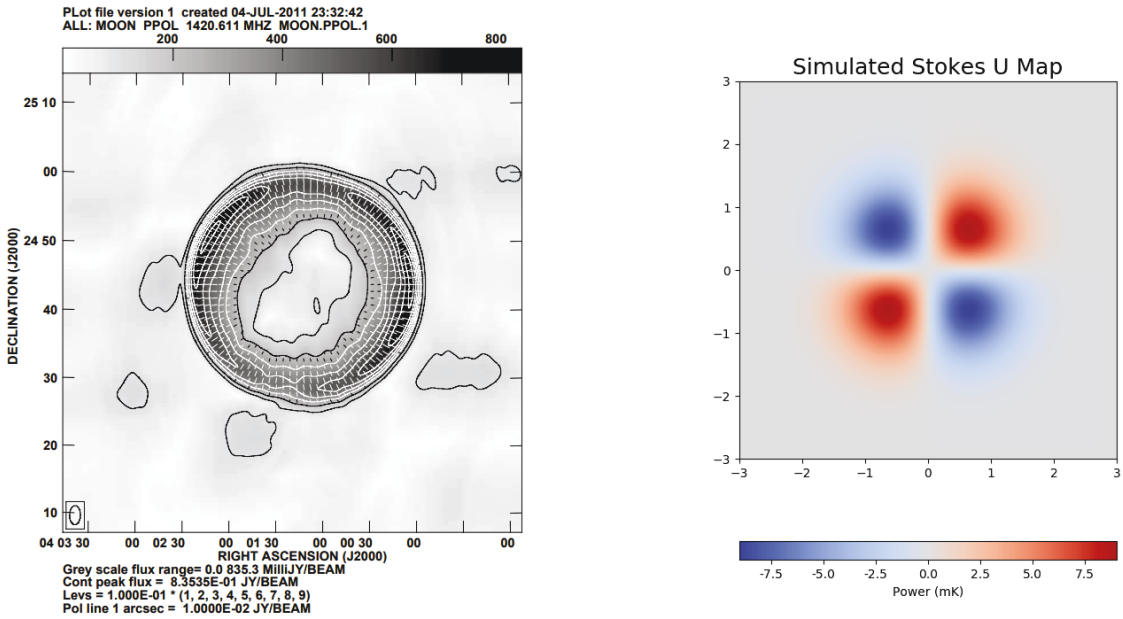

Figure 5.12: The Moon's polarization map and simulation. On the left is shown the distribution of the polarization intensity (grey and contours) and the polarization direction (indicated by the orientation of the bars) of the Moon at 1.4 GHz. This figure is Figure 6 in Zhang et al 2012.[39] On the right, simulated Stokes parameter U map, convolved with the CLASS 40 GHz beam, is presented, with the amplitude around 8 mK.

the CLASS 40 GHz telescope is estimated to be more than three orders of magnitude lower than the intensity, similar to the ratio of CMB temperature fluctuations to polarization. Therefore, demonstrating polarization signal can be isolated at this level indicates that the CMB polarization signal can also be isolated for cosmological studies.

The variable-delay polarization modulator (VPM) modulates incoming polarization signal, another step is taken to extract the modulated polarization signal from raw data, which is called demodulation. After the Moon scan data were demodulated (via the demodulation package developed by Joseph Eimer and Katie Harrington),

beam maps were generated from the demodulated data. Beam maps from one detector pair were added together, equivalent to taking pair differences. Before performing pair differencing, different gains between paired detectors were balanced to remove temperature-to-polarization leakage. Finally, Moon scan intensity data were used as a template to subtract possible temperature-to-polarization leakage. These procedures were all performed in time-ordered data (TOD) space. Initially, a spurious polarization signal was observed for edge detectors. The forebaffle was then blackened (Figure 5.13), which removed the spurious signal.

Figure 5.13: Forebaffle blackening. The forebaffle was blackened with ECCOSORB HR-10 sheets in bags, which were firmly fixed to the forebaffle. The blackening increases detector loading by < 0.1 pW.

Quadrupole patterns emerged across the array, as shown in Figure 5.14. Polarization amplitude is $10 \sim 20$ mK, more than three orders of magnitude lower than the intensity amplitude, consistent with our simulation based on 1.4 GHz polar-

ization measurements[39] and intensity measurements[40] (Figure 5.12). The results in Figure 5.14 are from one moon scan, roughly 1,000 seconds for each detector. Stacking the maps provides higher signal-to-noise results. When the data in Figure 5.14 were taken, the Moon was halfway into the first quarter after the new Moon ($\sim$ 13% illuminated), therefore the upper left part of the maps have more power.

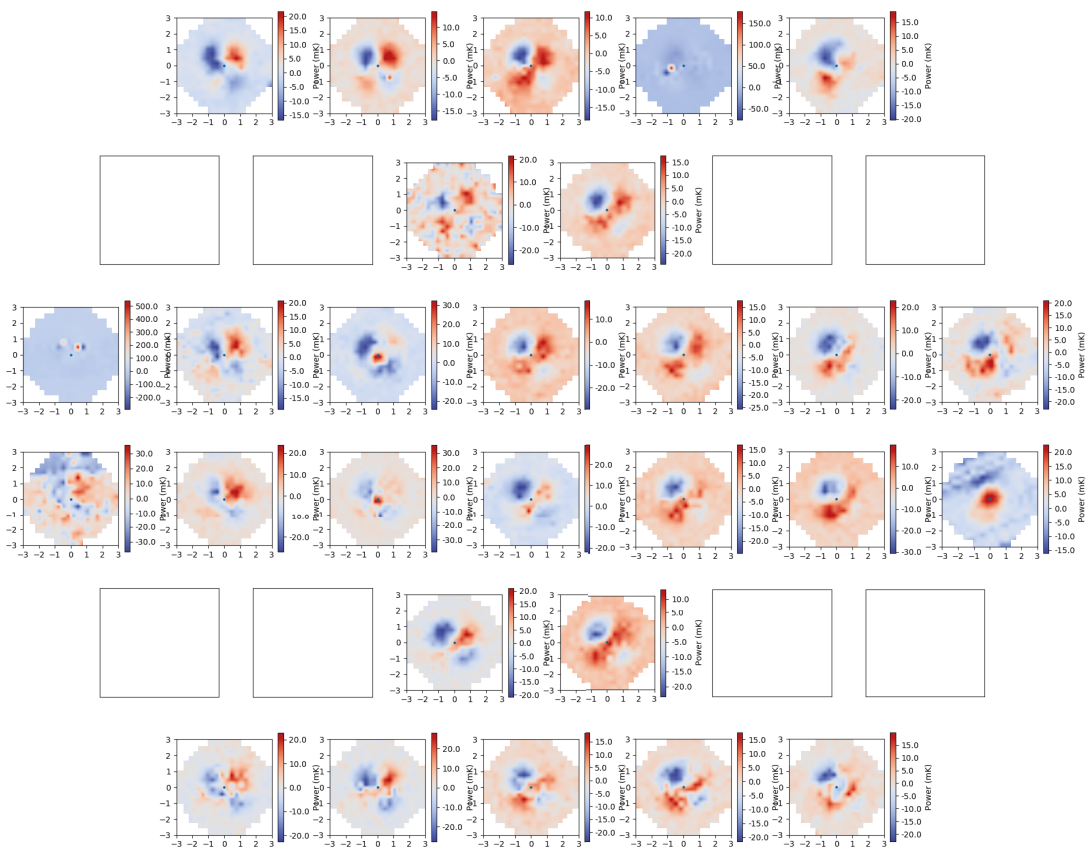

Figure 5.14: Polarization Moon maps. Quadrupole patterns are visible even for one moon scan, with amplitudes of 10 $\sim$ 20 mK. The imbalanced power is due to the phase of the Moon. The Moon was half way into the first quarter after the new Moon ($\sim$ 13% illuminated) when the data were taken, so that the upper left parts of the patterns have more power. Some detectors show unexpected patterns due to detector glitches during this moon scan. This moon scan was taken around 16:46 UTC on July 27th, 2017.

5.2.3 Polarization Angle Determination

Assuming the Moon polarization is circularly symmetric, the orientation of quadrupole patterns in polarization Moon maps can be used to determine the telescope far-field polarization angle. An effective way to extract the quadrupole components in the polarization beam maps is needed. Gauss-Hermite functions form a complete and orthogonal basis for a 2-D space,[14] with an analytical expression

$$f_{i,j}(\theta,\phi) = \left(\frac{\exp[-\theta^2/(2\sigma^2)]}{\sqrt{2^{i+j}i!j!\pi\sigma^2}}\right) \times H_i\left(\frac{\theta\cos\phi}{\sigma}\right) H_j\left(\frac{\theta\sin\phi}{\sigma}\right), \tag{5.1}$$

where θ and ϕ describe the map in polar coordinate system, H_i and H_j are Hermite polynomials, and $\sigma = \mathrm{FWHM}/\sqrt{8\ln 2}$ is the Gaussian width of the beam.

Patterns for different Gauss-Hermite function combinations are shown in Figure 5.15. The two orthogonal quadrupole patterns are presented rotated 45° from each other. Different ratios of the two patterns cover all possible orientations of quadrupole patterns. Orthogonality between Gauss-Hermite functions guarantees that all quadrupole information is stored within these two patterns.

Each polarization beam map was fitted with the Gauss-Hermite patterns up to order of 10, meaning $i + j \leq 10$. Any corrections beyond order 10 provide marginal improvement. The quadrupole patterns were then recovered with fitted coefficients on the two orthogonal Gauss-Hermite quadrupole patterns. The polarization angles were then calculated from the two coefficients. Therefore, the far-field polarization angle

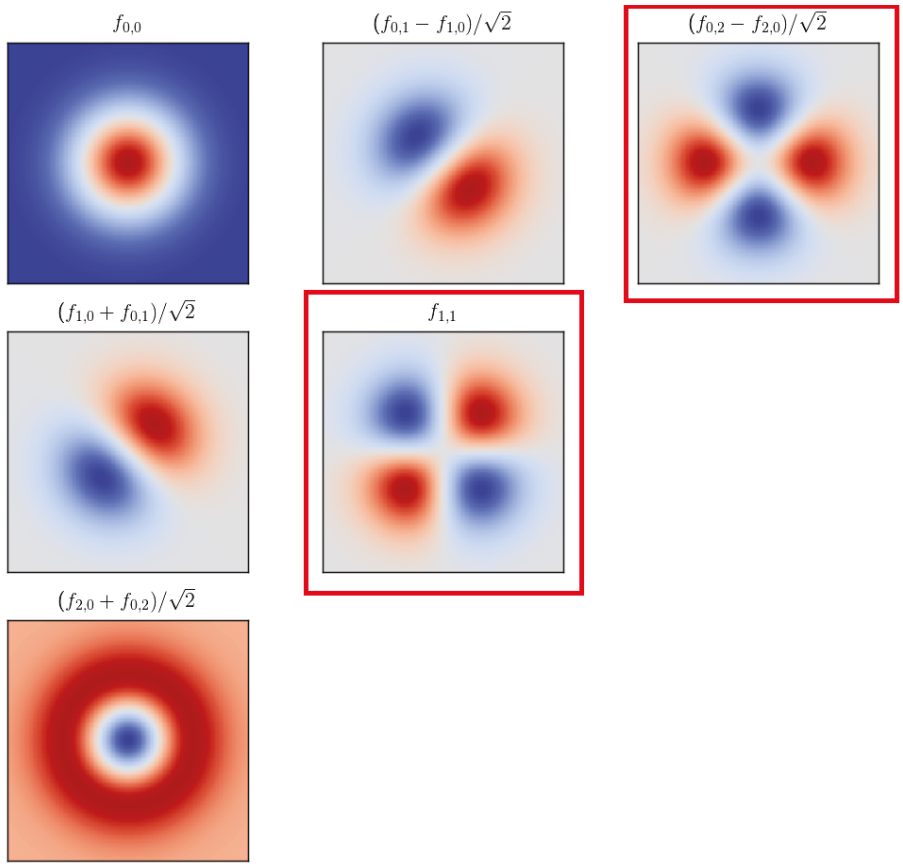

Figure 5.15: Patterns from some Gauss-Hermite function combinations. Patterns with different combinations from Gauss-Hermite functions are shown, with $f_{i,j}$ defined in Equation 5.1. The two quadrupole components are pointed out with red boxes. $i + j$ is defined as the order of the function.

of each detector is calibrated, as shown in Figure 5.16. A measurement for one corner feedhorn on the array is shown here. A quadrupole pattern (rotated slightly over 45°, as expected) is recovered from the measured map, determining the polarization angle of the detectors.

Together with near-field polarization angle calibration from the wire-grid insert (see Subsection 4.5.2), a comprehensive calibration of the polarization angle for each detector is obtained.

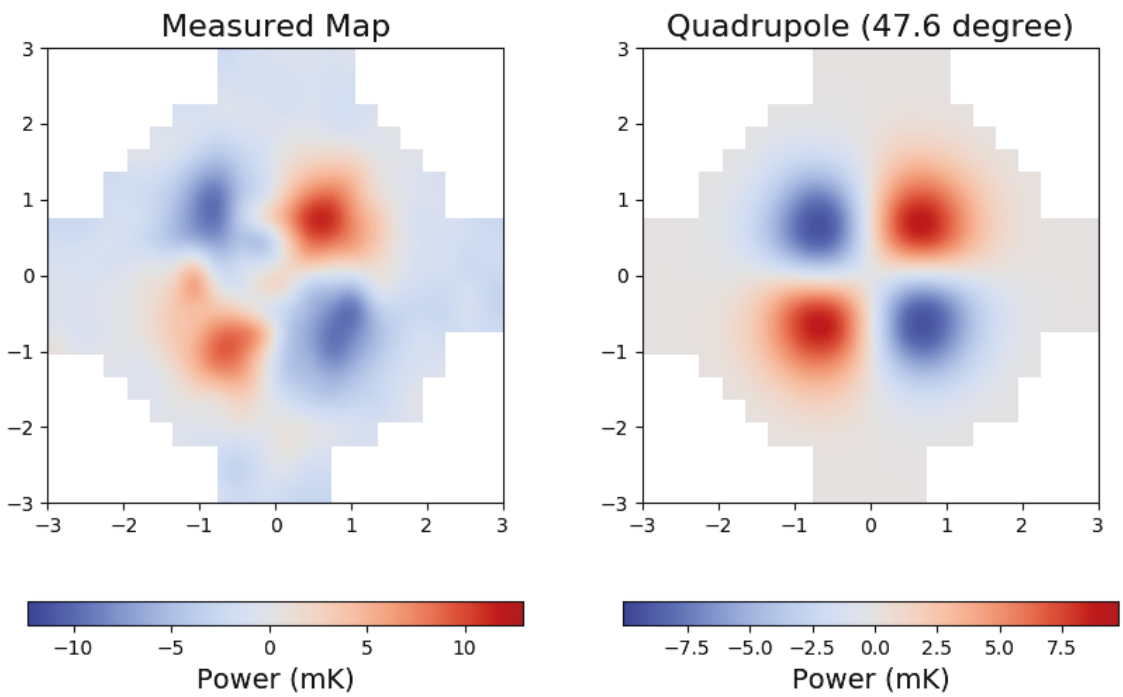

Figure 5.16: Polarization angle determination. A measured Moon polarization map is shown at left, with the extracted quadrupole component shown on the right. The polarization angle is determined as 47.6° from the Gauss-Hermite separation method.

5.3 Ground Pickup

Because ground pickup could be a major contaminant for CLASS, a forebaffle assembly was designed to mitigate it in hardware. Then, once the data were available, systematic ground pickup analyses were conducted to characterize the ground pickup signals.

The CLASS site horizon elevation is shown in Figure 5.17. The peak of Cerro Toco rises to 15° elevation. The measured horizon elevation curve is plotted over the photo. The horizon elevation curve will be used to determine whether the azimuth synchronized signal is from the ground emission throughout this section.

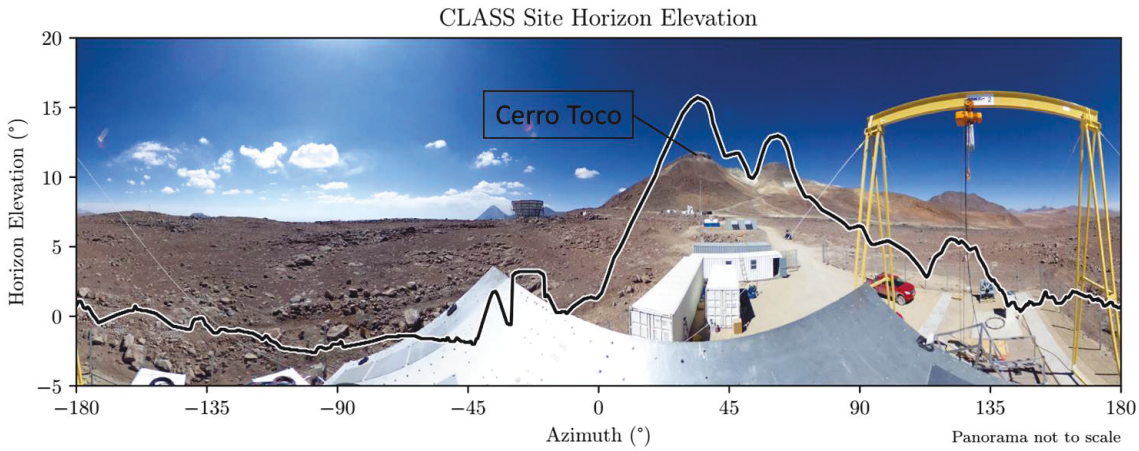

Figure 5.17: A panorama is taken on top of the boresight wedge (see Section 4.2) with the measured horizon elevation curve overplotted on the photo. The horizon elevation rises to around 15° at the peak of Cerro Toco. The yellow gantry in the photo was pushed away and is below horizon when viewed from the telescope. Figure credits: Matthew Petroff.

Since the observation configuration (e.g., boresight angle) stays unchanged within one day, data were analyzed in one-day units. During CMB scans, the telescope mechanically stays at constant elevation 45° and scans azimuthally at a constant speed (1 deg/s) before it turns around. One single azimuthal scan could span up to 720° depending on whether the Sun needs to be avoided. CMB scans were analyzed in the unit of single scan, separated by the turnarounds. A small fraction ($< 1\%$) of data were also cut out around turnarounds to reject data when the detectors may be unstable. Within one day, each 720° CMB scan data were analyzed separately. After some initial processing, CMB scan data were binned by azimuth position. Then results from all CMB scans within one day were averaged within each bin, which became the ground pickup signal for this day.

Intensity ground pickup was first characterized. When the demodulation data analysis package was available, polarization ground pickup was studied. Finally, special CMB scans at different elevations were performed to characterize the ground pickup signals at different observation elevation angles.

5.3.1 Intensity Ground Pickup

Intensity ground pickup was first analyzed following the analysis procedure described earlier. Initially, the azimuth synchronized signal is coherent with the ground profile, with the amplitude around 150 mK, with initial power calibration by John Appel. Given the ground is at $\sim$ 300 K, the amplitude 150 mK is $< 0.1\%$, which is consistent with the forebaffle design.

To further suppress the intensity of the ground pickup, hardware modifications were considered. It was noticed that detectors from the top row saw a similar amount of (or even more) ground pickup as those on the bottom row. Since the elevations of the top and bottom rows are different by almost 20°, they should not be seeing even the same amount of ground pickup. After reviewing the telescope design, I determined that the top panel of the forebaffle interface is a possible source of reflecting ground emission into the telescope, which loads the top row detector more than the bottom ones, as shown in Figure 5.18 on the bottom left. After blackening the panel with ECCOSORB HR-10 absorptive sheets, the intensity ground pickup was significantly reduced. Following the same idea, side panels of the forebaffle interface were also

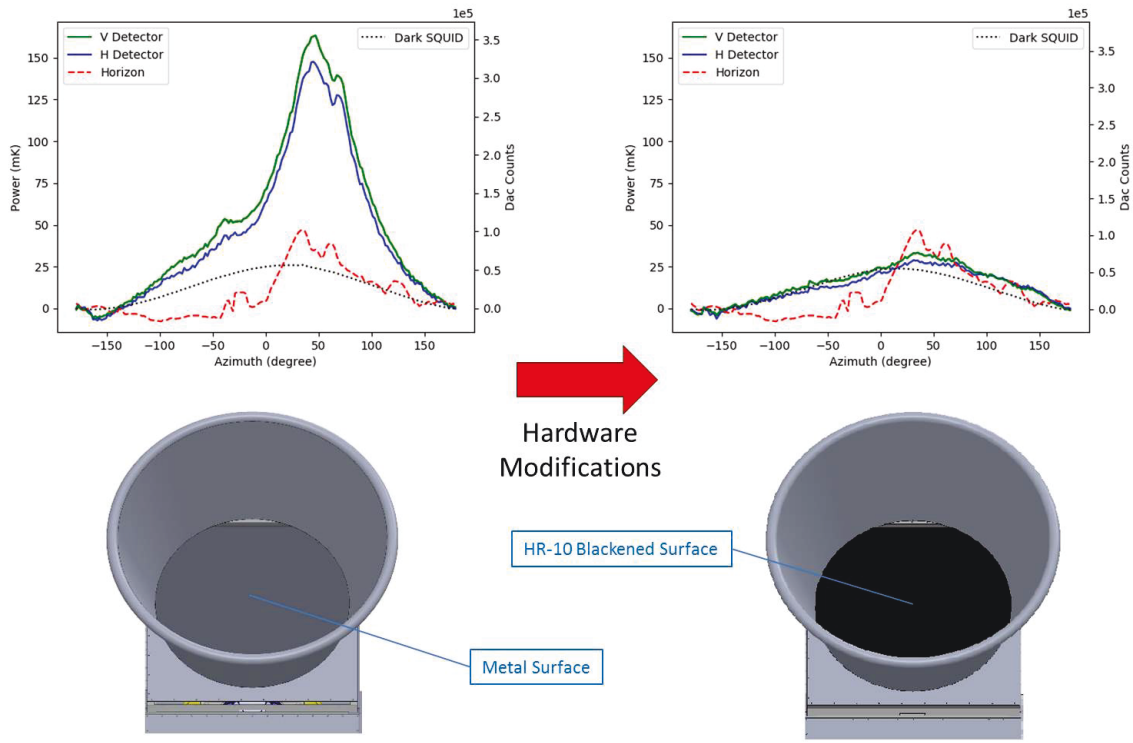

Figure 5.18: Intensity ground pickup improvement by hardware modifications. The improvement of intensity ground pickup for one feedhorn is shown from left to right on the top. The most efficient hardware modification is also presented from left to right on the bottom. On the top plots, V and H detectors are plotted, together with a dark SQUID (tracing the terrestrial magnetic pickup) through the same readout system. Two detectors are calibrated by power and counts, while the dark SQUID is only calibrated by counts. Two plots are set at the same scale for comparison. Horizon elevation is also shown as a red dashed line (not to scale). On the bottom, views of the forebaffle from 15° elevation (Cerro Toco peak) are presented. On the left, a reflective metal surface could reflect ground emission into the telescope. On the right, the metal surface is blackened with ECCOSORB HR-10 absorptive sheets, which significantly reduces the intensity of the ground pickup.

blackened, and a wooden cover of the warm-optics cage was backed with metal sheets to make it electromagnetically isolating, which yielded further improvement. The final results are shown in Figure 5.18. After three rounds of hardware modifications,

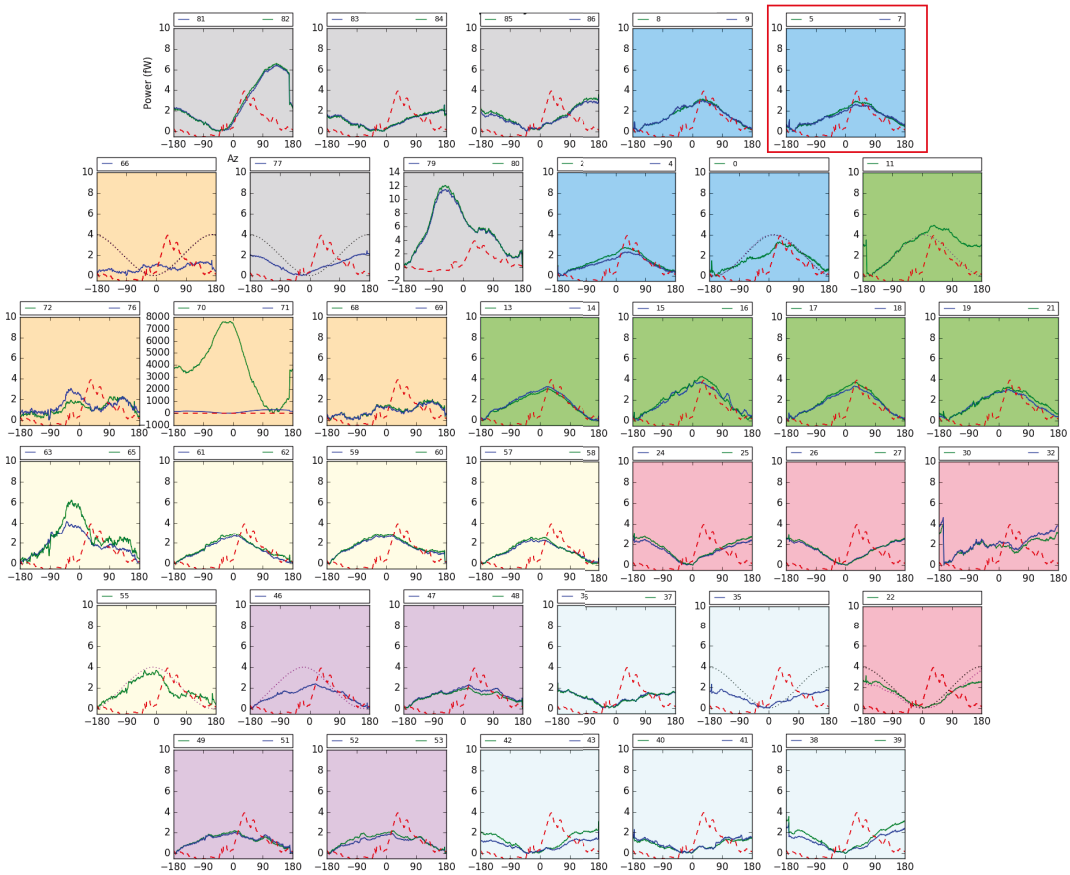

Figure 5.19: Intensity ground pickup after hardware modifications. V detectors and H detectors are represented by green and blue curves respectively. Red dashed lines are the horizon elevation as shown in Figure 5.17. Background colors distinguish detectors read out from same columns, implying that they are sharing the same magnetic pickup. One subplot for each background color has data plotted (in dots) from dark detector or dark SQUID, which traces the magnetic pickup for detectors read out through the same column. Both the ground profile and the magnetic pickup curves are not to scale; only their shapes are informative. On the bottom right part of the array, the magnetic pickup reaches its bottom when the ground profile rises to its peak. The signal clearly follows the magnetic pickup trend, indicating that the magnetic pickup is the dominant source of emission after the hardware modifications. The subplot used as an example in Figure 5.18 is pointed out in a red box on the top right. Some feedhorns have abnormal results due to detector glitches. The data were taken on December 6th, 2016.

the azimuth synchronized signal was reduced from 150 mK to around 40 mK, whose shape implies that the magnetic pickup became the dominant component after the hardware modifications.

After the hardware modifications, intensity signal for all detectors is presented in Figure 5.19. The azimuth synchronized signal was reduced at around 40 mK level across the array. The shape of magnetic pickup measured by dark detectors and dark SQUIDs is sinusoidal, because projection of fixed terrestrial magnetic field on rotating SQUIDs is sinusoidal. Some detectors have the magnetic pickup exactly out of phase with the ground profile. The fact that the azimuth synchronized signal is coherent with the magnetic pickup at these detectors clearly shows that the dominant source for the signal has become the magnetic pickup. The azimuth synchronized signal is around 40 mK. Templates of the azimuth synchronized signal are being generated to subtract from the CMB data, which will reduce the signal to a even lower level.

5.3.2 Towards Polarization

After the demodulation analysis packaged was developed by Joseph Eimer and Kathleen Harrington, the azimuth synchronized signal analysis was extended from intensity to polarization. Figure 5.20 shows the intensity signal along with the polarization signal plotted together, where the polarization signal is basically a flat line under this scale implying the polarization signal is much smaller than that from intensity (three orders of magnitude below). Polarization ground pickup analysis is still

ongoing, complete results will be published in a paper later.

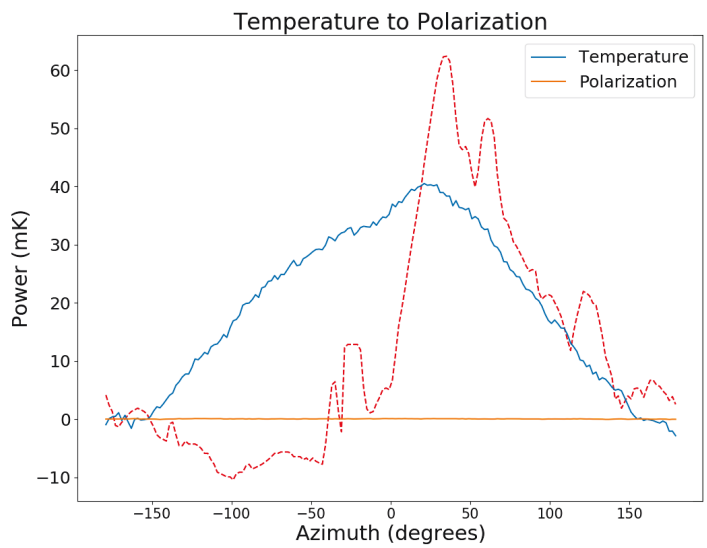

Figure 5.20: Azimuth synchronized signal containing both intensity and polarization signals. The temperature signal for detector 14 is shown in Figure 5.19. Horizon elevation is also indicated by the red dashed line. Polarization signal from the same data set is presented (almost a flat line in this scale), meaning its amplitude is much smaller than that of intensity.

The dependence of ground pickup signals (both intensity and polarization) on elevation angle was investigated with special CMB scans at 30°, 40°, 45°, 50°, and 55° elevation angles. After comprehensive analysis, 45° elevation is proved to be the optimized value, as designed.

Chapter 6

Summary

CLASS is a project to measure the largest-scale polarization patterns on the sky via frequency bands across 40 GHz, 90 GHz, 150 GHz, and 220 GHz. This unique measurement will answer fundamental questions in physics and cosmology, including but not limited to the origin of the universe (inflation paradigm), cosmic dawn (reionization), the sum of neutrino masses, and various Galactic sciences.

The first CLASS telescope, at 40 GHz, was deployed in 2016 and has been observing for more than one year. The following three telescopes will be deployed in the coming two years. As a five-year survey, the CLASS survey will observe through at least 2021 with ground-breaking scientific results to be expected.

Appendix A

Fourier Transform Spectrometer (FTS)

In recent years, Fourier Transform Spectrometers (FTS) have been widely used in instrument development and as instruments on telescopes, since they have several advantages over conventional spectrometers. First of all, FTS is slit-free, which means all the radiation entering the field of view (FoV) is accepted, so the efficiency is high. Secondly, FTS provides spectra of all pixels in the FoV.[18]

For the CLASS project, it is essential to determine the frequency response of the detector and the spectral transmission of the different materials used in the optical system. The FTS constructed and tested in our lab is used for this measurement. In the broad band configuration, there are roughly three main parts in the entire system (see Figure A.1): optical components, a thermal source, and a bolometer.

The bolomoter measures the radiation intensity while a linear stage carrying the

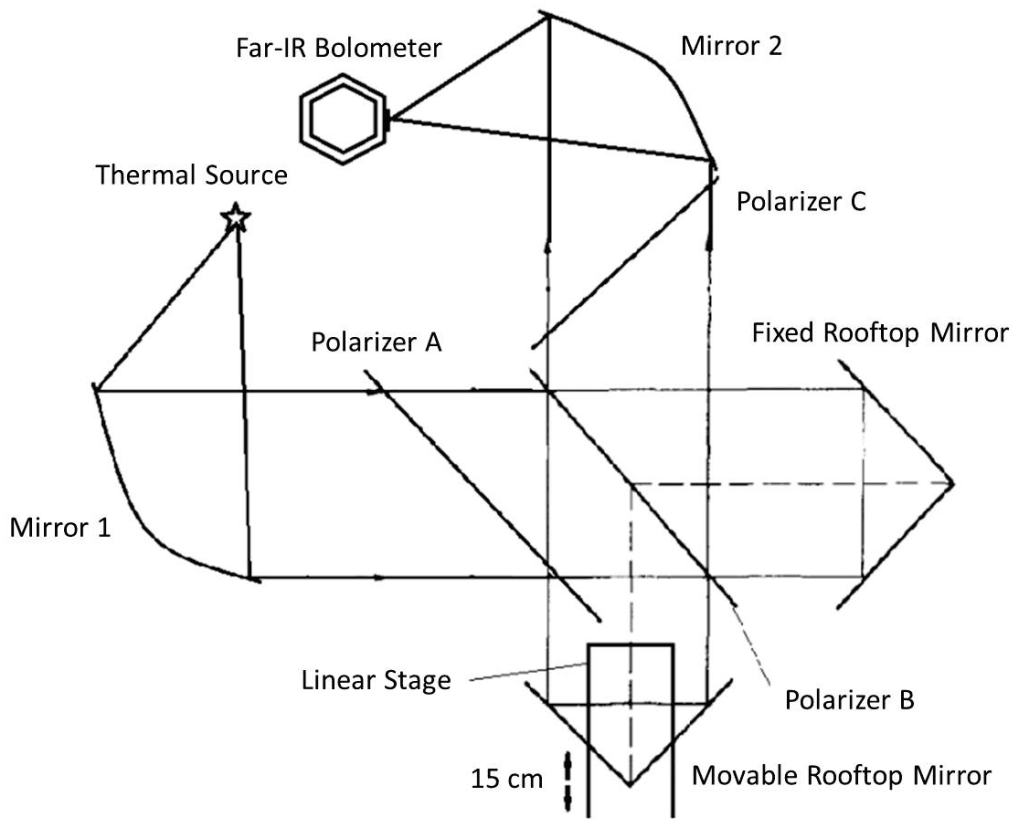

Figure A.1: Schematic layout of the Fourier Transform Spectrometer, which contains two reflective mirrors, three polarizers, one fixed rooftop mirror, one movable rooftop mirror, a source, and a detector.

movable mirror records its position from 0 to 150 mm. Therefore, the raw data are an interferogram (see Figure A.2). A sharp peak is in the center, which means the source is broadband as we expected. A long-scale trend is also visible in the plot. To remove the trend, the data are fitted with a degree-4 polynomial (considering the simplicity of the background, this should be more than enough). After de-trending, Fourier transforming the data should, in principle, provide the spectrum. However, some other techniques were applied to better interpret the data due to the noise and

the boundary condition.

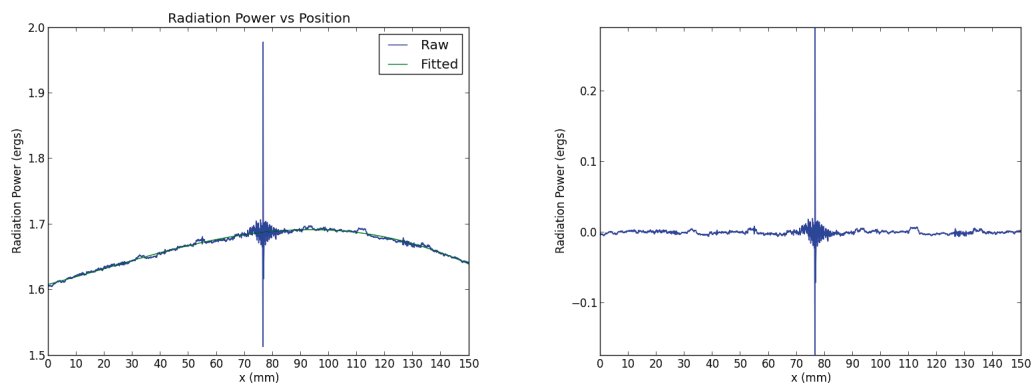

Figure A.2: Left: Raw interferogram (blue line) and quartic polynomial fitted background (green line); Right: interferogram after subtracting the trend.

Theoretically, the interferogram should be perfectly symmetric about the peak, which is not the case in reality, especially at large scales. We can see in Figure A.2 that the interferogram becomes more symmetric closer to the peak, however, symmetry weakens when observing farther away from the peak. On the other hand, asymmetry implies that the data contain noise instead of signal. Thus the farther away from the peak we observe, the more the signal is dominated by noise. Therefore, data points should be weighted differently.

The most straightforward idea would be simply to accept one part of the interferogram, say 25 mm – 125 mm, and then perform a Fourier transform. However, the sharp edge of a top-hat window function results in a sinc function, implying that apodization should be used. A Gaussian profile is selected since its Fourier transform is itself (ripple-free), so we applied a Gaussian window function to the middle of the interferogram. There is always a trade-off between the resolution and contamination.

The resolution of the spectrum is directly related to the length of the interferogram, so if too small a patch is used, the spectrum resolution would be too low. On the other hand, the more of the interferogram is used the more contamination would leak into the final spectrum. Results in all cases depend on only one parameter, the standard deviation σ in the Gaussian window function. By trying different values of σ, we got the optimized number as $\sigma = 25$ mm, as shown in Figure A.3.

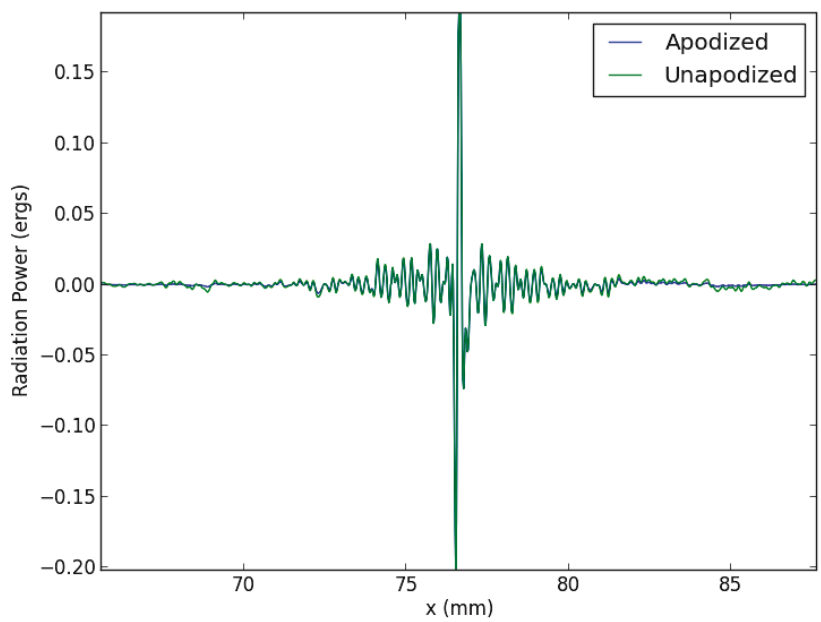

Figure A.3: Apodized data patch (blue line) and unapodized data patch (green line). The two data sets fit well around the center while the apodized data go flat faster than the unapodized data as well as going farther from the center.

A Fourier transform was applied to the data with the apodization. The results are shown in Figure A.4. In the upper graph, spectra from 15 different independent measurements are exhibited. All these spectra are consistent with each other in the

range between 100 GHz – 1000 GHz. The range is limited by the bolometer. The lower graph shows the average of the 15 measurements shown in the upper graph. The averaged spectrum shown in the bottom of Figure A.4 is trustworthy and repeatable within the frequency range from 100 GHz to 1000 GHz. Prominent features in the spectra are three absorption lines, which come from gaseous molecules in the air.

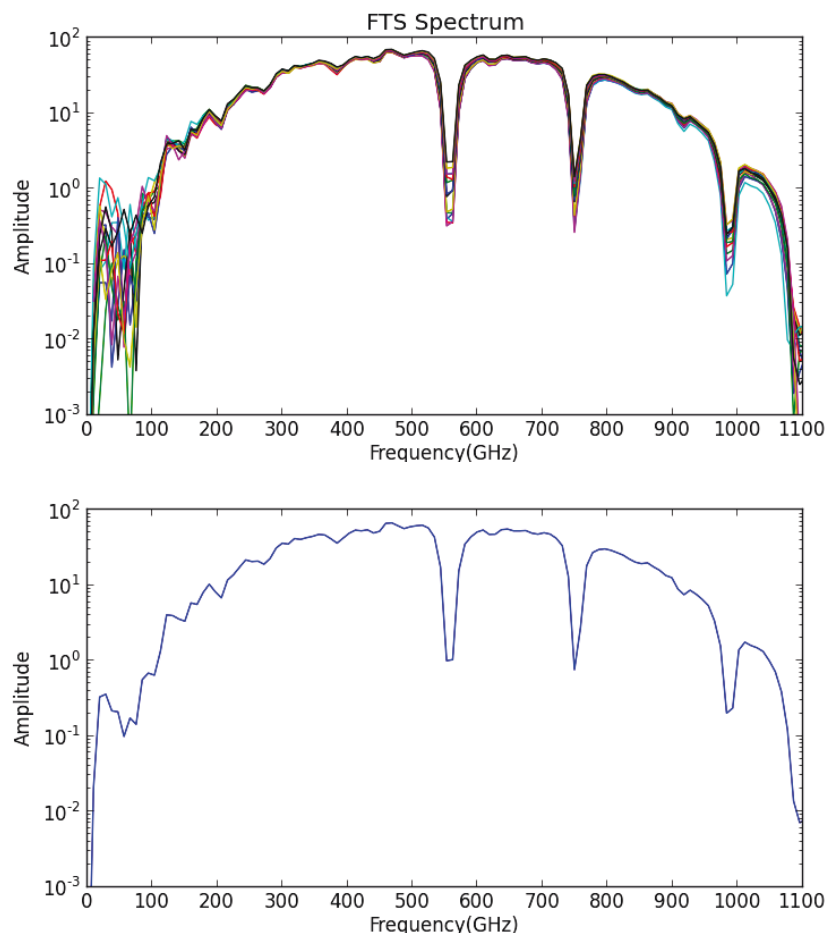

Figure A.4: Upper graph shows the 15 different spectra taken from 15 different measurement; lower graph shows the average of all the measurements. Molecular absorption lines from the air are easily seen.

The Fourier Transform Spectrometer has shown its capability of detecting spec-

trum at frequency between 100 GHz – 1000 GHz in its broadband configuration. In its narrow band configuration, frequency ranges around 40 GHz and 90 GHz are covered similarly to the above discussion. With the FTS, different optical materials can be characterized. The system frequency response is calibrated during integration tests.

Appendix B

Boresight Wedge Drawings

Two wedges for CLASS telescopes have been made. They are deliberately made identically for compatibility, except for bolt patterns on the top plates (where the cryogenic receivers and the warm-optics cages sit).

The first wedge has a bolt pattern for two cryogenic receivers, assuming the 40 GHz telescope design. Some auxiliary bolt patterns were also designed for future use. The second wedge does not have bolt patterns for the receivers, nor does it have auxiliary bolt patterns, which are planned to be placed when needed. However, the two wedges share an identical bolt patterns for the warm-optics cages, which can be used as a reliable anchor for optical alignment.

Drawings of the two wedges are attached, which were generated by John Karakla.

Drawings for the First Wedge

Wedge top plate 1 top view

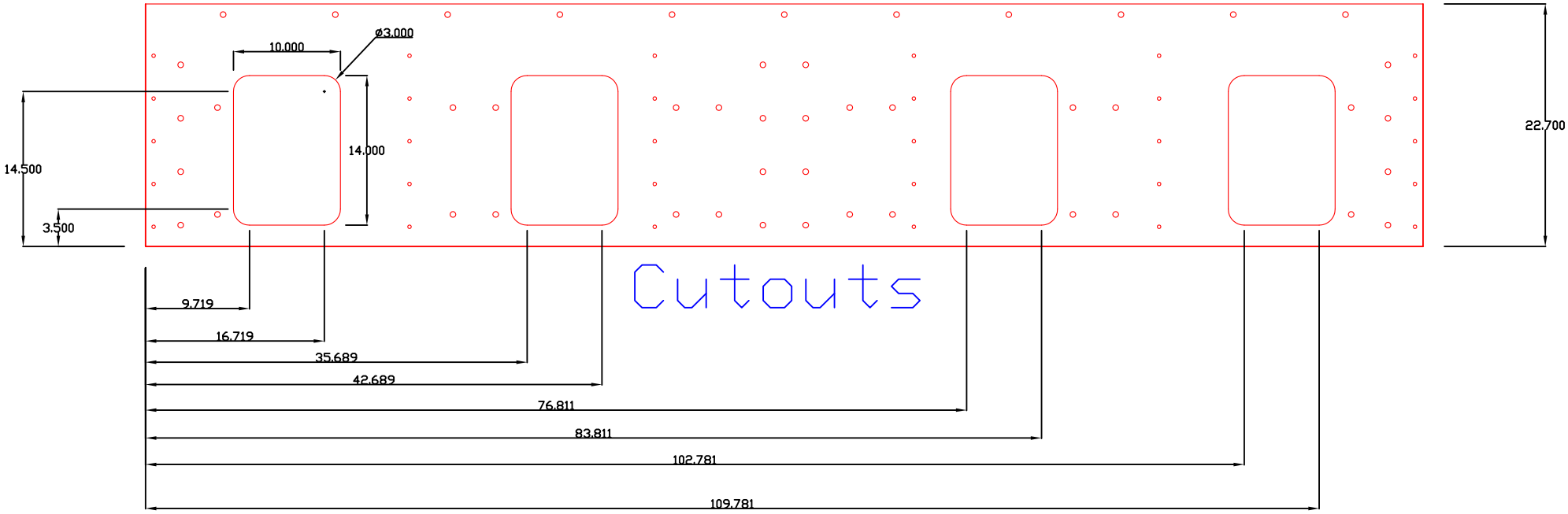

½" Aluminum T6061

Wedge top plate 1 top view

0.332 Holes

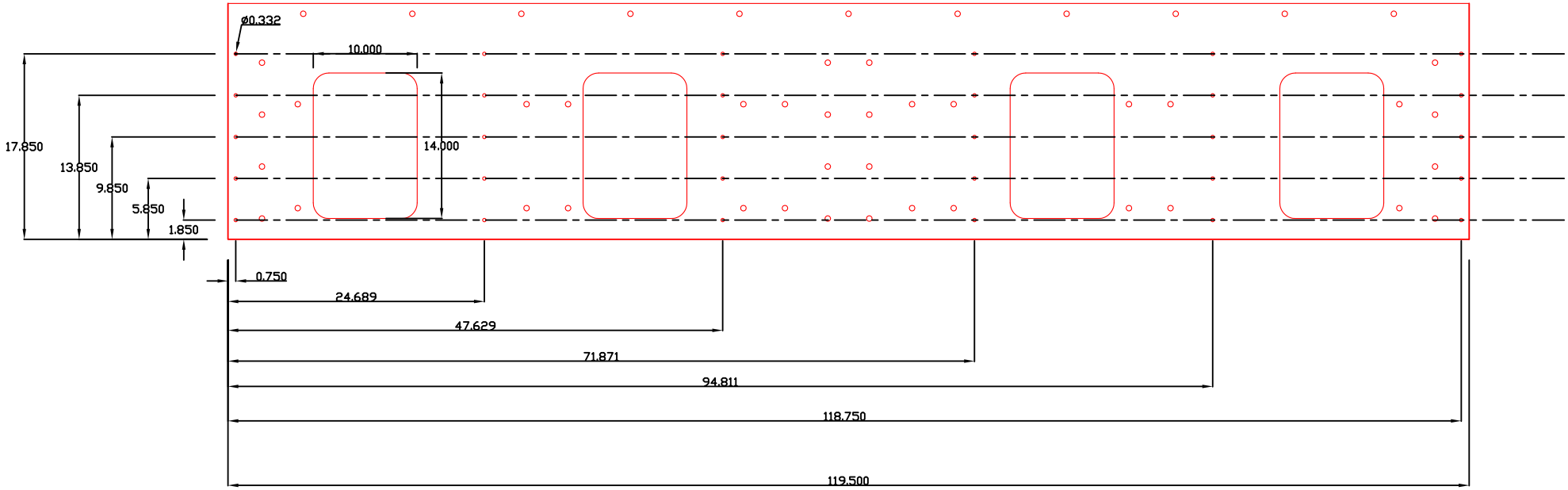

Wedge top plate 1 top view

0.531 Holes

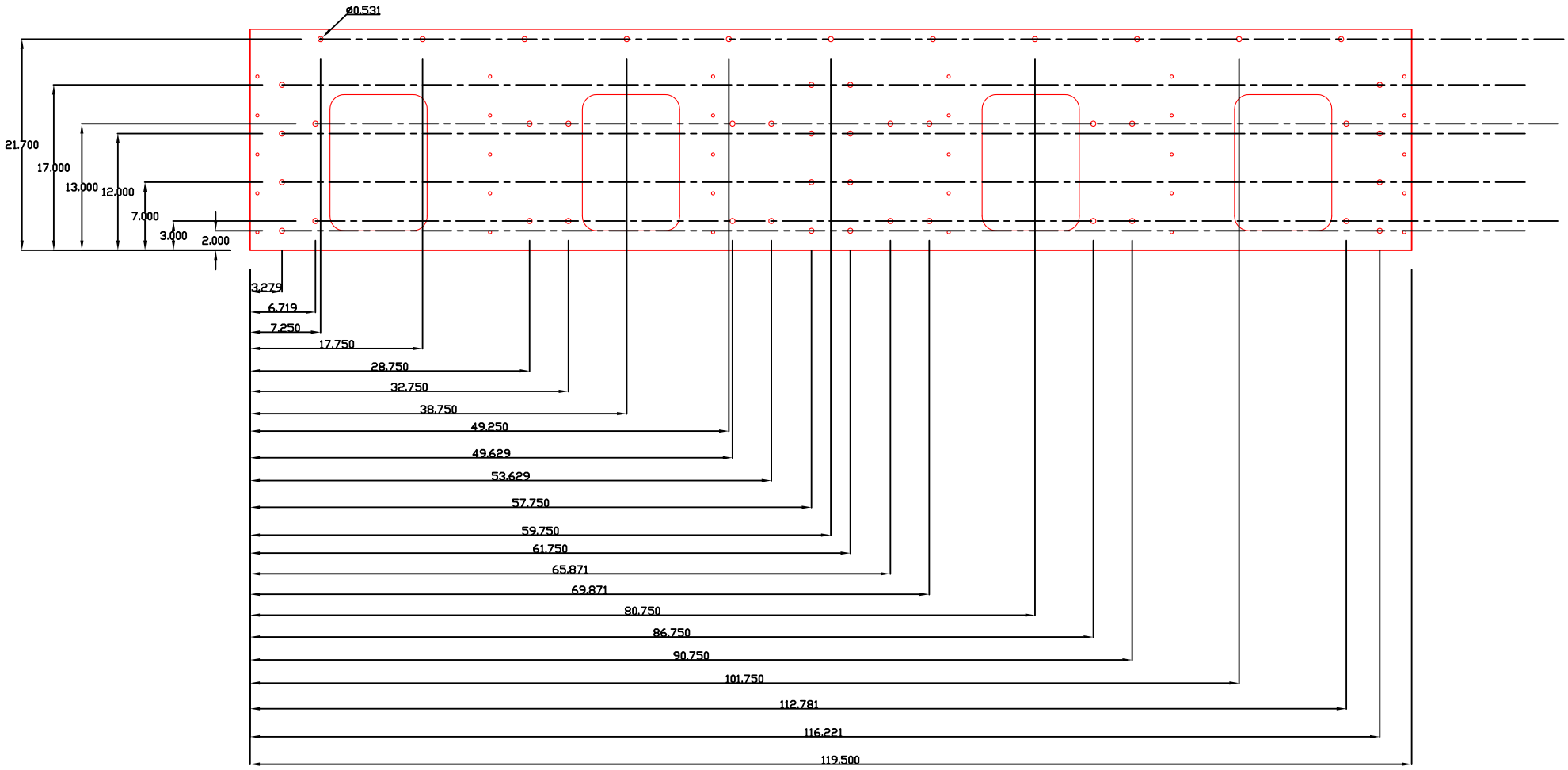

Wedge top plate 2 top view

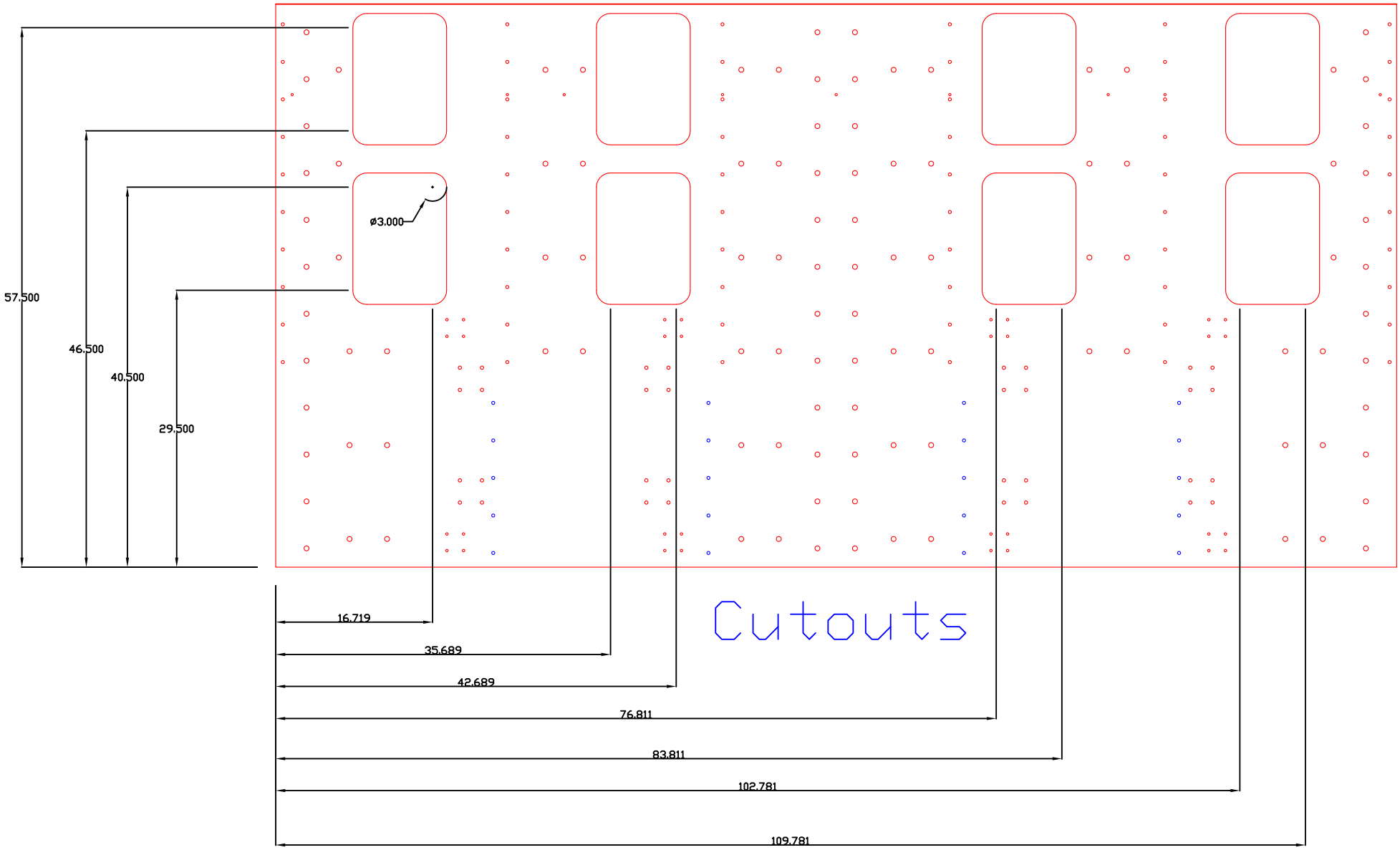

Wedge top plate 2 top view

0.268 Holes

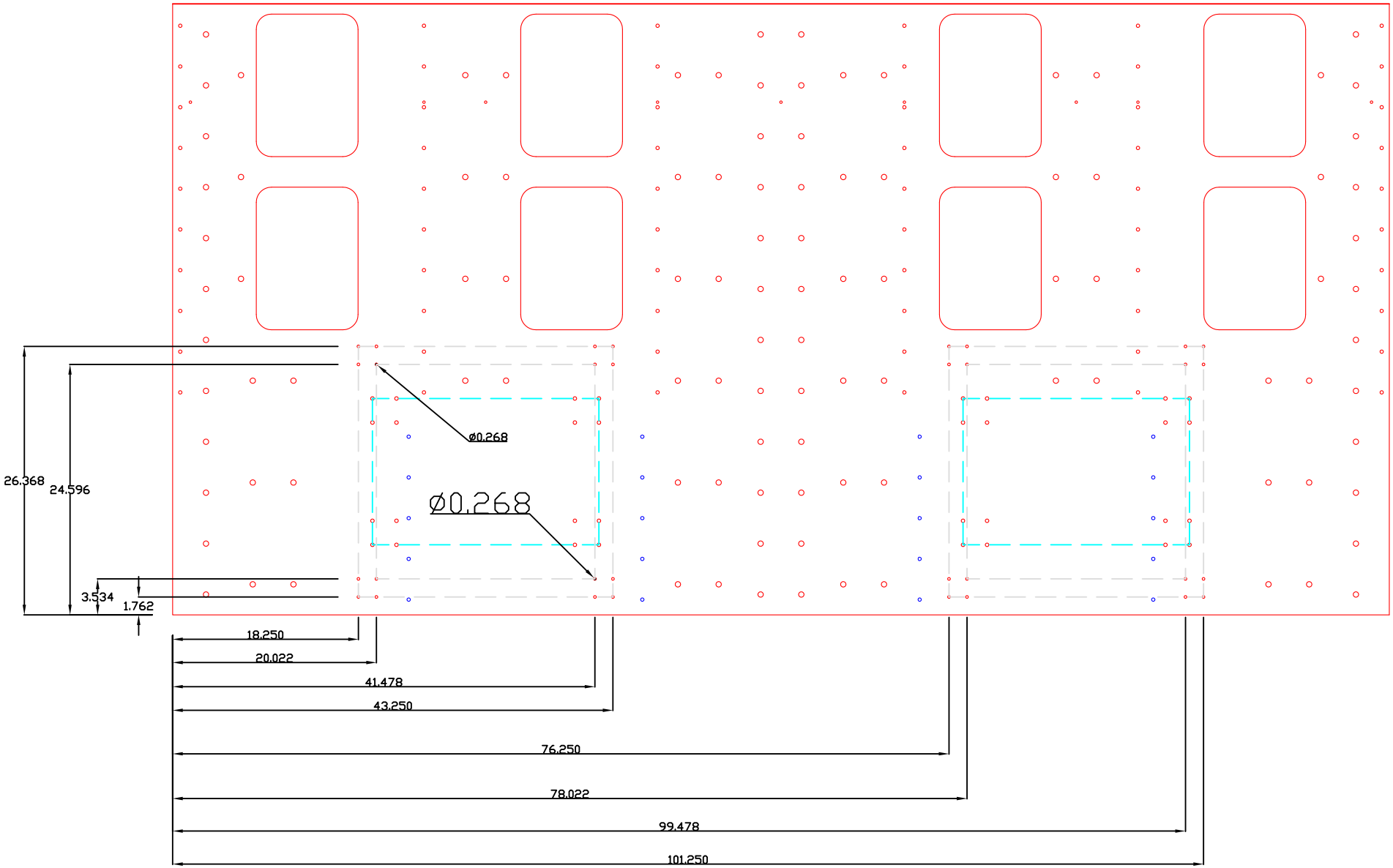

Wedge top plate 2 top view

0.354 Holes

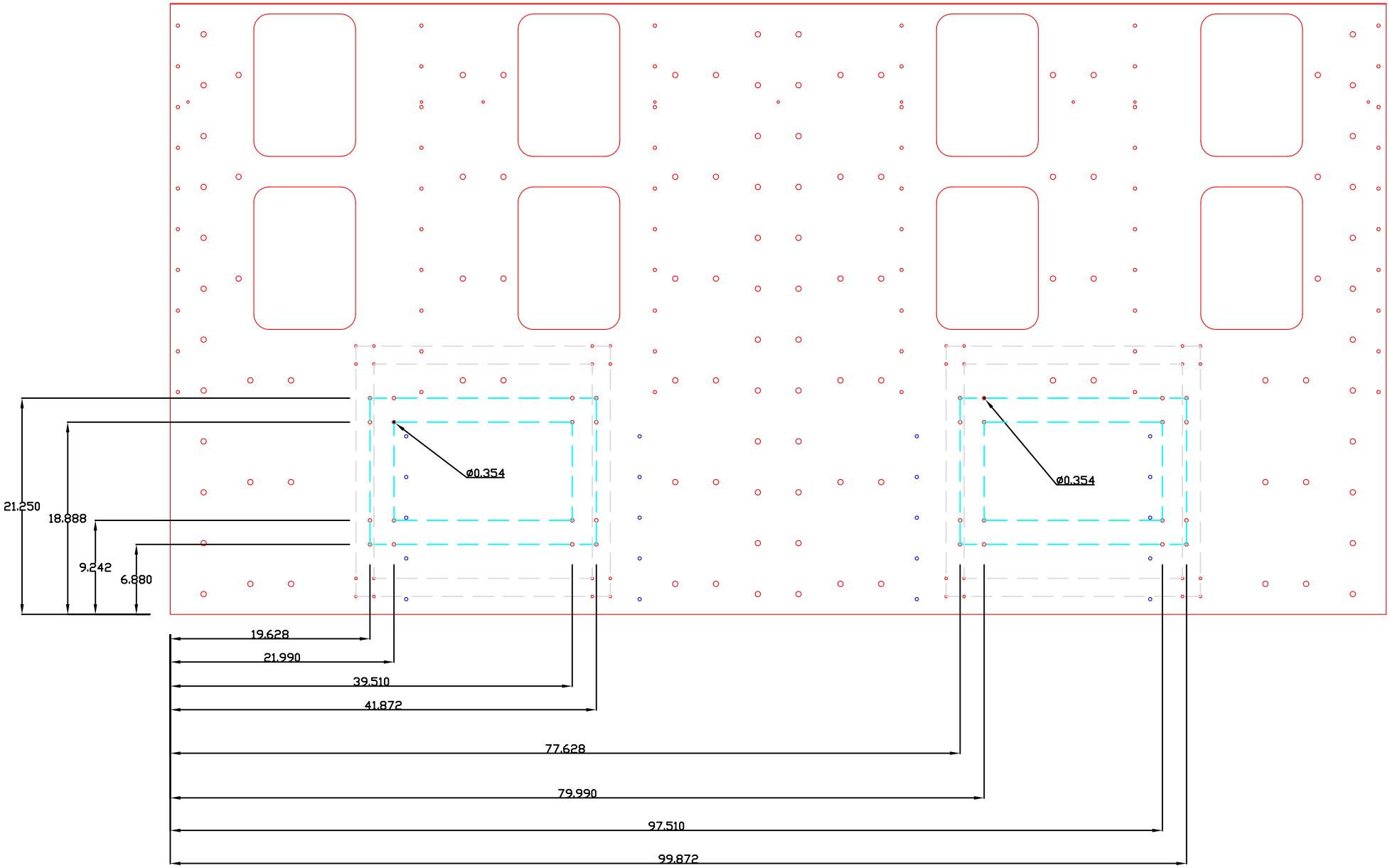

Wedge top plate 2 top view

0.332 Holes

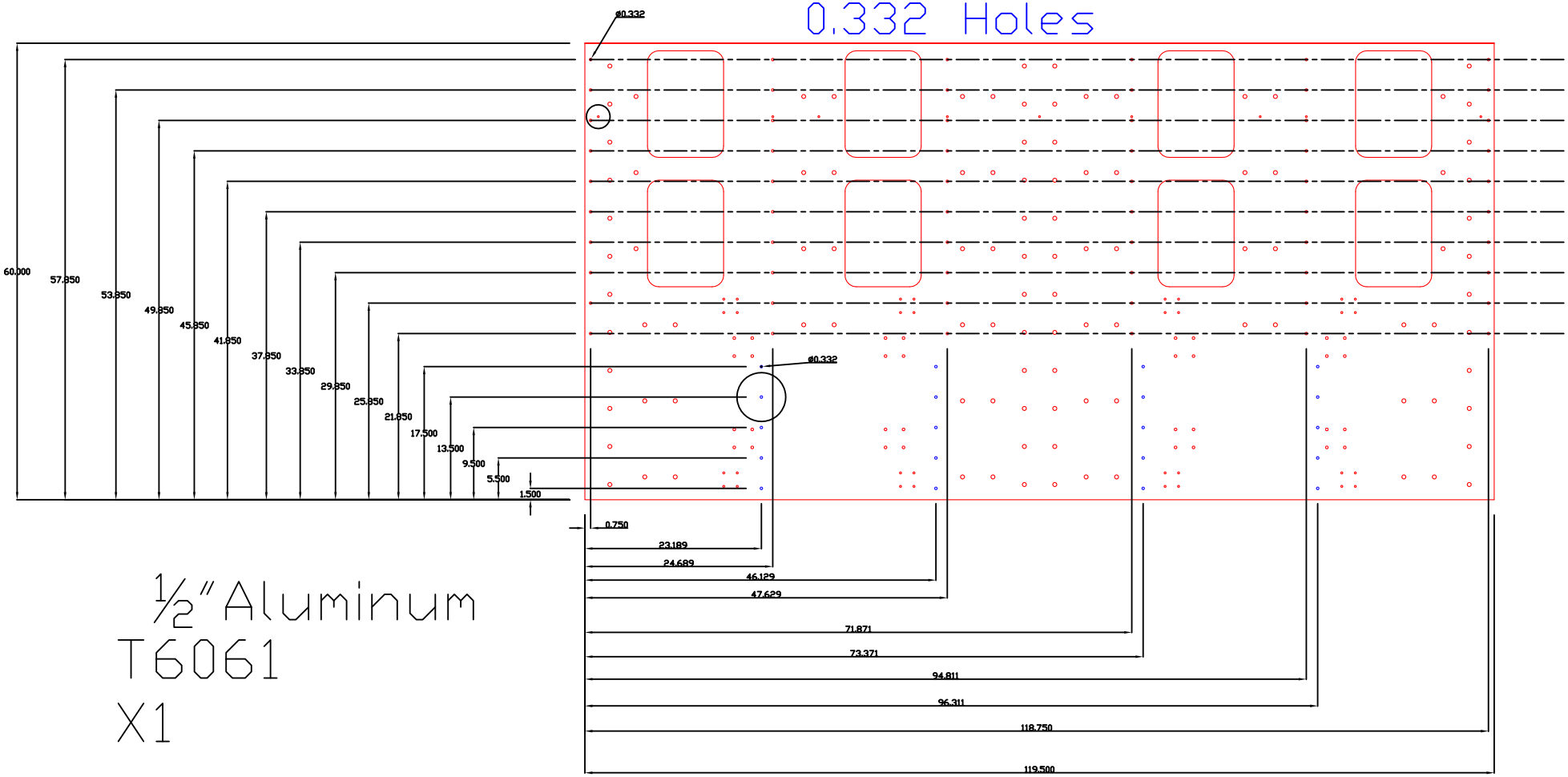

½" Aluminum
T6061
X1

Wedge top plate 2 top view

0.531 Holes

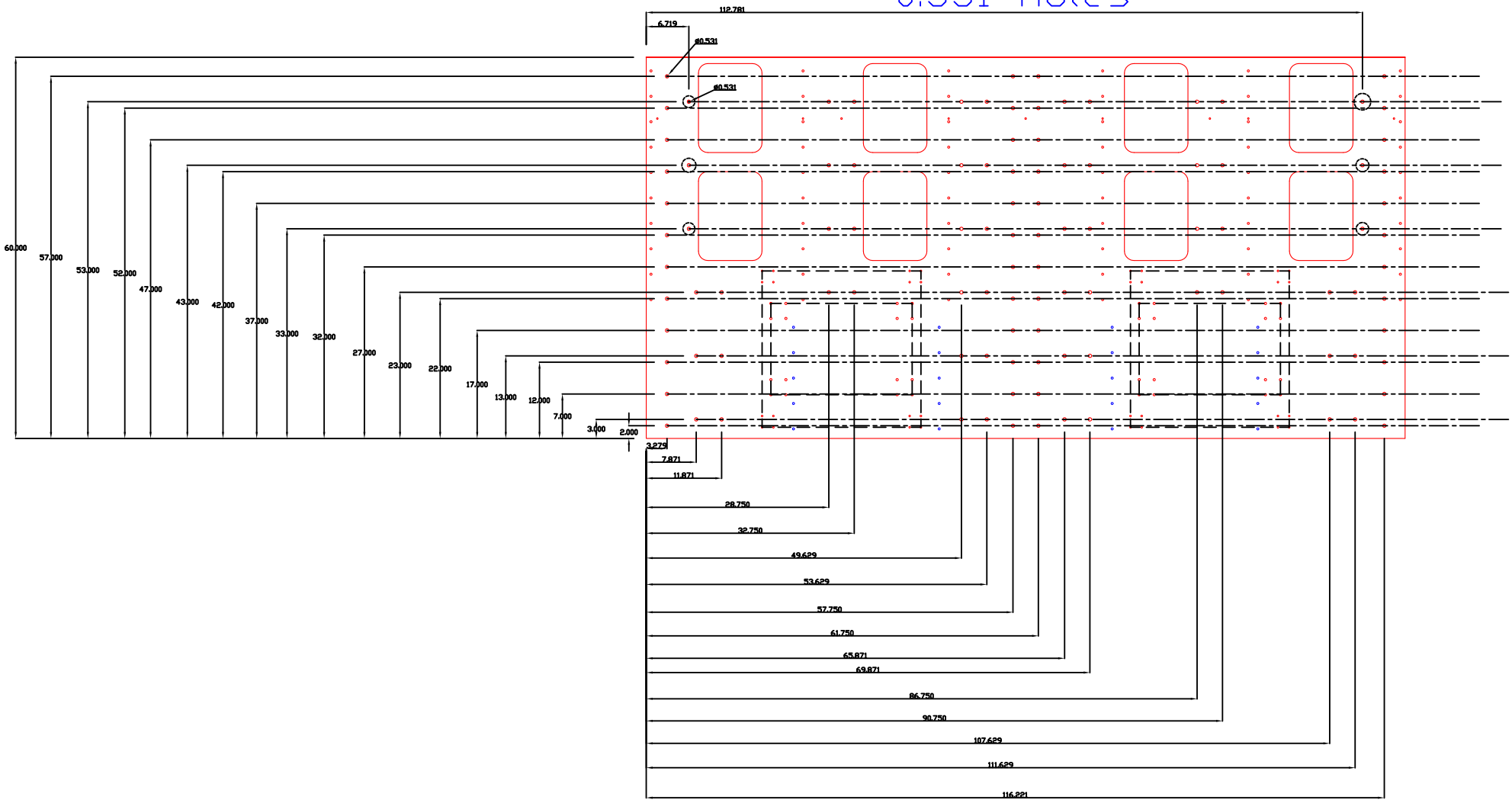

Wedge back plate back view

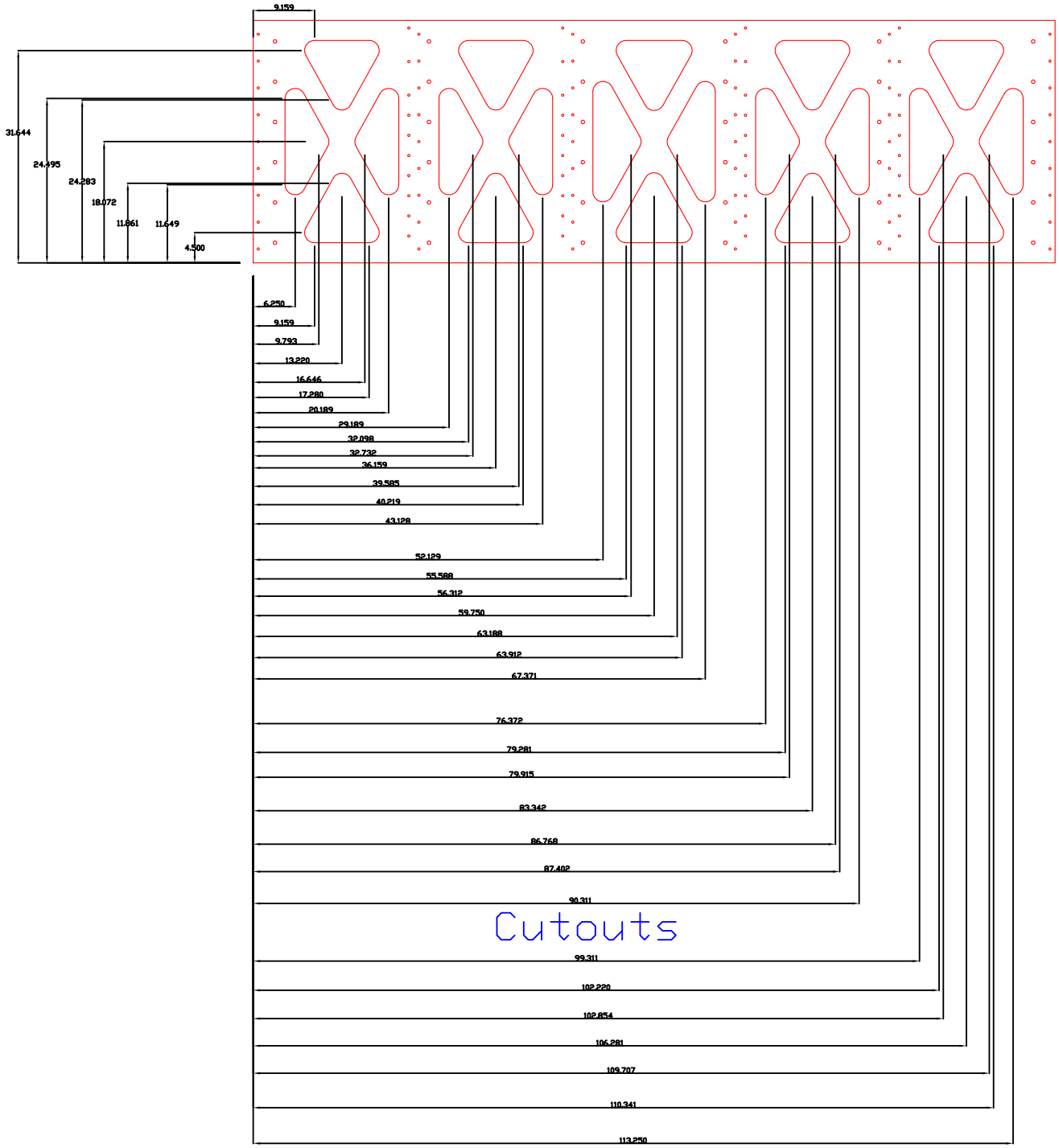

Wedge back plate back view

ALL THRU HOLES 0.531 Holes

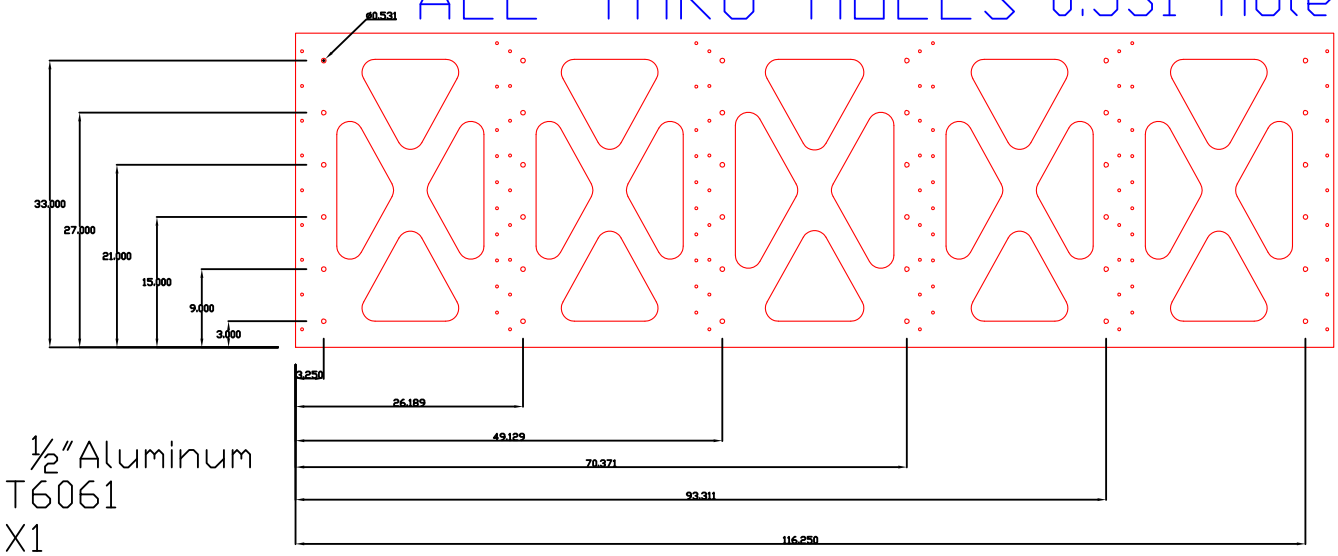

½"Aluminum
T6061
X1

Wedge back plate back view

ALL THRU HOLES 0.332 Holes

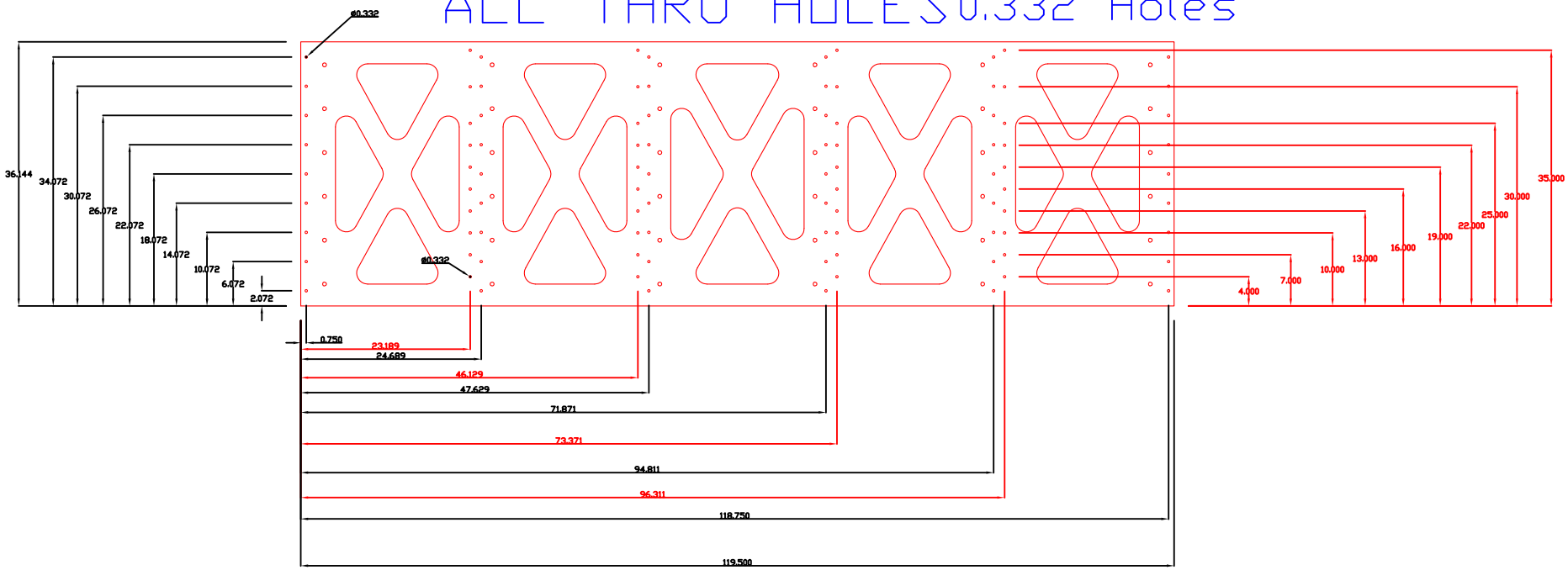

Wedge bottom plate bottom view

ALL THRU HOLES 0.332 Holes

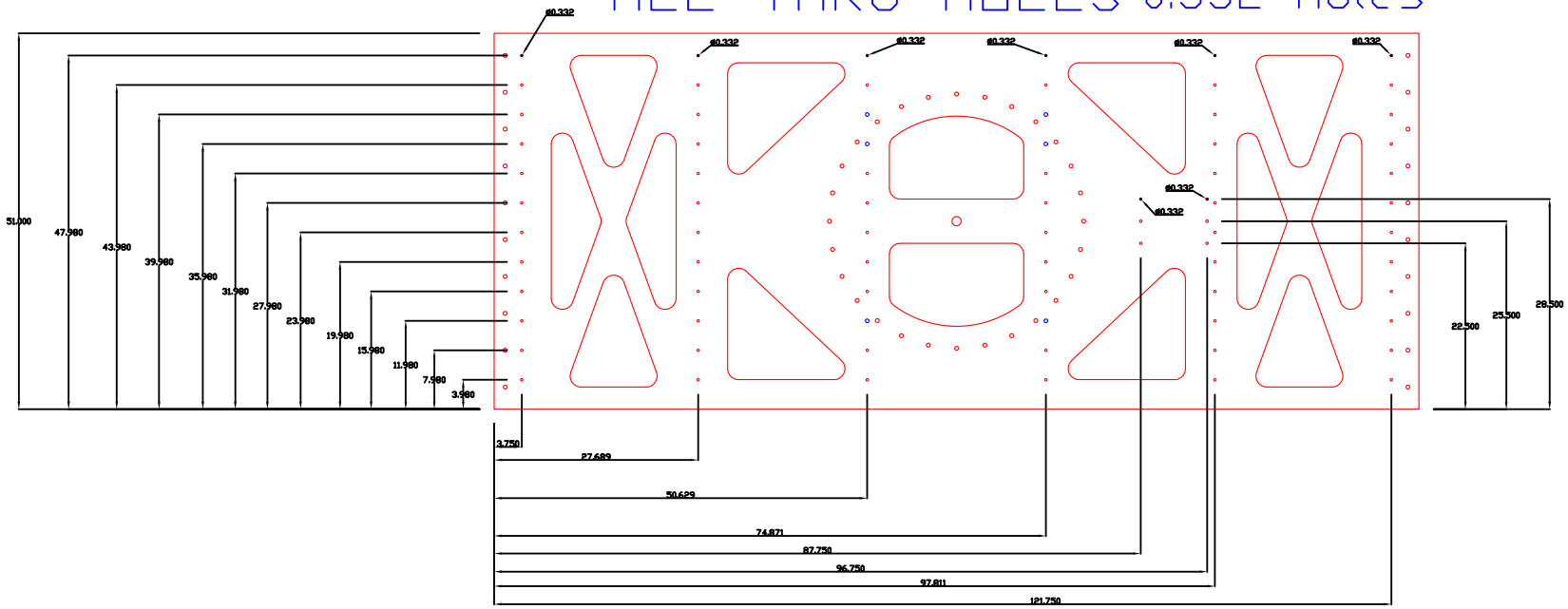

ALL THRU HOLES 0.531 Holes and 1.25 Hole

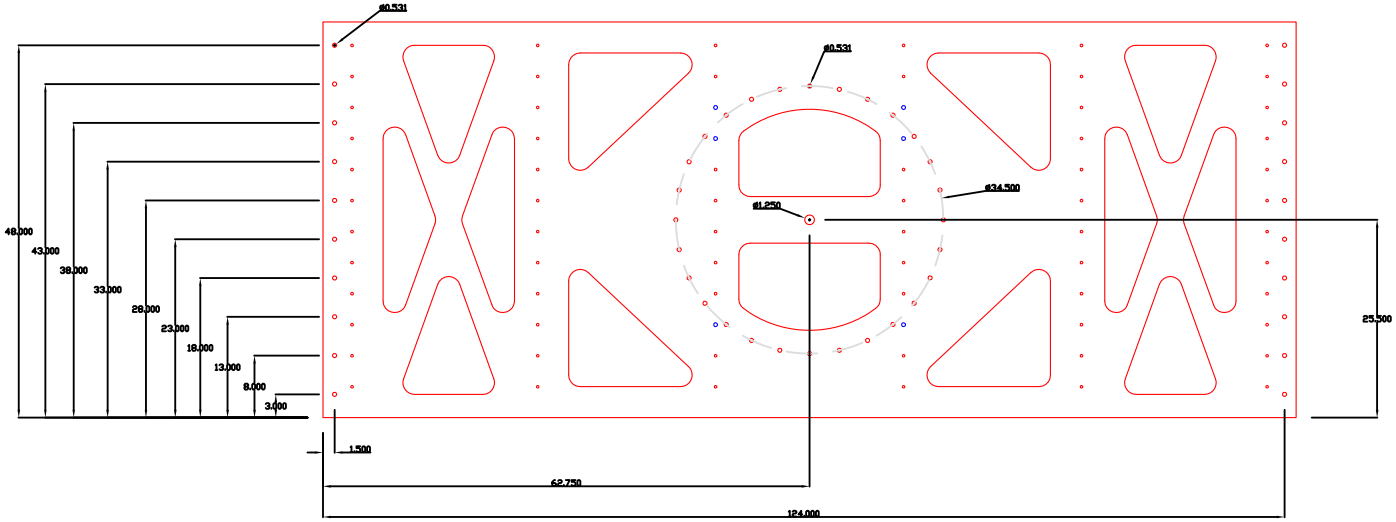

Wedge bottom plate bottom view

Wedge bottom plate bottom view

Cutouts

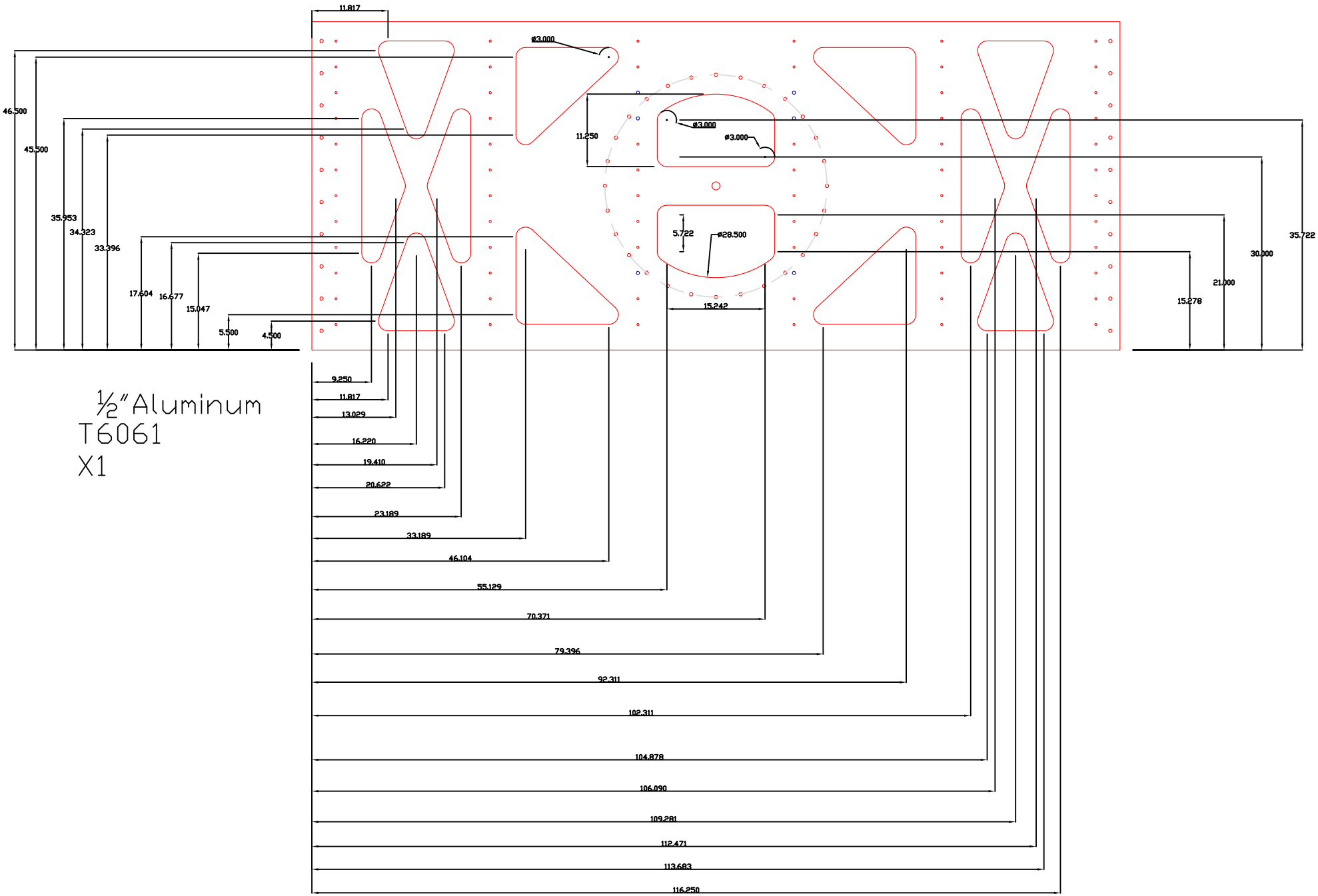

½"Aluminum
T6061
X1

Wedge rib side
top view

3/4 "Aluminum
T6061
X4

All Triangle Holes
Helicoiled for
5/16x18

Wedge rib side
side view

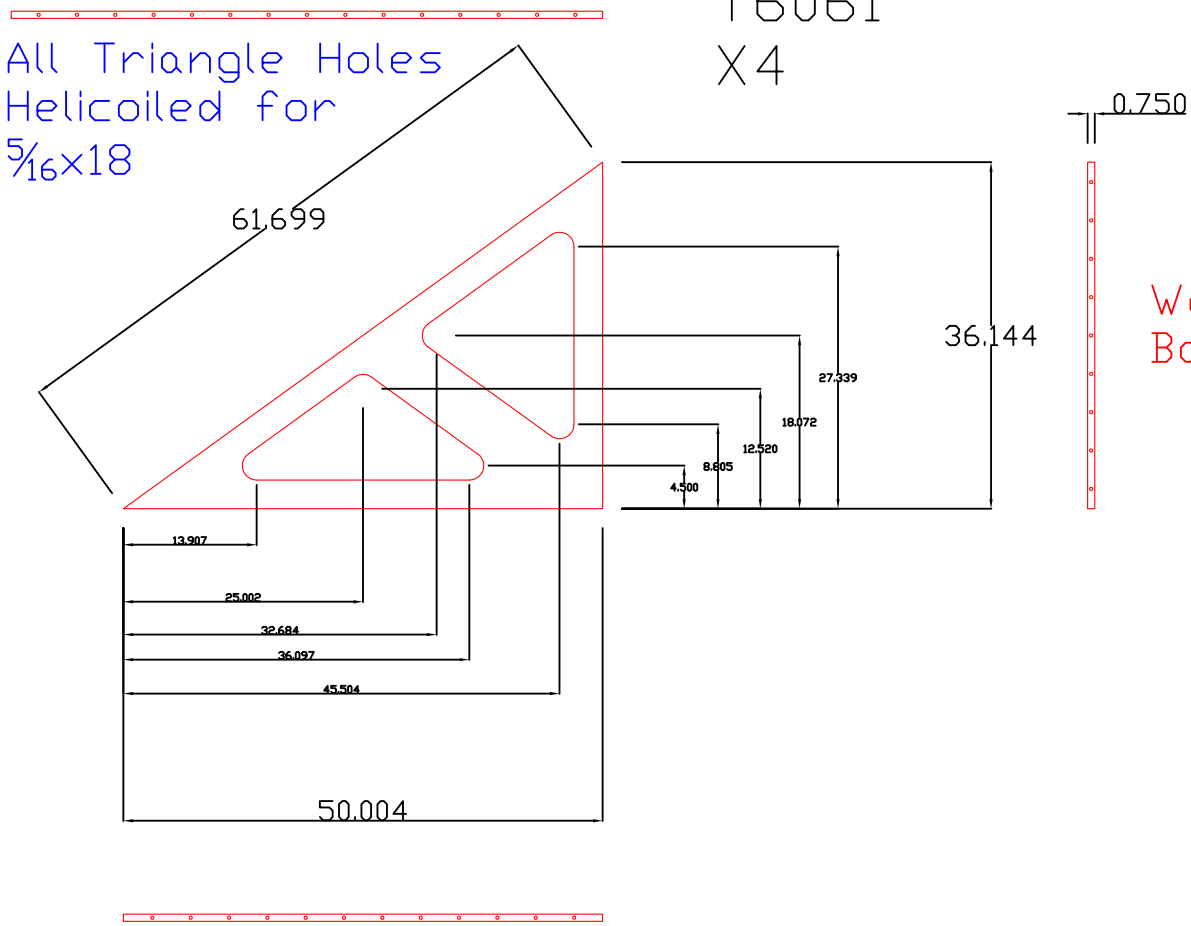

Wedge rib side
Back view

Wedge rib side
Bottom view

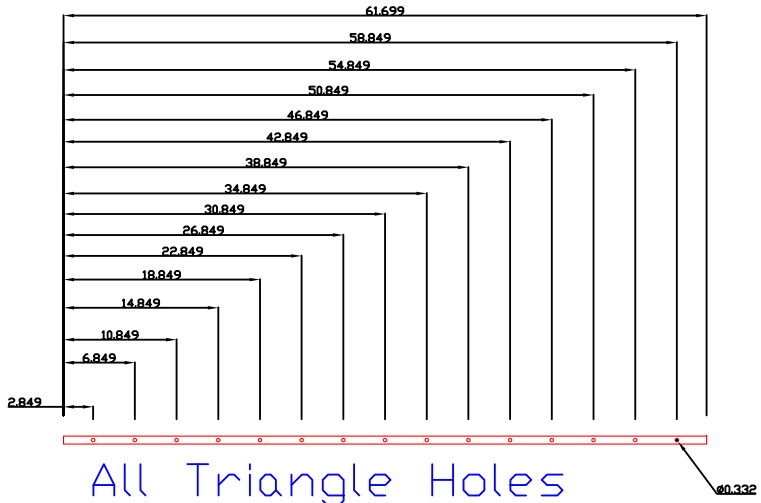

All Triangle Holes Helicoiled for 5/16x18

3/4 "Aluminum T6061 X2

Wedge rib solid center side view

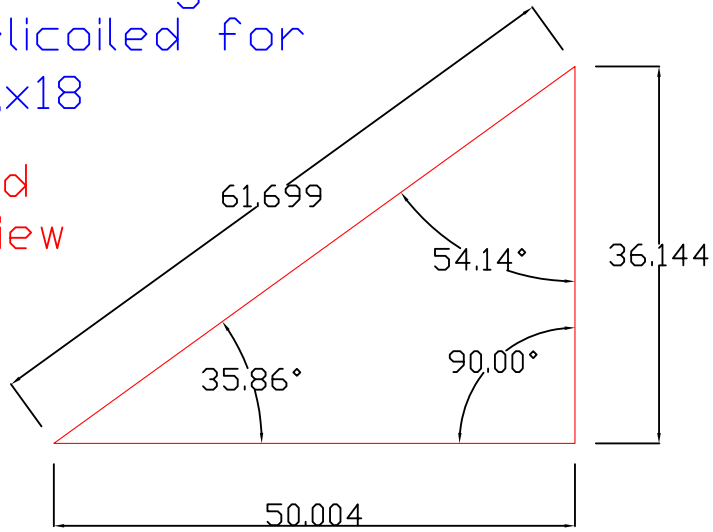

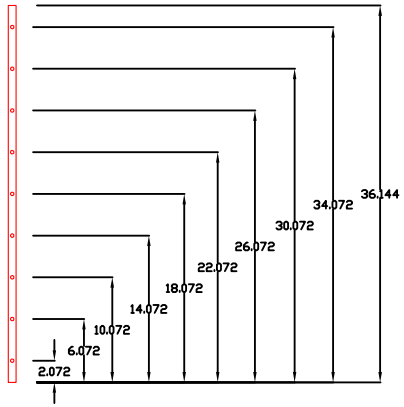

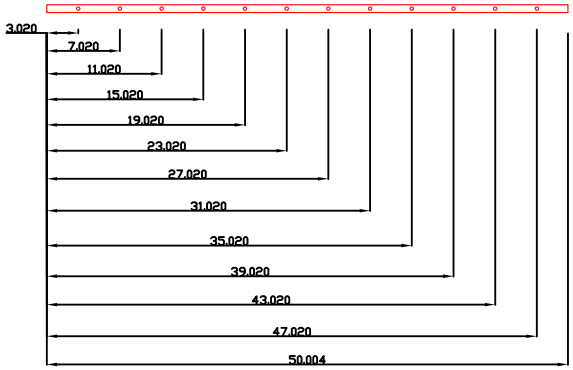

Wedge diving board strut
front view

All Diving board
Holes Helicoiled
for 5/16x18

3/4 "Aluminum
T6061
X4

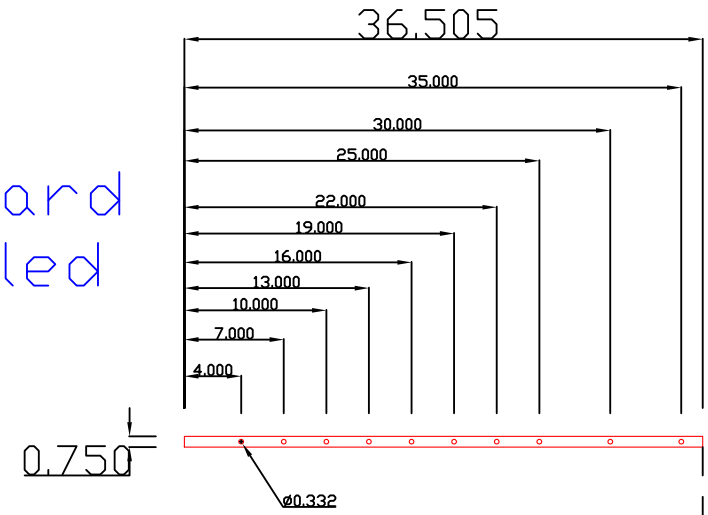

Wedge diving board
strut top view

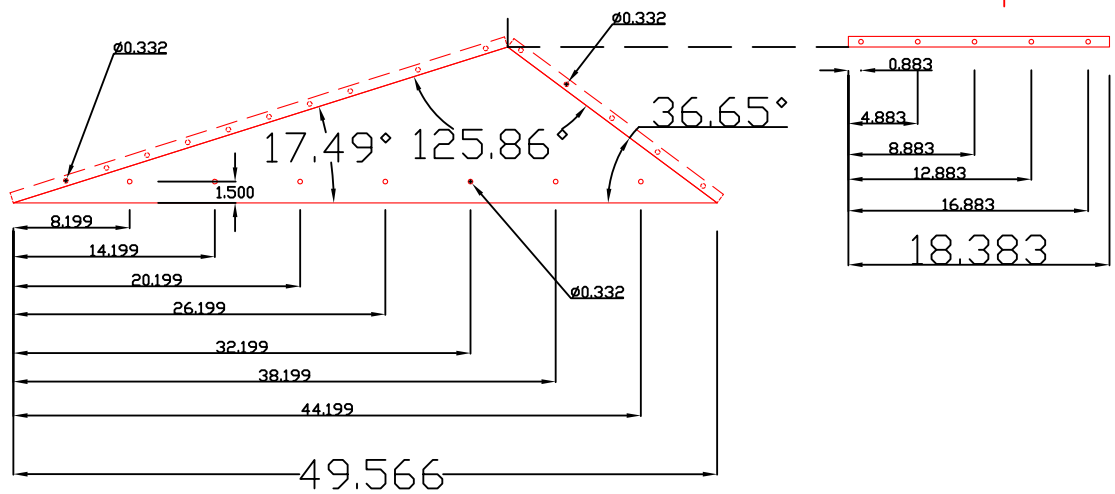

Wedge diving board strut
side view

Drawings for the Second Wedge

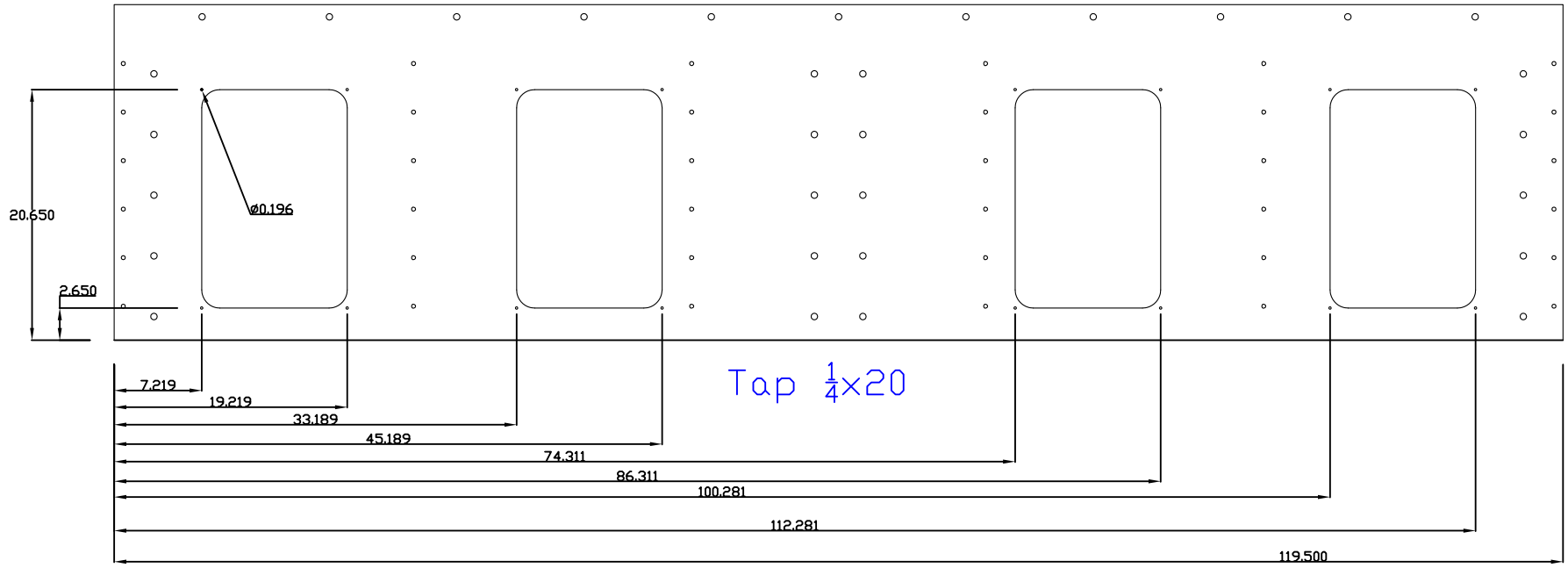

Wedge top plate 1 top view

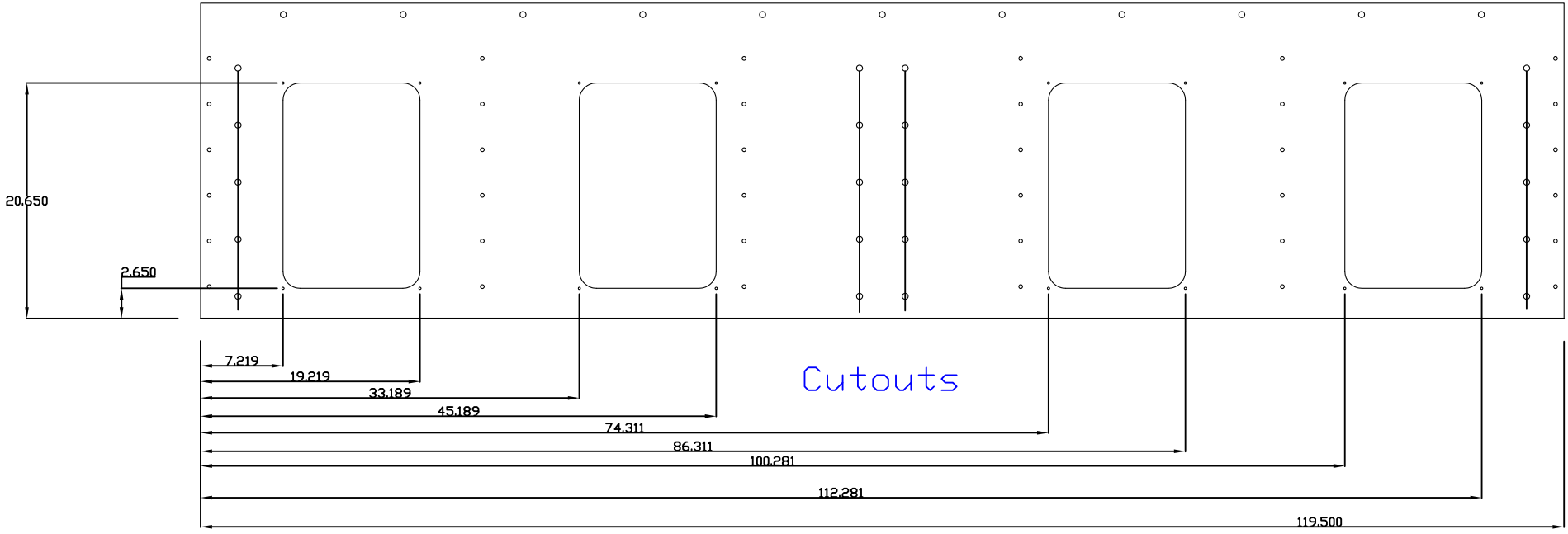

½"Aluminum T6061 Tap ¼x20

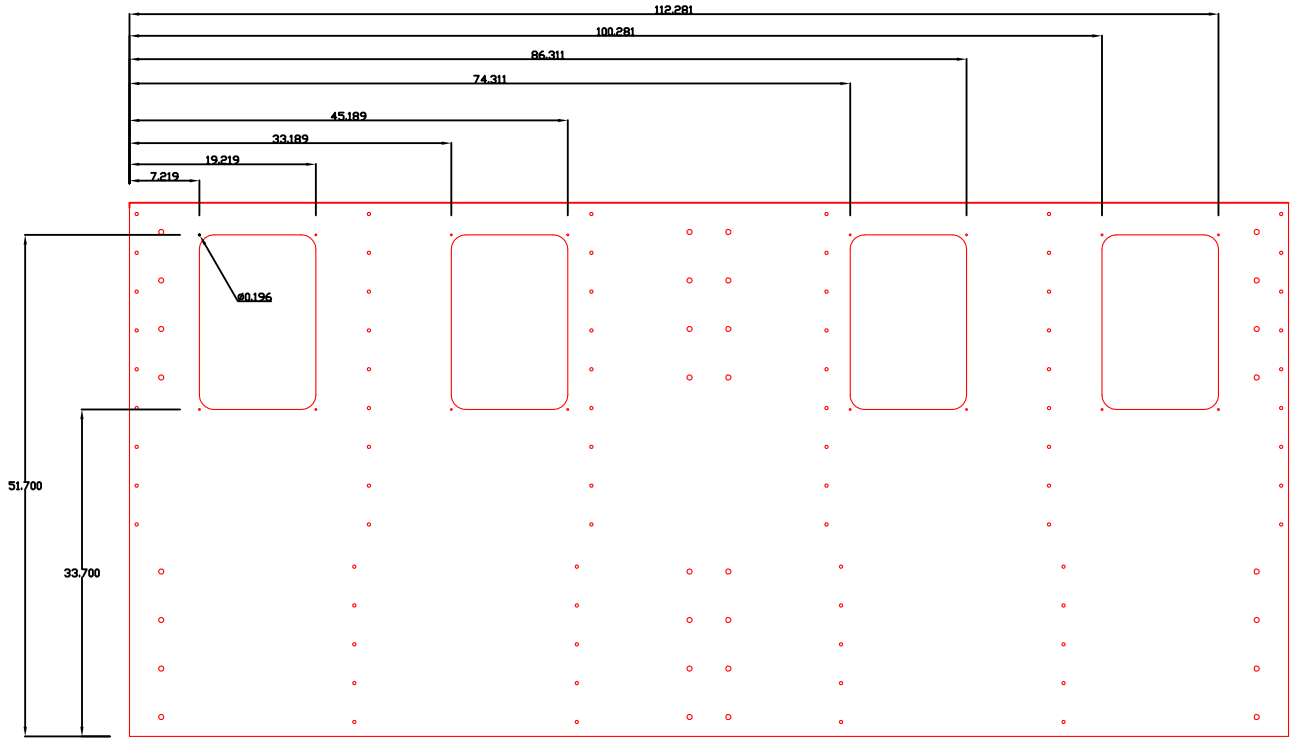

Wedge top plate 2 top view

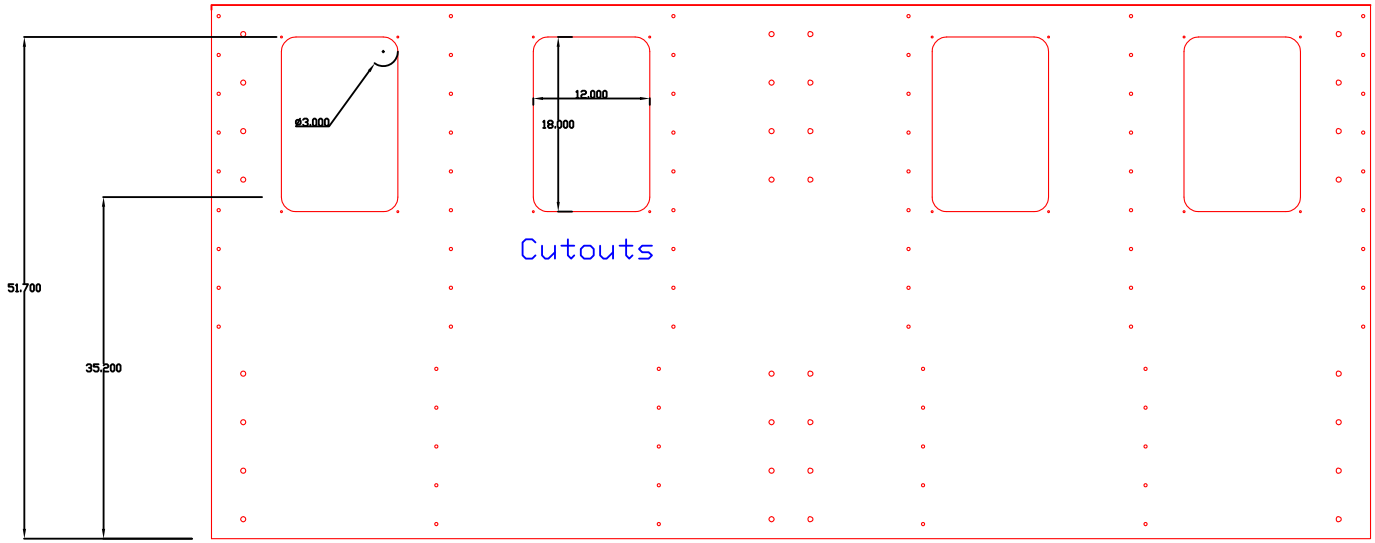

Wedge top plate 1 top view

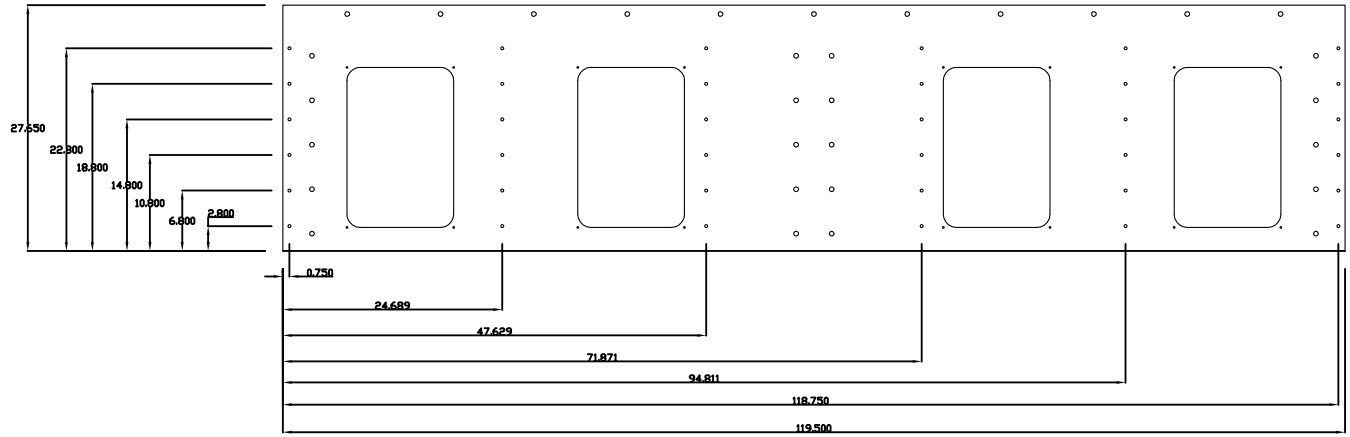

ALL THRU HOLES 0.332 Holes

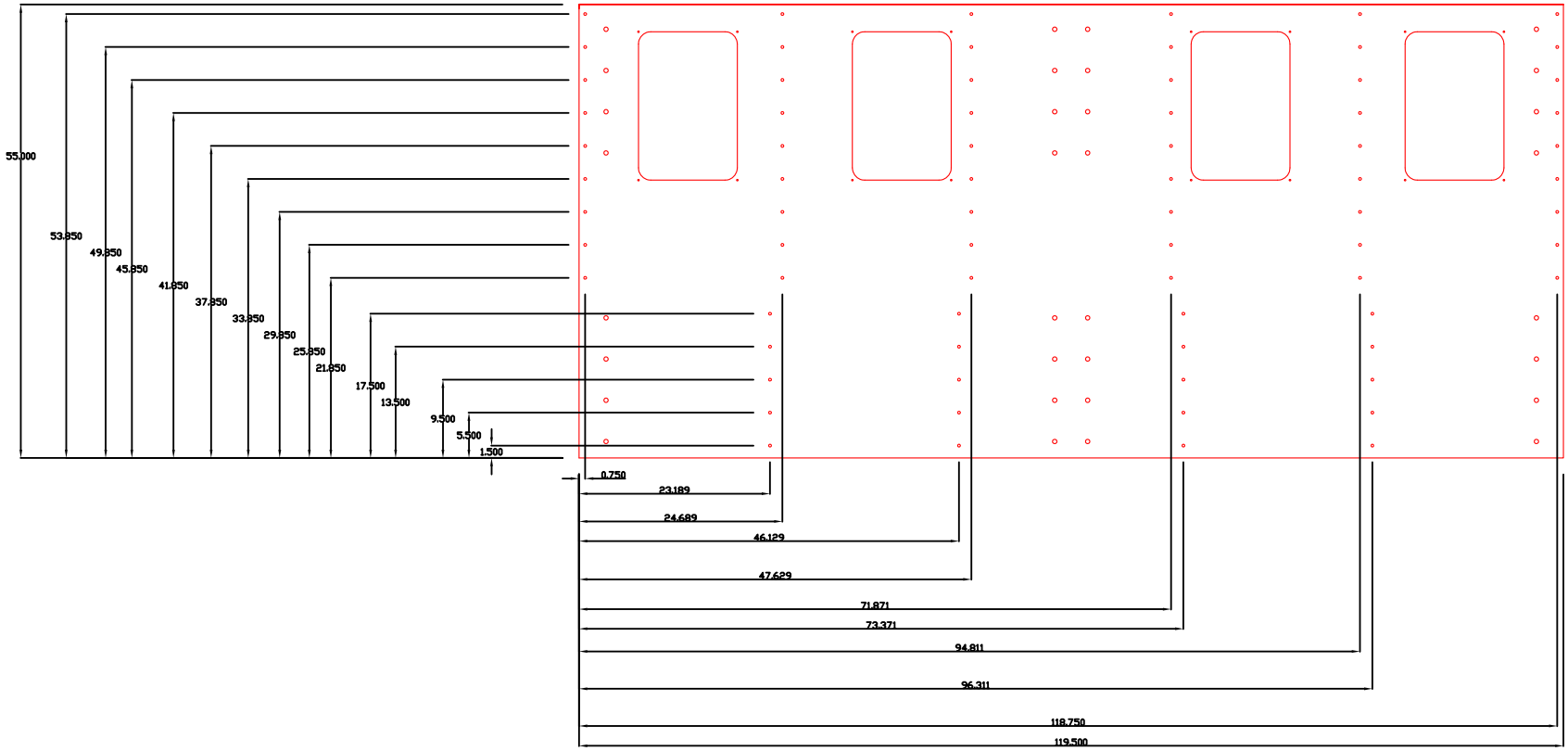

Wedge top plate 2 top view

Wedge top plate 1 top view

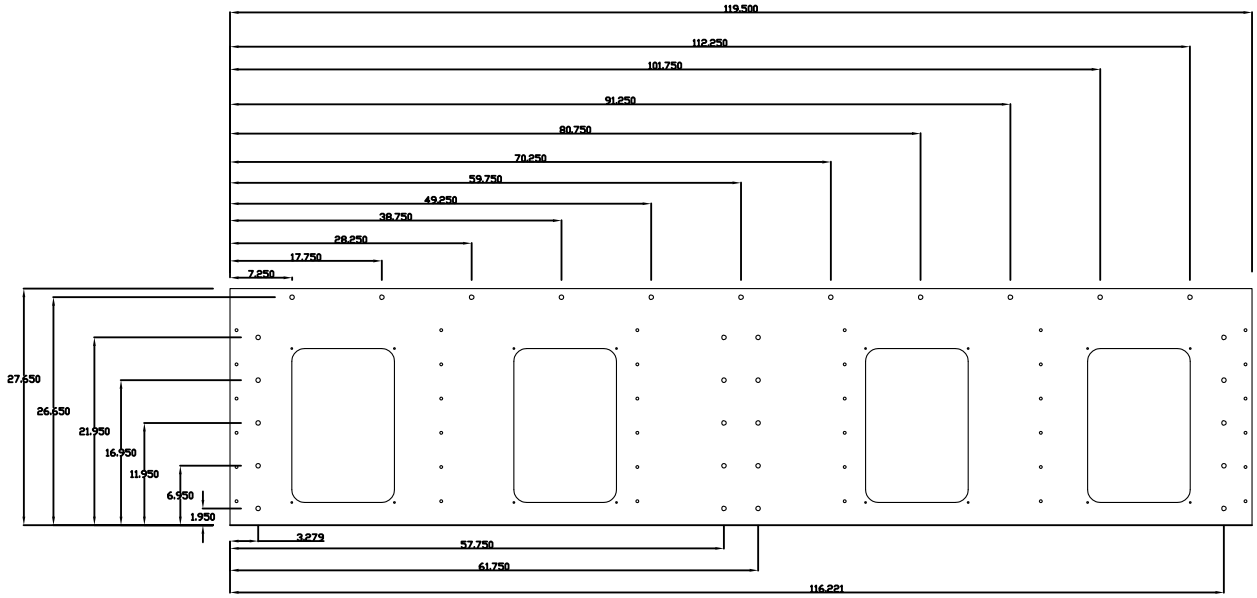

½"Aluminum
T6061
X1

ALL THRU HOLES 0.531 Holes

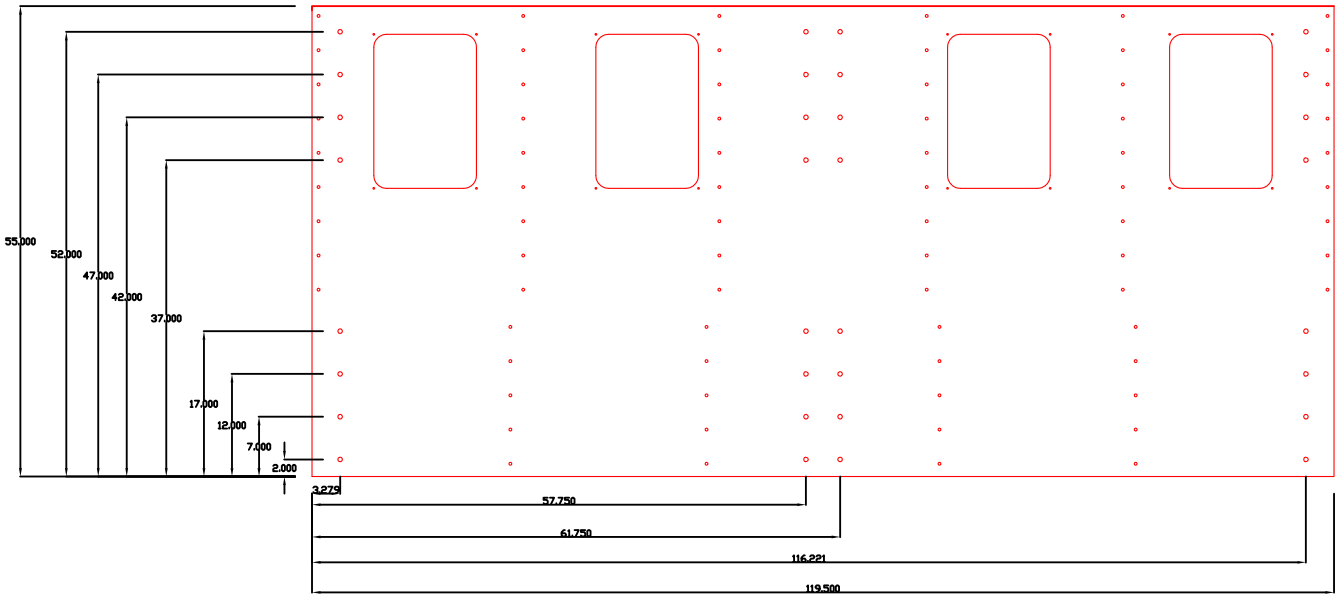

Wedge top plate 2 top view

Wedge back plate back view

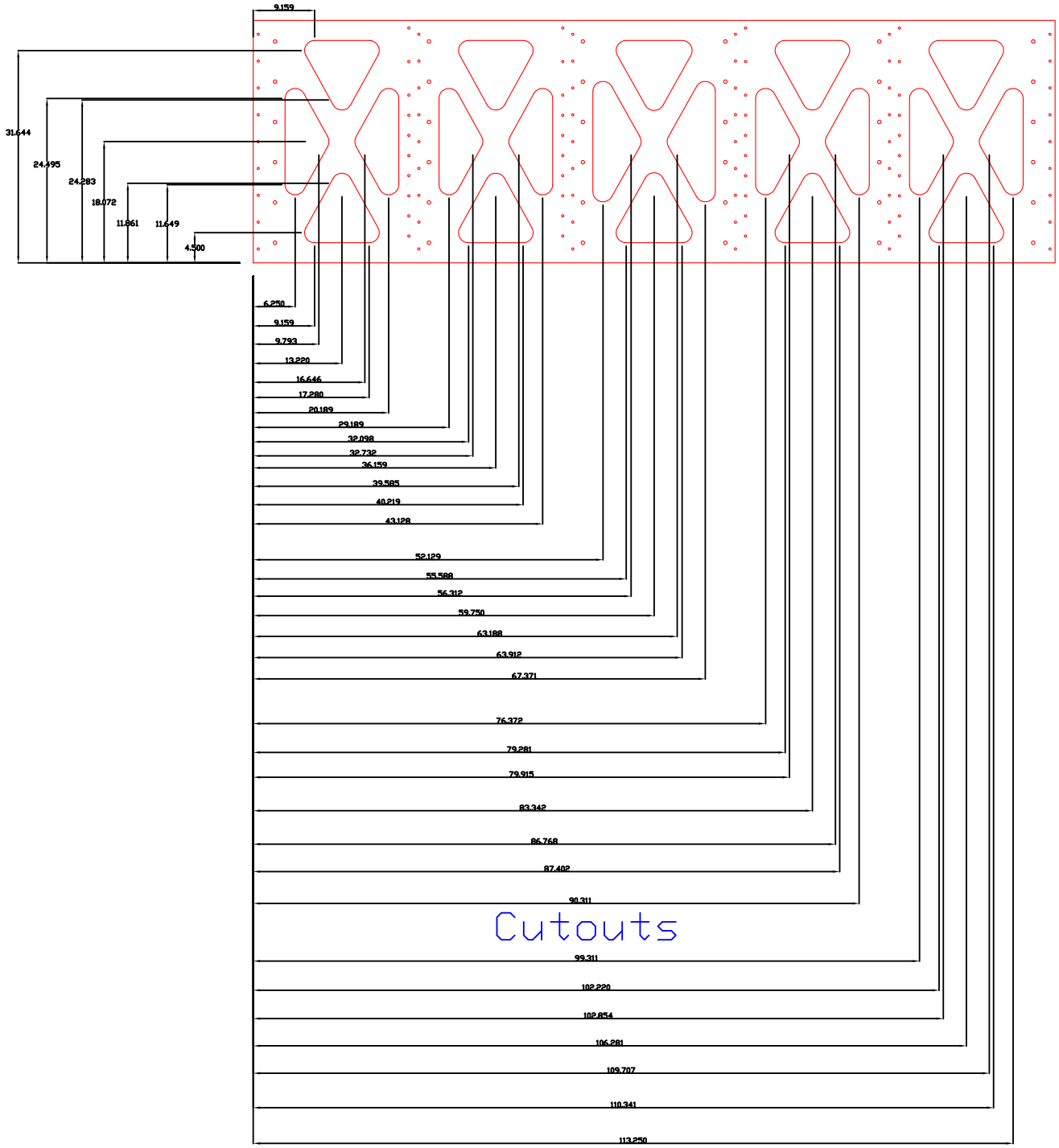

Wedge back plate back view

ALL THRU HOLES 0.531 Holes

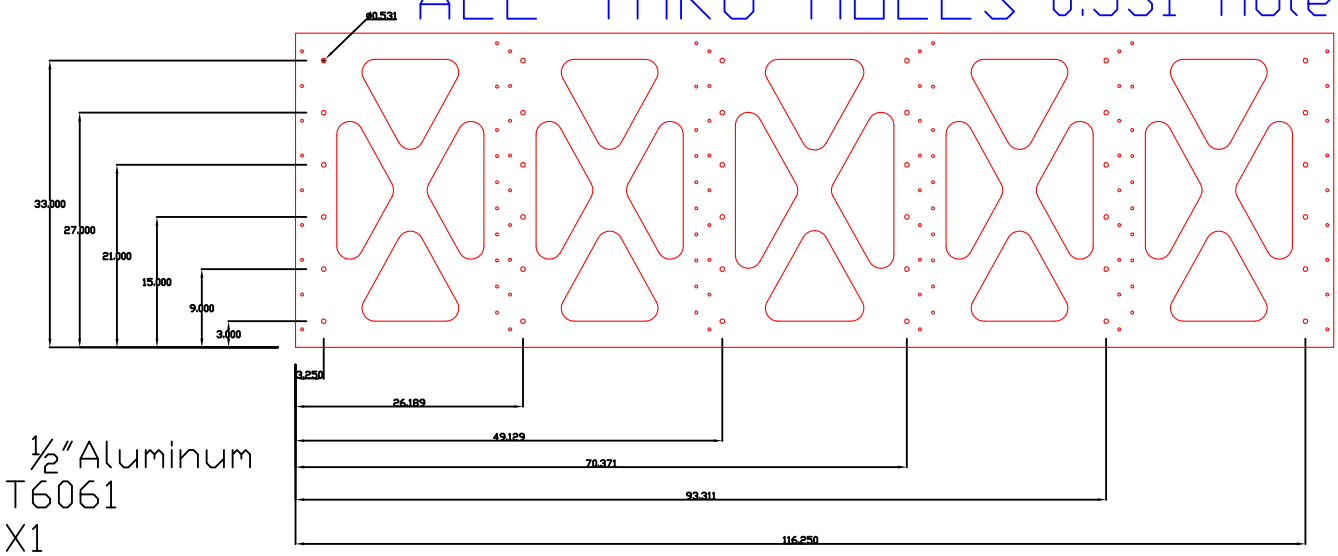

½"Aluminum
T6061
X1

Wedge back plate back view

ALL THRU HOLES 0.332 Holes

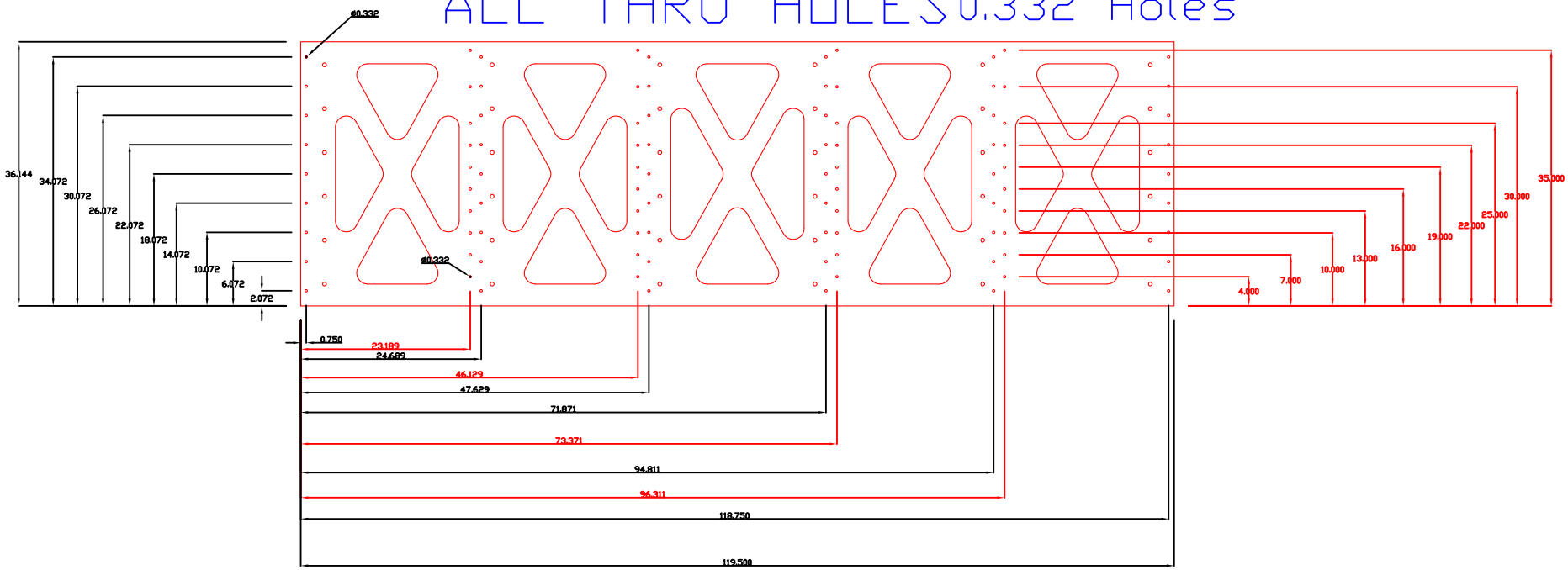

Wedge bottom plate bottom view

ALL THRU HOLES 0.332 Holes

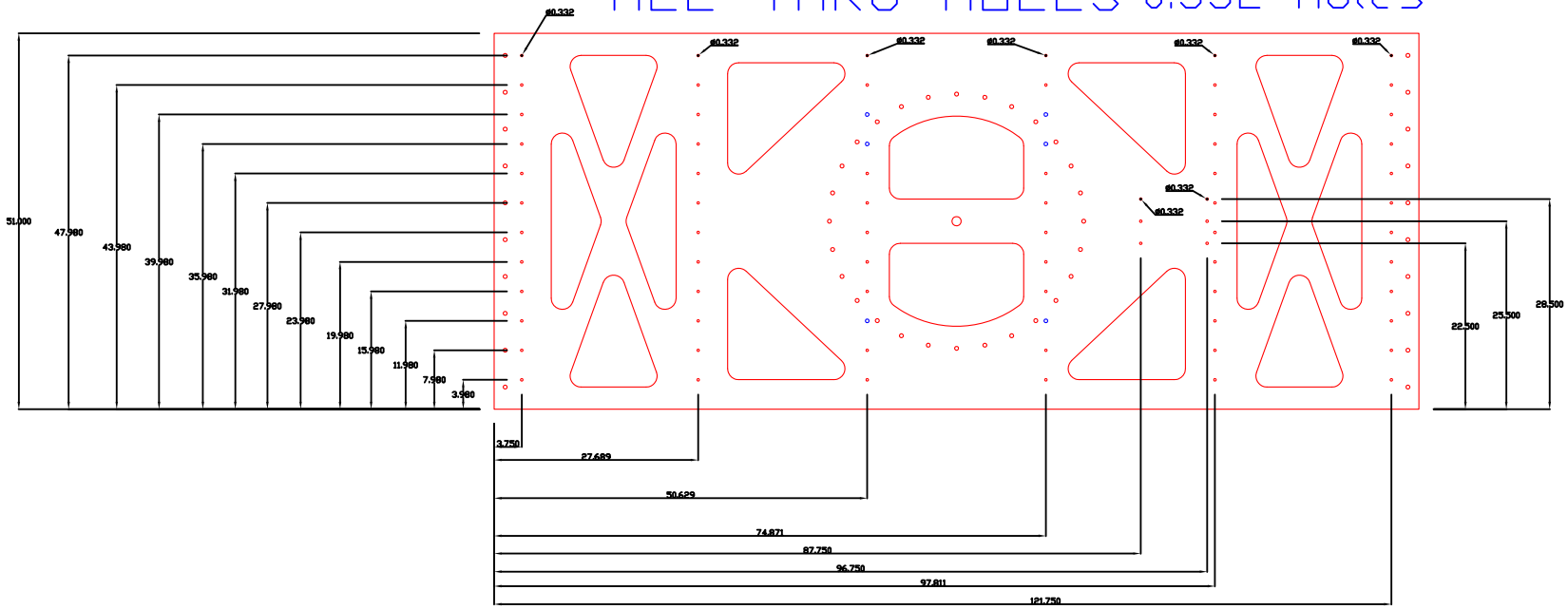

ALL THRU HOLES 0.531 Holes and 1.25 Hole

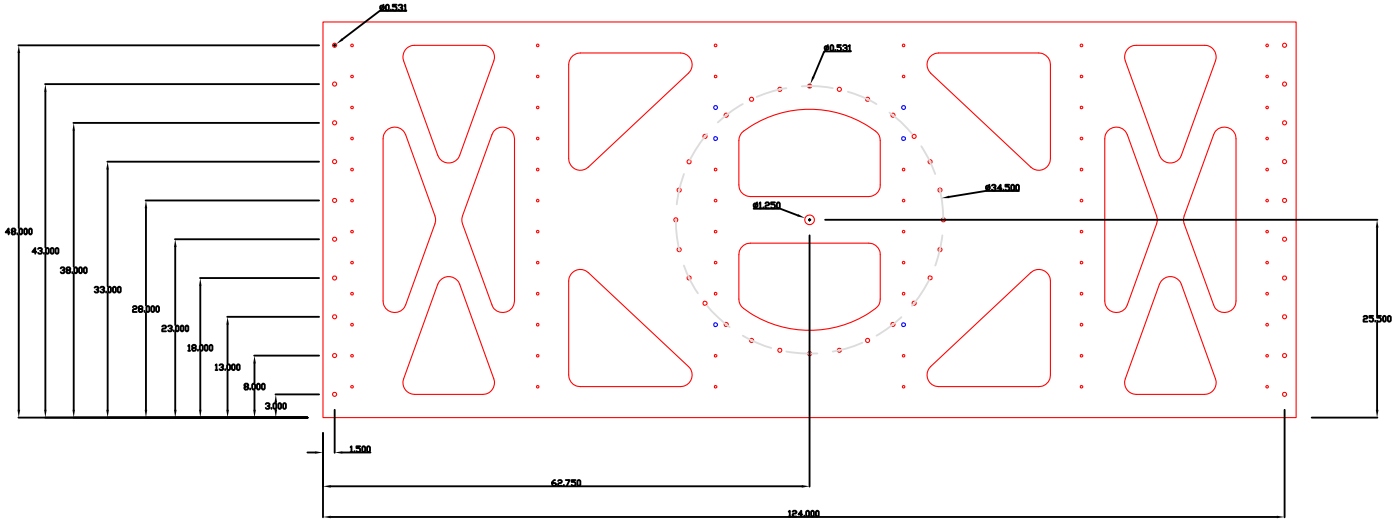

Wedge bottom plate bottom view

Wedge bottom plate bottom view

Cutouts

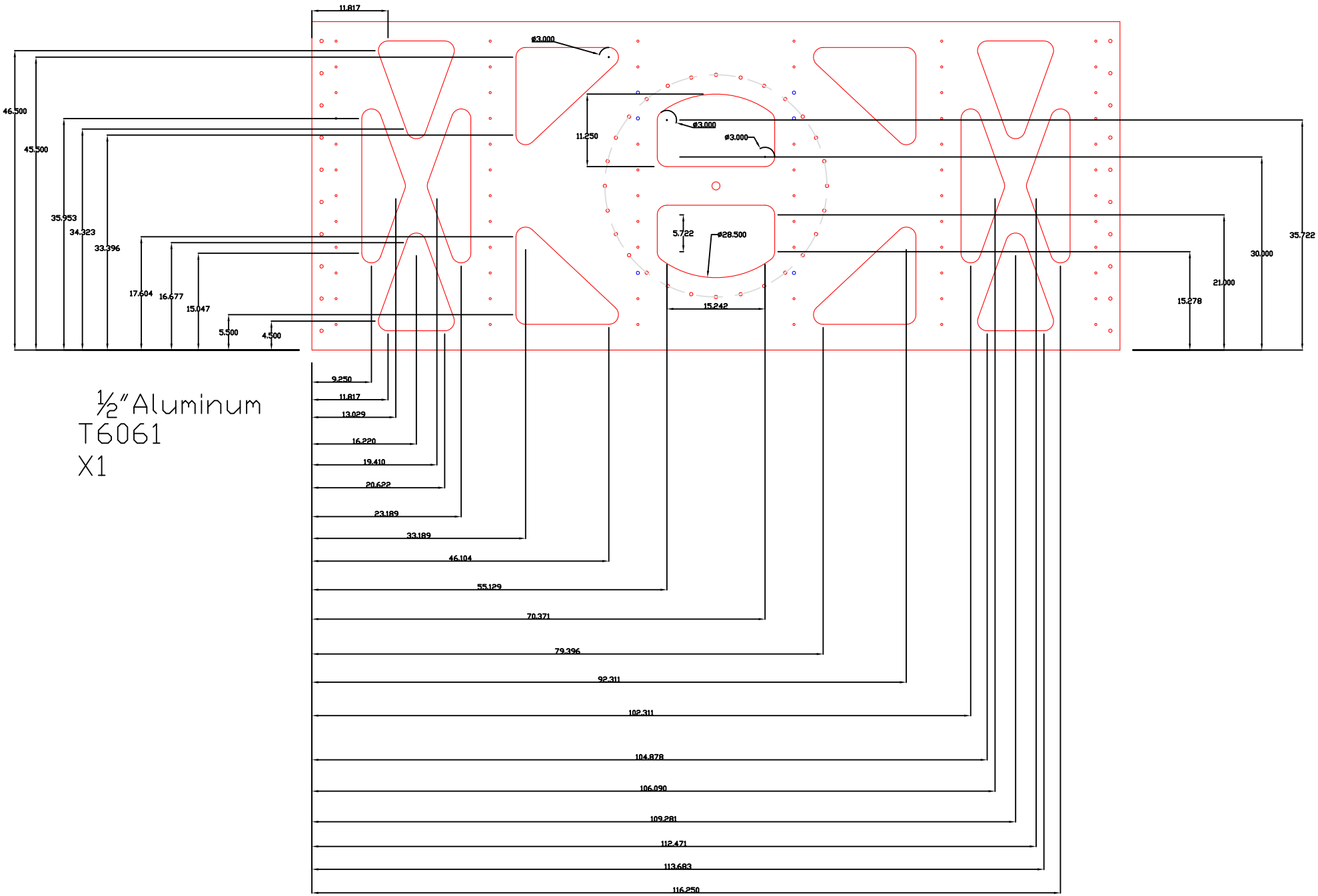

½"Aluminum
T6061
X1

Wedge rib side
top view

3/4 "Aluminum
T6061
X4

All Triangle Holes
Helicoiled for
5/16x18

Wedge rib side
side view

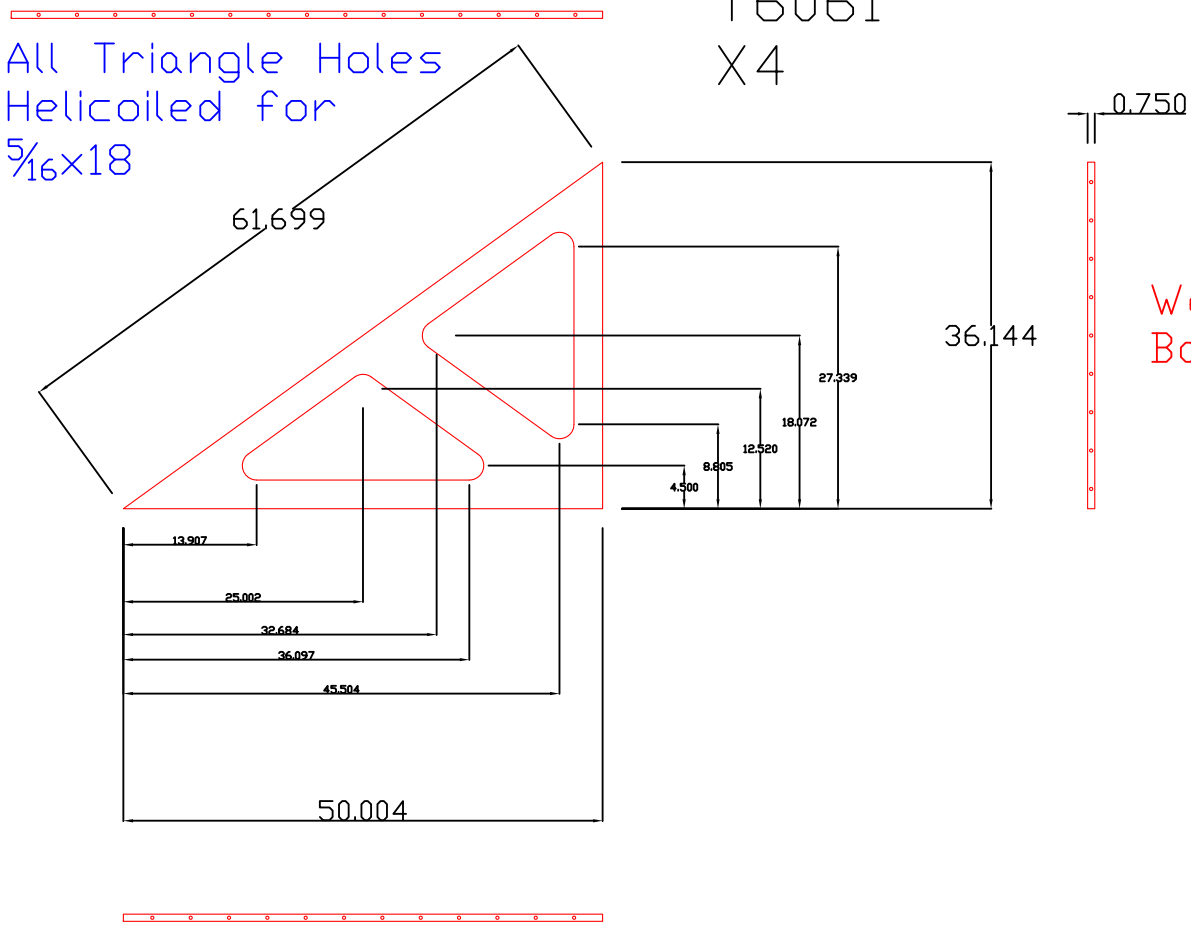

Wedge rib side
Back view

Wedge rib side
Bottom view

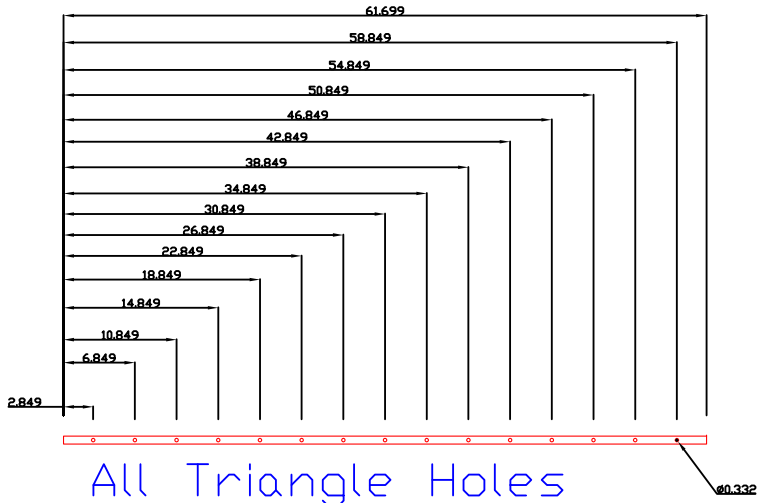

All Triangle Holes Helicoiled for 5/16x18

3/4 "Aluminum T6061 X2

Wedge rib solid center side view

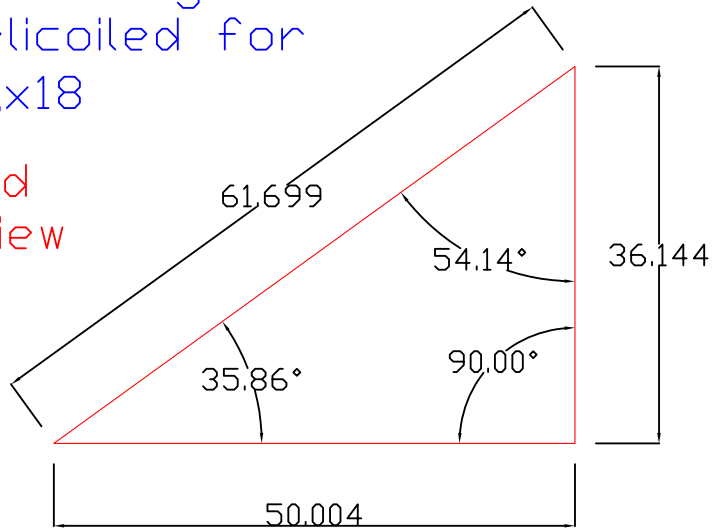

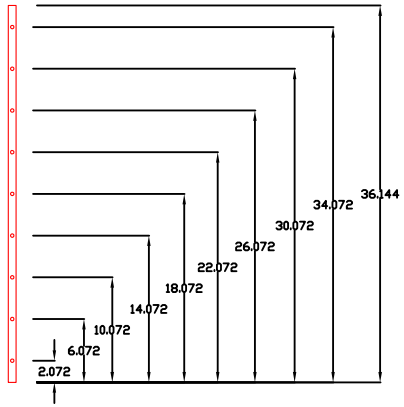

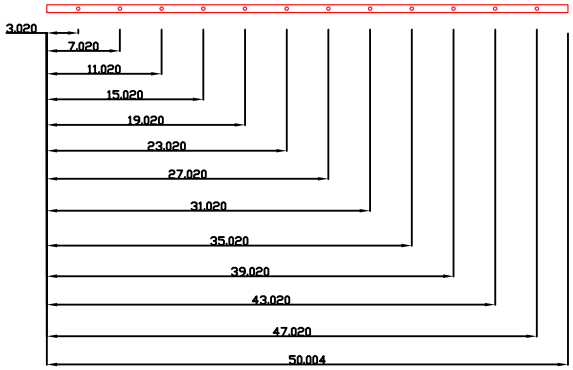

Wedge diving board strut
front view

All Diving board
Holes Helicoiled
for 5/16x18

3/4 "Aluminum
T6061
X4

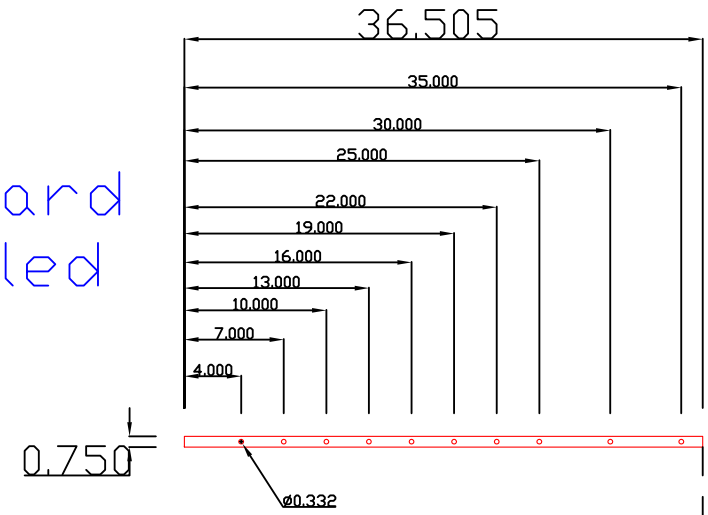

Wedge diving board
strut top view

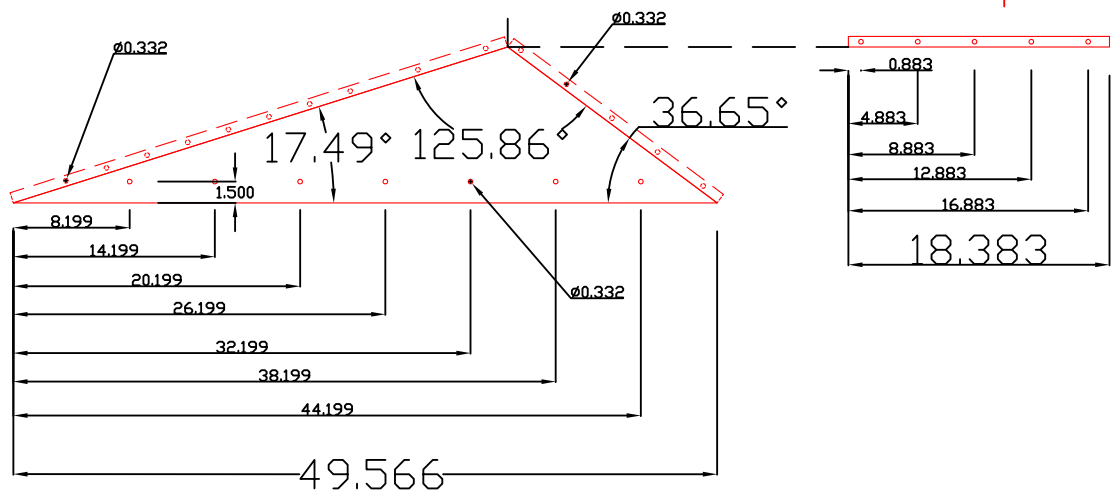

Wedge diving board strut
side view

Appendix C

Warm-optics Cage Drawings

One warm-optics cage was first manufactured in 2014. Once the cage was fully tested and equipped with necessary components, it was deployed with the 40 GHz telescope in 2016. During the observations, valuable feedback on the design was obtained. Modifications are then made according to the on-field feedback.

Two additional warm-optics cages were manufactured in late 2016 according to the updated design. One is for the deployed 40 GHz telescope, while the other one is for the first 90 GHz telescope to be deployed. They both incorporated modifications learned from the first cage, therefore they will be easier to work with. With both of them in North America, their compatibility on one mount can be checked before being deployed.

The drawings attached are for the two warm-optics cages built in 2016, and are referred to as the 'cage port' and 'cage starboard'. The definition of 'port' and

'starboard' assumes the observer is looking out through the forebaffle. Also attached are honeycomb panel drawings.

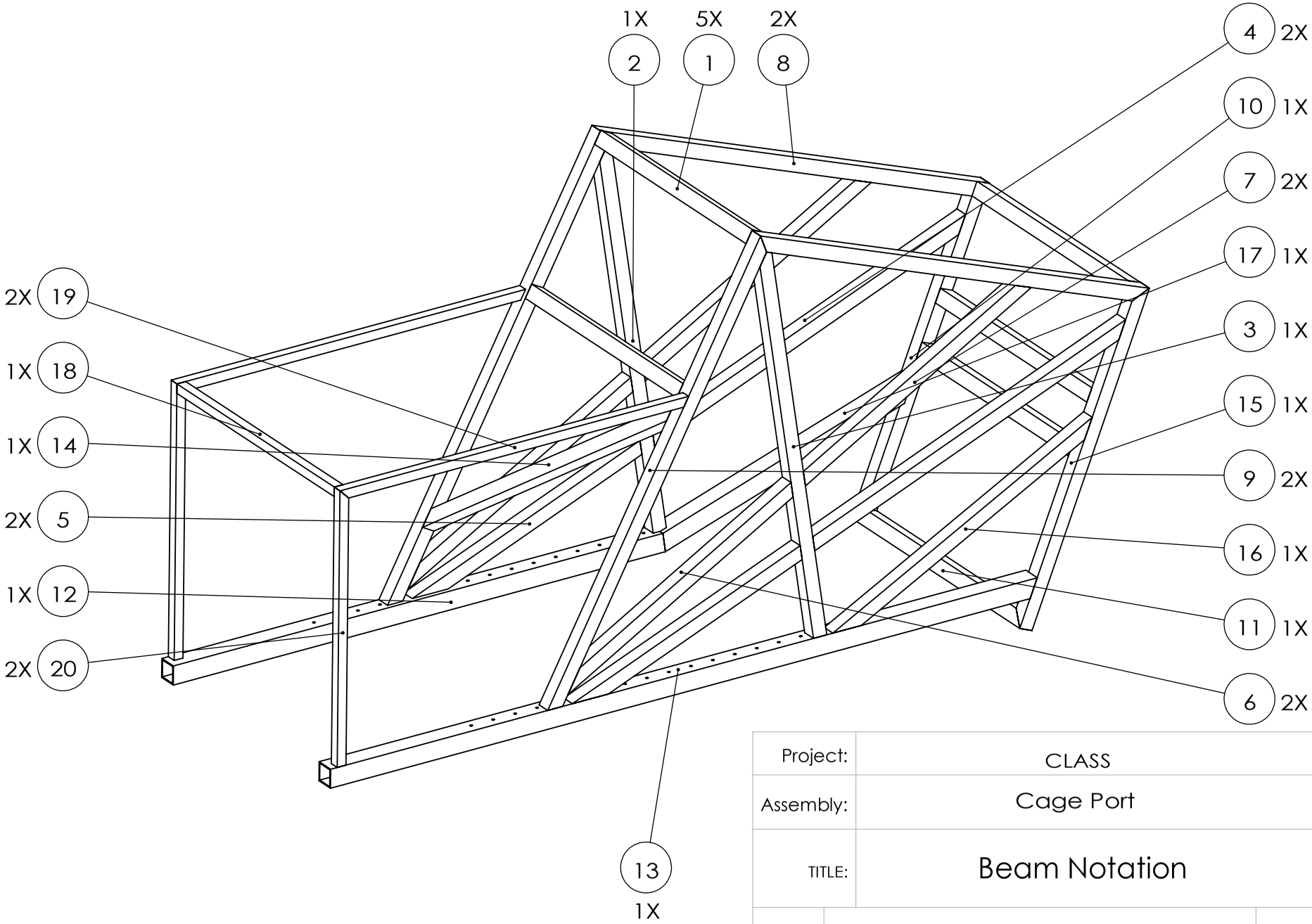

Project:	CLASS			
Assembly:	Cage Port			
TITLE:	Beam Notation			
SIZE A	Drawn By: Zhilei Xu			REV 1
	Date: 1 Oct 2016			
Dimensions in inches	SCALE: 1:25	Material: Aluminum	Quantity: 1	SHEET 1 OF 11

5 4 3 2 1

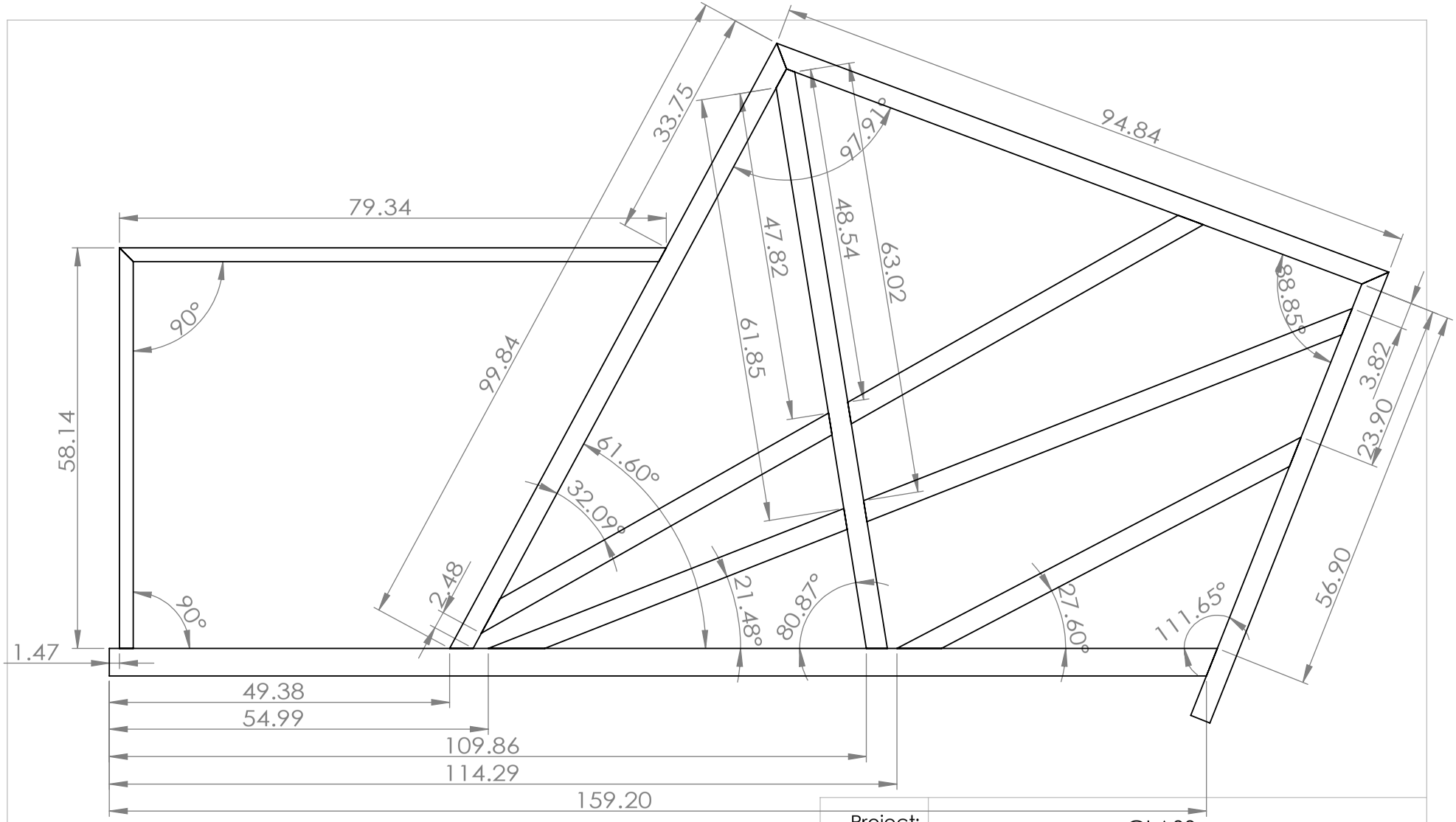

Project:	CLASS
Assembly:	Cage Port
TITLE:	Left Side

SIZE	Drawn By:	Zhilei Xu	REV
A	Date:	10 Oct 2016	1

Dimensions in inches		Material: Aluminum	Quantity: 1	SHEET 2 OF 11

5 4 3 2 1

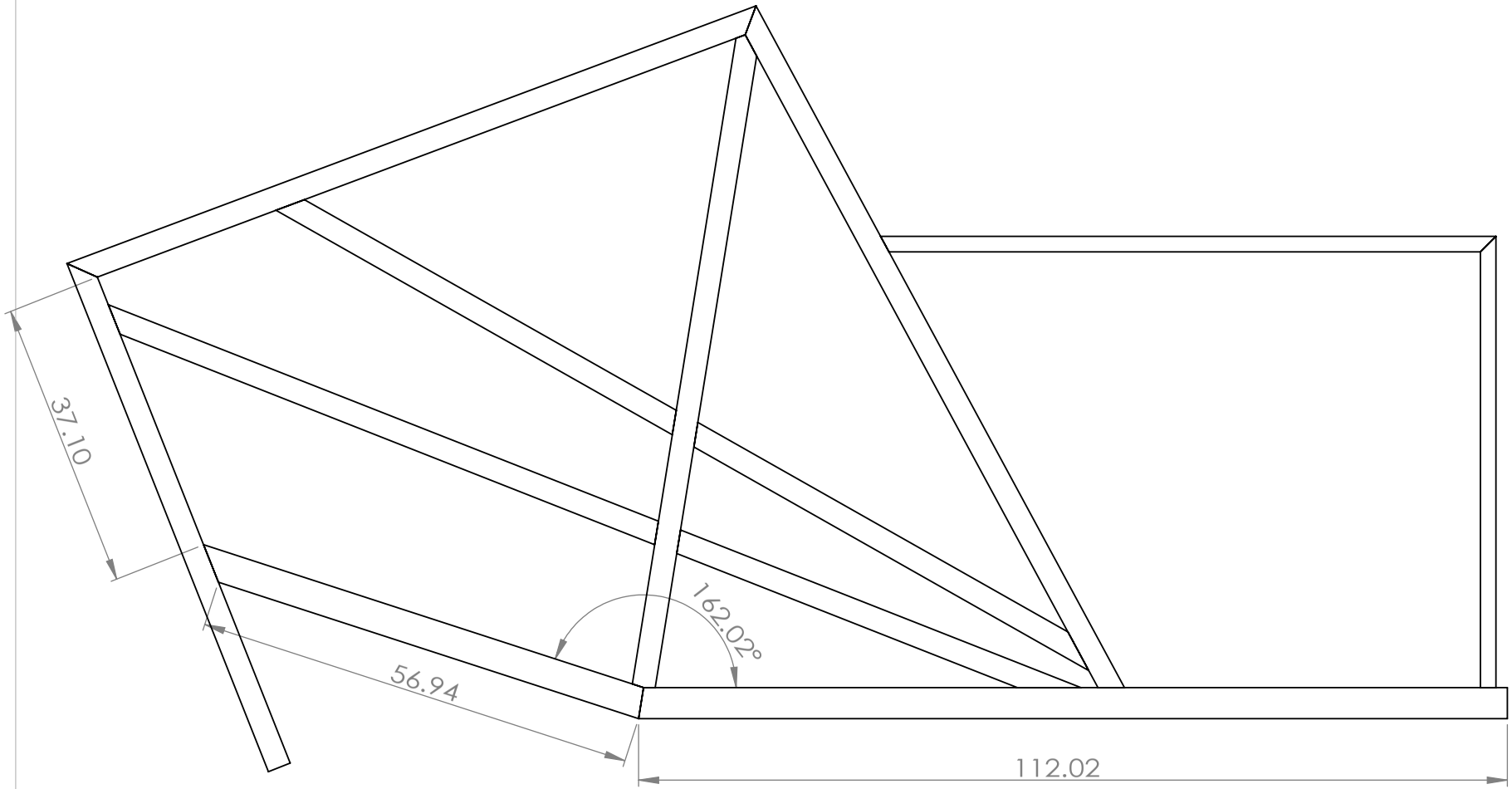

Note: All dimentions are identical to the Left Side
except for the noted ones

Project:	CLASS
Assembly:	Cage Port
TITLE:	Right Side

SIZE	Drawn By:	Zhilei Xu	REV
A	Date:	10 Oct 2016	1

Dimensions in inches	Material: Aluminum	Quantity: 1	SHEET 3 OF 11

5 4 3 2 1

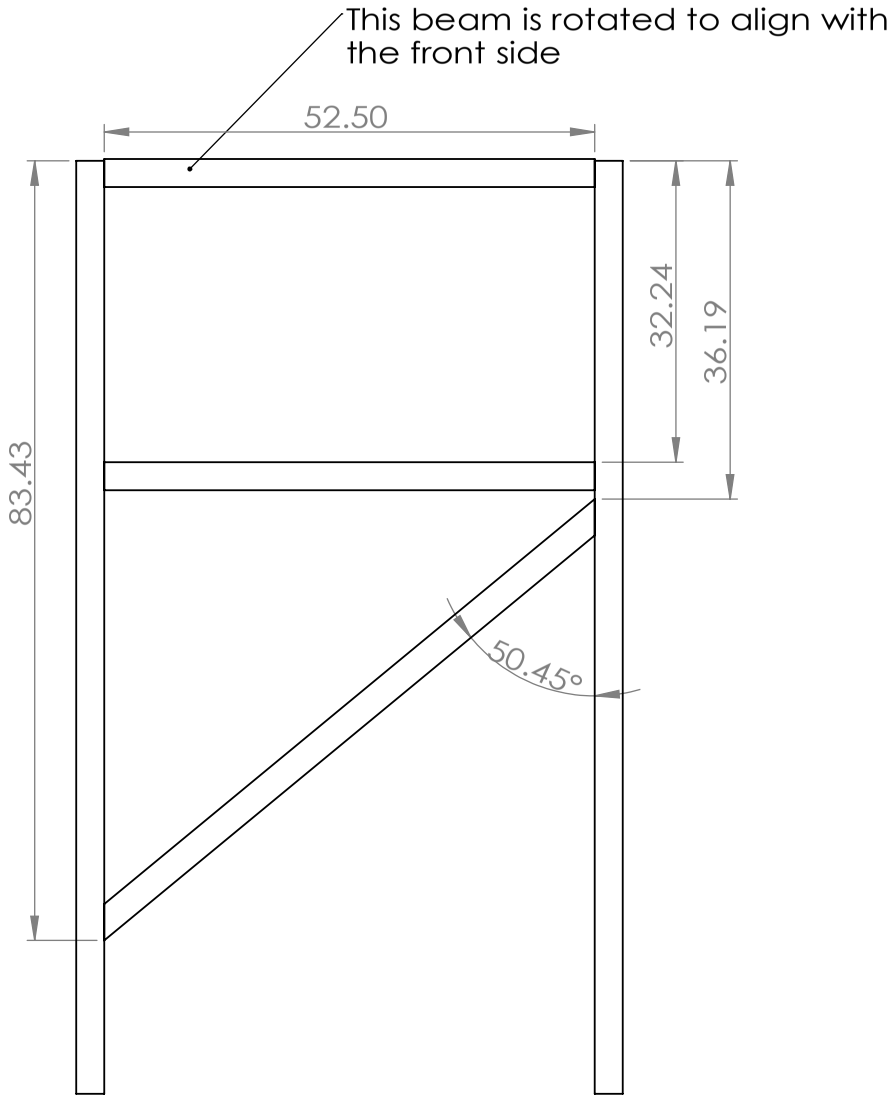

Front Side

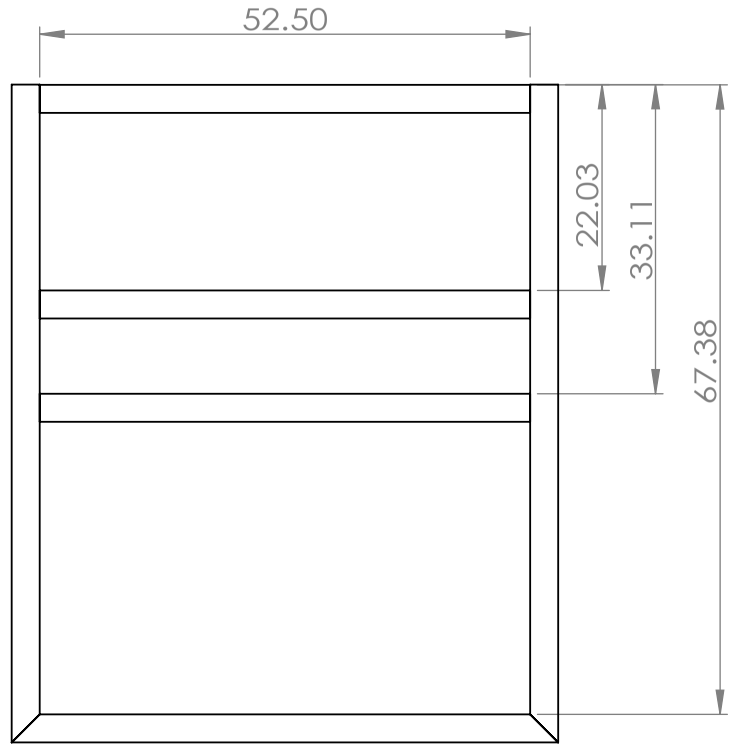

Back Side

Important Note: All cross beams are rotated to align with front/back side

Project:	CLASS
Assembly:	Cage Port
TITLE:	Front/Back Side
SIZE A	Drawn By: Zhilei Xu
	Date: 10 Oct 2016
REV 1	

Dimensions in inches | Material: Aluminum | Quantity: 1 | SHEET 4 OF 11

5 4 3 2 1

ITEM NO.	QTY.	LENGTH	ANGLE1	ANGLE2	Description
1	5	52.5	0.00	0.00	3 SQ x .250 Wall
2	1	85.119194	-	-	3 SQ x .250 Wall
3	1	85.359458	9.13	-	3 SQ x .250 Wall
4	2	76.867123	43.12	12.35	3 SQ x .250 Wall
5	2	55.460203	12.35	68.52	3 SQ x .250 Wall
6	2	59.610033	20.37	57.91	3 SQ x .250 Wall
7	2	58.715246	40.00	20.37	3 SQ x .250 Wall
8	2	94.836582	45.58	41.05	3 SQ x .250 Wall
9	2	99.843525	28.40	41.05	3 SQ x .250 Wall
10	1	70.414258	45.00	45.58	3 SQ x .250 Wall
11	1	58.5	45.00	45.00	3 SQ x .250 Wall
12	1	112.015814	8.99	0.00	4 SQ x .250 Wall
13	1	160.791797	0.00	21.65	4 SQ x .250 Wall
14	1	70.560492	39.55	39.55	3 SQ x .250 Wall
15	1	70.414258	45.58	45.00	3 SQ x .250 Wall
16	1	66.211312	62.40	49.24	3 SQ x .250 Wall
17	1	60.255532	39.62	8.99	4 SQ x .250 Wall
18	1	54.5	0.00	0.00	2 SQ x .250 Wall
19	2	79.3377	45.00	28.40	2 SQ x .250 Wall
20	2	58.13976	0.00	45.00	2 SQ x .250 Wall

5 4 3 2 1

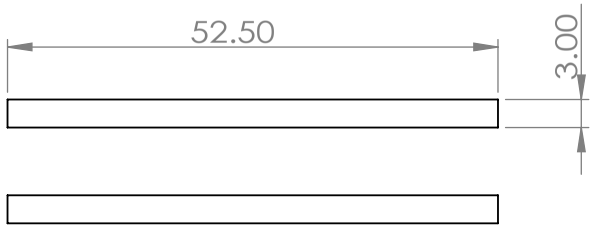

Beam 1

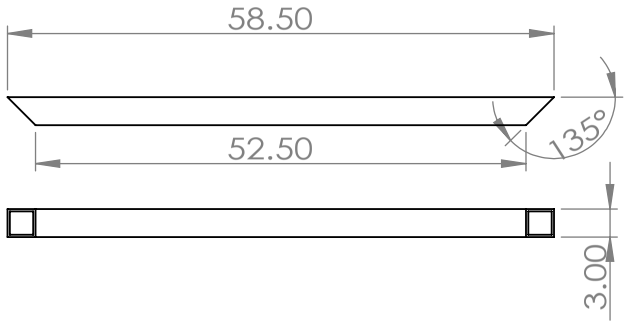

Beam 11

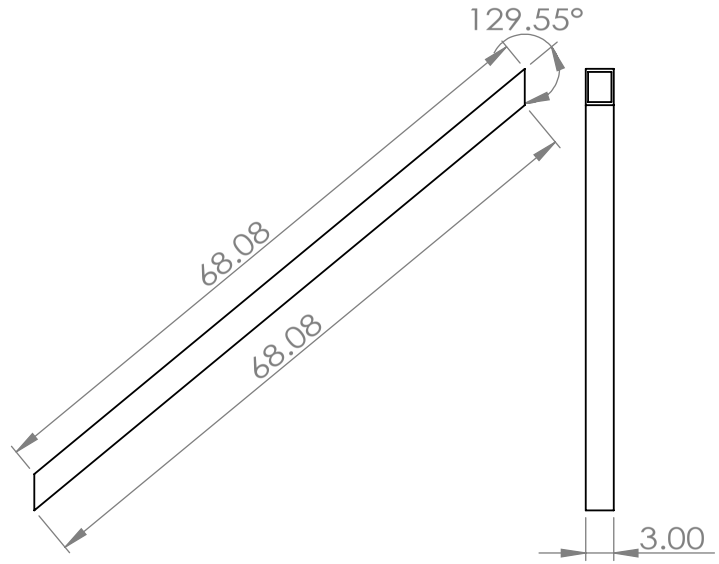

Beam 14

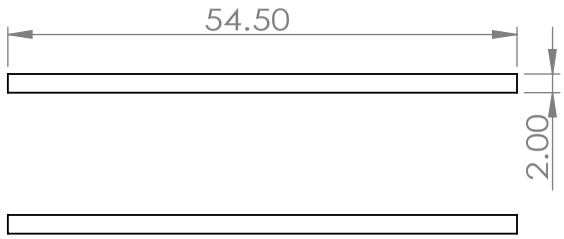

Beam 18

Project:	CLASS		
Assembly:	Cage Port		
TITLE:	Beam 1,11,14,18		
SIZE A	Drawn By: Zhilei Xu		REV 1
	Date: 1 Oct 2016		
Dimensions in inches	SCALE:	Material: Aluminum	Quantity:	SHEET 6 OF 11

5 4 3 2 1

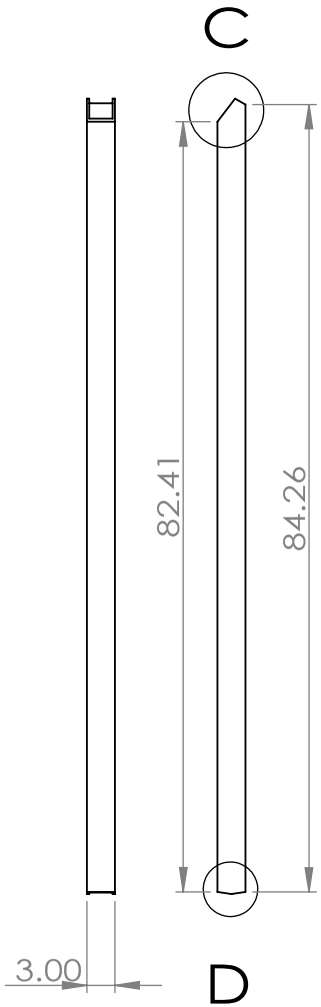

Beam 2

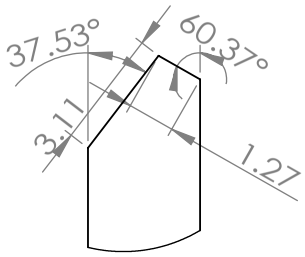

DETAIL C

SCALE 1 : 5

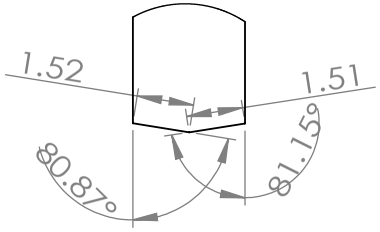

DETAIL D

SCALE 1 : 5

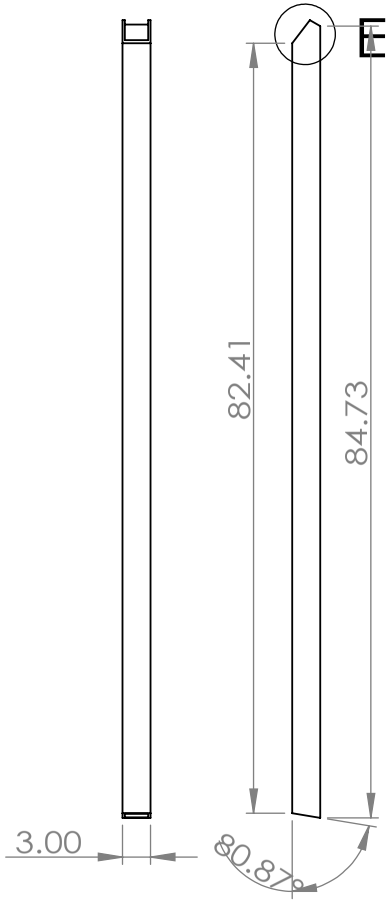

Beam 3

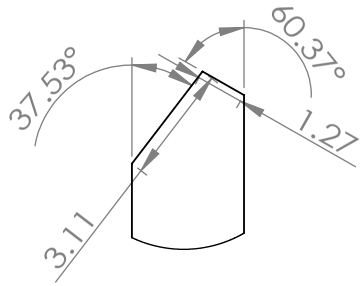

DETAIL E

SCALE 1 : 5

Project:	CLASS
Assembly:	Cage Port
TITLE:	Beam 2,3

SIZE	Drawn By:	Zhilei Xu	REV
A	Date:	1 Oct 2016	1

Dimensions in inches		Material: Aluminum	Quantity:	SHEET 7 OF 11

5 4 3 2 1

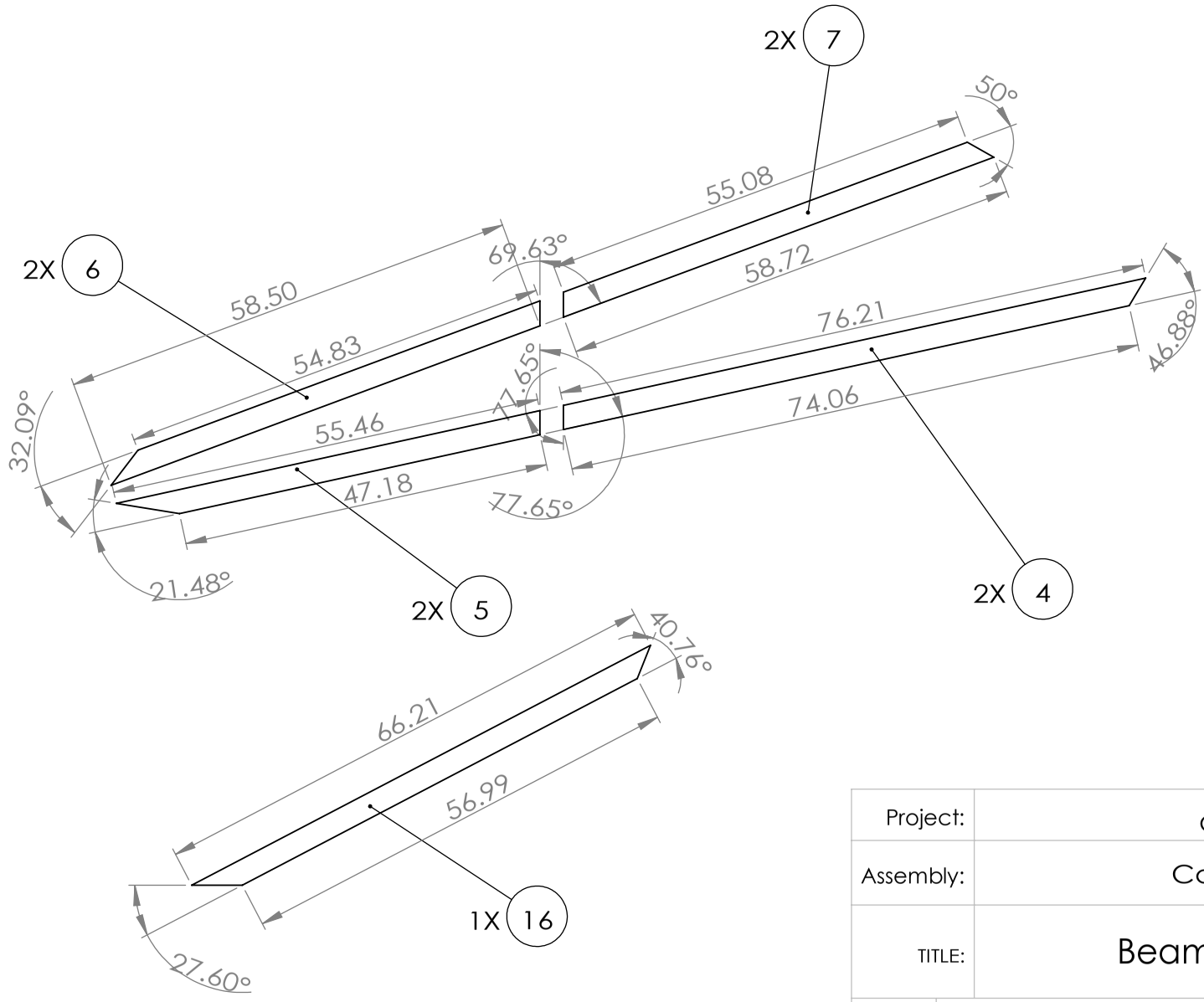

Project:	CLASS		
Assembly:	Cage Port		
TITLE:	Beam 4,5,6,7,16		
SIZE A	Drawn By: Zhilei Xu		REV 1
	Date: 1 Oct 2016		
Dimensions in inches	Material: Aluminum	Quantity:	SHEET 8 OF 11

5 4 3 2 1

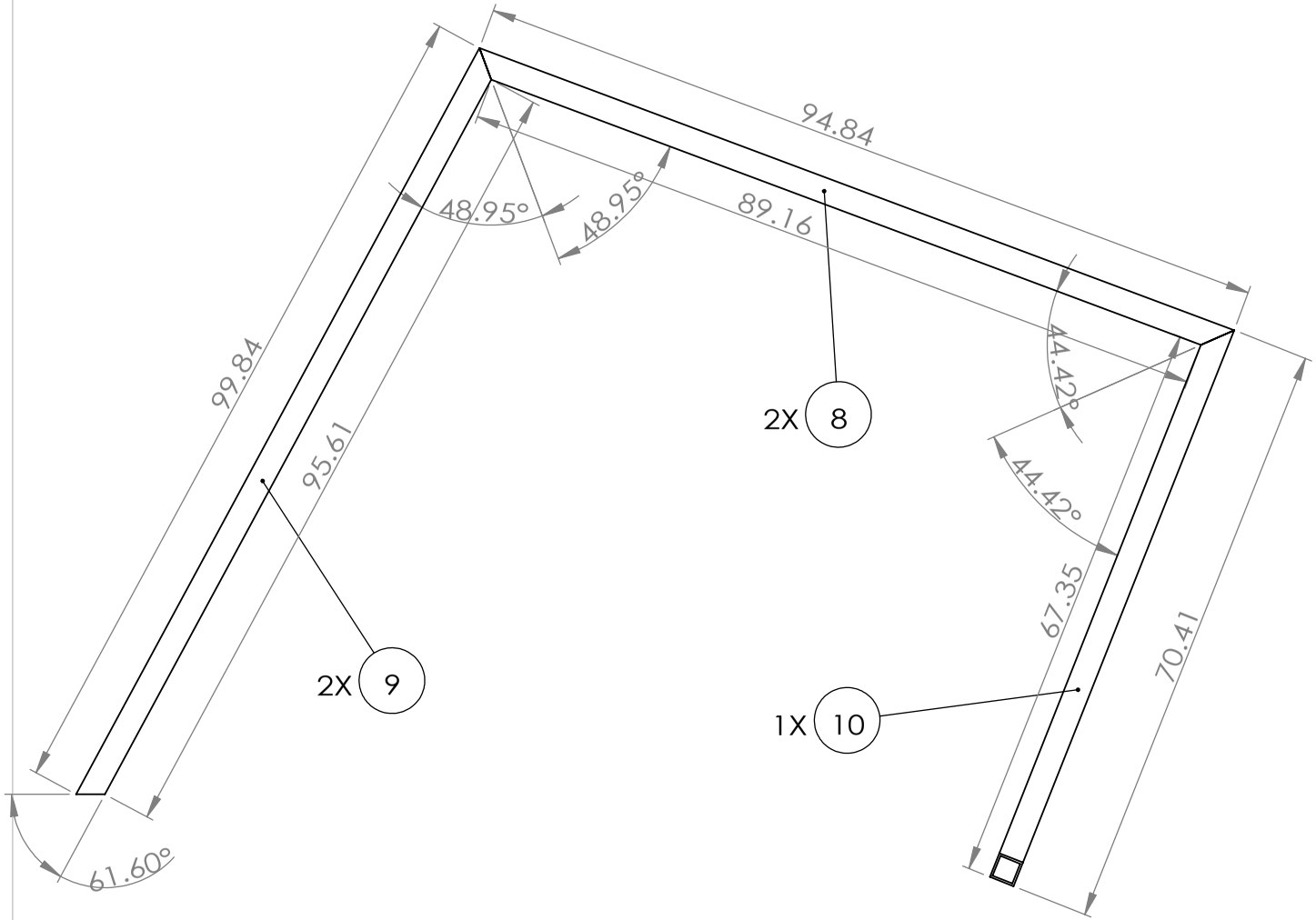

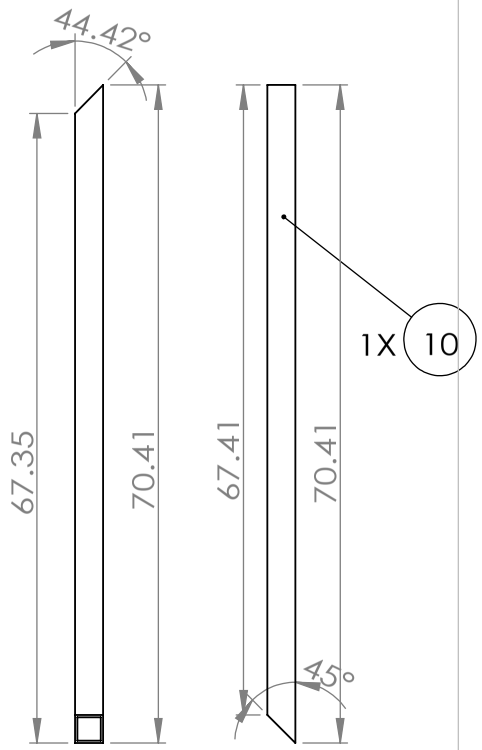

Note: Beam 10 and Beam 15 are identical.

Project:	CLASS
Assembly:	Cage Port
TITLE:	Beam 8,9,10,15

SIZE	Drawn By:	Zhilei Xu	REV
A	Date:	1 Oct 2016	1

Dimensions in inches		Material: Aluminum	Quantity:	SHEET 9 OF 11

5 4 3 2 1

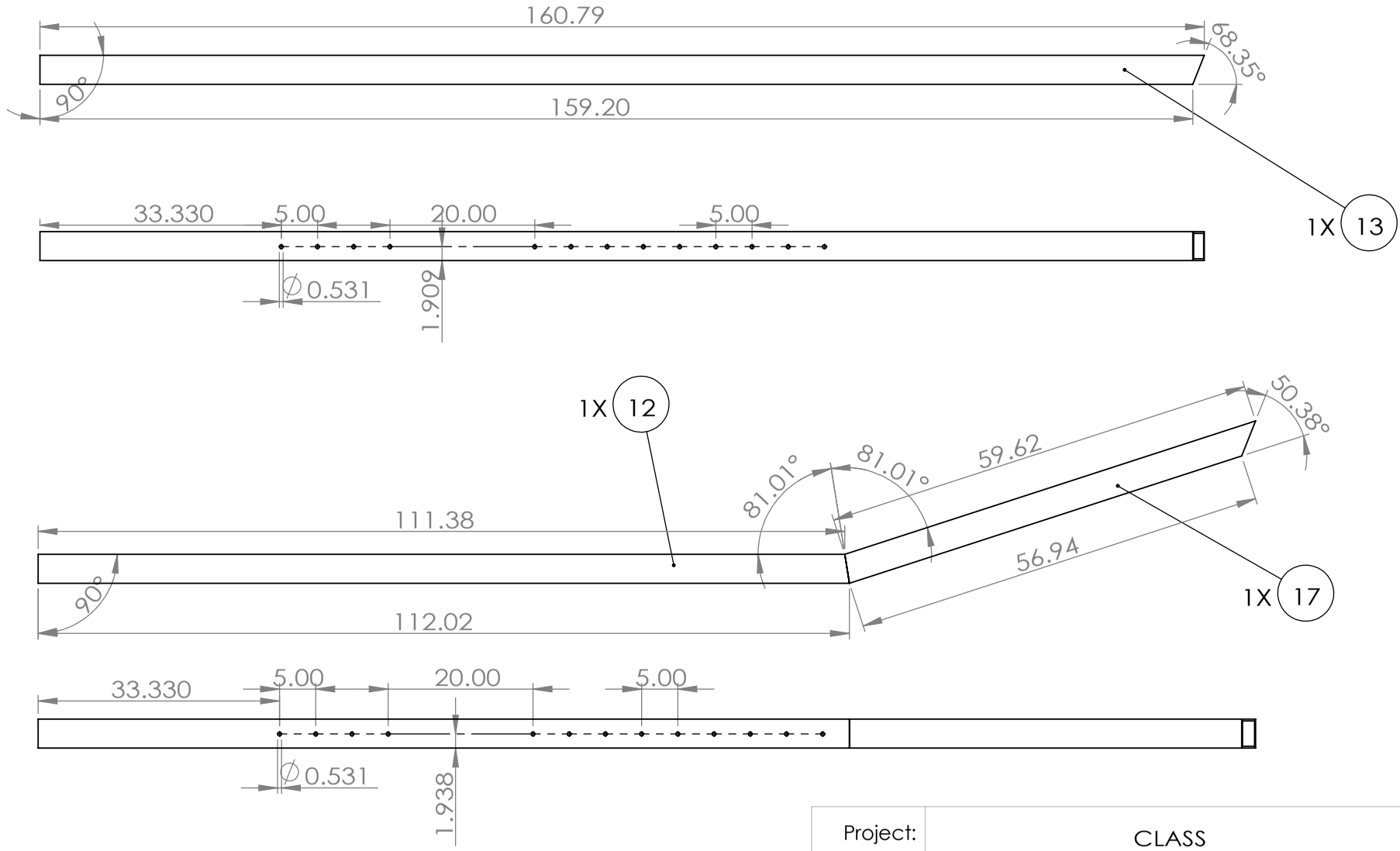

Project:	CLASS		
Assembly:	Cage Port		
TITLE:	Beam 12,13,17		
SIZE A	Drawn By: Zhilei Xu		REV 1
	Date: 1 Oct 2016		
Dimensions in inches	Material: Aluminum	Quantity:	SHEET 10 OF 11

5 4 3 2 1

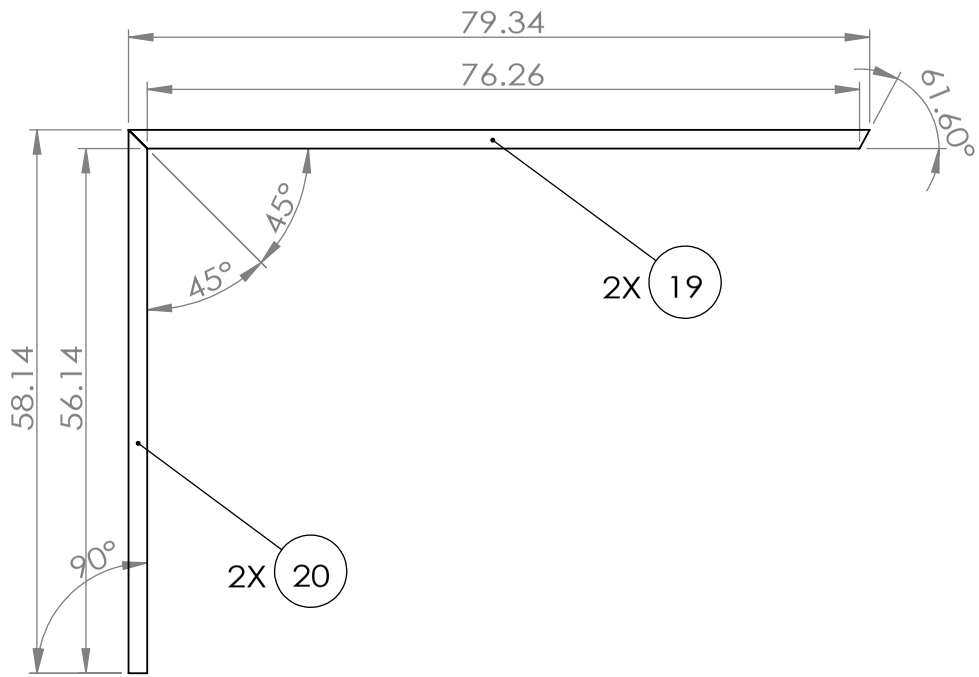

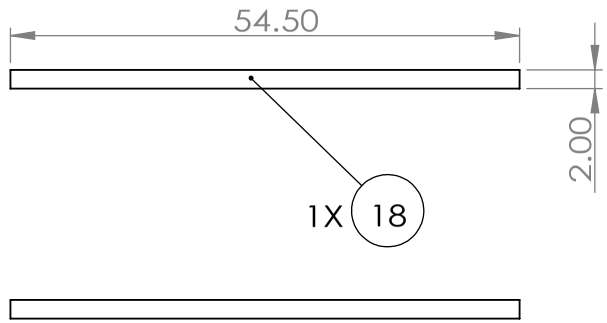

Project:	CLASS		
Assembly:	Cage Port		
TITLE:	Beam 18,19,20		
SIZE A	Drawn By: Zhilei Xu		REV 1
	Date: 1 Oct 2016		
Dimensions in inches	Material: Aluminum	Quantity:	SHEET 11 OF 11

5 4 3 2 1

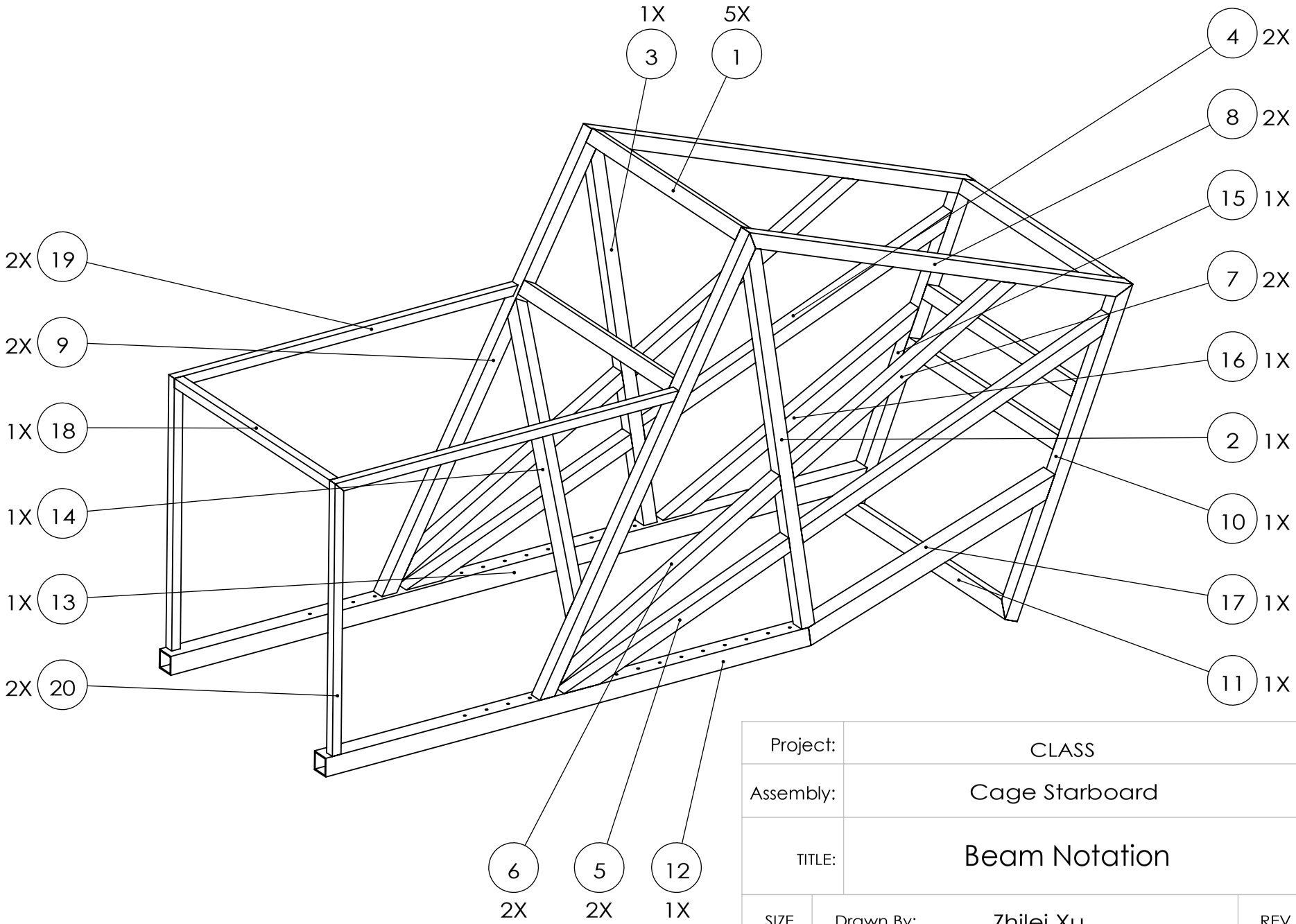

Project:	CLASS		
Assembly:	Cage Starboard		
TITLE:	Beam Notation		
SIZE A	Drawn By: Zhilei Xu		REV 1
	Date: 15 Oct 2016		

Dimensions in inches | SCALE: 1:25 | Material: Aluminum | Quantity: 1 | SHEET 1 OF 11

5 4 3 2 1

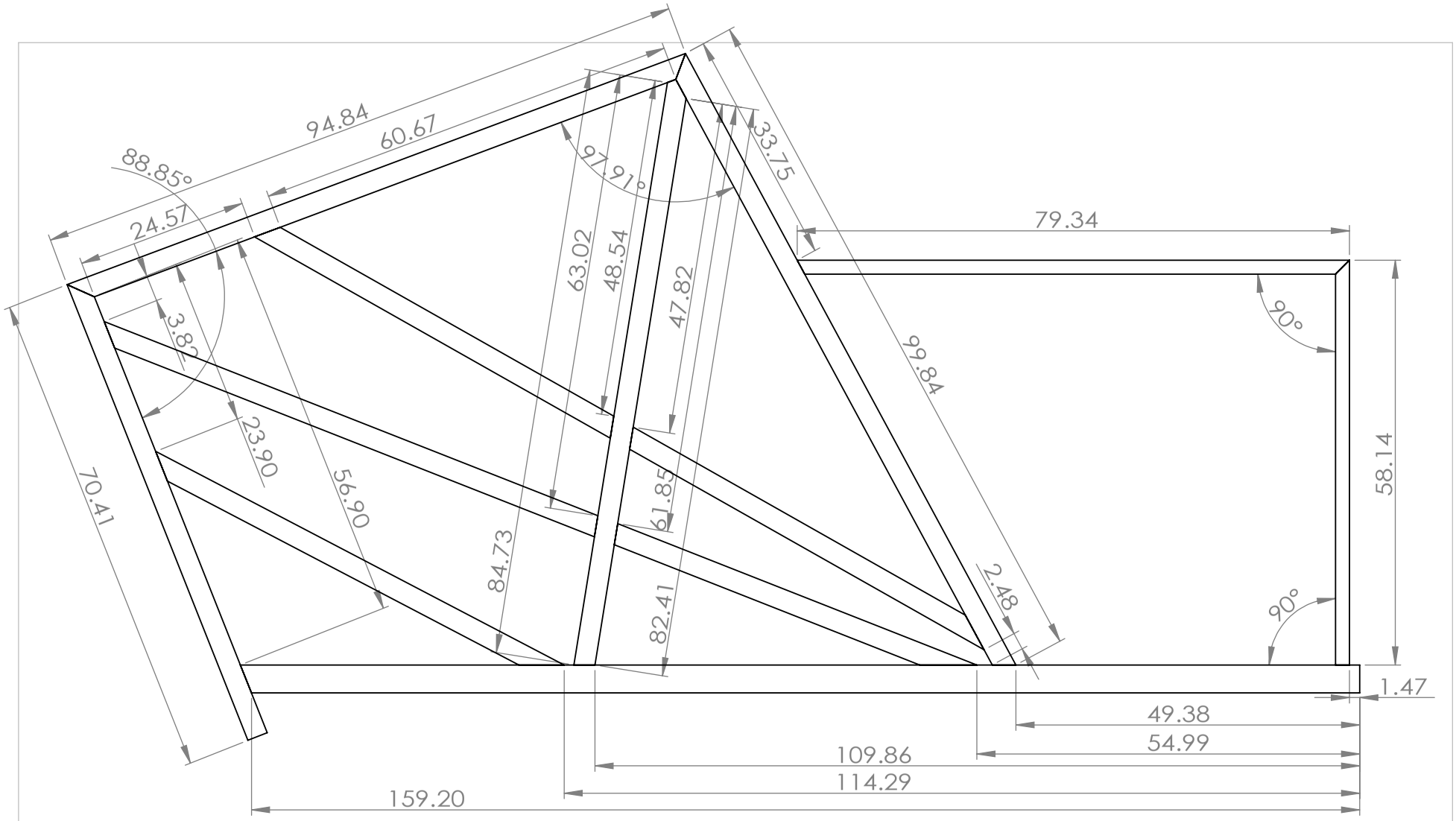

Project:	CLASS
Assembly:	Cage Starboard
TITLE:	Right Side

SIZE			REV
A	Drawn By: Zhilei Xu		1
	Date: 15 Oct 2016		

Dimensions in inches	Material: Aluminum	Quantity: 1	SHEET 2 OF 11

5 4 3 2 1

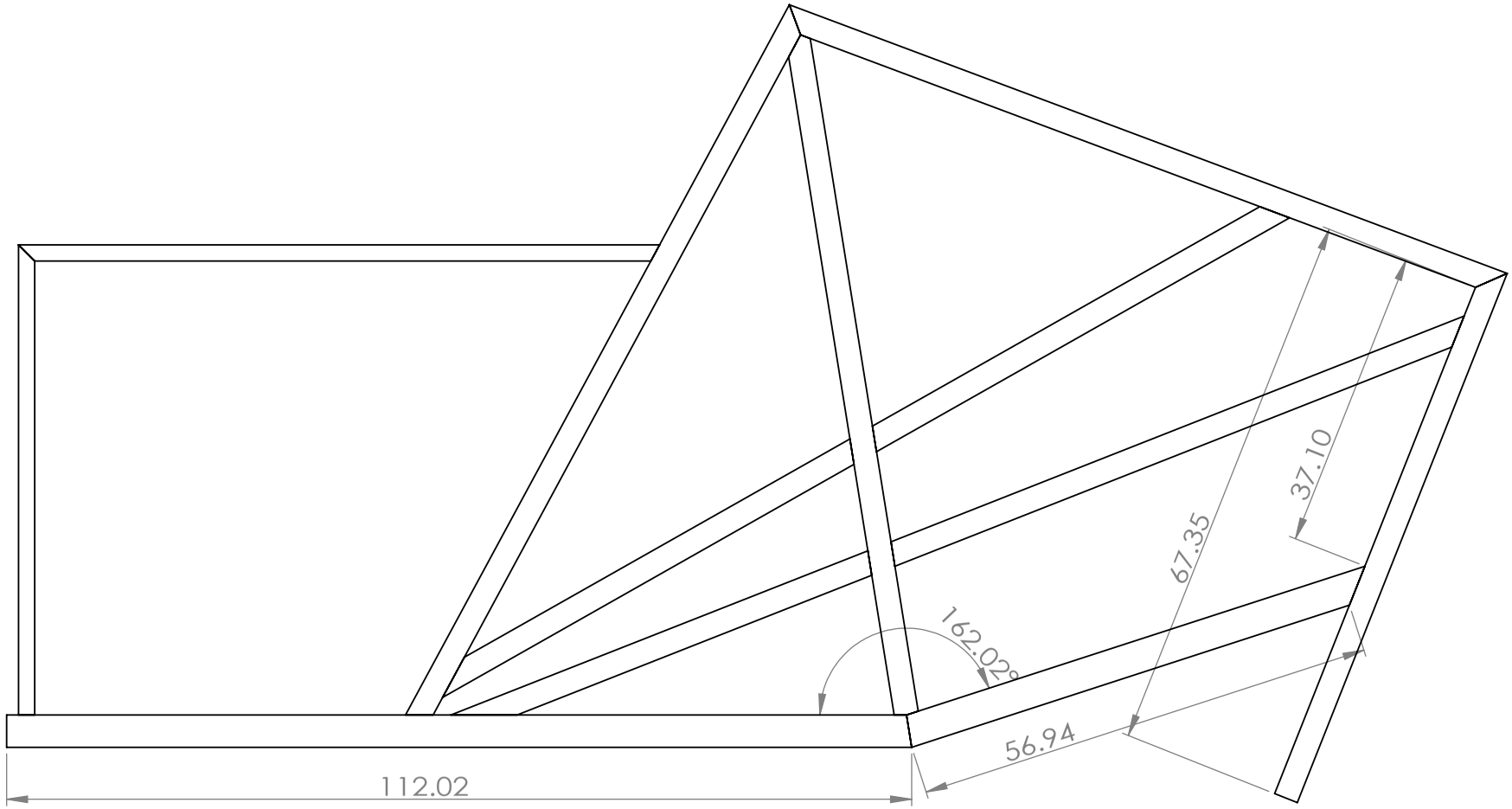

Note: All dimentions are identical to the Right Side
except for the noted ones

Project:	CLASS
Assembly:	Cage Starboard
TITLE:	Left Side

SIZE	Drawn By:	Zhilei Xu	REV
A	Date:	15 Oct 2016	1

Dimensions in inches	Material: Aluminum	Quantity: 1	SHEET 3 OF 11

5 4 3 2 1

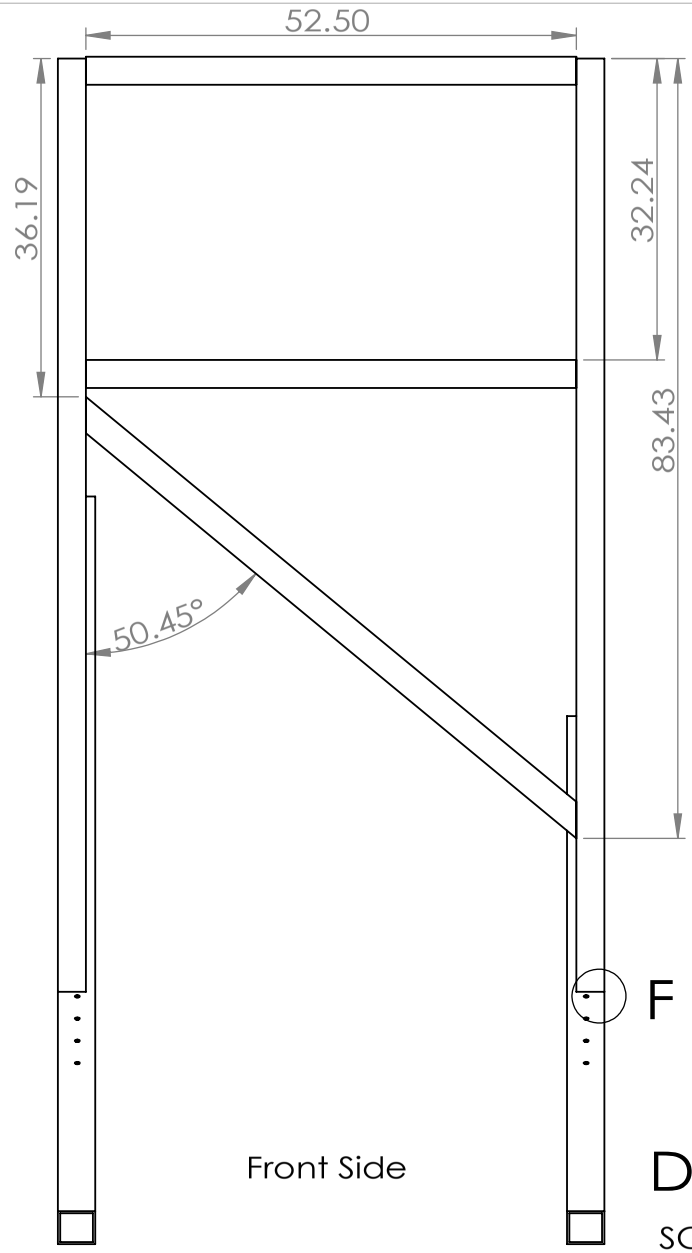

Front Side

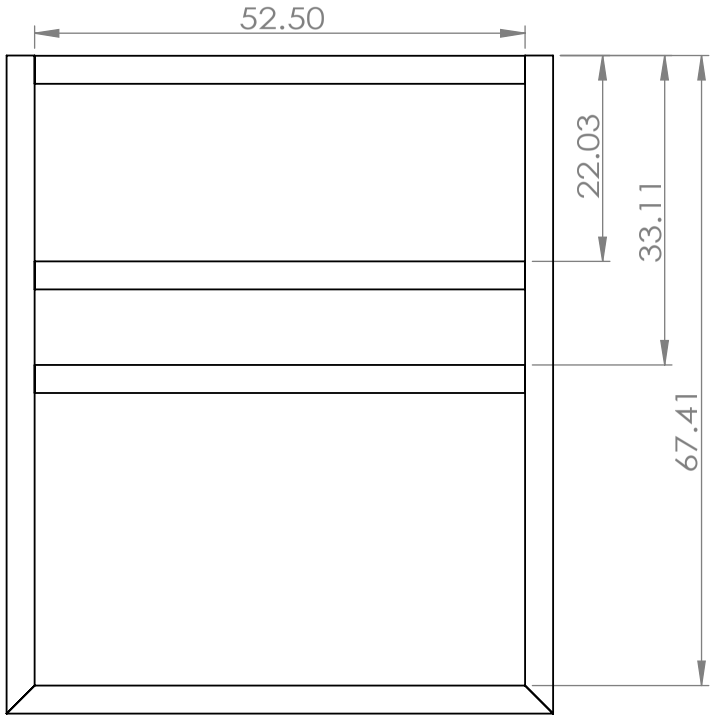

Back Side

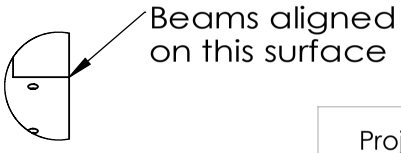

DETAIL F

SCALE 1 : 10

Important Note:

1. All cross beams are rotated to align with front/back side
2. All side beams are aligned to the outside surface

Project:	CLASS		
Assembly:	Cage Starboard		
TITLE:	Front/Back Side		
SIZE A	Drawn By: Zhilei Xu		REV 1
	Date: 15 Oct 2016		
Dimensions in inches	Material: Aluminum	Quantity: 1	SHEET 4 OF 11

5 4 3 2 1

ITEM NO.	QTY.	LENGTH	ANGLE1	ANGLE2	Description
1	5	52.5	0.00	0.00	3 SQ x .250 Wall
2	1	85.119194	-	-	3 SQ x .250 Wall
3	1	85.359458	9.13	-	3 SQ x .250 Wall
4	2	76.867123	43.12	12.35	3 SQ x .250 Wall
5	2	55.460203	12.35	68.52	3 SQ x .250 Wall
6	2	59.610033	20.37	57.91	3 SQ x .250 Wall
7	2	58.715246	40.00	20.37	3 SQ x .250 Wall
8	2	94.836582	45.58	41.05	3 SQ x .250 Wall
9	2	99.843525	28.40	41.05	3 SQ x .250 Wall
10	1	70.414258	45.58	45.00	3 SQ x .250 Wall
11	1	58.5	45.00	45.00	3 SQ x .250 Wall
12	1	112.015814	8.99	0.00	4 SQ x .250 Wall
13	1	160.791797	0.00	21.65	4 SQ x .250 Wall
14	1	70.560492	39.55	39.55	3 SQ x .250 Wall
15	1	70.414258	45.00	45.58	3 SQ x .250 Wall
16	1	66.211312	49.24	62.40	3 SQ x .250 Wall
17	1	60.255532	39.62	8.99	4 SQ x .250 Wall
18	1	54.5	0.00	0.00	2 SQ x .250 Wall
19	2	79.3377	45.00	28.40	2 SQ x .250 Wall
20	2	58.13976	0.00	45.00	2 SQ x .250 Wall

5 4 3 2 1

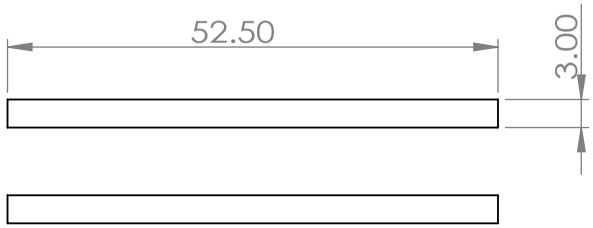

Beam 1

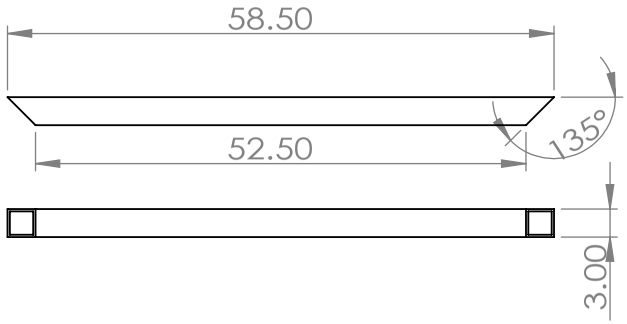

Beam 11

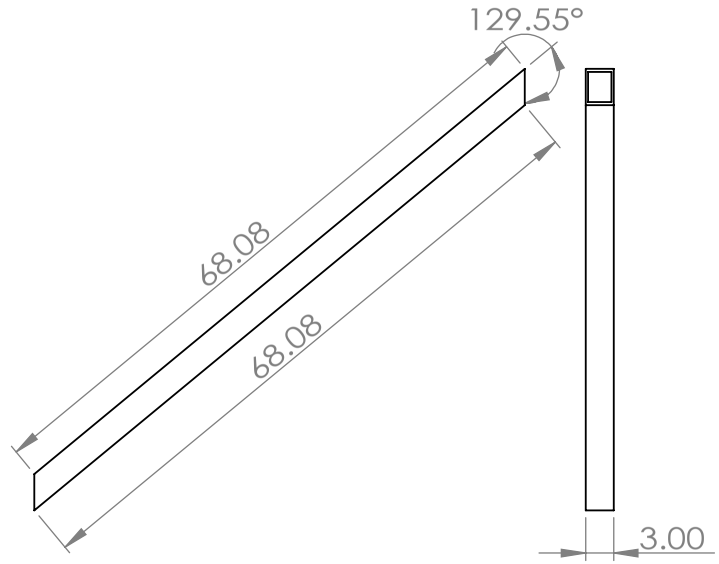

Beam 14

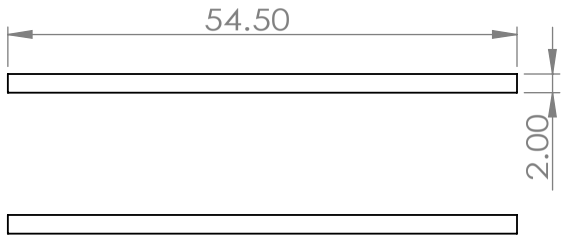

Beam 18

Project:	CLASS		
Assembly:	Cage Starboardt		
TITLE:	Beam 1,11,14,18		
SIZE A	Drawn By: Zhilei Xu		REV 1
	Date: 15 Oct 2016		

Dimensions in inches	SCALE:	Material: Aluminum	Quantity:	SHEET 6 OF 11

5 4 3 2 1

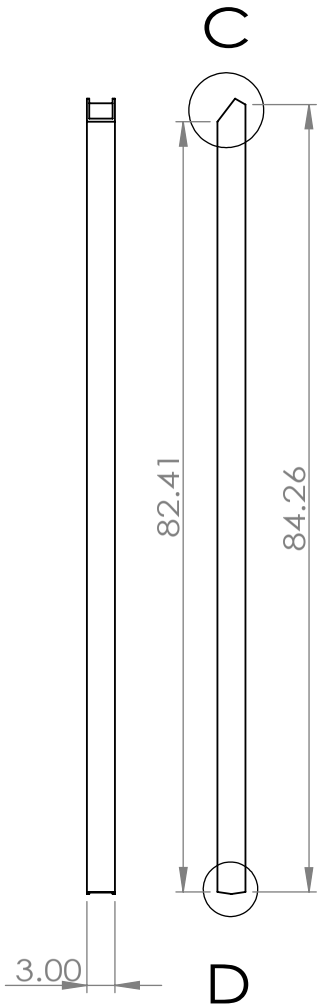

Beam 2

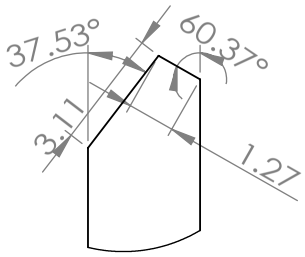

DETAIL C

SCALE 1 : 5

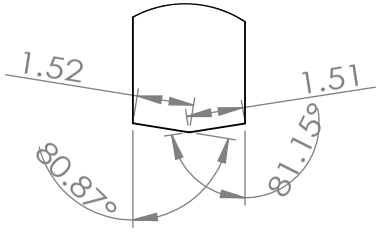

DETAIL D

SCALE 1 : 5

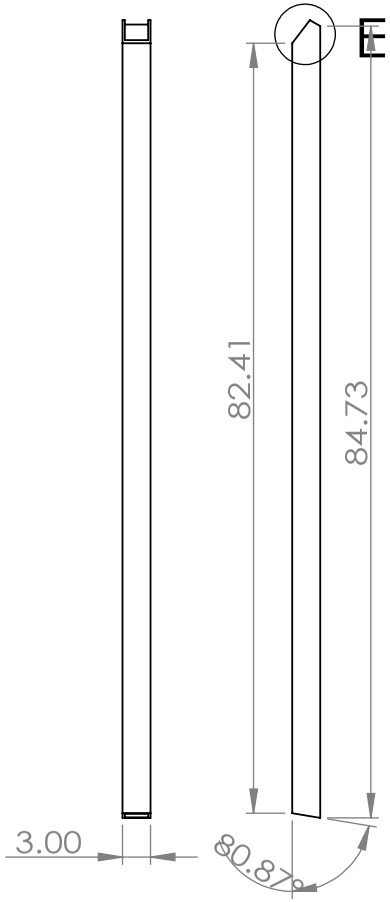

Beam 3

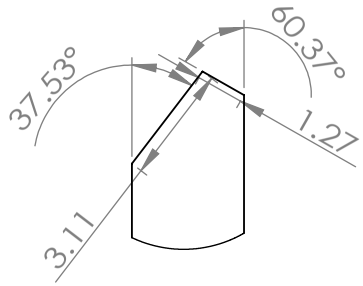

DETAIL E

SCALE 1 : 5

Project:	CLASS
Assembly:	Cage Starboard
TITLE:	Beam 2,3

SIZE	Drawn By:	Zhilei Xu	REV
A	Date:	15 Oct 2016	1

Dimensions in inches		Material: Aluminum	Quantity:	SHEET 7 OF 11

5 4 3 2 1

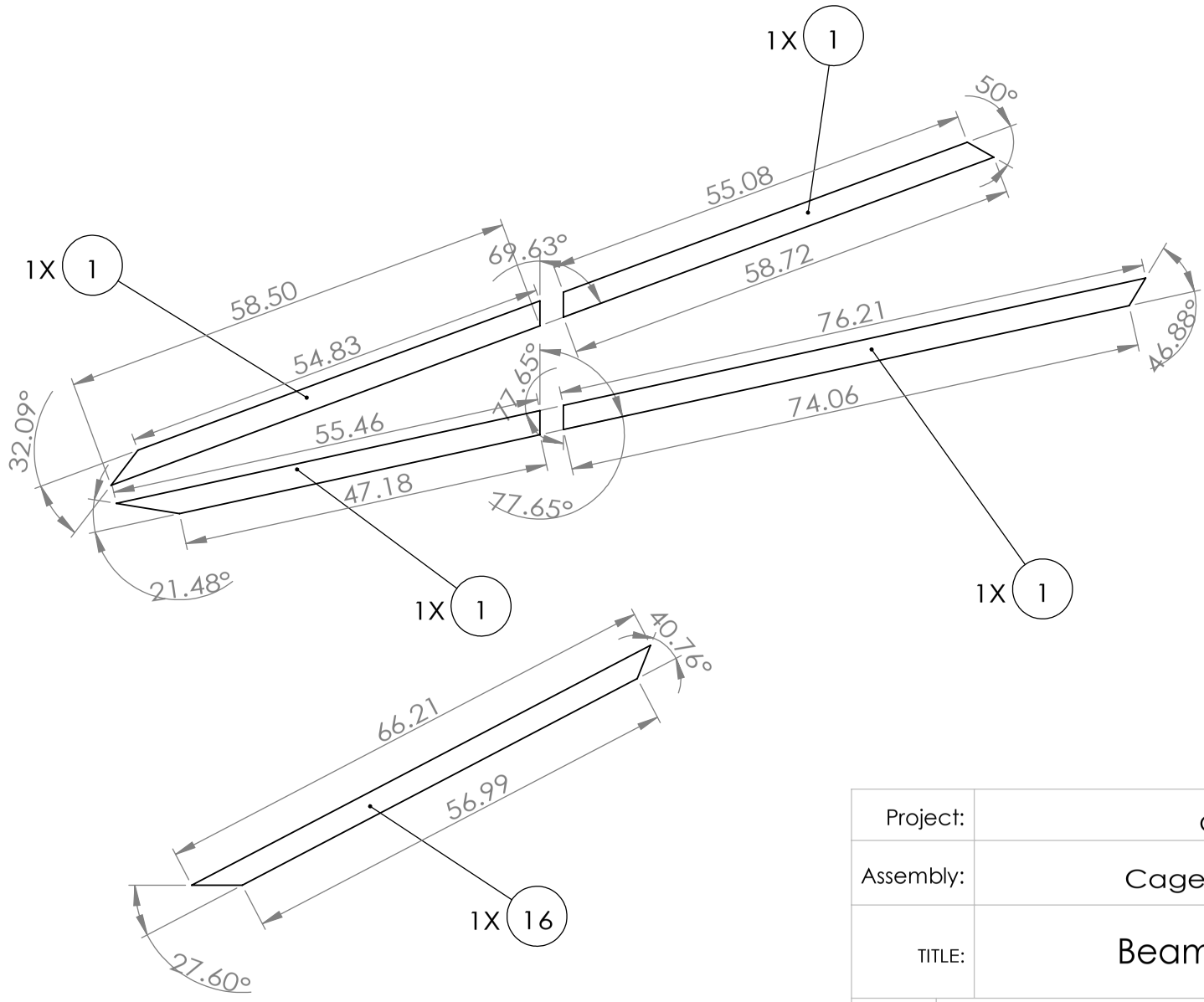

Project:	CLASS		
Assembly:	Cage Starboard		
TITLE:	Beam 4,5,6,7,16		
SIZE A	Drawn By: Zhilei Xu		REV 1
	Date: 15 Oct 2016		
Dimensions in inches	Material: Aluminum	Quantity:	SHEET 8 OF 11

5 4 3 2 1

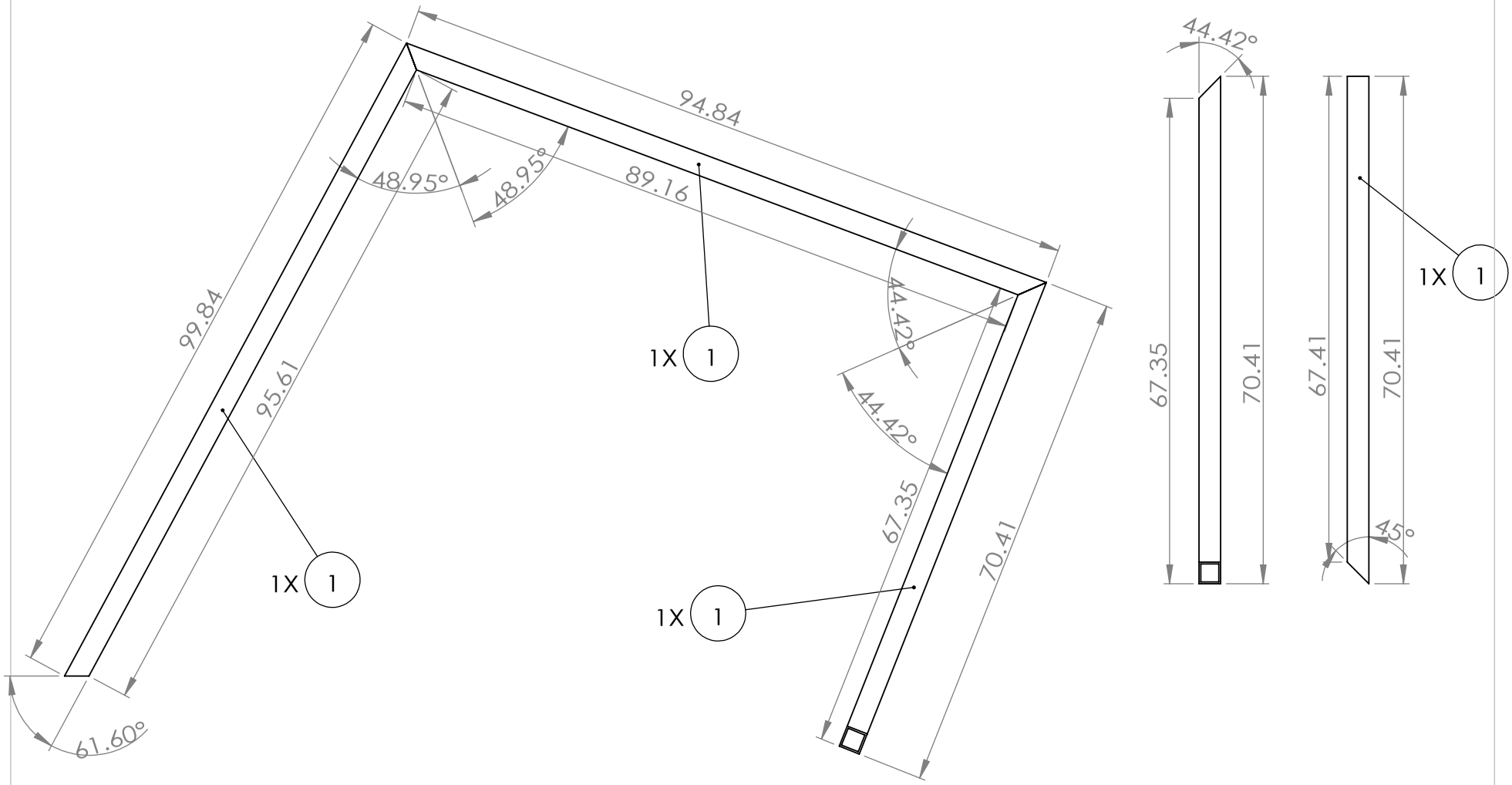

Note: Beam 10 and Beam 15 are identical.

Project:	CLASS
Assembly:	Cage Starboard
TITLE:	Beam 8,9,10,15

SIZE	Drawn By:	Zhilei Xu	REV
A	Date:	15 Oct 2016	1

Dimensions in inches		Material: Aluminum	Quantity:	SHEET 9 OF 11

5 4 3 2 1

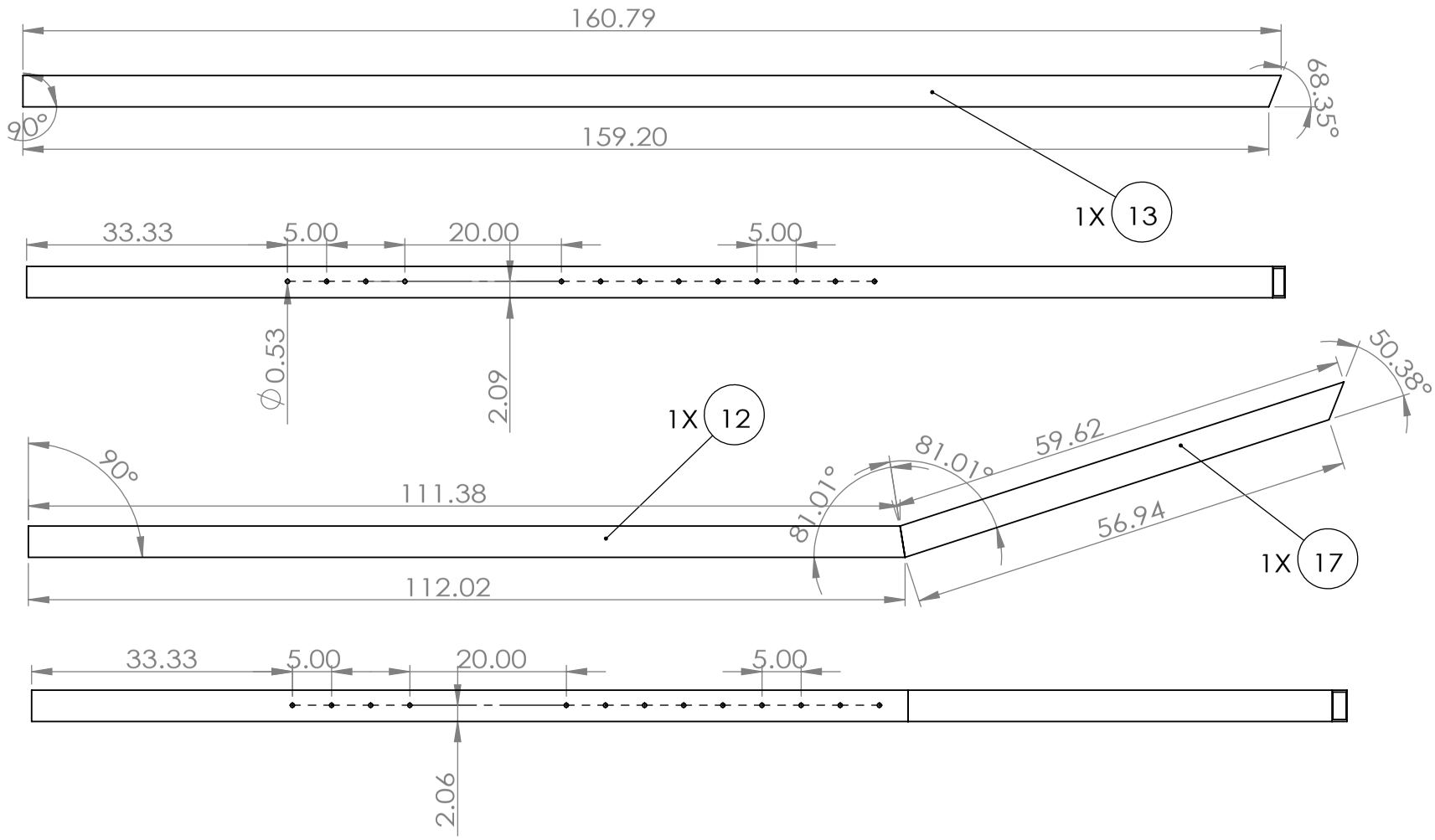

Project:	CLASS
Assembly:	Cage Starboard
TITLE:	Beam 12,13,17

SIZE	Drawn By:	Zhilei Xu	REV
A	Date:	15 Oct 2016	1

Dimensions in inches		Material: Aluminum	Quantity:	SHEET 10 OF 11

5 4 3 2 1

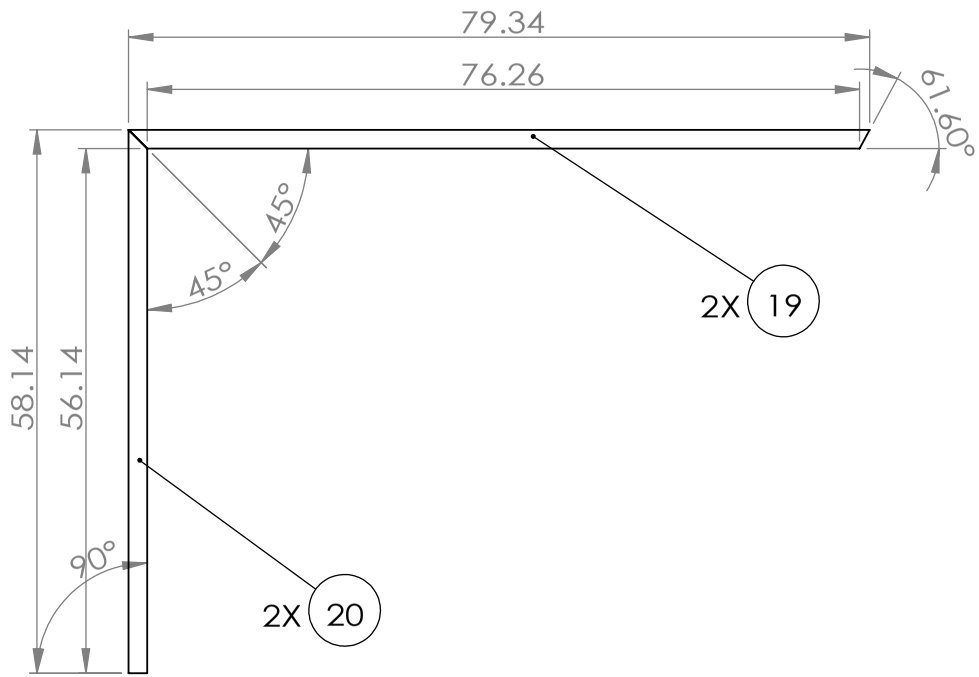

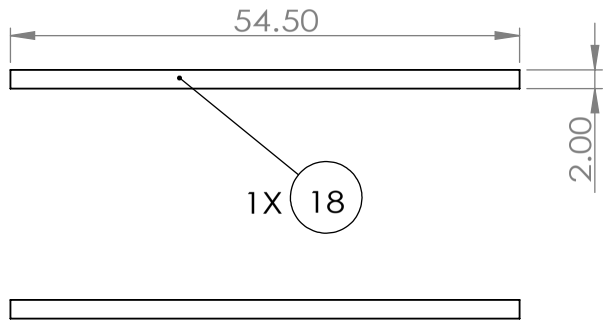

Project:	CLASS
Assembly:	Cage Starboard
TITLE:	Beam 18,19,20

SIZE	Drawn By:	Zhilei Xu	REV
A	Date:	15 Oct 2016	1

Dimensions in inches		Material: Aluminum	Quantity:	SHEET 11 OF 11

5 4 3 2 1

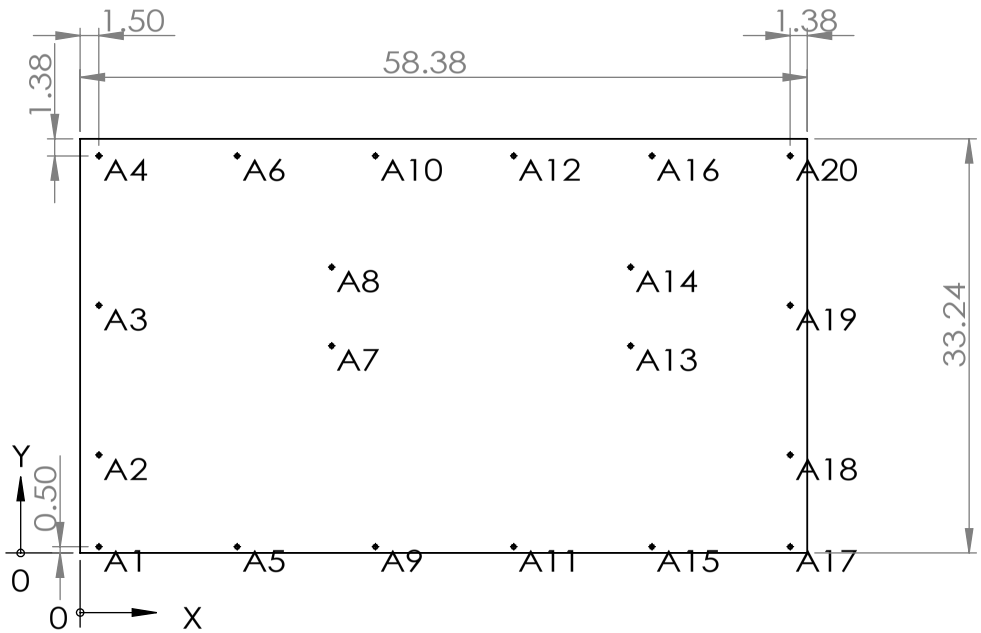

Note: all the other panels are also 0.5" thick.

Project:	CLASS
Assembly:	Panels
TITLE:	Primary Mirror Panel

SIZE	Drawn By:	Zhilei Xu	REV
A	Date:	20 November 2016	2

Dimensions in inches	SCALE: 1:15	Material: Al (HC)	Quantity: 2	SHEET 1 OF 12

5 4 3 2 1

TAG	XLOC	YLOC	SIZE
A1	1.50	0.50	∅0.33 THRU
A2	1.50	7.87	∅0.33 THRU
A3	1.50	19.87	∅0.33 THRU
A4	1.50	31.87	∅0.33 THRU
A5	12.60	0.50	∅0.33 THRU
A6	12.60	31.87	∅0.33 THRU
A7	20.19	16.62	∅0.33 THRU
A8	20.19	22.93	∅0.33 THRU
A9	23.70	0.50	∅0.33 THRU
A10	23.70	31.87	∅0.33 THRU
A11	34.80	0.50	∅0.33 THRU
A12	34.80	31.87	∅0.33 THRU
A13	44.19	16.62	∅0.33 THRU
A14	44.19	22.93	∅0.33 THRU
A15	45.90	0.50	∅0.33 THRU
A16	45.90	31.87	∅0.33 THRU
A17	57.00	0.50	∅0.33 THRU
A18	57.00	7.87	∅0.33 THRU
A19	57.00	19.87	∅0.33 THRU
A20	57.00	31.87	∅0.33 THRU

Project:	CLASS		
Assembly:	Panels		
TITLE:	Primary Mirror Panel Table		
SIZE A	Drawn By: Zhilei Xu		REV 2
	Date: 20 November 2016		

Dimensions in inches | SCALE: 1:15 | Material: Al (HC) | Quantity: 2 | SHEET 2 OF 12

5 4 3 2 1

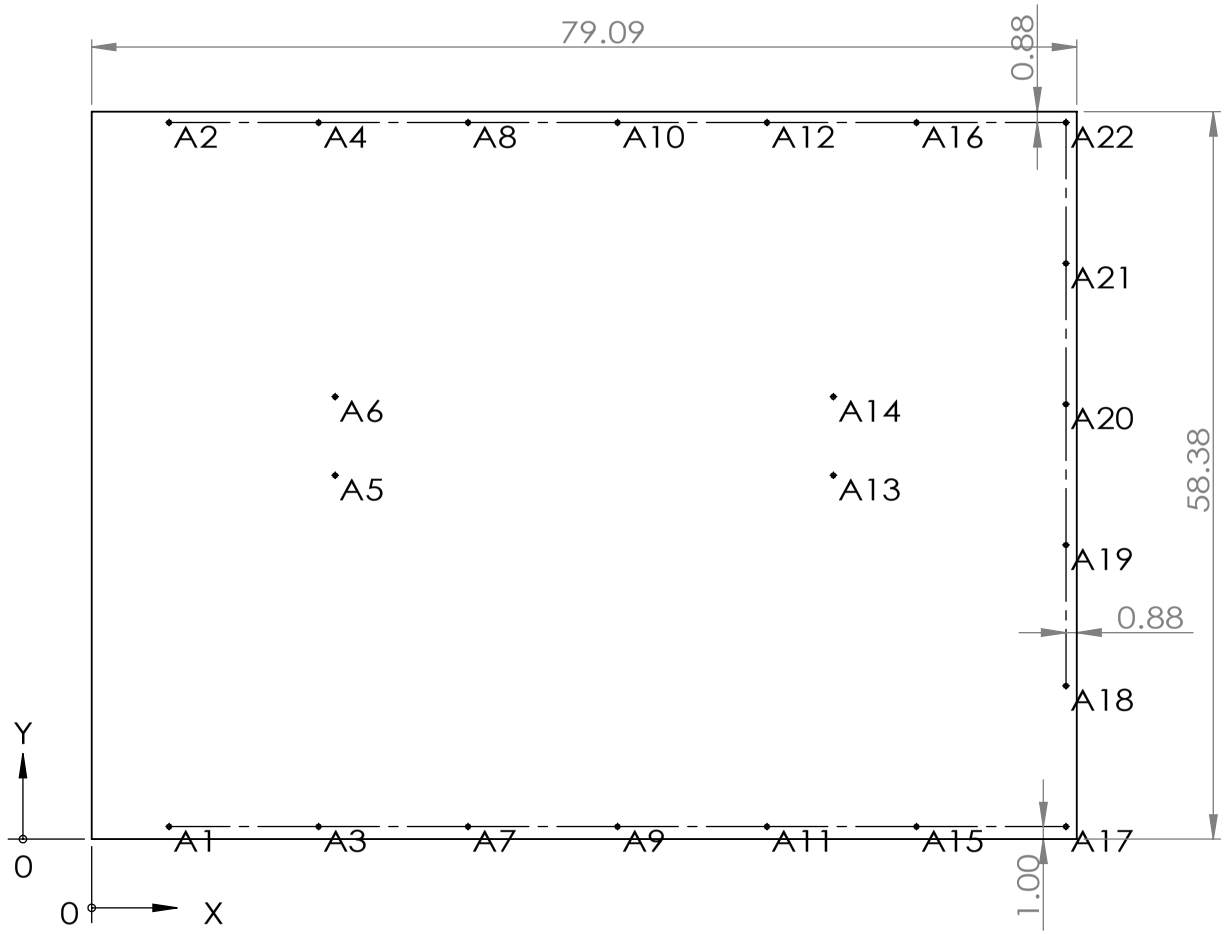

Project:	CLASS			
Assembly:	Panels			
TITLE:	Cube Top Panel			
SIZE A	Drawn By: Zhilei Xu			REV 2
	Date: 20 November 2016			
Dimensions in inches	SCALE: 1:15	Material: Al (HC)	Quantity: 2	SHEET 3 OF 12

5 4 3 2 1

TAG	XLOC	YLOC	SIZE
A1	6.21	1.00	∅0.33 THRU
A2	6.21	57.50	∅0.33 THRU
A3	18.21	1.00	∅0.33 THRU
A4	18.21	57.50	∅0.33 THRU
A5	19.54	29.19	∅0.33 THRU
A6	19.54	35.50	∅0.33 THRU
A7	30.21	1.00	∅0.33 THRU
A8	30.21	57.50	∅0.33 THRU
A9	42.21	1.00	∅0.33 THRU
A10	42.21	57.50	∅0.33 THRU
A11	54.21	1.00	∅0.33 THRU
A12	54.21	57.50	∅0.33 THRU
A13	59.54	29.19	∅0.33 THRU
A14	59.54	35.50	∅0.33 THRU
A15	66.21	1.00	∅0.33 THRU
A16	66.21	57.50	∅0.33 THRU
A17	78.21	1.00	∅0.33 THRU
A18	78.21	12.30	∅0.33 THRU
A19	78.21	23.60	∅0.33 THRU
A20	78.21	34.90	∅0.33 THRU
A21	78.21	46.20	∅0.33 THRU
A22	78.21	57.50	∅0.33 THRU

Project:	CLASS		
Assembly:	Panels		
TITLE:	Cube Top Panel Table		
SIZE A	Drawn By: Zhilei Xu		REV 2
	Date: 20 November 2016		
Dimensions in inches	SCALE: 1:15	Material: Al (HC)	Quantity: 2	SHEET 4 OF 12

5 4 3 2 1

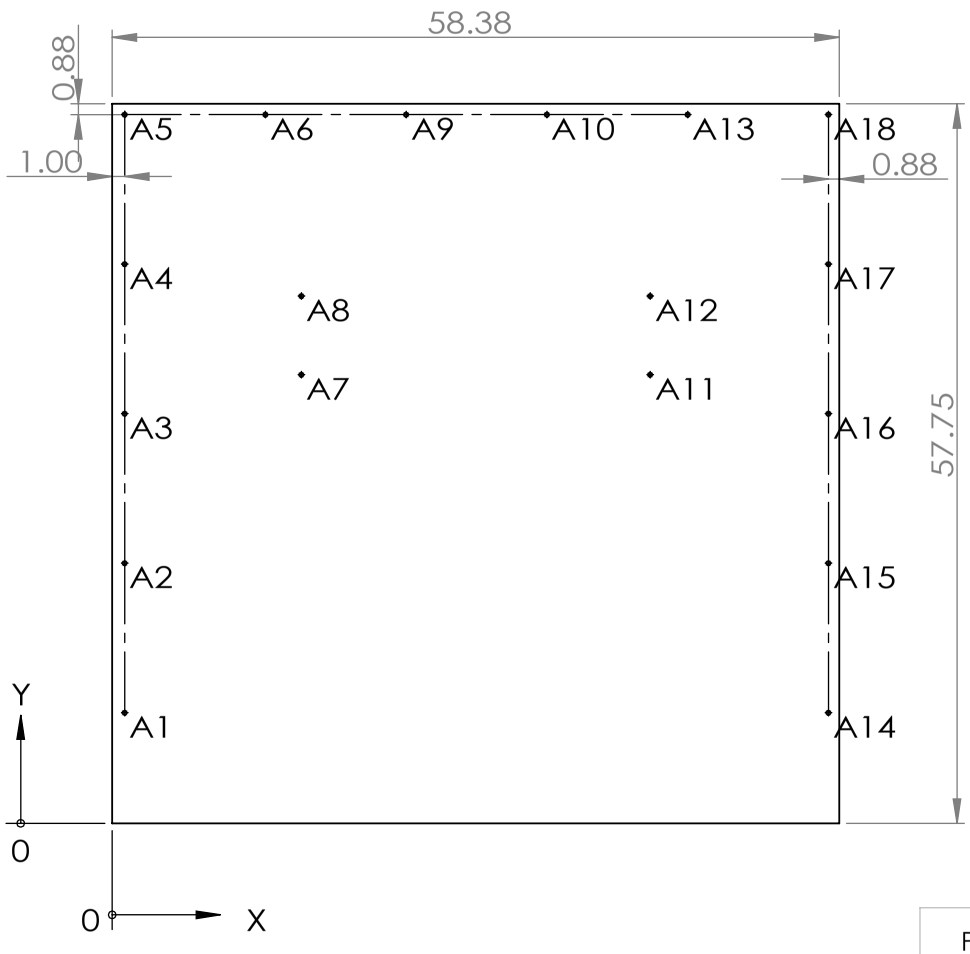

Project:	CLASS
Assembly:	Panels
TITLE:	Cube Back Panel

SIZE	Drawn By:	Zhilei Xu	REV
A	Date:	20 November 2016	2

Dimensions in inches	SCALE: 1:15	Material: Al (HC)	Quantity: 1	SHEET 5 OF 12

5 4 3 2 1

TAG	XLOC	YLOC	SIZE
A1	1.00	8.88	∅0.33 THRU
A2	1.00	20.88	∅0.33 THRU
A3	1.00	32.88	∅0.33 THRU
A4	1.00	44.88	∅0.33 THRU
A5	1.00	56.88	∅0.33 THRU
A6	12.30	56.88	∅0.33 THRU
A7	15.19	36.00	∅0.33 THRU
A8	15.19	42.31	∅0.33 THRU
A9	23.60	56.88	∅0.33 THRU
A10	34.90	56.88	∅0.33 THRU
A11	43.19	36.00	∅0.33 THRU
A12	43.19	42.31	∅0.33 THRU
A13	46.20	56.88	∅0.33 THRU
A14	57.50	8.88	∅0.33 THRU
A15	57.50	20.88	∅0.33 THRU
A16	57.50	32.88	∅0.33 THRU
A17	57.50	44.88	∅0.33 THRU
A18	57.50	56.88	∅0.33 THRU

Project:	CLASS		
Assembly:	Panels		
TITLE:	Cube Back Panel Table		
SIZE A	Drawn By: Zhilei Xu		REV 2
	Date: 20 November 2016		

Dimensions in inches | SCALE: 1:15 | Material: Al (HC) | Quantity: 1 | SHEET 6 OF 12

5 4 3 2 1

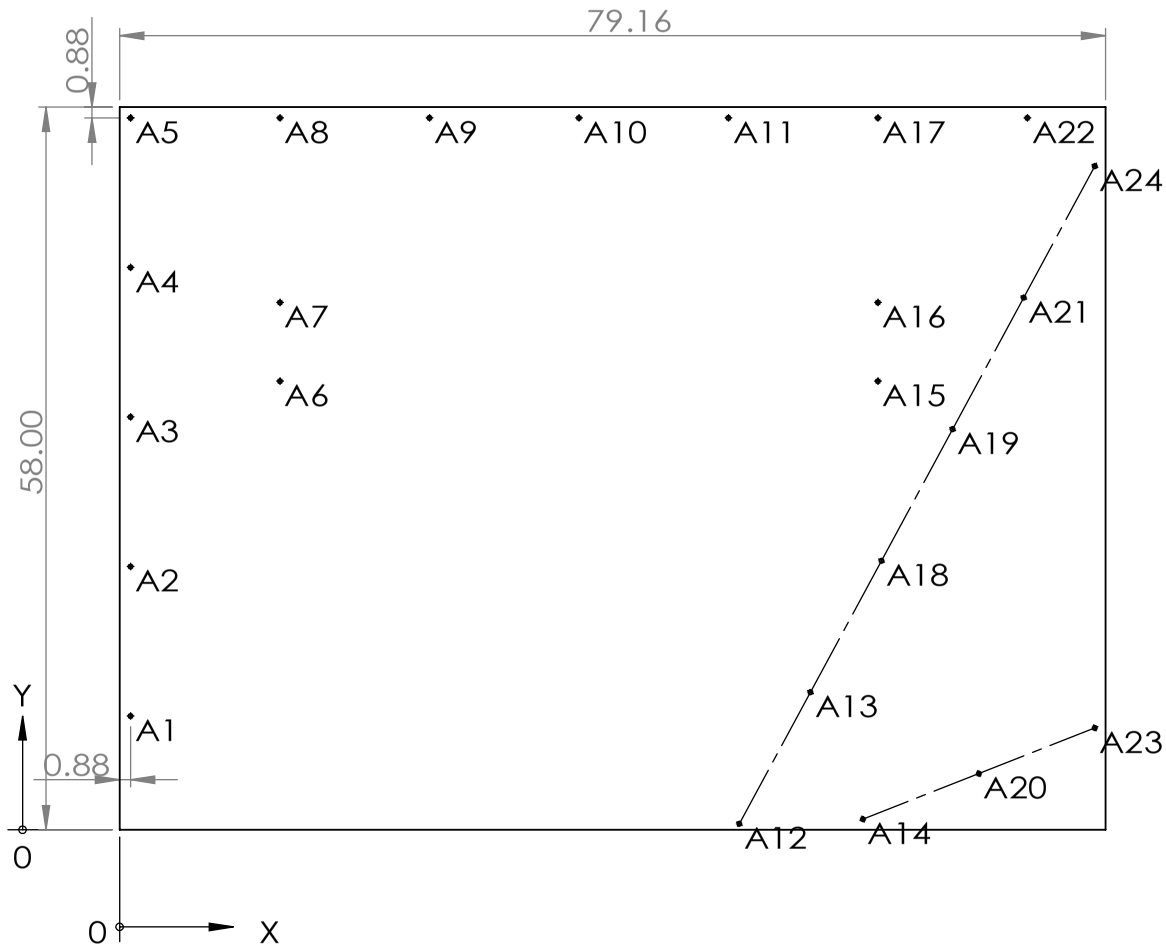

Project:	CLASS			
Assembly:	Panels			
TITLE:	Side Panel 1			
SIZE A	Drawn By: Zhilei Xu			REV 2
	Date: 20 November 2016			
Dimensions in inches	SCALE: 1:15	Material: Al (HC)	Quantity: 1	SHEET 7 OF 12

5 4 3 2 1

TAG	XLOC	YLOC	SIZE
A1	0.88	9.13	∅0.33 THRU
A2	0.88	21.13	∅0.33 THRU
A3	0.88	33.13	∅0.33 THRU
A4	0.88	45.13	∅0.33 THRU
A5	0.88	57.13	∅0.33 THRU
A6	12.88	36.00	∅0.33 THRU
A7	12.88	42.31	∅0.33 THRU
A8	12.88	57.13	∅0.33 THRU
A9	24.88	57.13	∅0.33 THRU
A10	36.88	57.13	∅0.33 THRU
A11	48.88	57.13	∅0.33 THRU
A12	49.75	0.48	∅0.33 THRU
A13	55.46	11.04	∅0.33 THRU
A14	59.68	0.85	∅0.33 THRU
A15	60.88	36.00	∅0.33 THRU
A16	60.88	42.31	∅0.33 THRU
A17	60.88	57.13	∅0.33 THRU
A18	61.16	21.59	∅0.33 THRU
A19	66.87	32.15	∅0.33 THRU
A20	68.98	4.51	∅0.33 THRU
A21	72.58	42.70	∅0.33 THRU
A22	72.88	57.13	∅0.33 THRU
A23	78.29	8.17	∅0.33 THRU
A24	78.29	53.26	∅0.33 THRU

Project:	CLASS		
Assembly:	Panels		
TITLE:	Side1 Panel 1 Table		
SIZE A	Drawn By: Zhilei Xu		REV 2
	Date: 20 November 2016		

Dimensions in inches | SCALE: 1:15 | Material: Al (HC) | Quantity: 1 | SHEET 8 OF 12

5 4 3 2 1

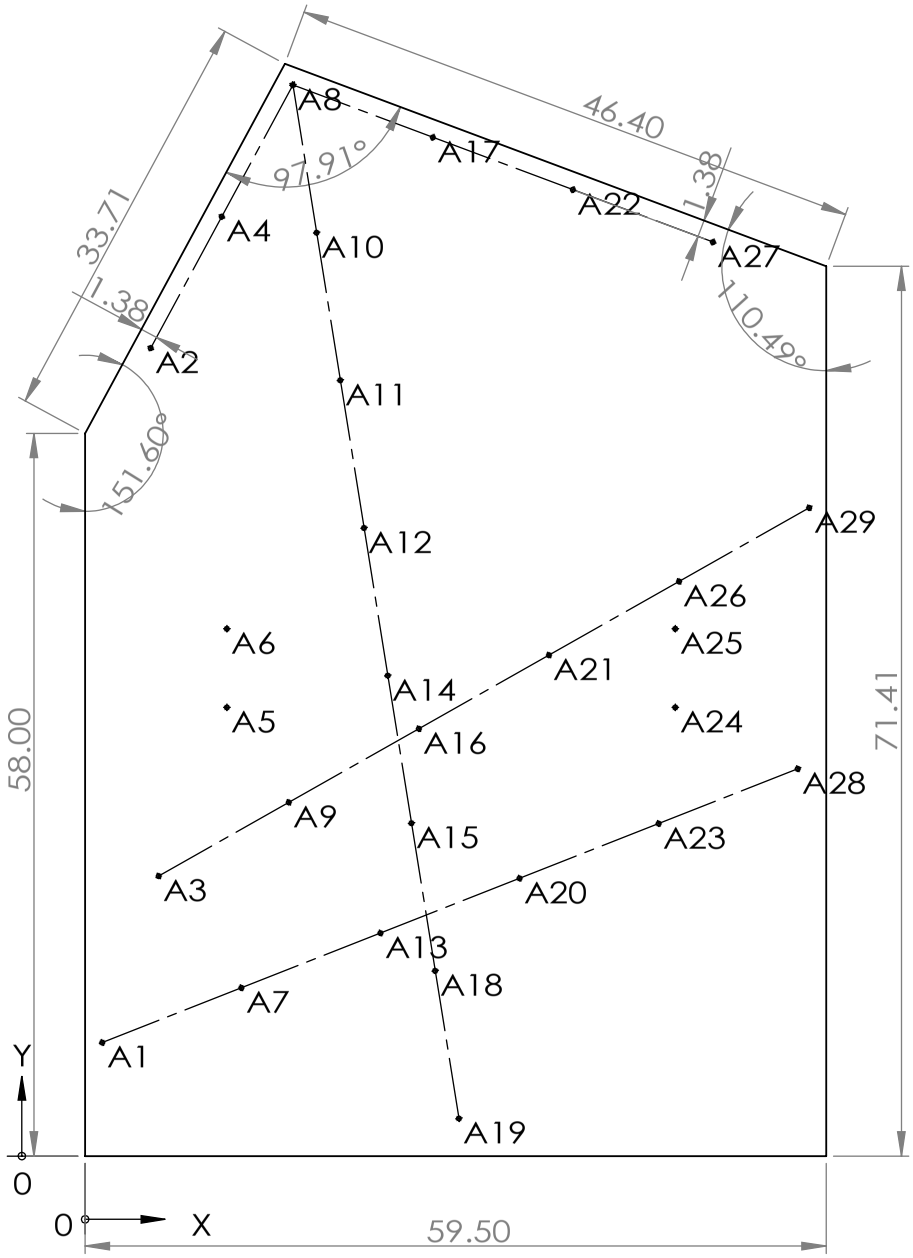

Project:	CLASS		
Assembly:	Panels		
TITLE:	Side Panel 2		
SIZE A	Drawn By: Zhilei Xu		REV 3
	Date: 20 November 2016		

Dimensions in inches | SCALE: 1:15 | Material: Al (HC) | Quantity: 2 | SHEET 9 OF 12

5 4 3 2 1

TAG	XLOC	YLOC	SIZE
A1	1.38	9.11	∅0.33 THRU
A2	5.26	64.84	∅0.33 THRU
A3	5.91	22.47	∅0.33 THRU
A4	10.97	75.39	∅0.33 THRU
A5	11.38	36.00	∅0.33 THRU
A6	11.38	42.31	∅0.33 THRU
A7	12.54	13.50	∅0.33 THRU
A8	16.68	85.95	∅0.33 THRU
A9	16.35	28.38	∅0.33 THRU
A10	18.58	74.10	∅0.33 THRU
A11	20.48	62.25	∅0.33 THRU
A12	22.39	50.41	∅0.33 THRU
A13	23.71	17.89	∅0.33 THRU
A14	24.29	38.56	∅0.33 THRU
A15	26.20	26.71	∅0.33 THRU
A16	26.79	34.29	∅0.33 THRU
A17	27.92	81.75	∅0.33 THRU
A18	28.10	14.86	∅0.33 THRU

TAG	XLOC	YLOC	SIZE
A19	30.00	3.01	∅0.33 THRU
A20	34.88	22.29	∅0.33 THRU
A21	37.24	40.20	∅0.33 THRU
A22	39.16	77.55	∅0.33 THRU
A23	46.04	26.68	∅0.33 THRU
A24	47.38	36.00	∅0.33 THRU
A25	47.38	42.31	∅0.33 THRU
A26	47.68	46.11	∅0.33 THRU
A27	50.40	73.35	∅0.33 THRU
A28	57.21	31.07	∅0.33 THRU
A29	58.13	52.02	∅0.33 THRU

Project:	CLASS
Assembly:	Panels
TITLE:	Side Panel 2 Table

SIZE	Drawn By:	Zhilei Xu	REV
A	Date:	20 November 2016	3

Dimensions in inches | SCALE: 1:15 | Material: Al (HC) | Quantity: 2 | SHEET 10 OF 12

5 4 3 2 1

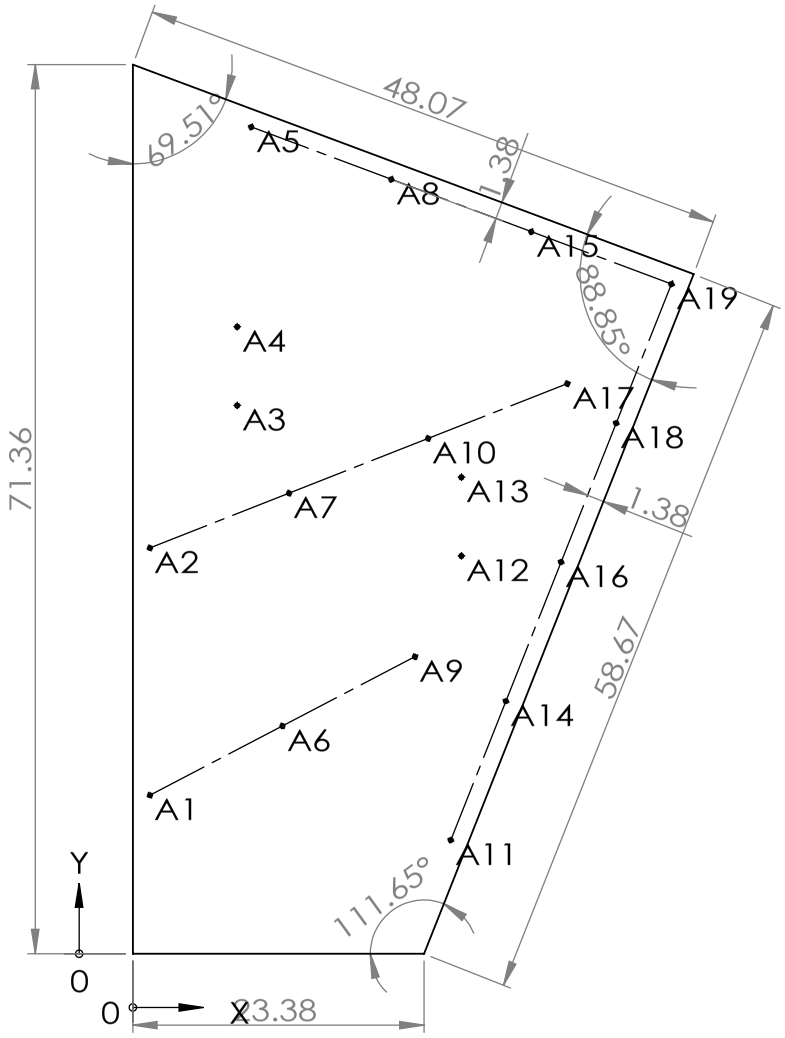

Project:	CLASS			
Assembly:	Panels			
TITLE:	Side Panel 3			
SIZE A	Drawn By: Zhilei Xu			REV 3
	Date: 20 November 2016			
Dimensions in inches	SCALE: 1:15	Material: Al (HC)	Quantity: 2	SHEET 11 OF 12

5 4 3 2 1

TAG	XLOC	YLOC	SIZE
A1	1.38	12.72	∅0.33 THRU
A2	1.38	32.57	∅0.33 THRU
A3	8.38	44.00	∅0.33 THRU
A4	8.38	50.31	∅0.33 THRU
A5	9.51	66.34	∅0.33 THRU
A6	12.01	18.28	∅0.33 THRU
A7	12.54	36.96	∅0.33 THRU
A8	20.75	62.14	∅0.33 THRU
A9	22.64	23.84	∅0.33 THRU
A10	23.71	41.35	∅0.33 THRU
A11	25.52	9.12	∅0.33 THRU
A12	26.38	31.93	∅0.33 THRU
A13	26.38	38.24	∅0.33 THRU
A14	29.95	20.28	∅0.33 THRU
A15	31.99	57.94	∅0.33 THRU
A16	34.37	31.43	∅0.33 THRU
A17	34.88	45.75	∅0.33 THRU
A18	38.80	42.58	∅0.33 THRU
A19	43.23	53.74	∅0.33 THRU

Project:	CLASS		
Assembly:	Panels		
TITLE:	Side Panel 3 Table		
SIZE A	Drawn By: Zhilei Xu		REV 3
	Date: 20 November 2016		
Dimensions in inches	SCALE: 1:15	Material: Al (HC)	Quantity: 2	SHEET 12 OF 12

5 4 3 2 1

Appendix D

Cable Wraps

As introduced in Chapter 4, the CLASS telescopes have three rotation axes. The cryogenic receiver rotates about the three axes while its auxiliary equipment (such as pulse-tube compressor, gas handling system, etc.) sits on the azimuth platform, which only rotates about the azimuth axis. Therefore, a cable wrap system needs to be designed to safely guide the vacuum hoses through rotations about another two axes (elevation and boresight). This work was mainly done by Joseph Eimer and Lucas Parker.

The cable wrap system is separated into two parts: a boresight cable wrap and an elevation cable wrap. Each of them handles a rotation about one axis.

The schematic diagram of boresight cable wrap is presented in Figure D.1. The traveling end is connected to the cable wrap tray introduced in Section 4.3. The cable tray is installed on the turbo station that rotates with the cryogenic receiver about the

boresight axis. The fixed end is installed to the boresight bearing plate which does not have boresight rotation. As the traveling end moves, the boresight cable wrap bundles the cables and hoses. They extend or retreat in a guided configuration. The cable wrap shape transformation during boresight rotation is controlled by other auxiliary structures. During rotation, the cable wrap keeps a large enough turning radius so that even the 2-inch diameter metal vacuum hoses have no difficulty wrapping around.

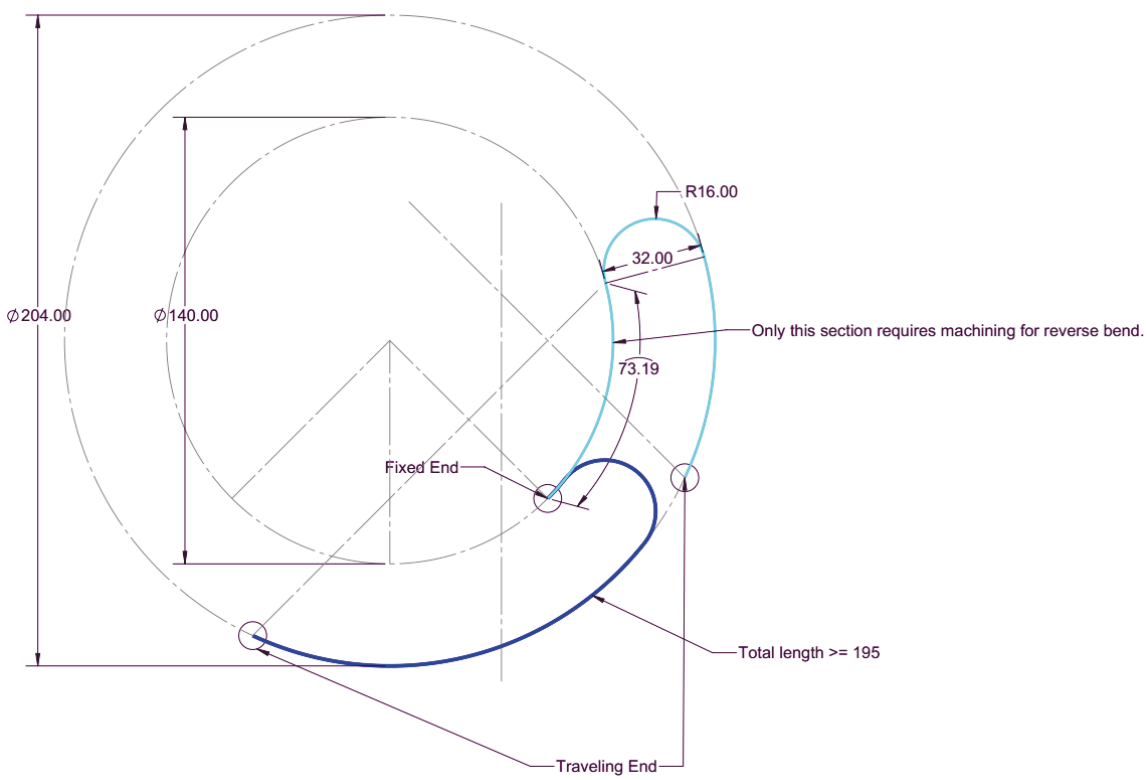

Figure D.1: Boresight cable wrap schematic diagram. Looking from the top, two colored curves shown the cable wrap configuration at two extreme boresight angles: -45° and 45°. The fixed end is installed at the boresight bearing plate while the traveling end travels with the above telescope. Some dimensions (in inches) are also pointed out in this figure. Figure credits: Joseph Eimer.

Renderings of the boresight cable wrap at different angles are presented in Figure

D.2. The boresight cable wrap handles the boresight rotation. Starting from the boresight cable wrap fixed end, the elevation cable wrap starts again repeating the same philosophy.

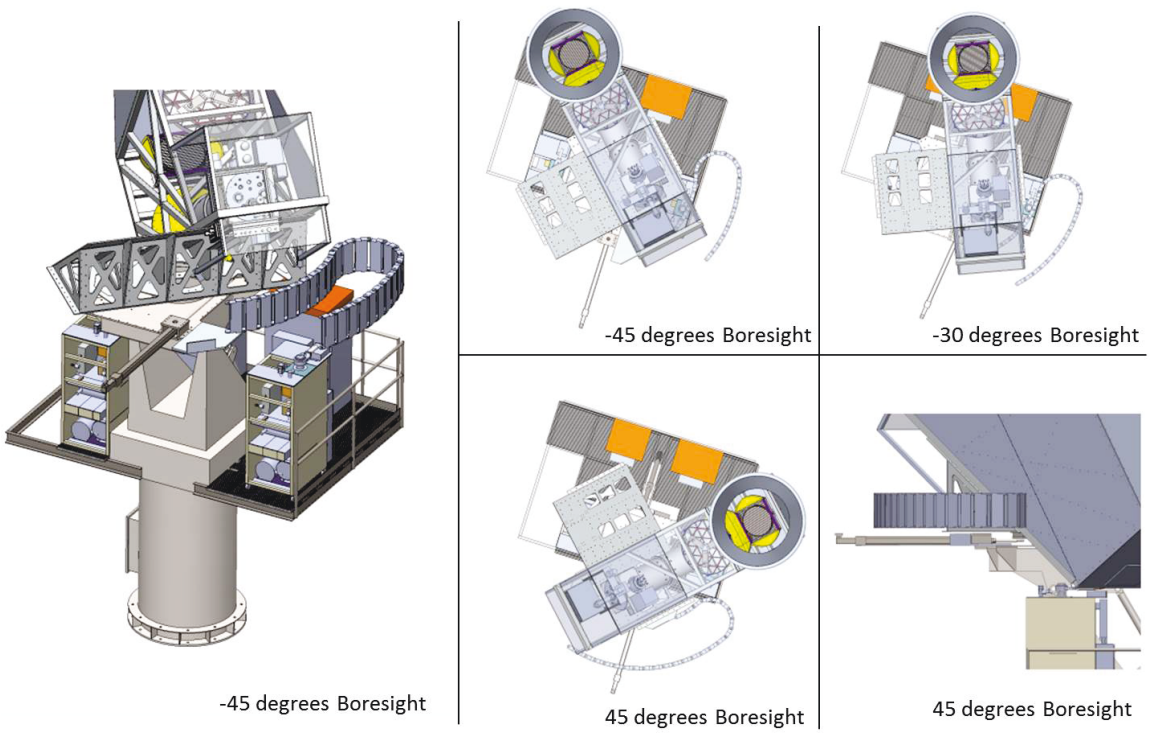

Figure D.2: Boresight cable wrap at different boresight angles. Each picture shows the boresight cable wrap in one configuration from a certain perspective. Figure credits: Joseph Eimer

The elevation cable wrap picks up where the boresight cable wrap ends. A schematic side view is presented in Figure D.3. Two extreme configurations are shown in the figure. One is at 90° elevation angle when the elevation platform is horizontal, while the other one is at 20° elevation angle when the elevation platform is rotated 70° counterclockwise. At these two positions, the elevation cable wrap configuration is shown in two curves. This cable wrap bundles the hoses and cables together and

bends them in a controlled way so that the rotation can be safely performed across the designed range.

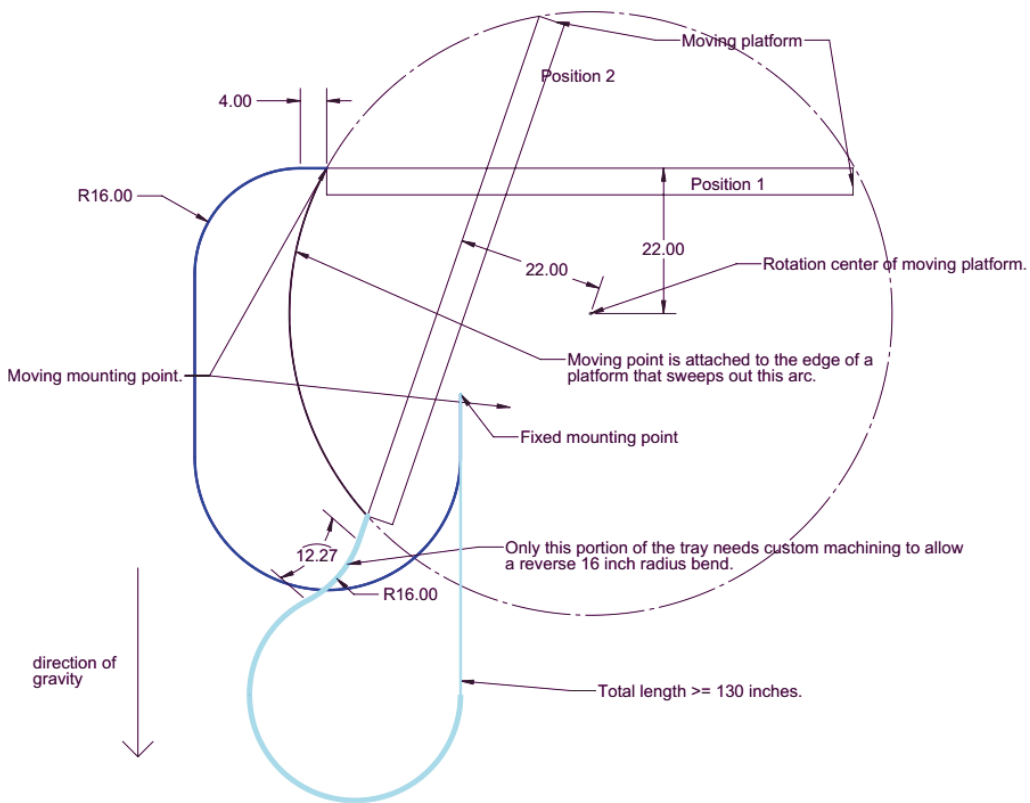

Figure D.3: Elevation cable wrap schematic diagram. Looking from the side, two colored curves shown the cable wrap configuration at two extreme boresight angles: 20° and 90°. The fixed end is installed at the azimuth platform while the traveling end travels with the boresight bearing plate. Some dimensions (in inches) are also pointed out in this figure. Figure credits: Joseph Eimer

The elevation cable wrap is presented at two extreme elevation angles with different perspectives in Figure D.4. The elevation cable wrap further handles the rotation about the elevation axis. Thanks to the boresight cable wrap and the elevation cable wrap, equipment on the azimuth platform can be safely connected to the cryogenic receiver.

Since the boresight cable wrap is also shown in Figure D.4, this figure provides an overall picture of the two-step CLASS cable wrap system.

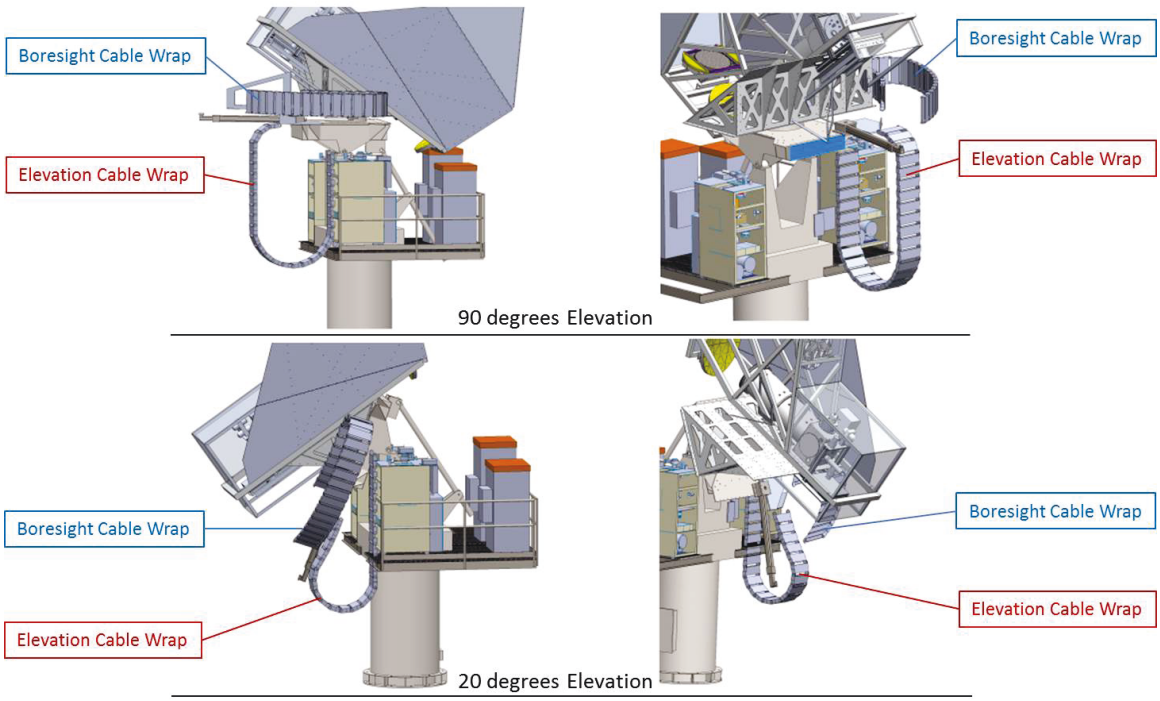

Figure D.4: Elevation cable wrap at different elevation angles. Top two figures show the elevation cable (pointed out by red texts) wrap at 90° elevation angle from two perspectives; bottom two figures show that at 20° elevation angle from two perspectives. The boresight cable wrap (pointed out in blue texts) is also shown in the figures at 0 boresight angle. Figure credits: Joseph Eimer

The cable wrap system has been successfully operating for more than one year. It provides automatic smooth transitions between different telescope configurations.

Appendix E

Adjustment Stages

Drawings for the adjustment stages for both mirrors and the VPM are presented here. The drawings are the 'vanilla' version. Assuming the warm-optics cage manufacturing is exactly accurate, the 'vanilla' version adjustment stages put the optics right in place at the middle of the adjustment range.

In reality, warm-optics cage manufacturing cannot be exactly accurate. The adjustment stages are designed to absorb twice the allowed warm-optics cage tolerance. Therefore, as long as the tolerance on the warm-optics cages is held, the adjustment stages can put the optical components back into position. If the tolerance is not held and is exceeded by more than twice the nominal value, modifications can be made on the adjustment stage hardware to shift the adjustment range.

The attached drawings are organized in the order of the primary mirror adjustment stage, the secondary mirror adjustment stage, and the VPM adjustment stage.

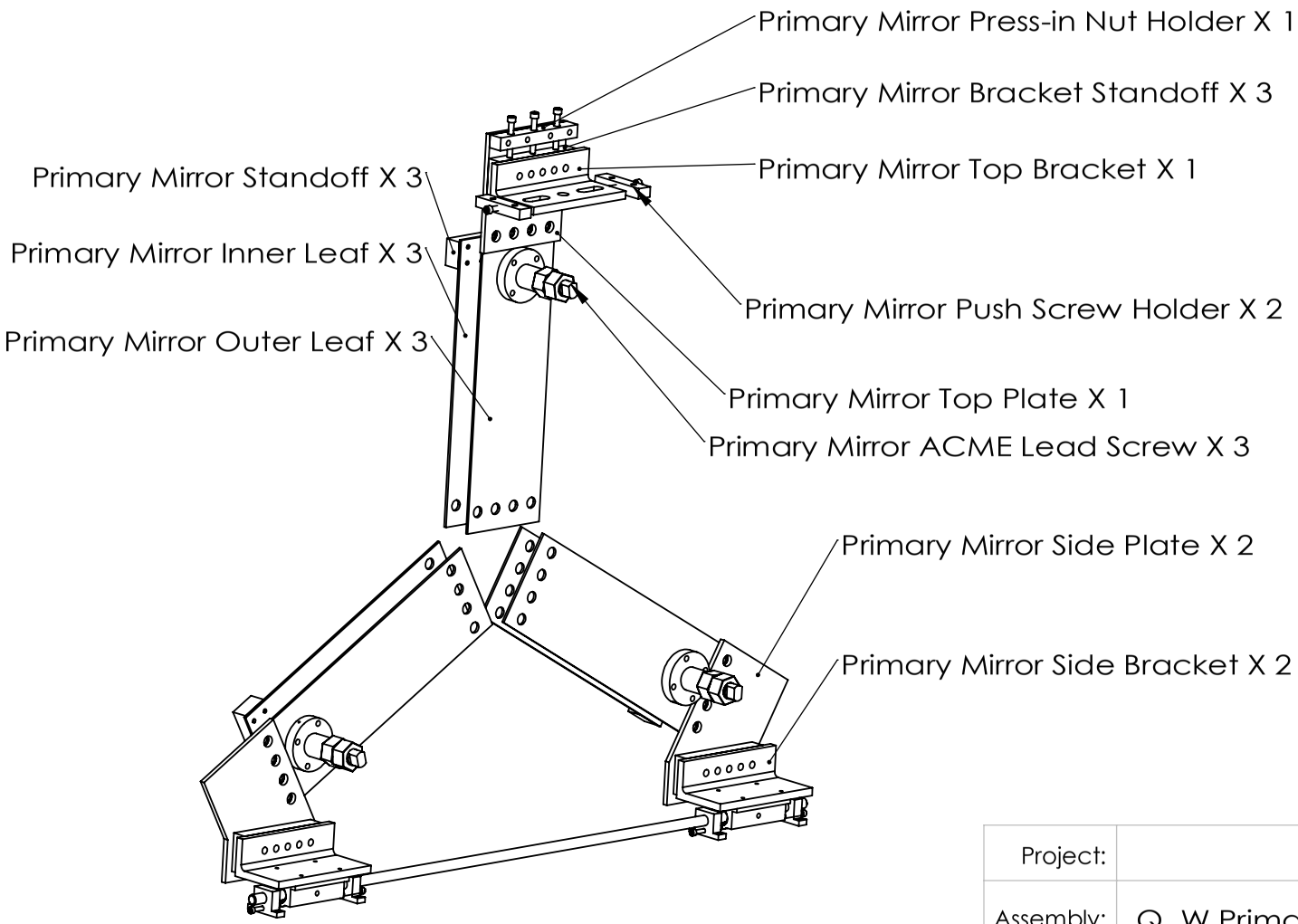

Dimensions with two decimal digits requires tolerance of +- 0.01"
Dimensions with three decimal digits requires tolerance of +- 0.005"

Project:	CLASS		
Assembly:	Q, W Primary Mirror Adjustment Stage		
TITLE:	Overview		
SIZE A	Drawn By: Zhilei Xu		REV 1
	Date: 21 Jun. 2017		
Dimensions in inches	SCALE: 1:8	Material:	Quantity: 2

5 4 3 2 1

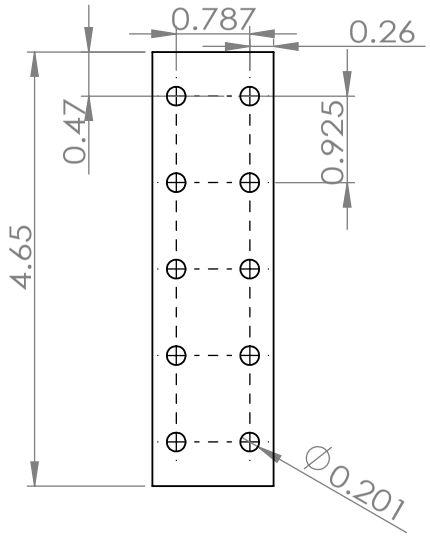

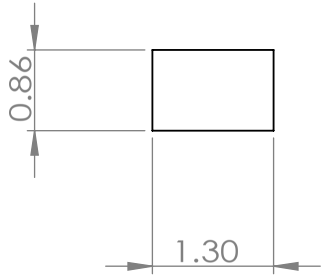

Project:	CLASS		
Assembly:	Q, W Primary Mirror Adjustment Stage		
TITLE:	Mirror Standoff		
SIZE A	Drawn By: Zhilei Xu		REV 1
	Date: 21 Jun. 2017		

Dimensions in inches	SCALE: 1:2	Material: Aluminum	Quantity: 3	SHEET 2 OF 12

5 4 3 2 1

Project:	CLASS			
Assembly:	Q,W Primary Mirror Adjsutment Stage			
TITLE:	Inner Leaf			
SIZE A	Drawn By: Zhilei Xu			REV 1
	Date: 21 June 2017			
Dimensions in inches	SCALE: 2	Material: 1095 Steel	Quantity: 3	SHEET 3 OF 12

5 4 3 2 1

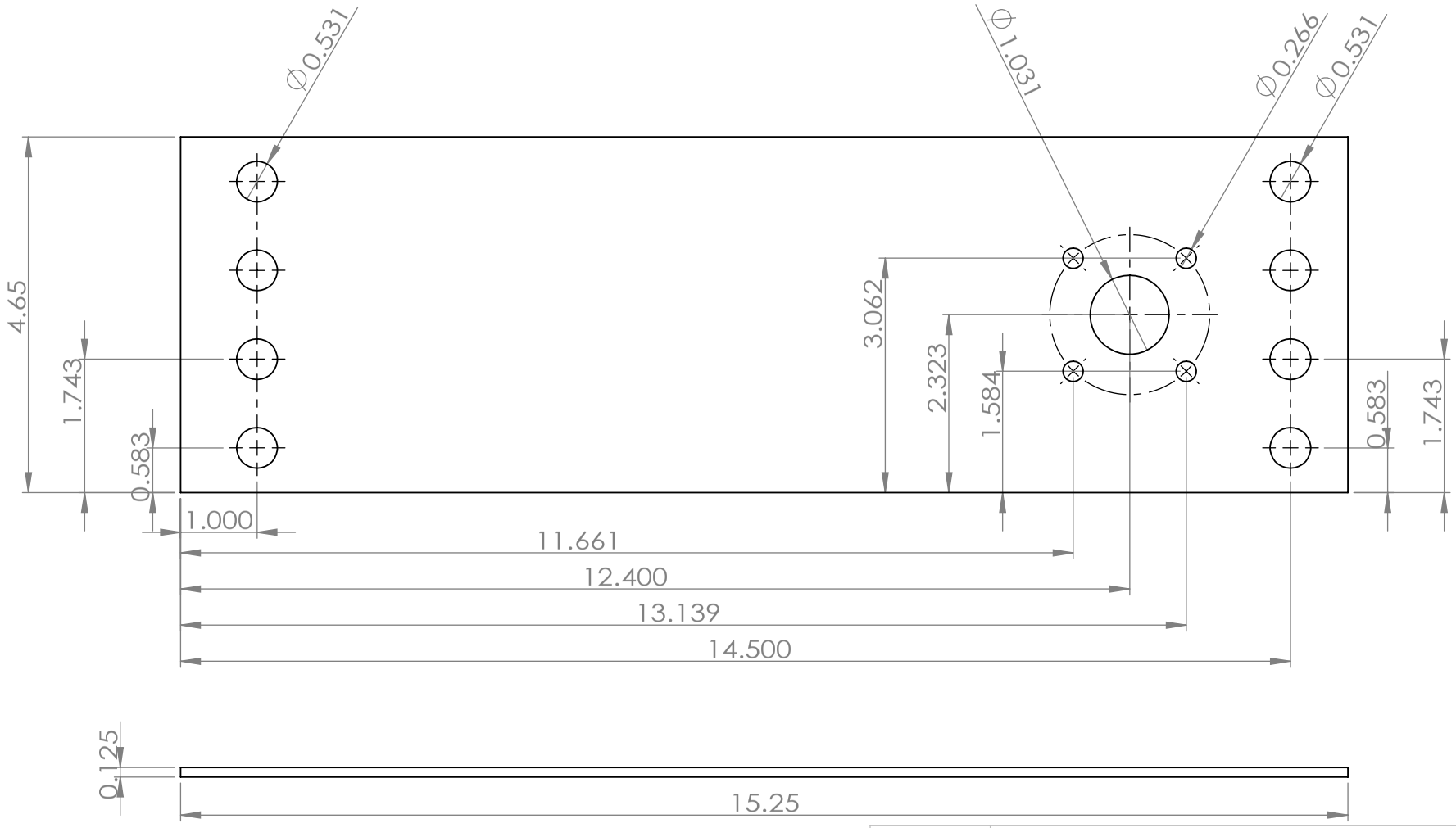

Project:	CLASS
Assembly:	Q,W Primary Mirror Adjsutment Stage
TITLE:	Outer Leaf

SIZE	Drawn By:	Zhilei Xu	REV
A	Date:	21 June 2017	1

Dimensions in inches	SCALE: 2	Material: 1095 Steel	Quantity: 3	SHEET 4 OF 12

5 4 3 2 1

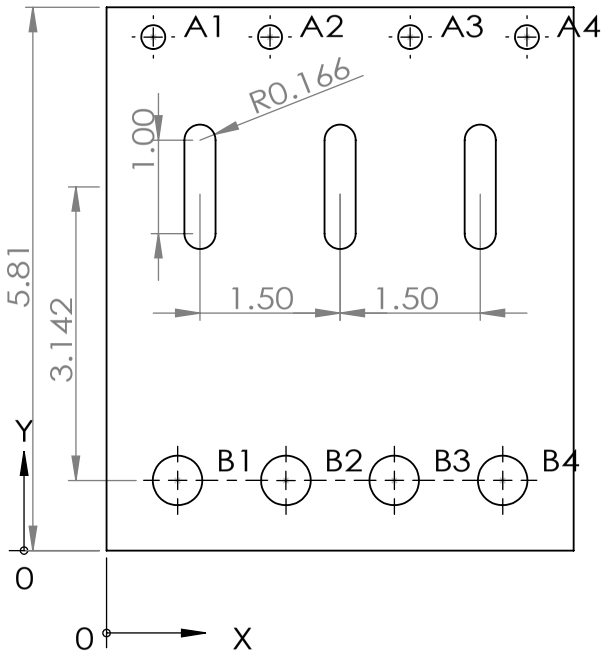

TAG	XLOC	YLOC	SIZE
A1	0.500	5.494	∅0.257 THRU
A2	1.750	5.494	∅0.257 THRU
A3	3.250	5.494	∅0.257 THRU
A4	4.500	5.494	∅0.257 THRU
B1	0.760	0.750	∅0.531 THRU
B2	1.920	0.750	∅0.531 THRU
B3	3.080	0.750	∅0.531 THRU
B4	4.240	0.750	∅0.531 THRU

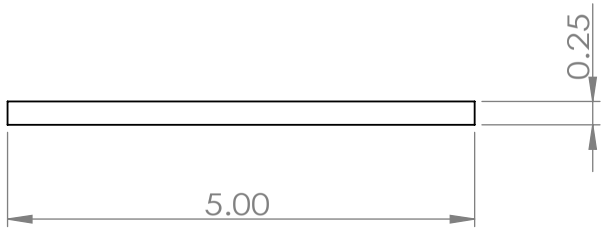

Project:	CLASS		
Assembly:	Q,W Primary Mirror Adjustment Stage		
TITLE:	Top Plate		
SIZE A	Drawn By: Zhilei Xu		REV 1
	Date: 21 Jun. 2017		

Dimensions in inches | SCALE: 1:2 | Material: Aluminum | Quantity: 1 | SHEET 5 OF 12

5 4 3 2 1

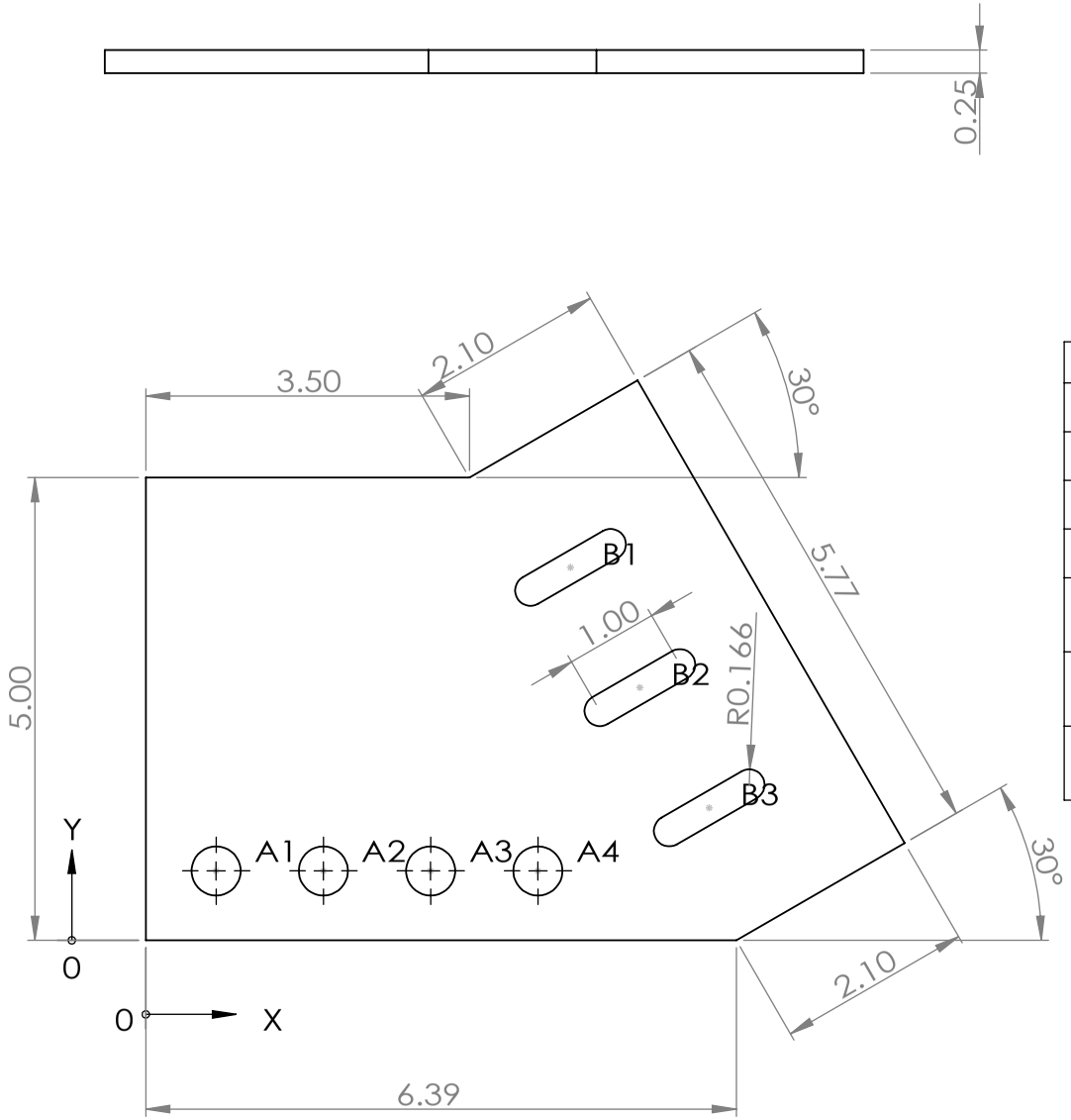

TAG	XLOC	YLOC	SIZE
A1	0.760	0.750	∅0.531 THRU
A2	1.920	0.750	∅0.531 THRU
A3	3.080	0.750	∅0.531 THRU
A4	4.240	0.750	∅0.531 THRU
B1	4.593	4.030	
B2	5.343	2.731	
B3	6.093	1.431	

Project:	CLASS
Assembly:	Q,W Primary Mirror Adjustment Stage
TITLE:	Side Plate

SIZE	Drawn By:	Zhilei Xu	REV
A	Date:	21 Jun. 2017	1

Dimensions in inches	SCALE: 1:2	Material: Aluminum	Quantity: 2	SHEET 6 OF 12

5 4 3 2 1

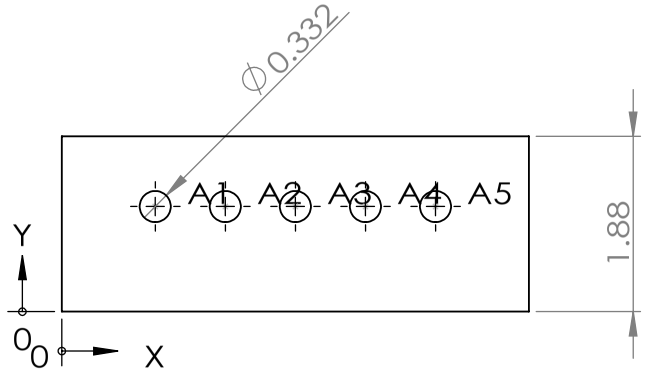

TAG	XLOC	YLOC	SIZE
A1	1.000	1.125	∅0.33 THRU
A2	1.750	1.125	∅0.33 THRU
A3	2.500	1.125	∅0.33 THRU
A4	3.250	1.125	∅0.33 THRU
A5	4.000	1.125	∅0.33 THRU

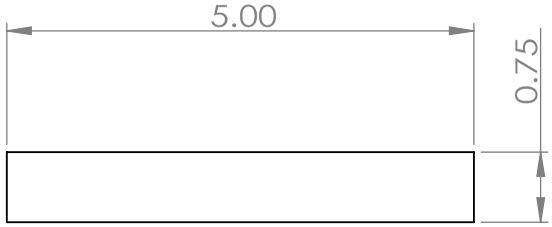

Project:	CLASS		
Assembly:	Q,W Primary Mirror Adjustment Stage		
TITLE:	Bracket Standoff		
SIZE A	Drawn By: Zhilei Xu		REV 1
	Date: 21 Jun. 2017		
Dimensions in inches	SCALE: 1:2	Material: Aluminum	Quantity: 3	SHEET 7 OF 12

5 4 3 2 1

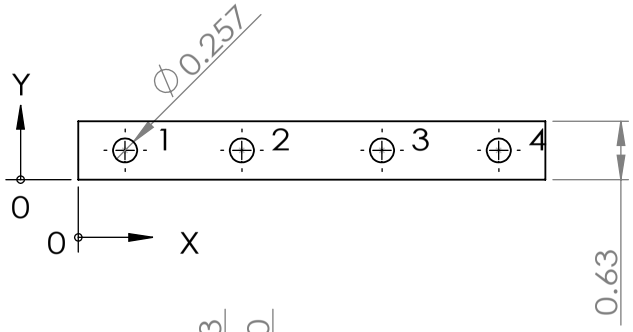

TAG	XLOC	YLOC	SIZE
1	0.500	0.313	∅0.26 THRU
2	1.750	0.313	∅0.26 THRU
3	3.250	0.313	∅0.26 THRU
4	4.500	0.313	∅0.26 THRU

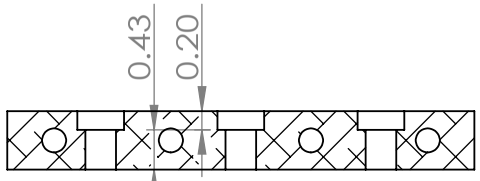

SECTION A-A

SCALE 1 : 2

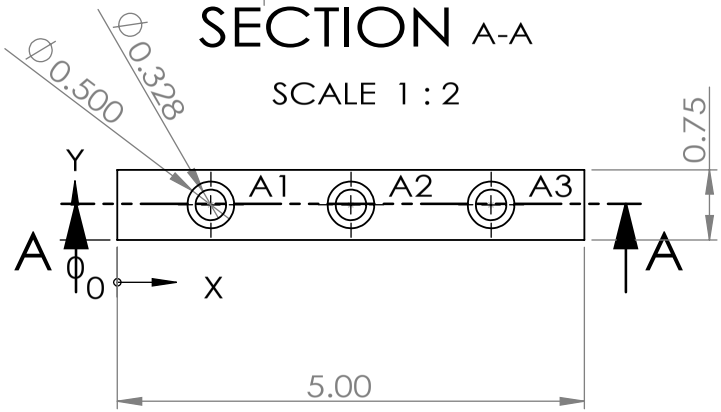

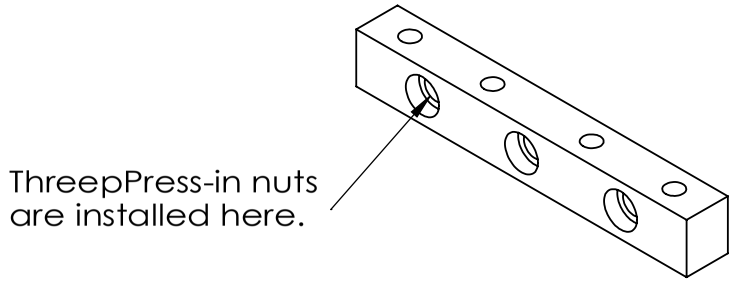

TAG	XLOC	YLOC	SIZE
A1	1.000	0.375	∅0.33 THRU ⌴ ∅0.50 ↧ 0.20
A2	2.500	0.375	∅0.33 THRU ⌴ ∅0.50 ↧ 0.20
A3	4.000	0.375	∅0.33 THRU ⌴ ∅0.50 ↧ 0.20

Project:	CLASS
Assembly:	Q,W Primary Mirror Adjustment Stage
TITLE:	Press-in Nut Holder
SIZE A	Drawn By: Zhilei Xu
	Date: 21 Jun. 2017
REV	1

Dimensions in inches | SCALE: 1:2 | Material: Aluminum | Quantity: 1 | SHEET 8 OF 12

5 4 3 2 1

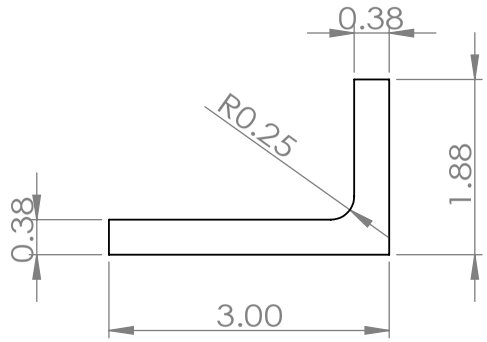

TAG	XLOC	YLOC	SIZE
A1	1.125	1.500	∅0.33 THRU
A2	1.125	2.250	∅0.33 THRU
A3	1.125	3.000	∅0.33 THRU
A4	1.125	3.750	∅0.33 THRU
A5	1.125	4.500	∅0.33 THRU

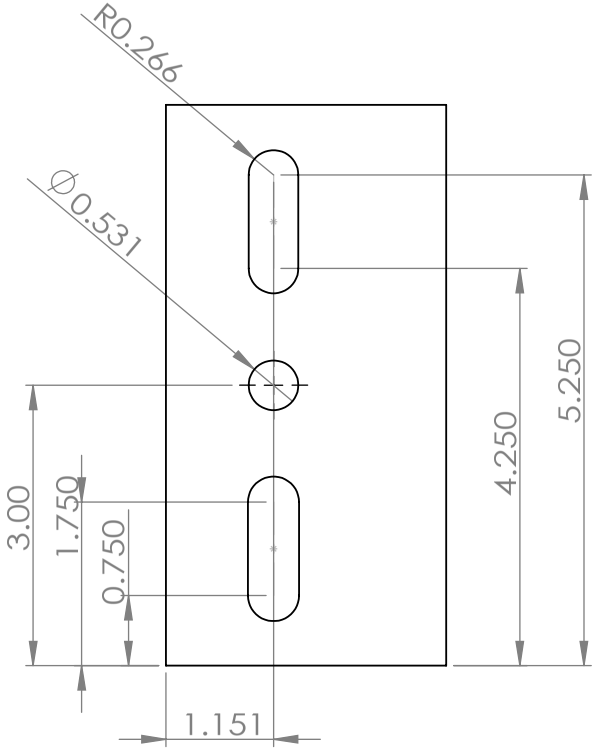

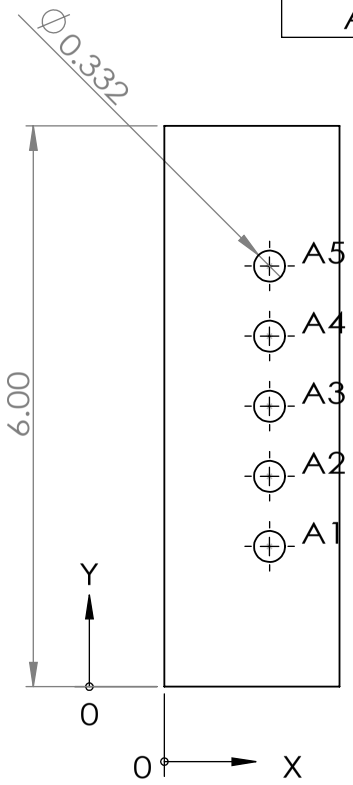

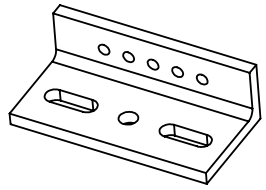

Project:	CLASS		
Assembly:	Q,W Primary Mirror Adjustment Stage		
TITLE:	Top Bracket		
SIZE A	Drawn By: Zhilei Xu		REV 1
	Date: 21 Jun. 2017		
Dimensions in inches	SCALE: 1:2	Material: Aluminum	Quantity: 1	SHEET 9 OF 12

5 4 3 2 1

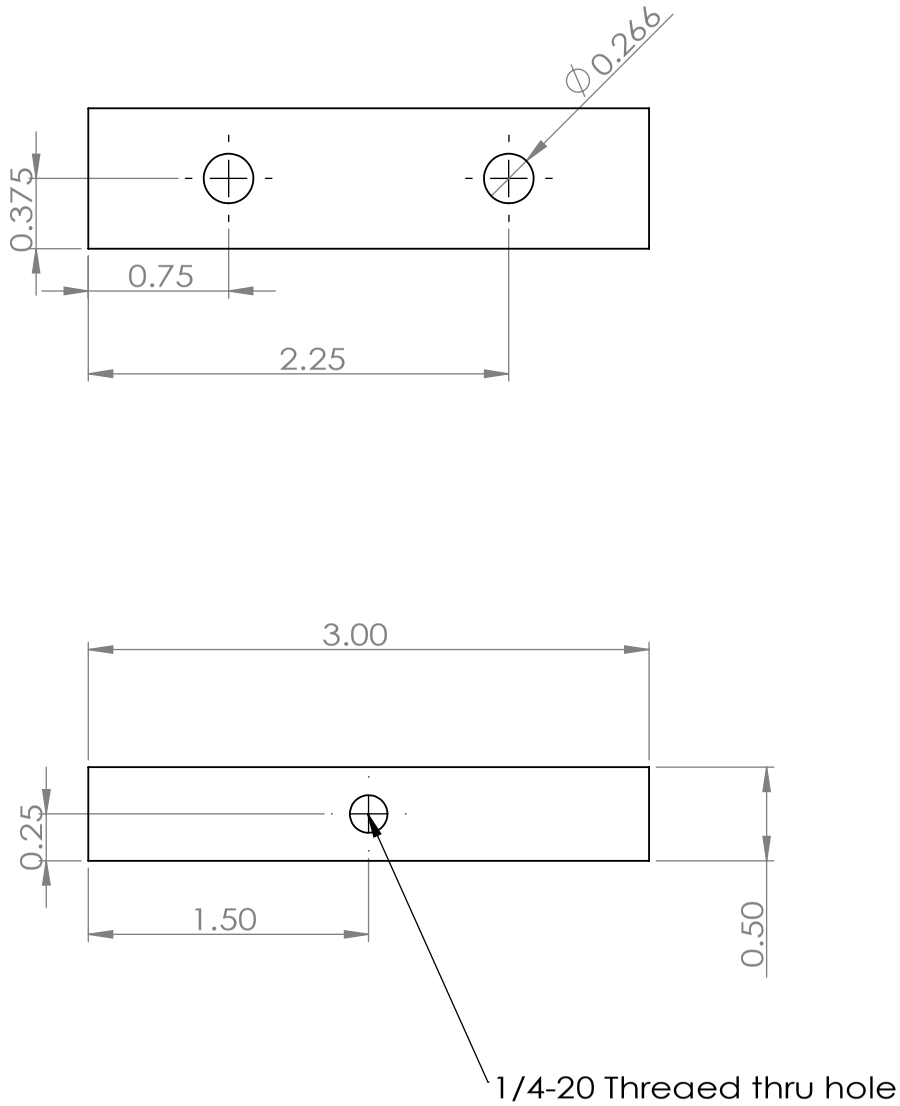

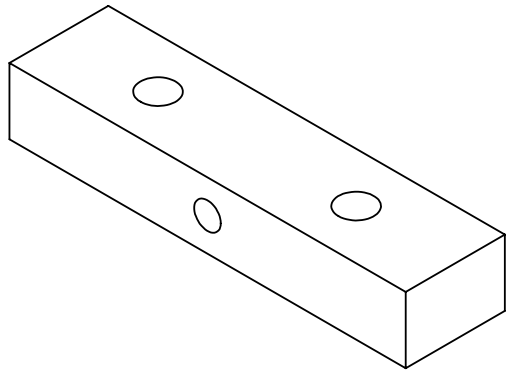

Project:	CLASS		
Assembly:	Q, W Primary Mirror Adjustment Stages		
TITLE:	Push Screw Holder		
SIZE A	Drawn By: Zhilei Xu		REV 1
	Date: 21 Jun. 2017		

Dimensions in inches	SCALE: 1:1	Material: Aluminum	Quantity: 2	SHEET 10 OF 12

5 4 3 2 1

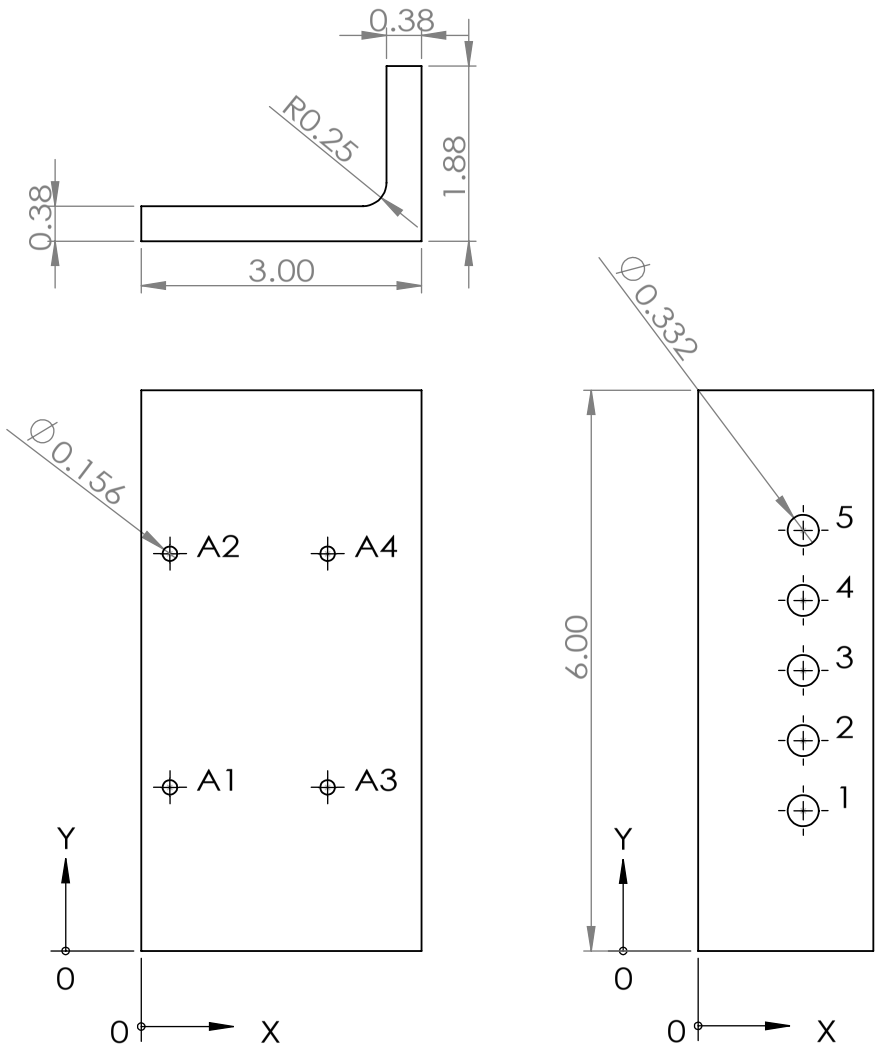

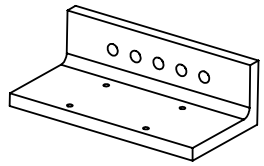

TAG	XLOC	YLOC	SIZE
1	1.125	1.500	∅0.33 THRU
2	1.125	2.250	∅0.33 THRU
3	1.125	3.000	∅0.33 THRU
4	1.125	3.750	∅0.33 THRU
5	1.125	4.500	∅0.33 THRU

TAG	XLOC	YLOC	SIZE
A1	0.307	1.750	∅0.16 THRU
A2	0.307	4.250	∅0.16 THRU
A3	1.995	1.750	∅0.16 THRU
A4	1.995	4.250	∅0.16 THRU

Project:	CLASS
Assembly:	Q,W Primary Mirror Adjustment Stage
TITLE:	Side Bracket
SIZE A	Drawn By: Zhilei Xu
	Date: 21 Jun. 2017
REV	1

Dimensions in inches | SCALE: 1:2 | Material: Aluminum | Quantity: 2 | SHEET 11 OF 12

5 4 3 2 1

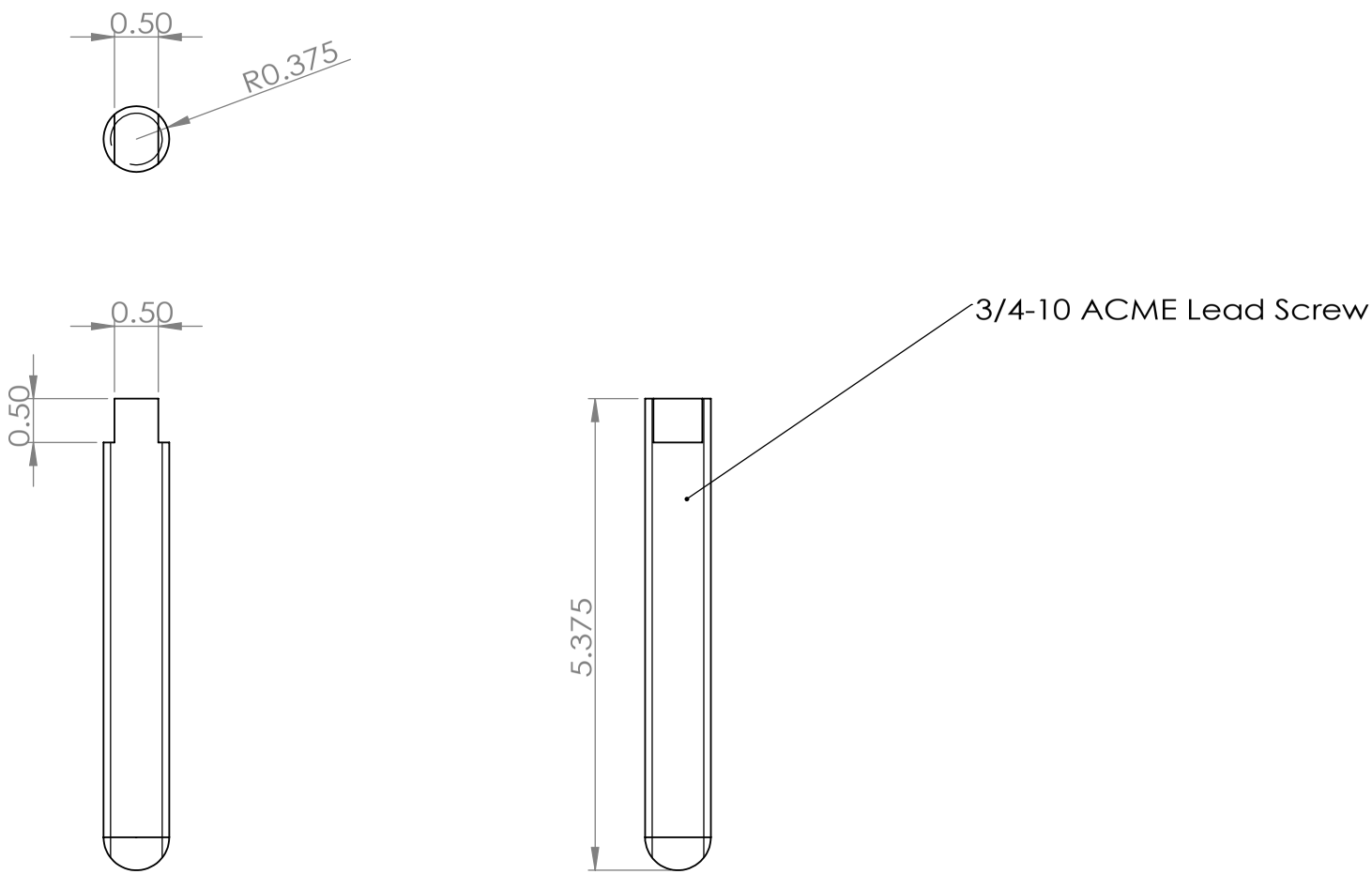

Project:	CLASS
Assembly:	Q, W Primary Mirror Adjustment Stages
TITLE:	ACME Lead Screw

SIZE	Drawn By:	Zhilei Xu	REV
A	Date:	21 Jun. 2017	1

Dimensions in inches	SCALE: 1:2	Material: SS	Quantity: 3	SHEET 12 OF 12

5 4 3 2 1

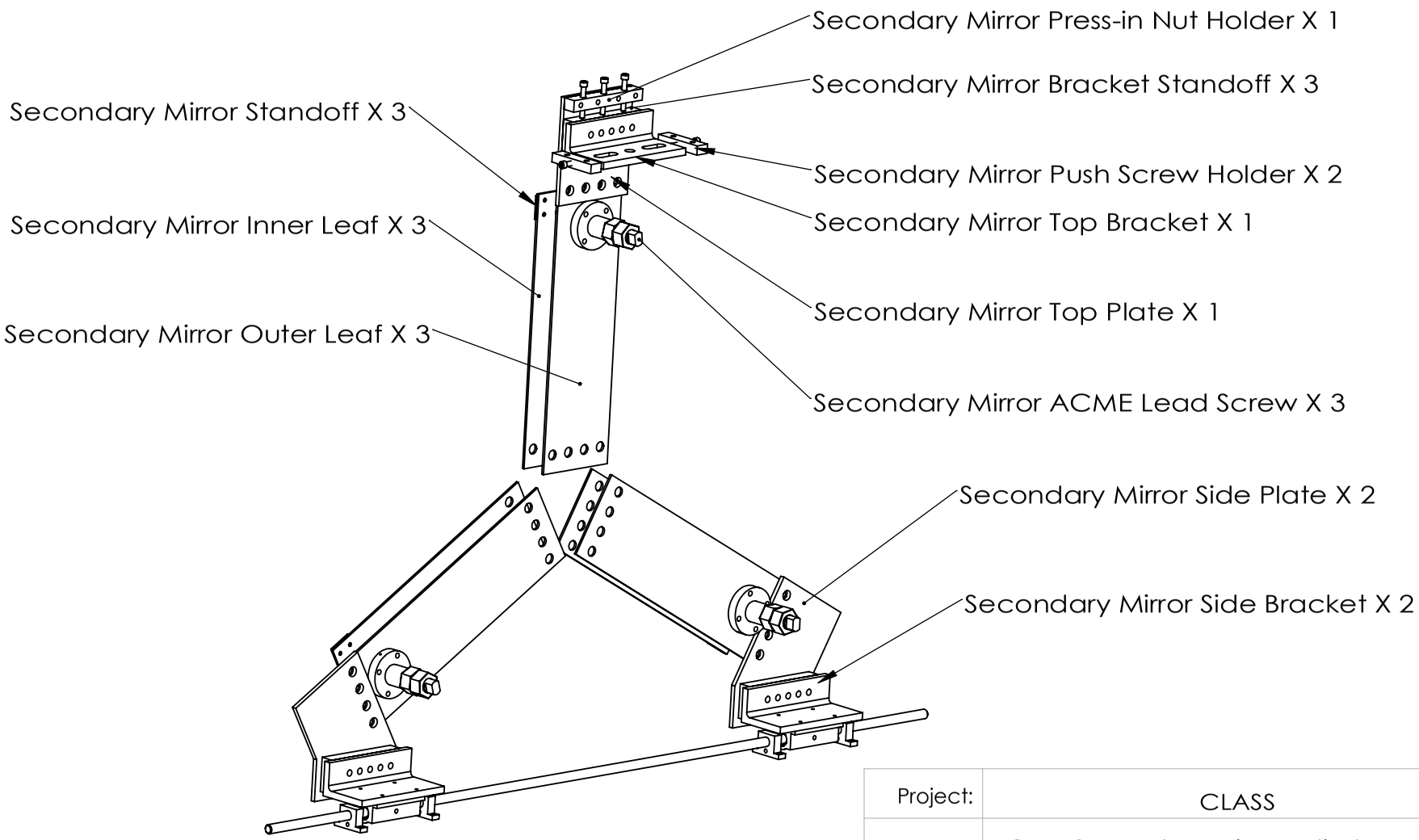

Dimensions with two decimal digits requires tolerance of +- 0.01"
Dimensions with three decimal digits requires tolerance of +- 0.005"

Project:	CLASS		
Assembly:	Q, W Secondary Mirror Adjustment Stage		
TITLE:	Overview		
SIZE A	Drawn By: Zhilei Xu		REV 1
	Date: 21 Jun. 2017		

Dimensions in inches	SCALE: 1:8	Material:	Quantity: 2	SHEET 1 OF 12

5 4 3 2 1

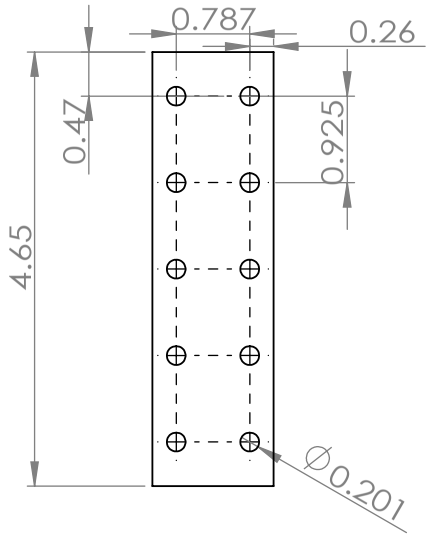

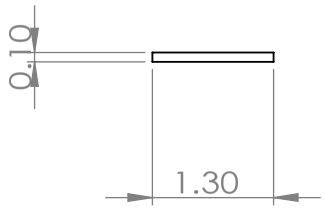

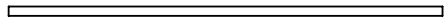

Project:	CLASS		
Assembly:	Q, W Secondary Mirror Adjustment Stage		
TITLE:	Mirror Standoff		
SIZE A	Drawn By: Zhilei Xu		REV 1
	Date: 21 Jun. 2017		

Dimensions in inches	SCALE: 1:2	Material: Aluminum	Quantity: 3	SHEET 2 OF 12

5 4 3 2 1

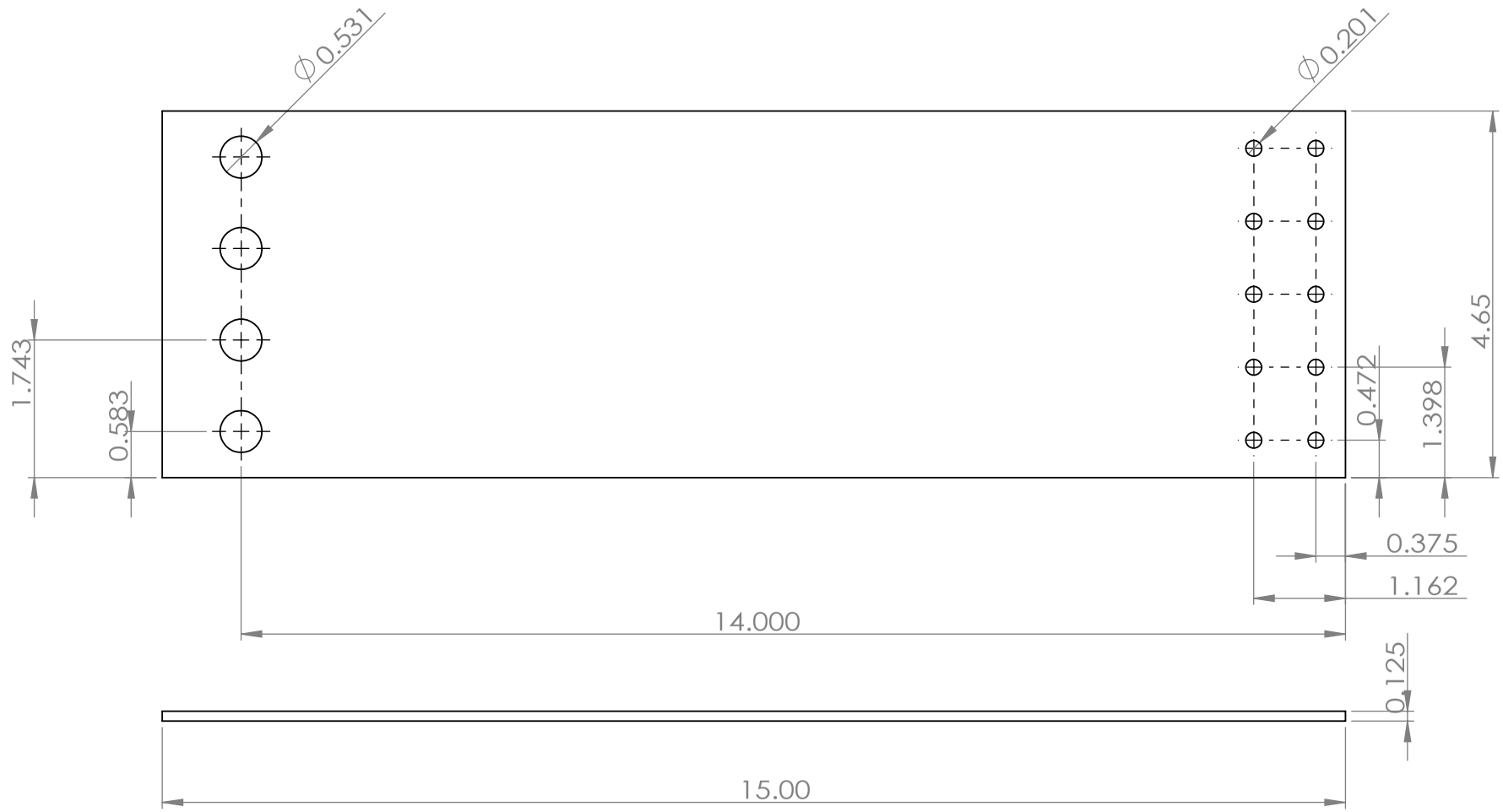

Project:	CLASS			
Assembly:	Q,W Primary Mirror Adjsutment Stage			
TITLE:	Inner Leaf			
SIZE A	Drawn By: Zhilei Xu			REV 1
	Date: 21 June 2017			
Dimensions in inches	SCALE: 2	Material: 1095 Steel	Quantity: 3	SHEET 3 OF 12

5 4 3 2 1

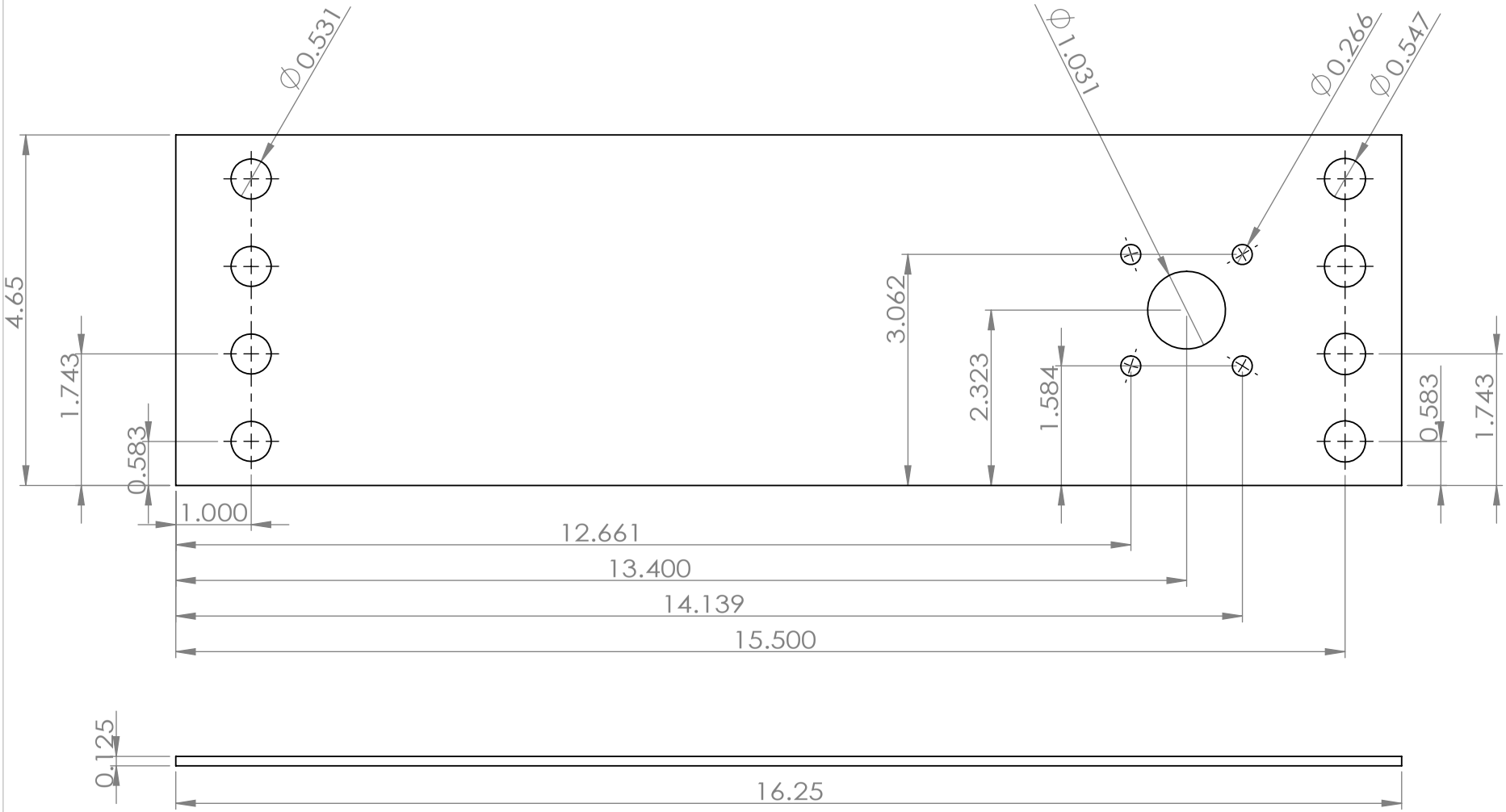

Project:	CLASS			
Assembly:	Q, W Secondary Mirror Adjustment Stage			
TITLE:	Outer Leaf			
SIZE A	Drawn By: Zhilei Xu			REV 1
	Date: 21 June 2017			
Dimensions in inches	SCALE: 2	Material: 1095 Steel	Quantity: 3	SHEET 4 OF 12

5 4 3 2 1

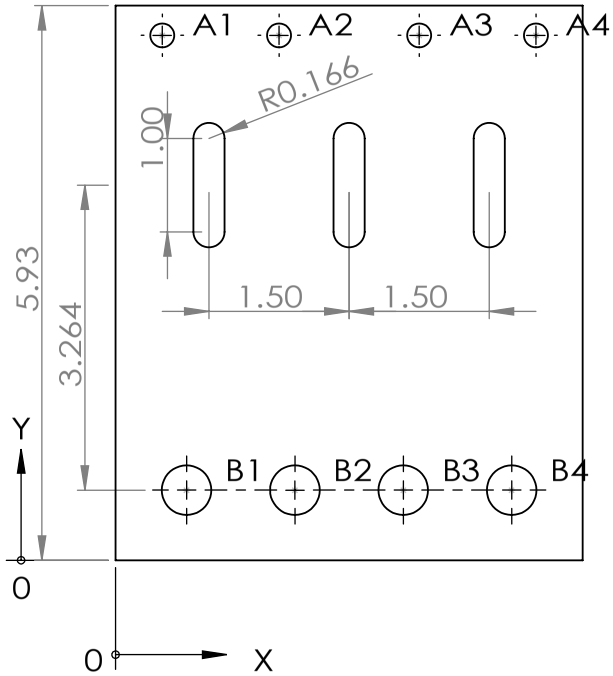

TAG	XLOC	YLOC	SIZE
A1	0.500	5.616	∅0.26 THRU
A2	1.750	5.616	∅0.26 THRU
A3	3.250	5.616	∅0.26 THRU
A4	4.500	5.616	∅0.26 THRU
B1	0.760	0.750	∅0.53 THRU
B2	1.920	0.750	∅0.53 THRU
B3	3.080	0.750	∅0.53 THRU
B4	4.240	0.750	∅0.53 THRU

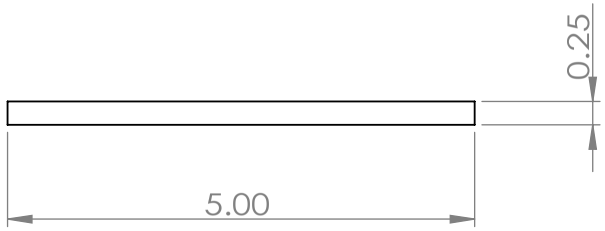

Project:	CLASS		
Assembly:	Q, W Secondary Mirror Adjustment Stage		
TITLE:	Top Plate		
SIZE A	Drawn By: Zhilei Xu		REV 1
	Date: 21 Jun. 2017		
Dimensions in inches	SCALE: 1:2	Material: Aluminum	Quantity: 1	SHEET 5 OF 12

5 4 3 2 1

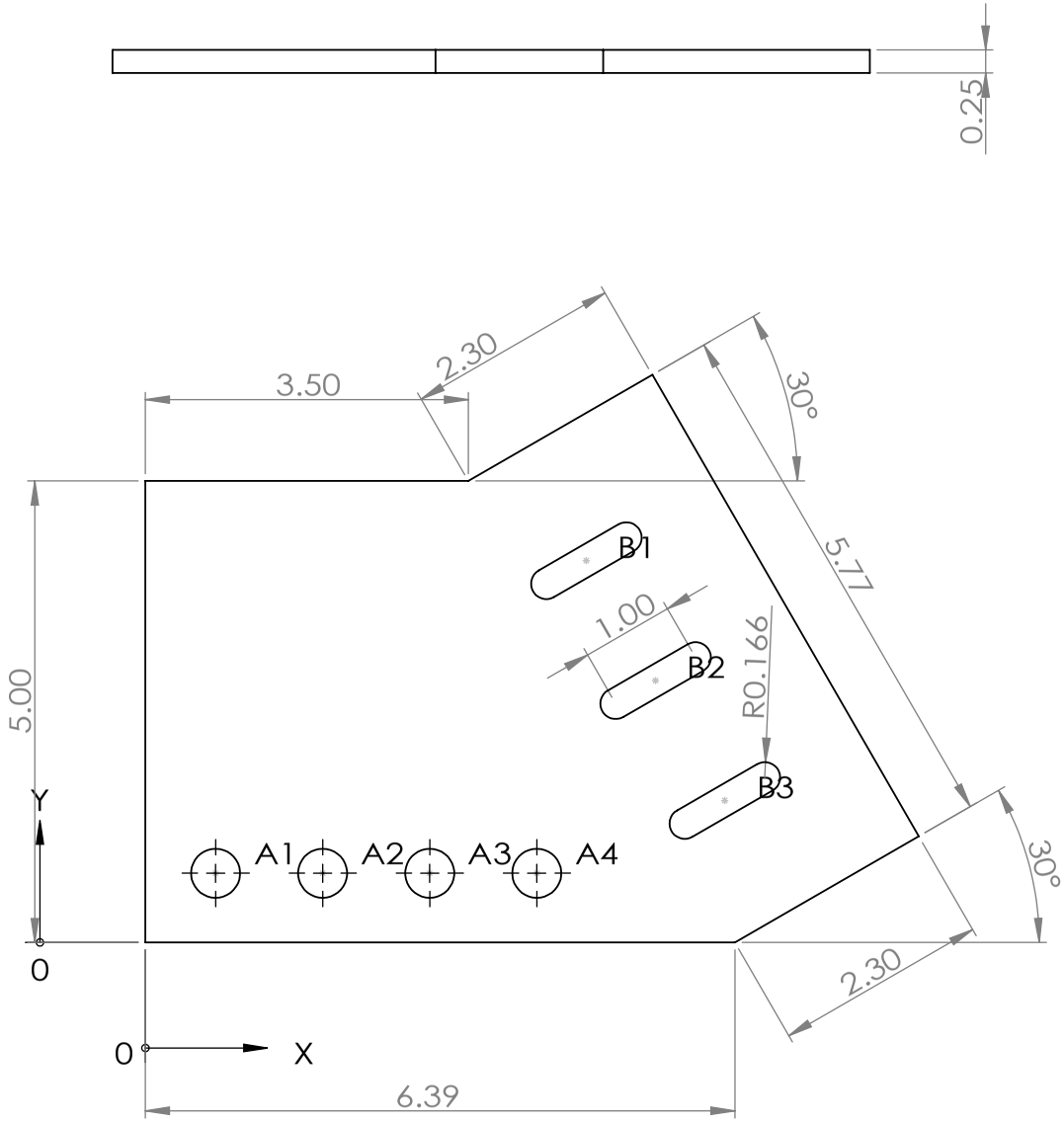

TAG	XLOC	YLOC	SIZE
A1	0.760	0.750	∅0.53 THRU
A2	1.920	0.750	∅0.53 THRU
A3	3.080	0.750	∅0.53 THRU
A4	4.240	0.750	∅0.53 THRU
B1	4.777	4.136	0.33 X 1.33
B2	5.527	2.837	0.33 X 1.33
B3	6.277	1.538	0.33 X 1.33

Project:	CLASS		
Assembly:	Q, W Secondary Mirror Adjustment Stage		
TITLE:	Side Plate		
SIZE A	Drawn By: Zhilei Xu		REV 1
	Date: 21 Jun. 2017		
Dimensions in inches	SCALE: 1:2	Material: Aluminum	Quantity: 2	SHEET 6 OF 12

5 4 3 2 1

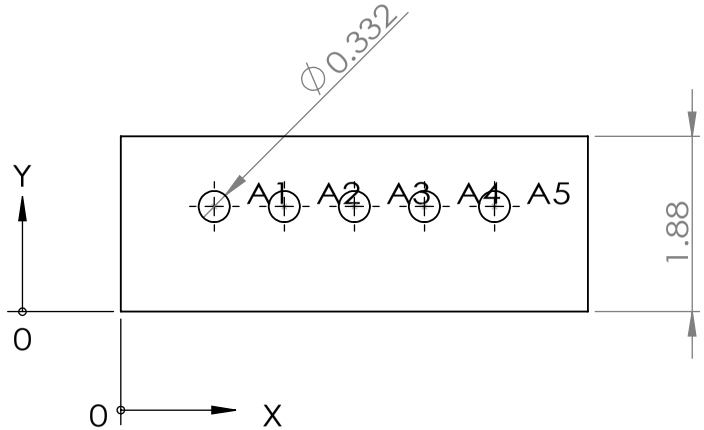

TAG	XLOC	YLOC	SIZE
A1	1.000	1.125	∅0.33 THRU
A2	1.750	1.125	∅0.33 THRU
A3	2.500	1.125	∅0.33 THRU
A4	3.250	1.125	∅0.33 THRU
A5	4.000	1.125	∅0.33 THRU

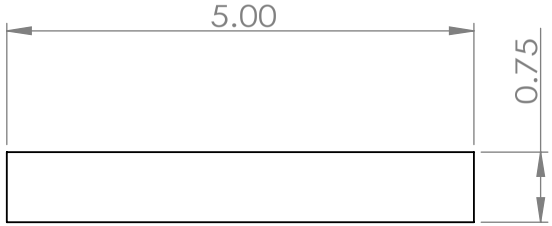

Project:	CLASS
Assembly:	Q, W Secondary Mirror Adjustment Stage
TITLE:	Bracket Standoff
SIZE A	Drawn By: Zhilei Xu
	Date: 21 Jun. 2017
REV	1

Dimensions in inches | SCALE: 1:2 | Material: Aluminum | Quantity: 3 | SHEET 7 OF 12

5 4 3 2 1

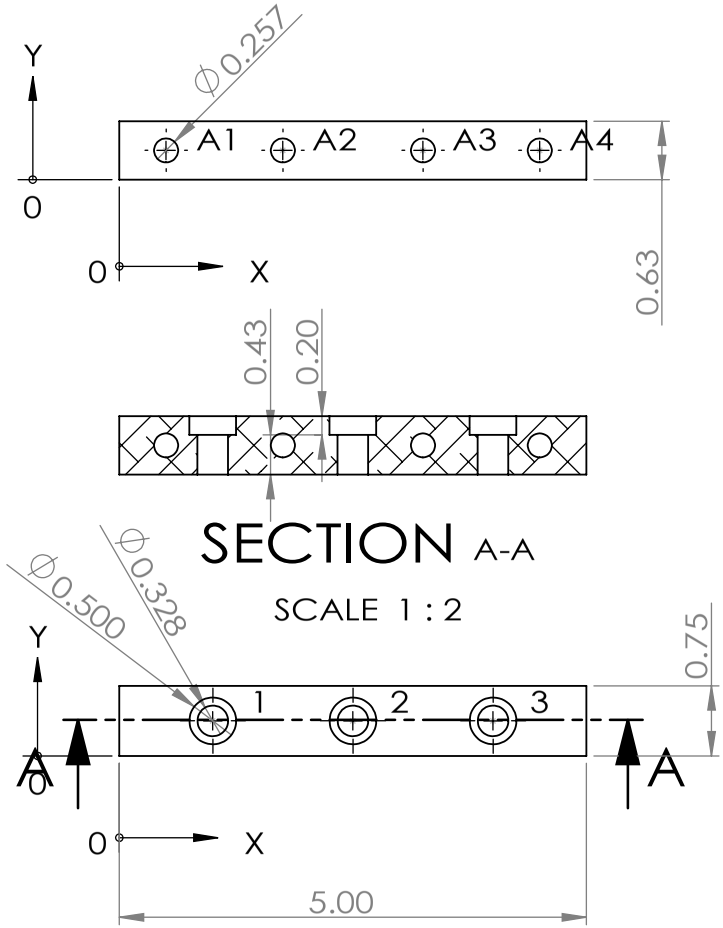

TAG	XLOC	YLOC	SIZE
A1	0.500	0.313	∅0.26 THRU
A2	1.750	0.313	∅0.26 THRU
A3	3.250	0.313	∅0.26 THRU
A4	4.500	0.313	∅0.26 THRU

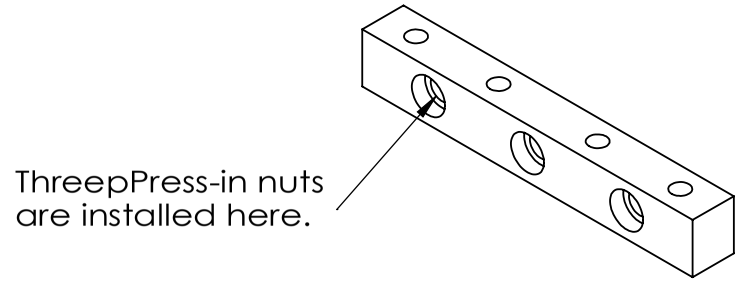

TAG	XLOC	YLOC	SIZE
1	1.000	0.375	∅0.33 THRU ⌴ ∅0.50 ↧ 0.20
2	2.500	0.375	∅0.33 THRU ⌴ ∅0.50 ↧ 0.20
3	4.000	0.375	∅0.33 THRU ⌴ ∅0.50 ↧ 0.20

Project:	CLASS
Assembly:	Q, W Secondary Mirror Adjustment Stage
TITLE:	Press-in Nut Holder
SIZE A	Drawn By: Zhilei Xu
	Date: 21 Jun. 2017
REV	1

Dimensions in inches | SCALE: 1:2 | Material: Aluminum | Quantity: 1 | SHEET 8 OF 12

5 4 3 2 1

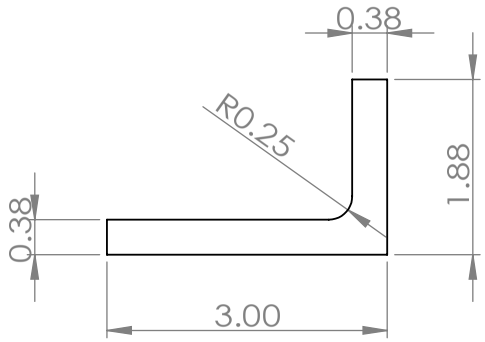

TAG	XLOC	YLOC	SIZE
A1	1.125	1.500	∅0.33 THRU
A2	1.125	2.250	∅0.33 THRU
A3	1.125	3.000	∅0.33 THRU
A4	1.125	3.750	∅0.33 THRU
A5	1.125	4.500	∅0.33 THRU

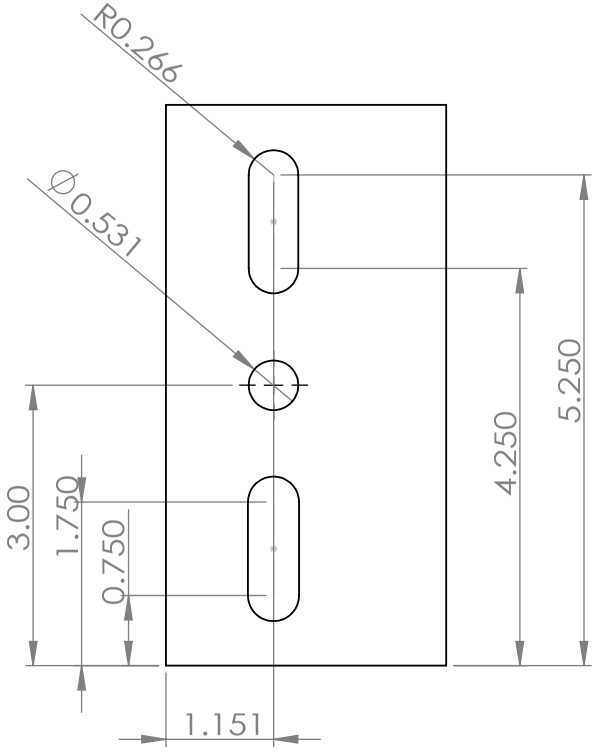

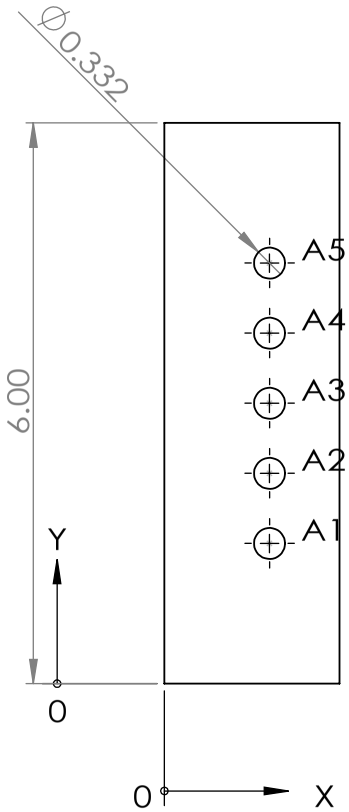

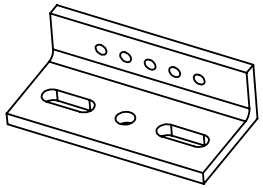

Project:	CLASS		
Assembly:	Q, W Secondary Mirror Adjustment Stage		
TITLE:	Top Bracket		
SIZE A	Drawn By: Zhilei Xu		REV 1
	Date: 21 Jun. 2017		

Dimensions in inches | SCALE: 1:2 | Material: Aluminum | Quantity: 1 | SHEET 9 OF 12

5 4 3 2 1

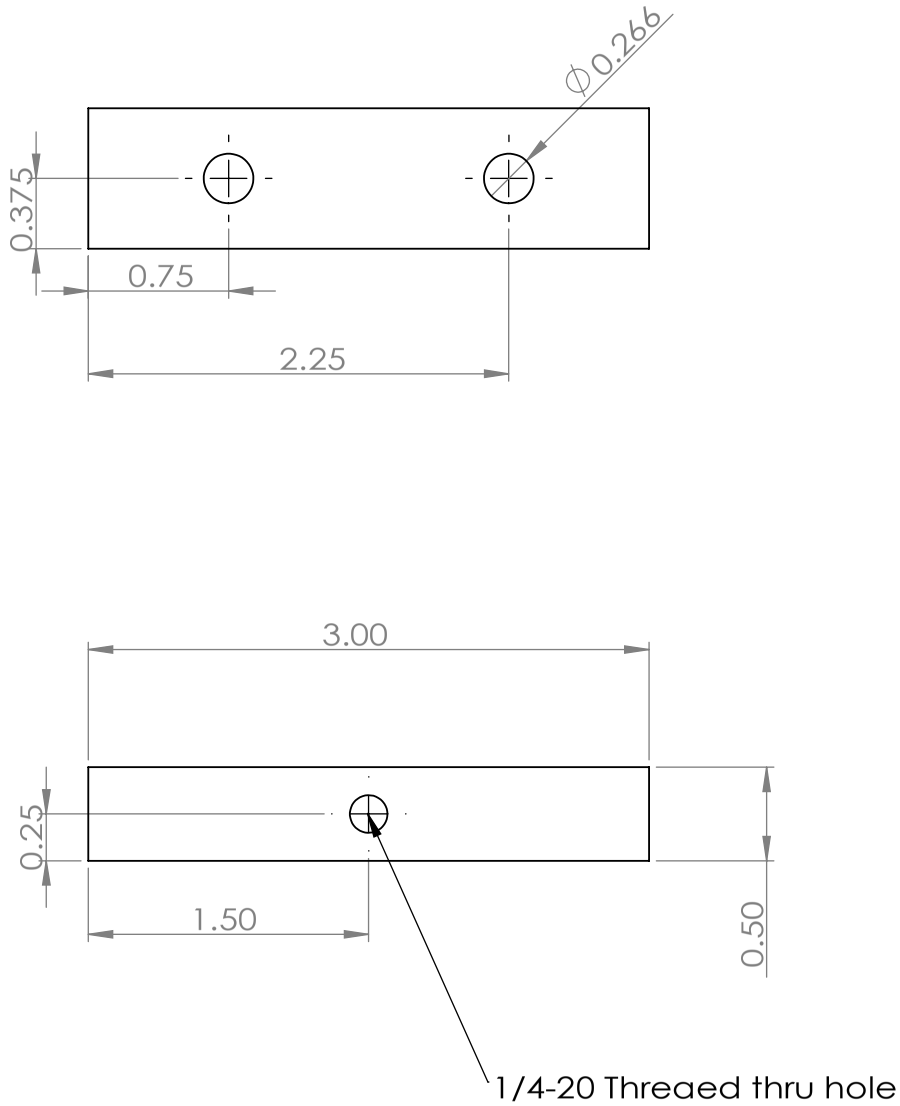

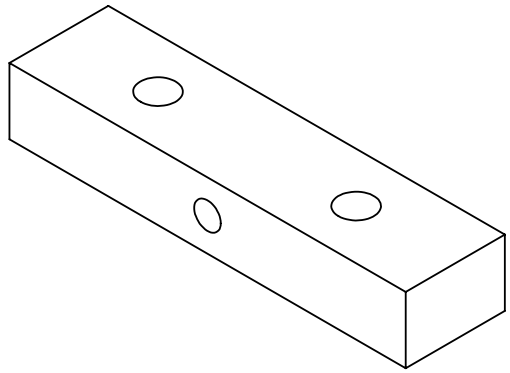

Project:	CLASS		
Assembly:	Q, W Secondary Mirror Adjustment Stage		
TITLE:	Push Screw Holder		
SIZE A	Drawn By: Zhilei Xu		REV 1
	Date: 21 Jun. 2017		

Dimensions in inches	SCALE: 1:1	Material: Aluminum	Quantity: 2	SHEET 10 OF 12

5 4 3 2 1

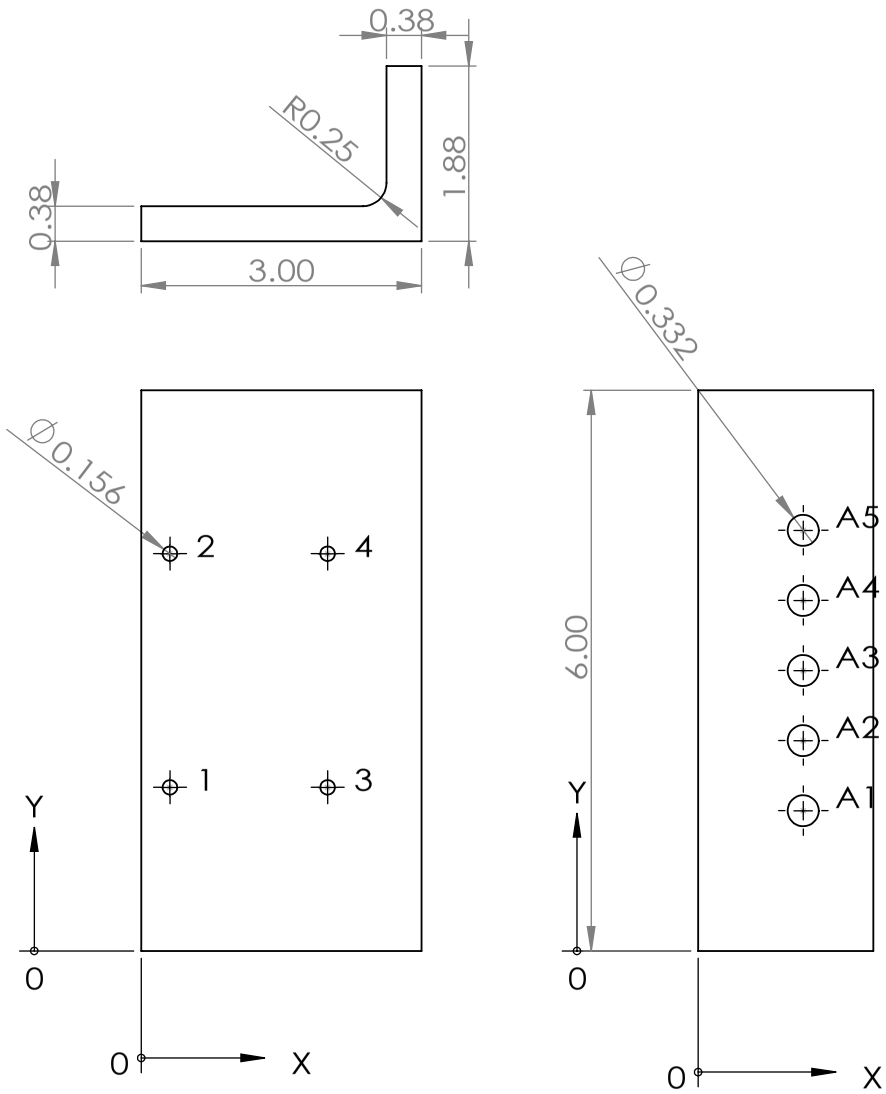

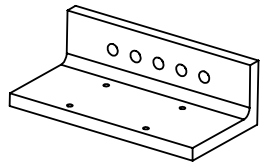

TAG	XLOC	YLOC	SIZE
A1	1.125	1.500	∅0.33 THRU
A2	1.125	2.250	∅0.33 THRU
A3	1.125	3.000	∅0.33 THRU
A4	1.125	3.750	∅0.33 THRU
A5	1.125	4.500	∅0.33 THRU

TAG	XLOC	YLOC	SIZE
1	0.307	1.750	∅0.16 THRU
2	0.307	4.250	∅0.16 THRU
3	1.995	1.750	∅0.16 THRU
4	1.995	4.250	∅0.16 THRU

Project:	CLASS		
Assembly:	Q, W Secondary Mirror Adjustment Stage		
TITLE:	Side Bracket		
SIZE A	Drawn By: Zhilei Xu		REV 1
	Date: 21 Jun. 2017		

Dimensions in inches | SCALE: 1:2 | Material: Aluminum | Quantity: 2 | SHEET 11 OF 12

5 4 3 2 1

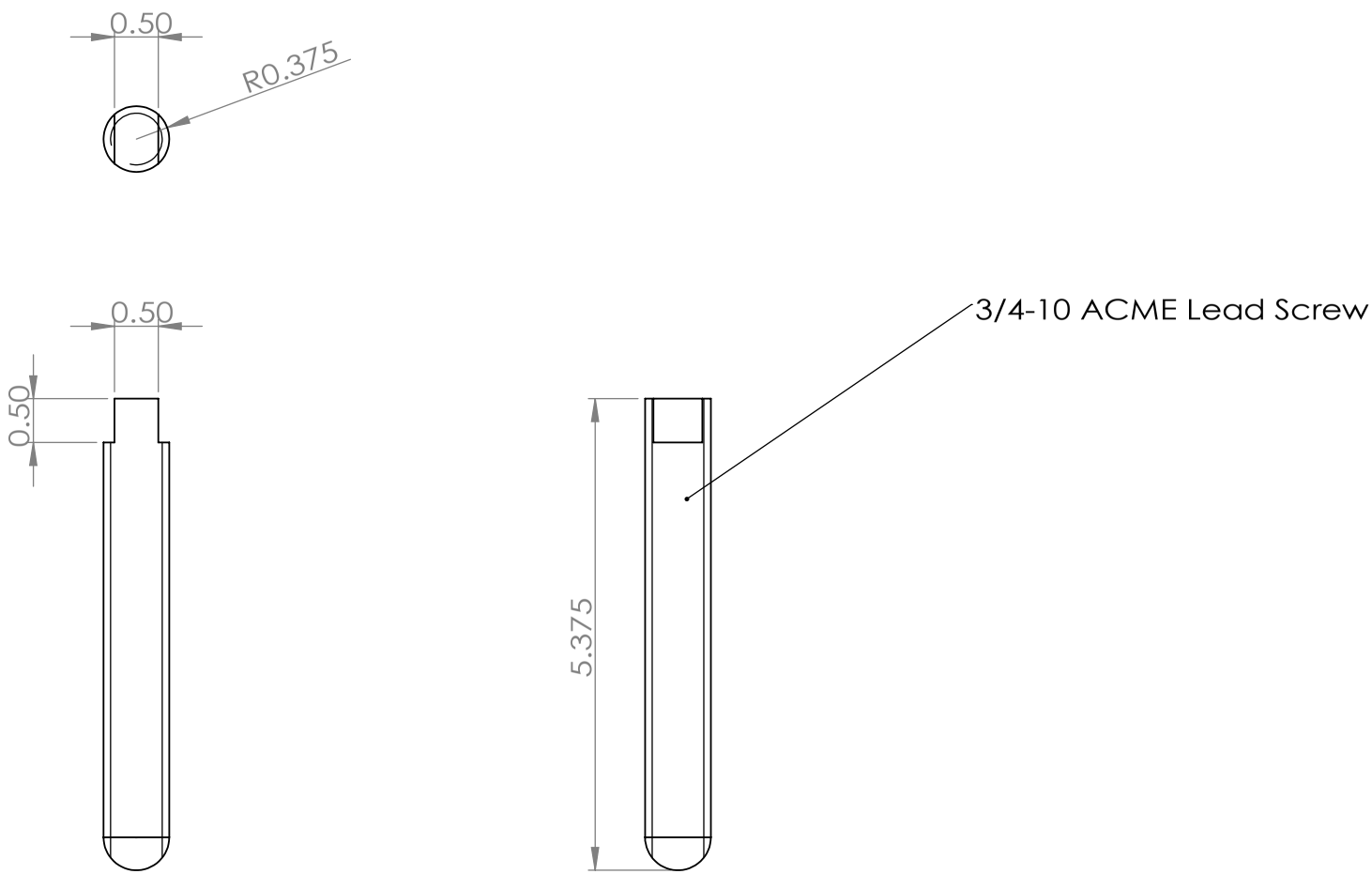

Project:	CLASS
Assembly:	Q, W Primary Mirror Adjustment Stages
TITLE:	ACME Lead Screw

SIZE	Drawn By:	Zhilei Xu	REV
A	Date:	21 Jun. 2017	1

Dimensions in inches	SCALE: 1:2	Material: SS	Quantity: 3	SHEET 12 OF 12

5 4 3 2 1

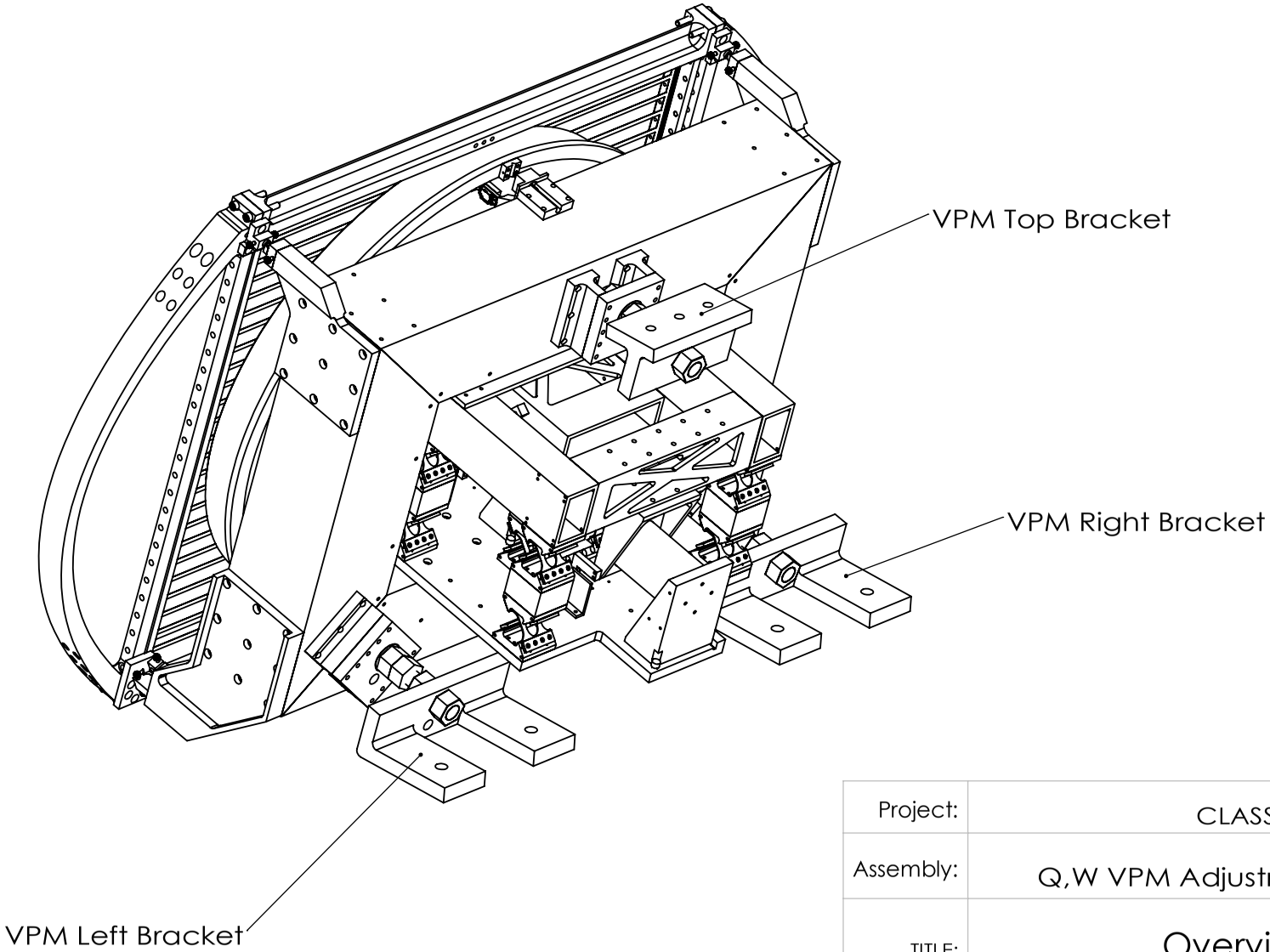

Project:	CLASS
Assembly:	Q,W VPM Adjustment Stages
TITLE:	Overview

SIZE	Drawn By:	Zhilei Xu	REV
A	Date:	21 Jun. 2017	1

Dimensions in inches	SCALE: 1:7	Material: Aluminum	Quantity: 2	SHEET 1 OF 4

5 4 3 2 1

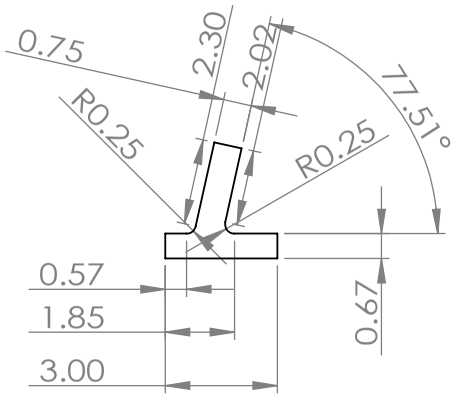

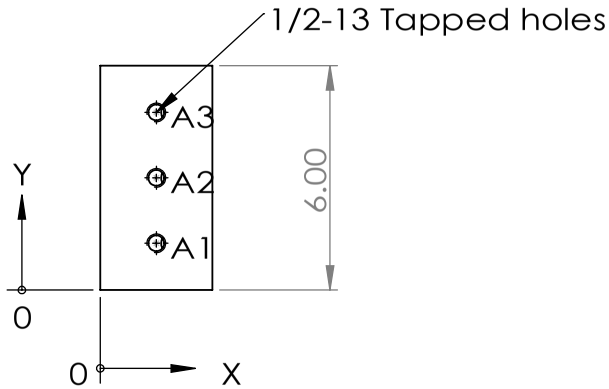

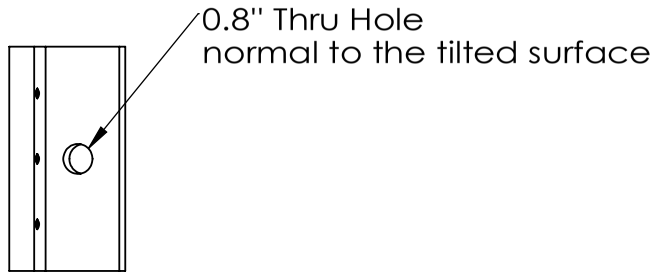

TAG	XLOC	YLOC	SIZE
A1	1.50	1.25	∅0.42 ↧ 0.75
A2	1.50	3.00	∅0.42 ↧ 0.75
A3	1.50	4.75	∅0.42 ↧ 0.75

Project:	CLASS
Assembly:	Q,W VPM Adjustment Stages
TITLE:	Top Bracket
SIZE A	Drawn By: Zhilei Xu
	Date: 21 Jun. 2017
REV	1

Dimensions in inches | SCALE: 1:5 | Material: Aluminum | Quantity: 1 | SHEET 2 OF 4

5 4 3 2 1

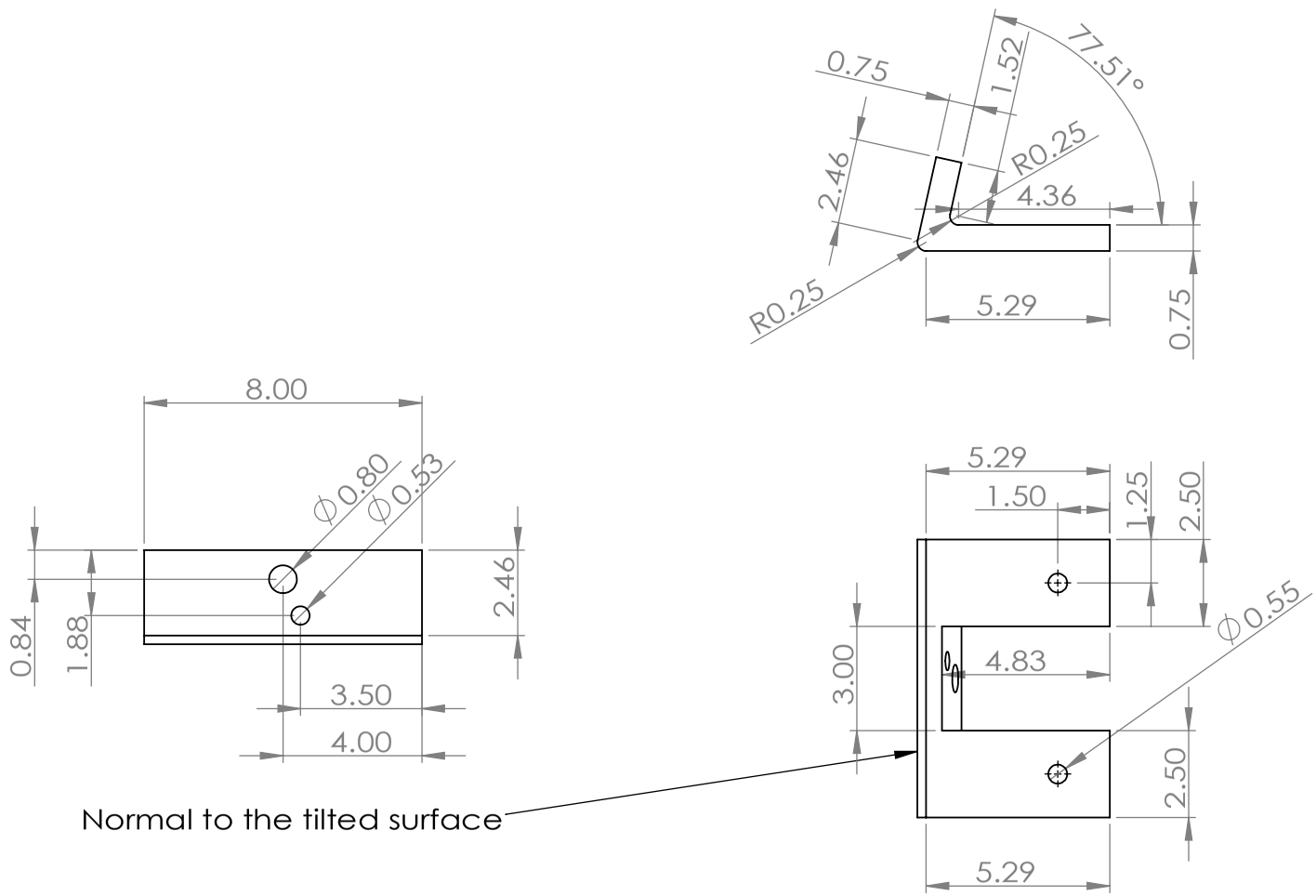

Project:	CLASS
Assembly:	Q,W VPM Adjustment Stages
TITLE:	Left Bracket

SIZE	Drawn By:	Zhilei Xu	REV
A	Date:	21 Jun. 2017	1

Dimensions in inches	SCALE: 1:5	Material: Aluminum	Quantity: 1	SHEET 3 OF 4

5 4 3 2 1

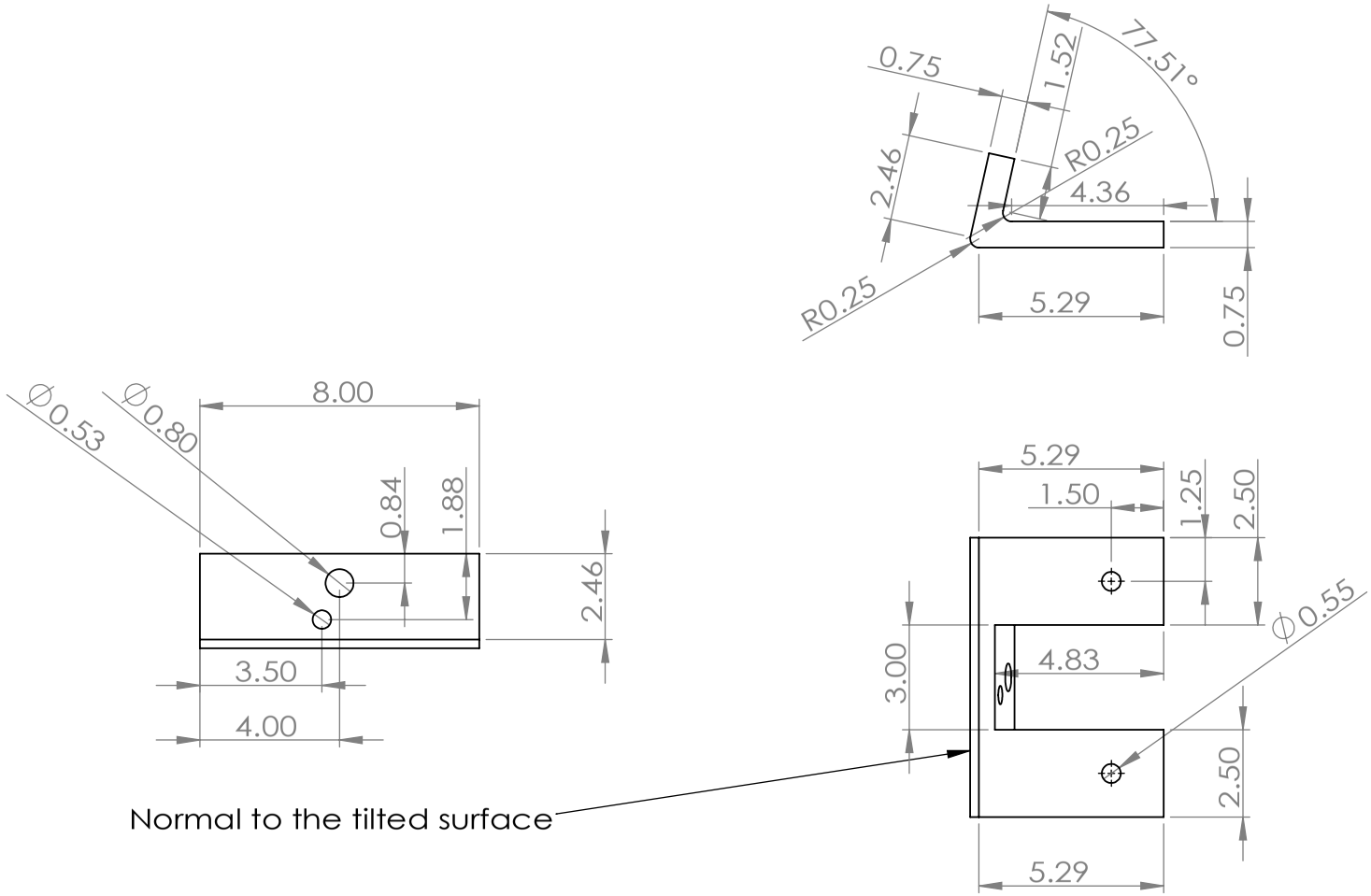

Project:	CLASS			
Assembly:	Q,W VPM Adjustment Stages			
TITLE:	Right Bracket			
SIZE A	Drawn By: Zhilei Xu			REV 1
	Date: 21 Jun. 2017			
Dimensions in inches	SCALE: 1:5	Material: Aluminum	Quantity: 1	SHEET 4 OF 4

5 4 3 2 1

Appendix F

Optical Alignment Strategy

General Strategy

The general strategy is to have the cryogenic receiver fixed and adjust the other components (the secondary mirror, the primary mirror, and the VPM). The overview of the optical component layout is shown in Figure F.1. Five targets are installed around the cryogenic receiver (C1, C2, C3, C4, C5), three targets are installed on the primary and secondary mirror respectively (P1, P2, P3, S1, S2, S3), four targets are also installed on the VPM (V1, V2, V3, V4). Details are shown in Figure F.2.

Coordinate System

The coordinate system is set up following these rules:

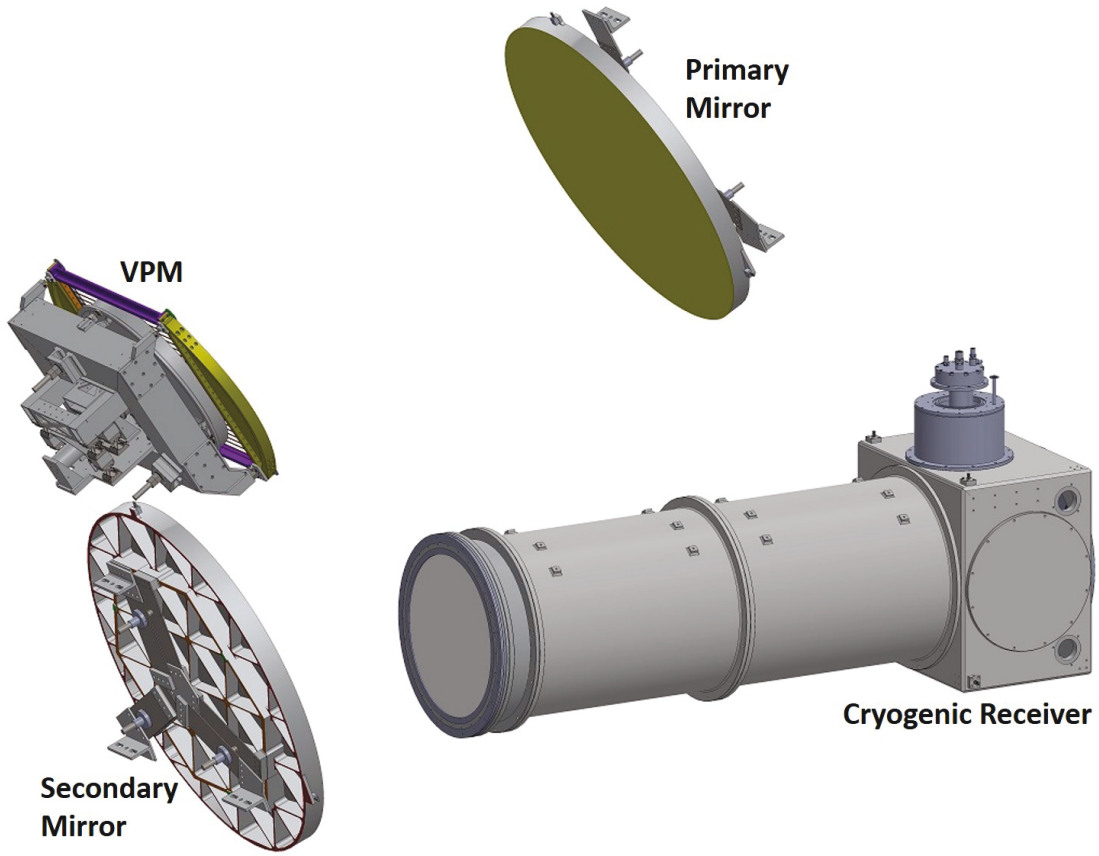

Figure F.1: Overview of CLASS 40 GHz telescope and measuring targets. The cube is used as an anchor to adjust the secondary mirror, the primary mirror, and the VPM.

- Origin: the midpoint of the segment connecting C1 and C5
- X-axis: parallel to the tube and pointing from the cube to the window
- Y-axis: along the segment connecting C1 and C5, pointing to C1
- Z-axis: pointing vertically up

In this coordinate system, all the targets are given in Table F.1:

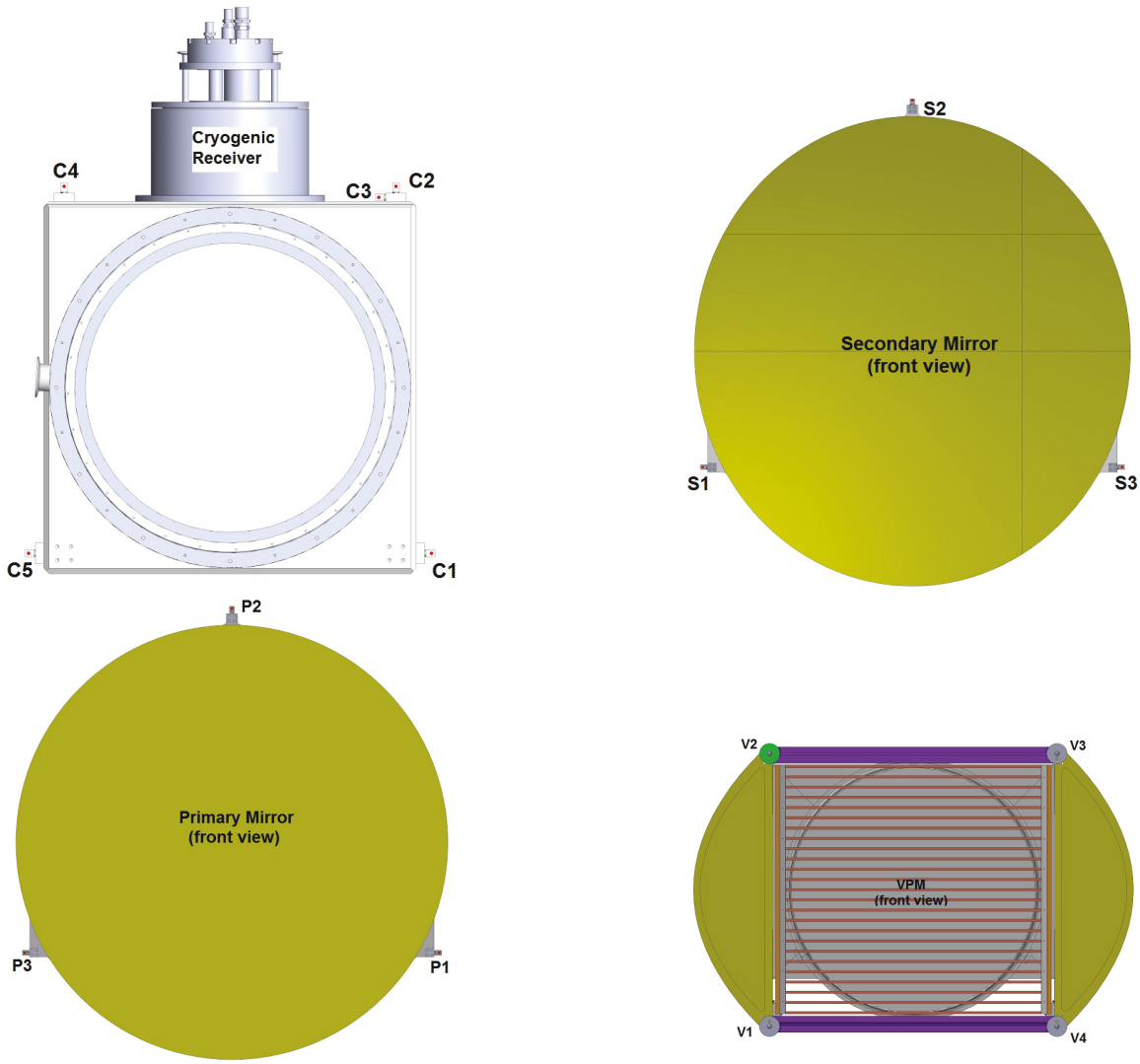

Figure F.2: Targets on different components: Top left: Looking from the window side, the cryogenic receiver and its five targets denoted as C1, C2, C3, C4, C5. Top right: Looking from the front, the secondary mirror and its three targets denoted as S1, S2, S3. Bottom left: Looking from the front, the primary mirror and its three targets denoted as P1, P2, P3, which are named mirror imaged to those on the secondary mirror. Bottom right: Looking from the front, the VPM and its four targets denoted as V1, V2, V3, V4.

VPM Targets

The VPM does not have any slots designed for the solid body targets, so we needed to apply some target tape at certain spots, whose positions were known. On

Table F.1: Target Coordinates

Target Name	X (inch)	Y (inch)	Z (inch)
C1	0	14.6039	0
C2	-0.1982	12.0276	26.6315
C3	-0.1982	10.7776	25.8315
C4	-0.1982	-12.0276	26.6315
C5	0	-14.6039	0
S1	100.9508	21.9570	-0.0272
S2	115.1136	0	35.6604
S3	100.9508	-21.9570	-0.0272
P1	36.9666	21.5212	60.2113
P2	53.9586	0	91.6348
P3	36.9666	-21.5212	60.2113
V1	103.4134	14.1579	42.2077
V2	117.7702	14.1425	63.6123
V3	117.7705	-14.1167	63.6121
V4	103.3227	-14.1171	42.2604

the VPM grid, we knew the positions of four screw holes for the shield, so we placed the tape target in reference to them. V1 and V4 are 0.5 inches vertically above the corresponding bolt holes; V2 and V3 are 0.5 inches vertically below the corresponding bolt holes, see Figure F.2 bottom right. Naturally, one may argue that we cannot control the tolerance to 0.5 inches by hand taping, but as long as the VPM is in the designed plane, some transverse offsets are forgiving. The plane is given by the following equation:

$$1.48433x - 0.00330y - z = 111.19829. \tag{F.1}$$

Actuator Points

The secondary mirror, primary mirror and VPM each have three actuator points, defined similarly to the targets. Their coordinates are shown in the following table:

Table F.2: Actuator Coordinates

Actuator Name	X (inch)	Y (inch)	Z (inch)
S1	106.04	10.20	4.66
S2	112.55	0.01	21.08
S3	106.04	-10.19	4.67
P1	36.86	10.60	66.32
P2	45.61	0.01	82.49
P3	36.87	-10.61	66.33
V1(Left Bottom)	117.32	10.30	42.11
V2(Top)	126.10	0.00	55.06
V3(Right Bottom)	117.32	-10.30	42.11

Note: These data are for the 40 GHz telescope adjustment stages deployed in 2016. Updated adjustment stages have different parameters.

Appendix G

Forebaffle Assembly

When the first CLASS telescope was deployed in 2016, the forebaffle was designed solely for the single 40 GHz telescope. Drawings on the forebaffle structure, the forebaffle interface, and the interface panels are attached here.

Soon the second CLASS telescope will be deployed, and a dual-forebaffle system is actively being designed and manufactured to accommodate the 40 GHz and new 90 GHz telescopes. The dual-forebaffle system is more than just doubling one single forebaffle design, because they would interfere between the two telescopes.

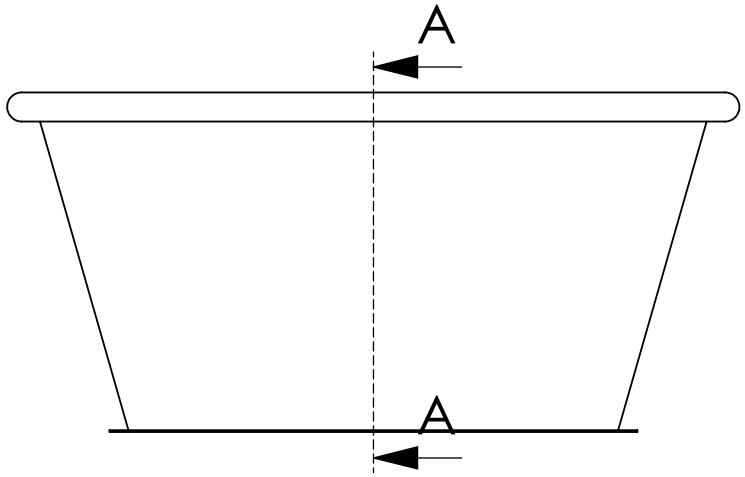

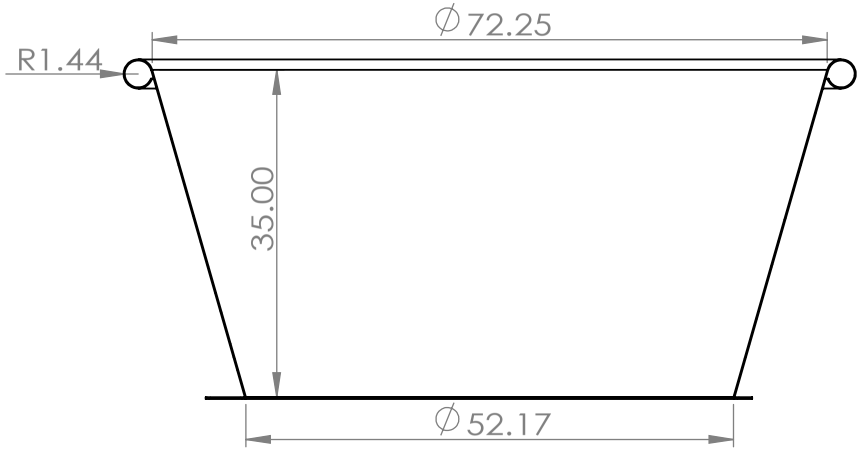

SECTION A-A

SCALE 1 : 20

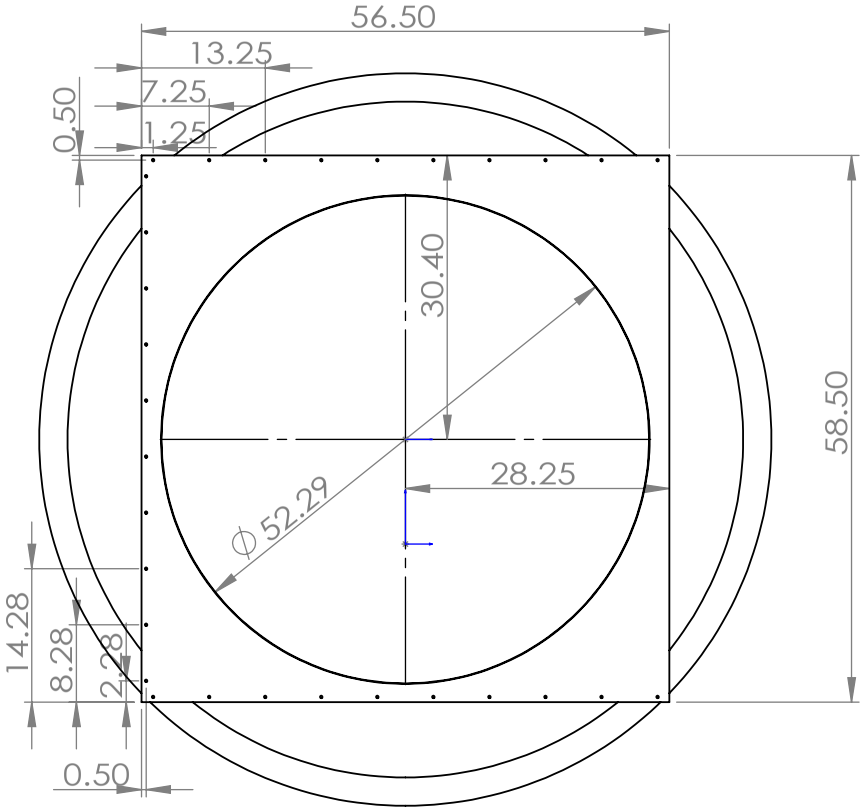

Note:

1. Dimensions measured in SECTION A-A are referenced from the inner surface
2. Bolts on the bottom Plate are all 1/4-20 clearance holes
3. The conical and flare parts use 1/8" sheet, while the bottom plate uses 3/16" sheet.
4. The welding joint between the conical and flare part needs to be smooth

Project:	CLASS		
Assembly:	Forebaffle Assembly		
TITLE:	Single Baffle		
SIZE A	Drawn By: Zhilei Xu		REV 1
	Date: 3 June 2015		

Dimensions in inches	SCALE: 1:20	Material: Aluminum	Quantity: 1	SHEET 1 OF 1

5 4 3 2 1

Baffle Holder

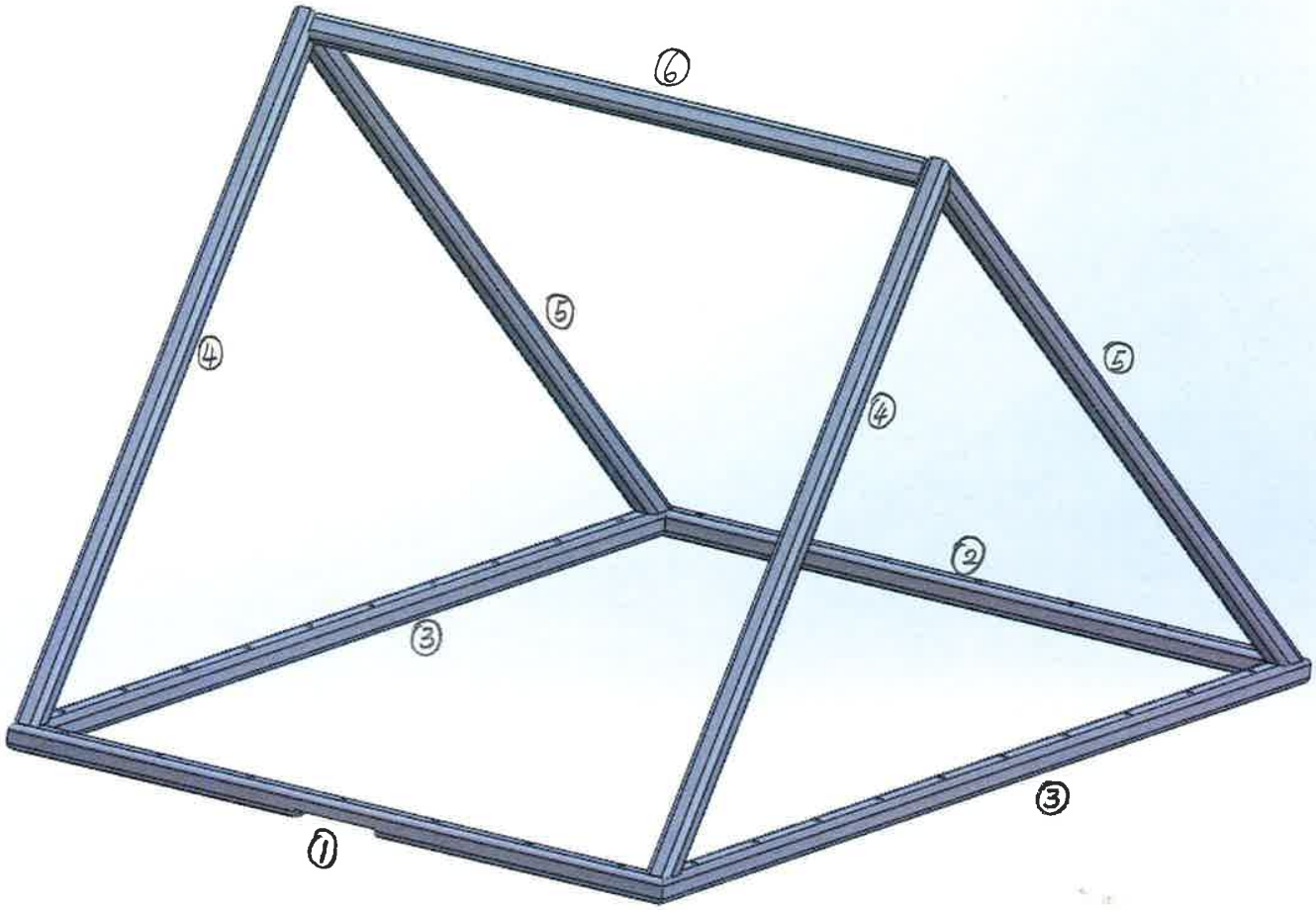

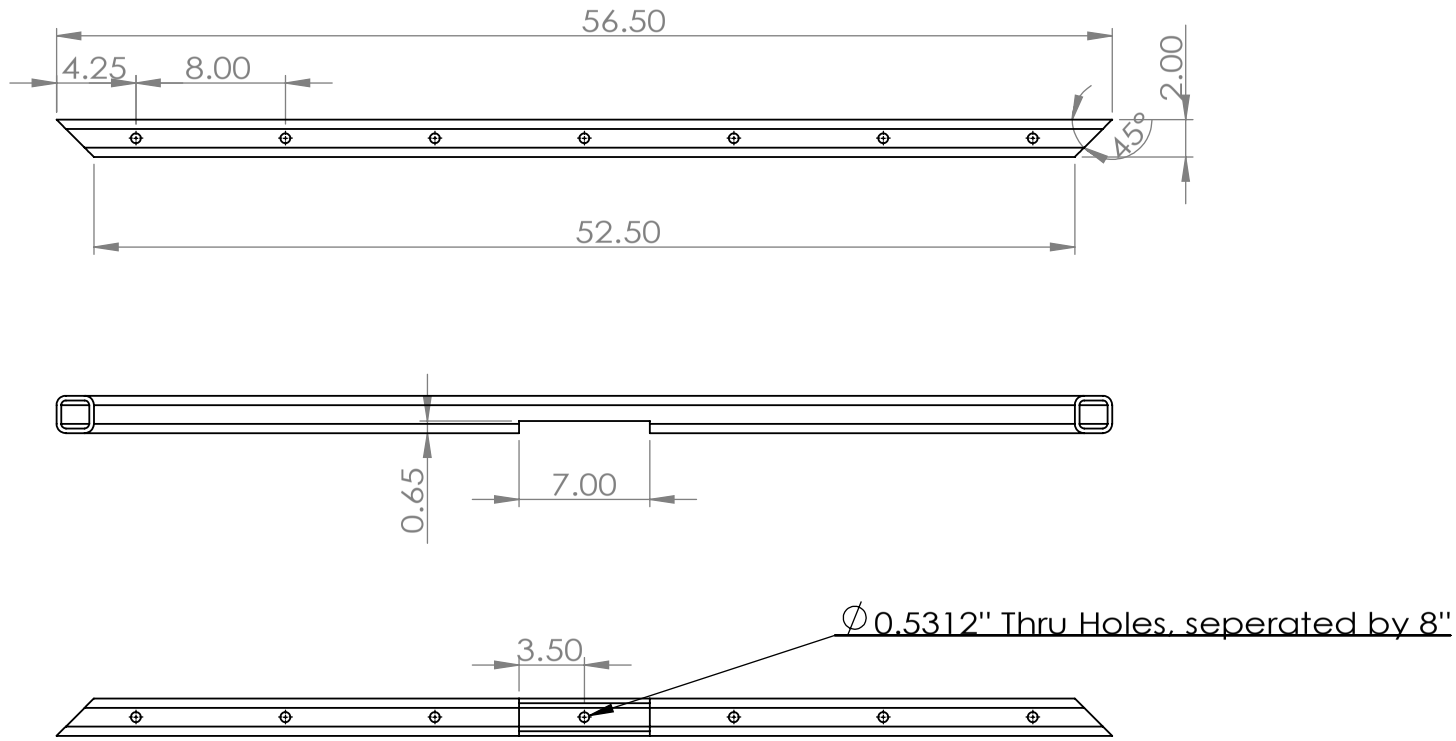

Project:	CLASS			
Assembly:	Baffle Holder			
TITLE:	Beam 1			
SIZE A	Drawn By: Zhilei Xu			REV 1
	Date: April 13, 2015			
Dimensions in inches	SCALE: 1:10	Material: Aluminum	Quantity: 1	SHEET 1 OF 6

5 4 3 2 1

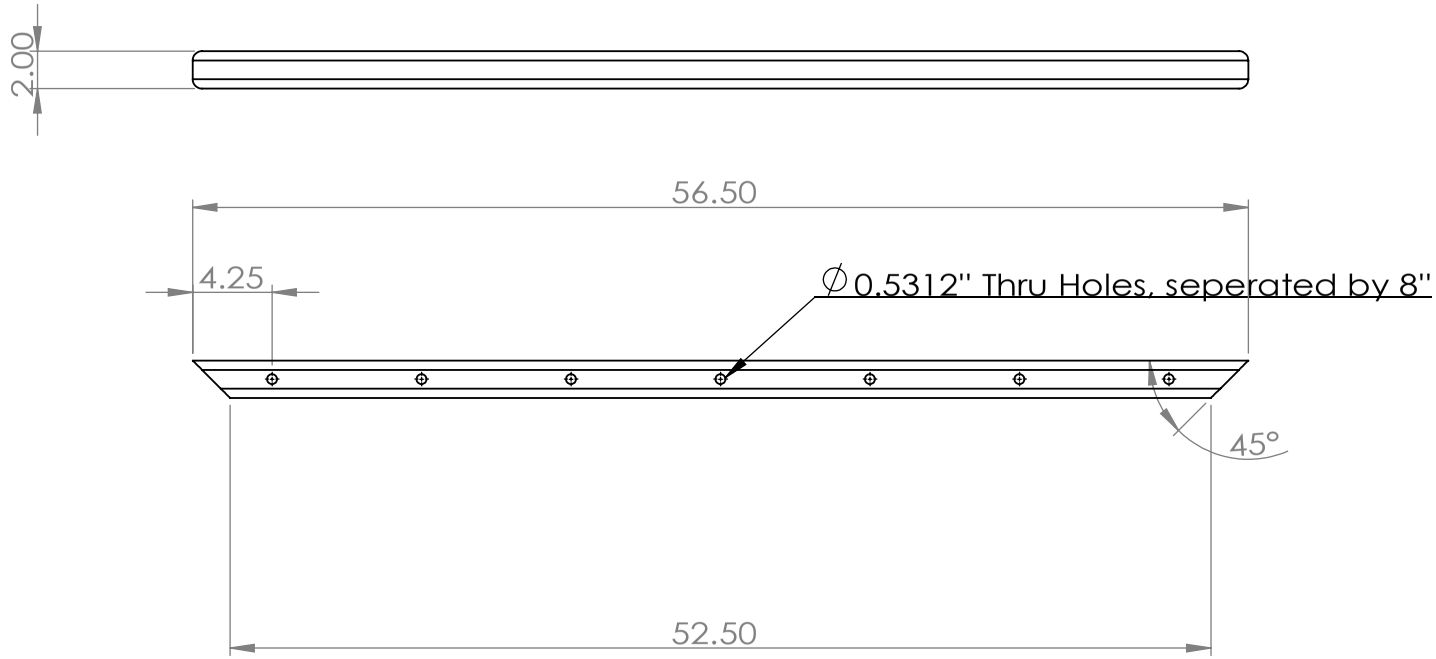

Project:	CLASS			
Assembly:	Baffle Holder			
TITLE:	Beam 2			
SIZE A	Drawn By: Zhilei Xu			REV 1
	Date: April 13, 2015			
Dimensions in inches	SCALE: 1:10	Material: Aluminum	Quantity: 1	SHEET 2 OF 6

5 4 3 2 1

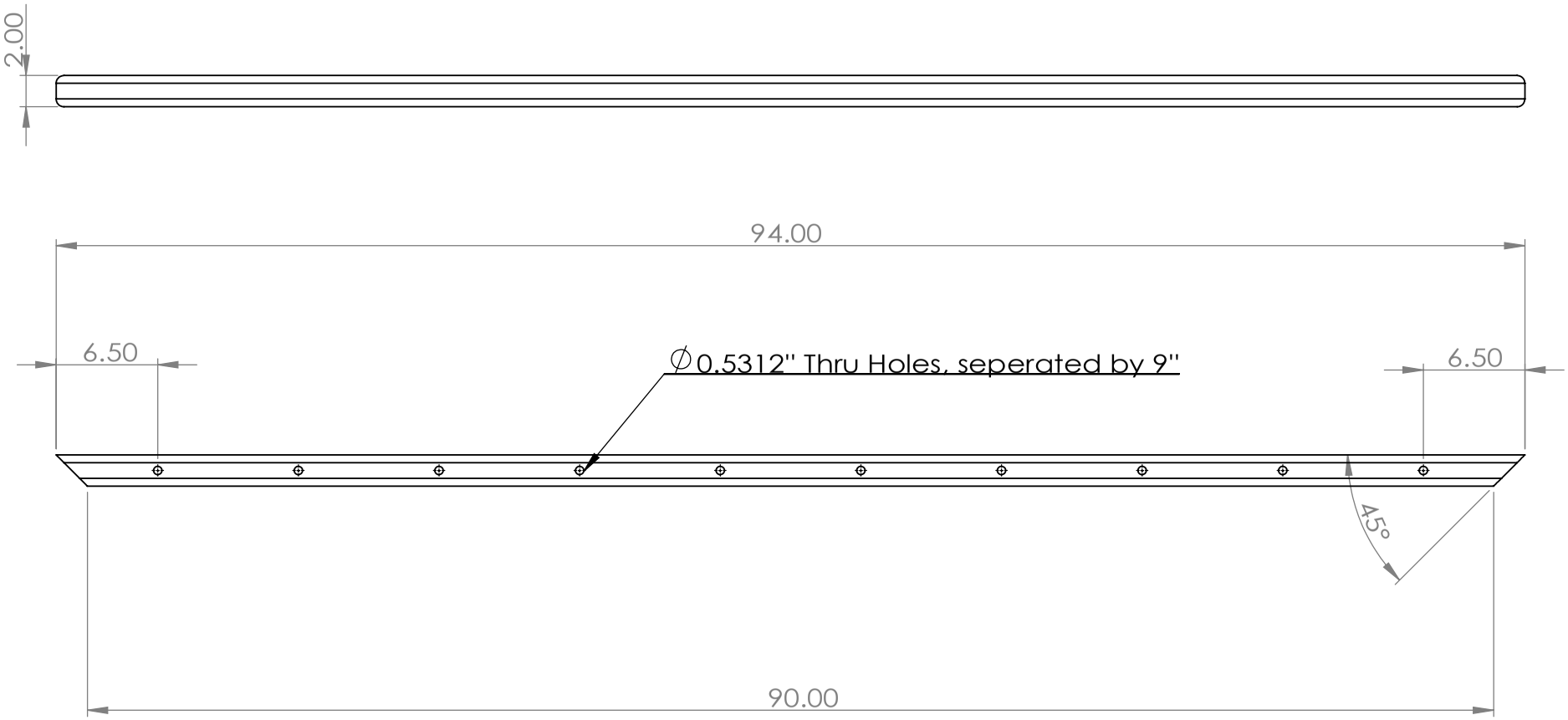

Project:	CLASS			
Assembly:	Baffle Holder			
TITLE:	Beam 3			
SIZE A	Drawn By: Zhilei Xu			REV 1
	Date: April 13, 2015			
Dimensions in inches	SCALE: 1:10	Material: Aluminum	Quantity: 2	SHEET 3 OF 6

5 4 3 2 1

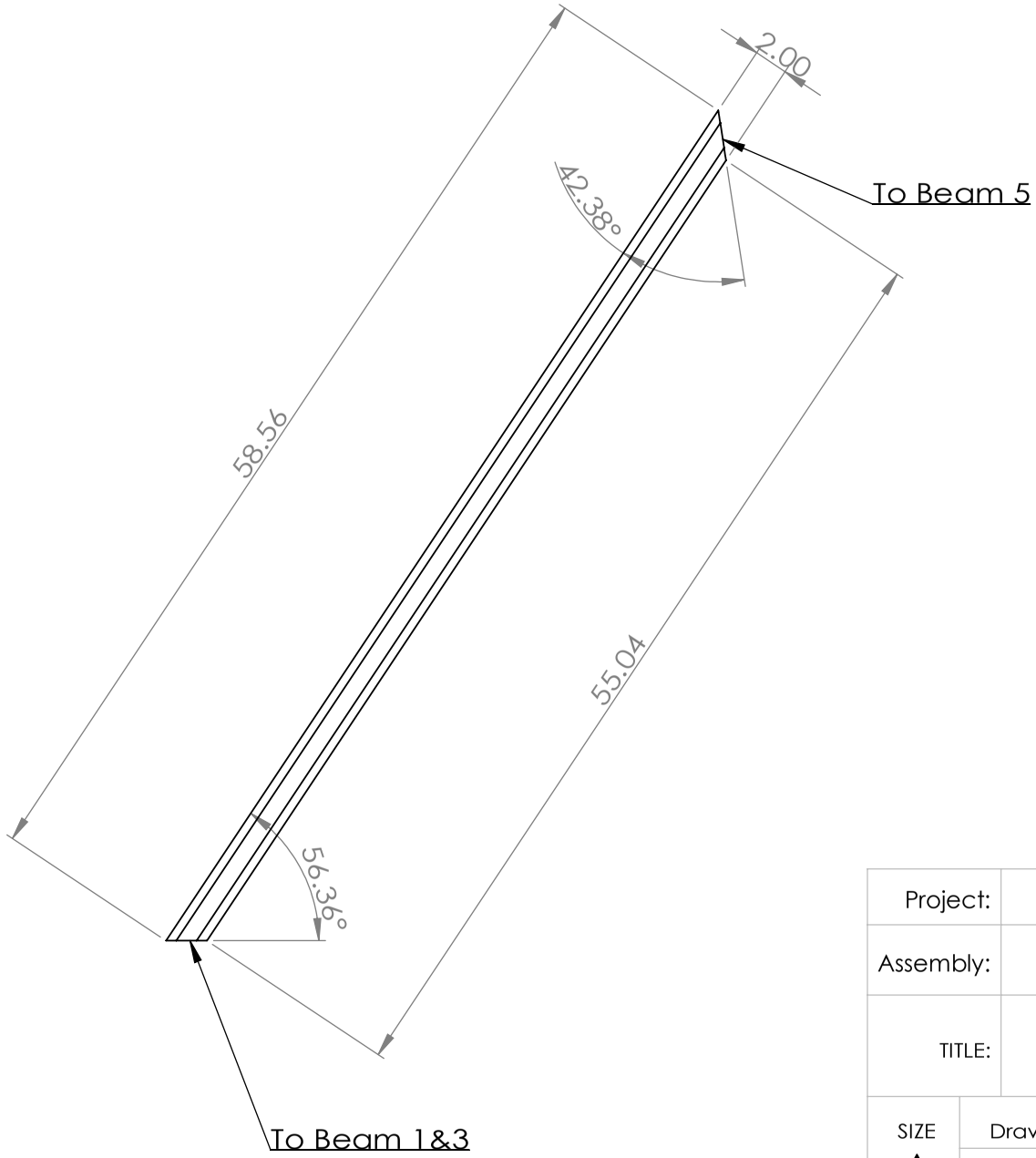

Project:	CLASS		
Assembly:	Baffle Holder		
TITLE:	Beam 4		
SIZE A	Drawn By: Zhilei Xu		REV 1
	Date: April 13, 2015		

Dimensions in inches	SCALE: 1:10	Material: Aluminum	Quantity: 2	SHEET 4 OF 6

5 4 3 2 1

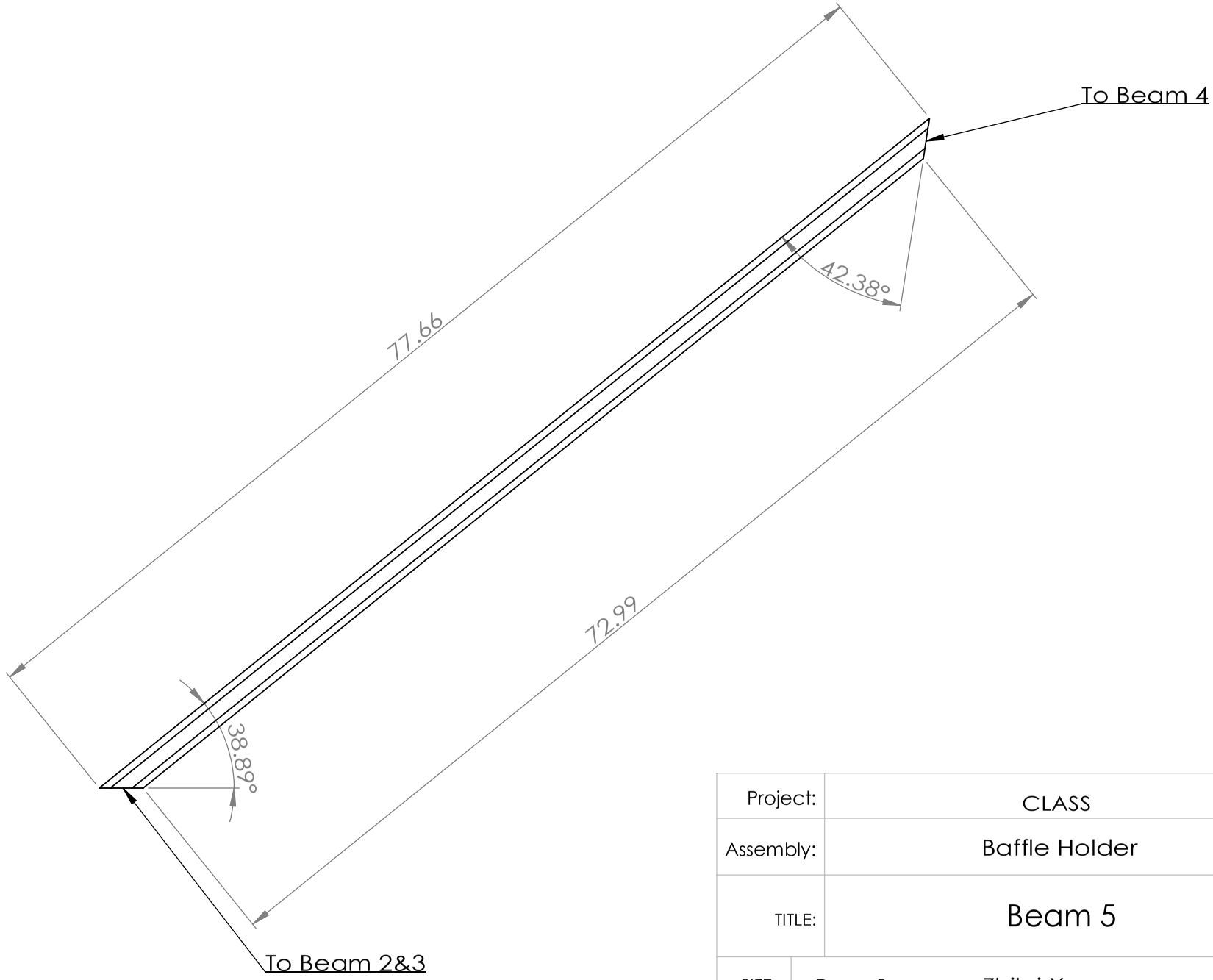

Project:	CLASS			
Assembly:	Baffle Holder			
TITLE:	Beam 5			
SIZE A	Drawn By: Zhilei Xu			REV 1
	Date: April 13, 2015			
Dimensions in inches	SCALE: 1:10	Material: Aluminum	Quantity: 2	SHEET 5 OF 6

5 4 3 2 1

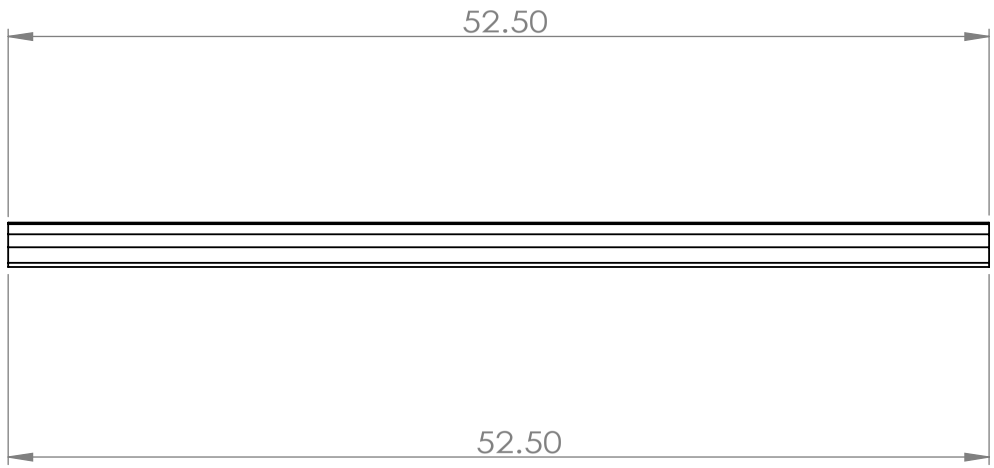

Project:	CLASS			
Assembly:	Baffle Holder			
TITLE:	Beam 6			
SIZE A	Drawn By: Zhilei Xu			REV 1
	Date: April 13, 2015			
Dimensions in inches	SCALE: 1:10	Material: Aluminum	Quantity: 1	SHEET 6 OF 6

5 4 3 2 1

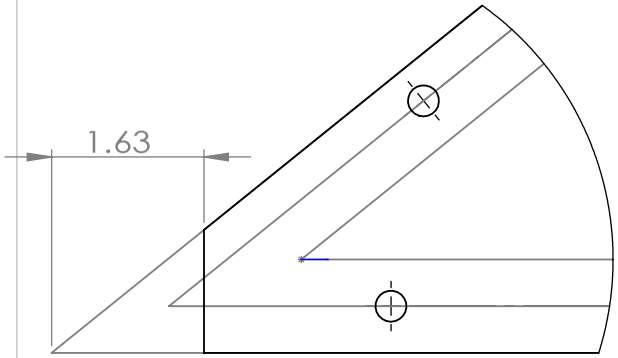

DETAIL C
SCALE 1 : 2

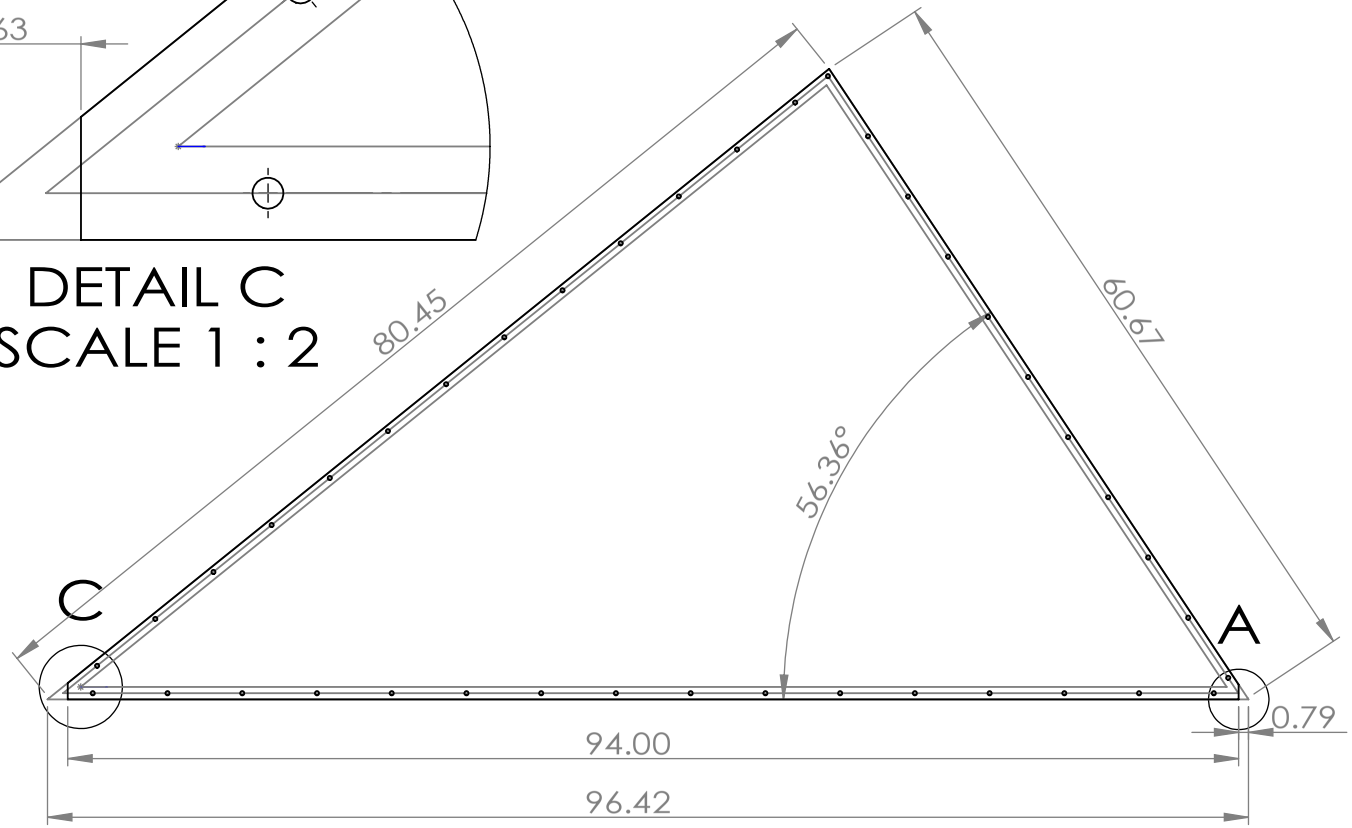

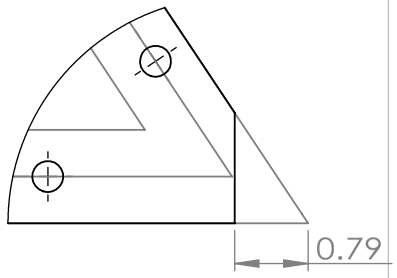

DETAIL A
SCALE 1 : 2

Note:

All the holes are 5/16 Clearance holes, ∅0.332"

Project:	CLASS		
Assembly:	Cage Panels		
TITLE:	Baffle Interface Side Panel		
SIZE A	Drawn By: Zhilei Xu		REV 1
	Date: 2015/05/21		
Dimensions in inches	SCALE: 1:15	Material: HC	Quantity: 2	SHEET 6 OF 9

5 4 3 2 1

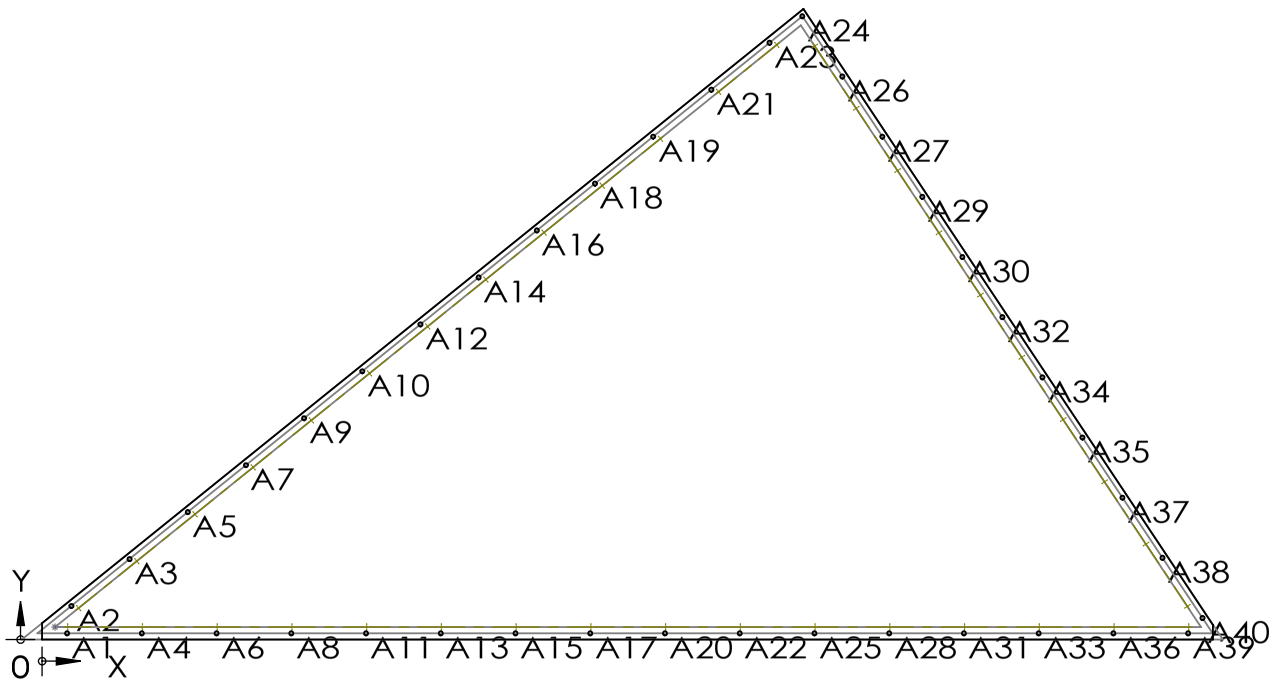

TAG	X LOC	Y LOC
A1	2.00	0.50
A2	2.35	2.70
A3	7.02	6.46
A4	8.00	0.50
A5	11.69	10.23
A6	14.00	0.50
A7	16.36	14.00
A8	20.00	0.50
A9	21.03	17.76
A10	25.70	21.53
A11	26.00	0.50
A12	30.37	25.30
A13	32.00	0.50
A14	35.04	29.06
A15	38.00	0.50
A16	39.71	32.83
A17	44.00	0.50
A18	44.38	36.60

Project:	CLASS
Assembly:	Cage Panels
TITLE:	Baffle Interface Side Panel
SIZE A	Drawn By: Zhilei Xu
	Date: 2015/05/21
REV	1

Dimensions in inches | SCALE: 1:15 | Material: HC | Quantity: 2 | SHEET 7 OF 9

5 4 3 2 1

TAG	X LOC	Y LOC
A19	49.05	40.36
A20	50.00	0.50
A21	53.72	44.13
A22	56.00	0.50
A23	58.39	47.90
A24	61.02	50.02
A25	62.00	0.50
A26	64.24	45.19
A27	67.45	40.36
A28	68.00	0.50
A29	70.66	35.53
A30	73.87	30.71
A31	74.00	0.50
A32	77.09	25.88
A33	80.00	0.50
A34	80.30	21.05
A35	83.51	16.22
A36	86.00	0.50
A37	86.73	11.39
A38	89.94	6.56
A39	92.00	0.50
A40	93.15	1.73

Project:	CLASS		
Assembly:	Cage Panels		
TITLE:	Baffle Interface Side Panel		
SIZE A	Drawn By: Zhilei Xu		REV 1
	Date: 2015/05/21		
Dimensions in inches	SCALE: 1:15	Material: HC	Quantity: 2	SHEET 8 OF 9

5 4 3 2 1

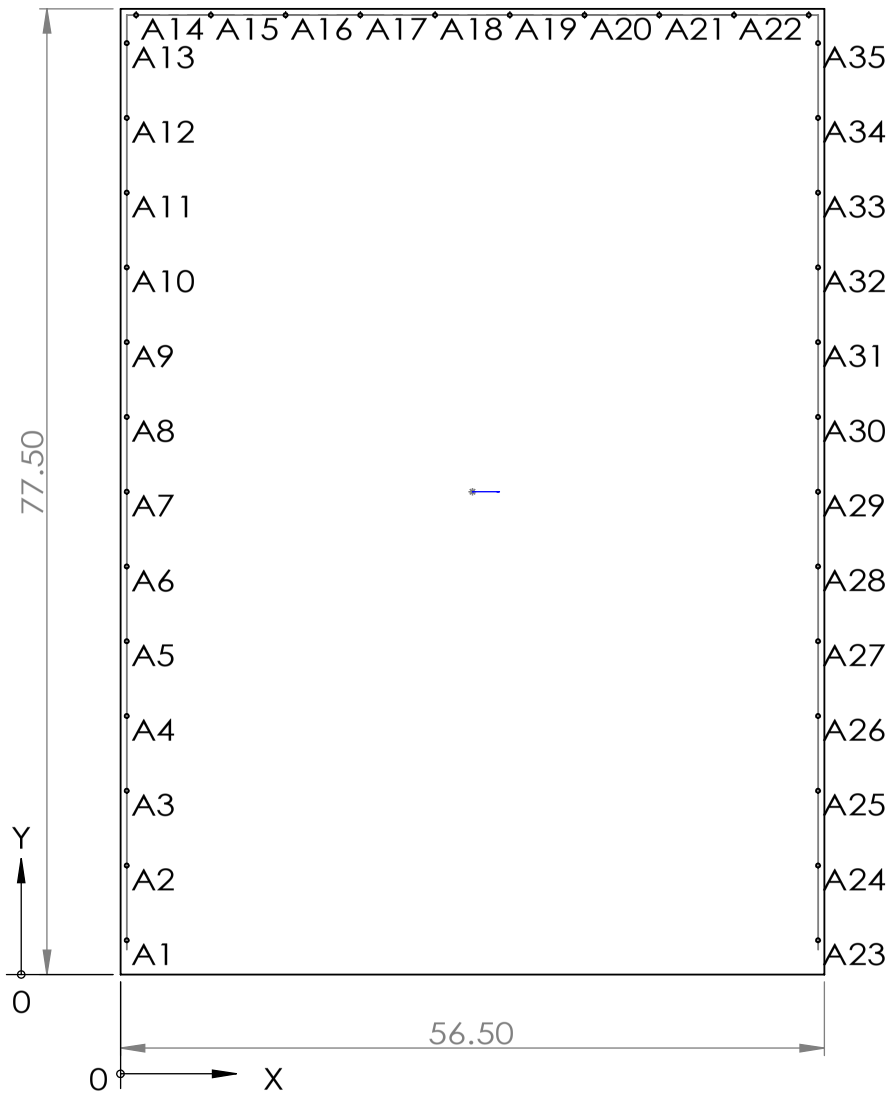

TAG	X LOC	Y LOC
A1	0.50	2.75
A2	0.50	8.75
A3	0.50	14.75
A4	0.50	20.75
A5	0.50	26.75
A6	0.50	32.75
A7	0.50	38.75
A8	0.50	44.75
A9	0.50	50.75
A10	0.50	56.75
A11	0.50	62.75
A12	0.50	68.75
A13	0.50	74.75
A14	1.25	77.00
A15	7.25	77.00
A16	13.25	77.00
A17	19.25	77.00
A18	25.25	77.00
A19	31.25	77.00
A20	37.25	77.00

TAG	X LOC	Y LOC
A21	43.25	77.00
A22	49.25	77.00
A23	56.00	2.75
A24	56.00	8.75
A25	56.00	14.75
A26	56.00	20.75
A27	56.00	26.75
A28	56.00	32.75
A29	56.00	38.75
A30	56.00	44.75
A31	56.00	50.75
A32	56.00	56.75
A33	56.00	62.75
A34	56.00	68.75
A35	56.00	74.75

Note:

All the holes are 5/16 Clearance holes, ∅0.332"

Project:	CLASS		
Assembly:	Cage Panels		
TITLE:	Baffle Intereface Front Panel		
SIZE A	Drawn By: Zhilei Xu		REV 1
	Date: 2015/05/21		
Dimensions in inches	SCALE: 1:15	Material: HC	Quantity: 1	SHEET 9 OF 9

5 4 3 2 1

Bibliography

[1] A. Albrecht and P. J. Steinhardt. "Cosmology for grand unified theories with radiatively induced symmetry breaking". In: *Physical Review Letters* 48 (Apr. 1982), pp. 1220–1223. DOI: 10.1103/PhysRevLett.48.1220.

[2] R. Allison et al. "Towards a cosmological neutrino mass detection". In: Phys. Rev. D 92.12, 123535 (Dec. 2015), p. 123535. DOI: 10.1103/PhysRevD.92.123535. arXiv: 1509.07471.

[3] R. A. Alpher, H. Bethe, and G. Gamow. "The Origin of Chemical Elements". In: *Phys. Rev.* 73 (7 Apr. 1948), pp. 803–804. DOI: 10.1103/PhysRev.73.803. URL: https://link.aps.org/doi/10.1103/PhysRev.73.803.

[4] J. W. Appel et al. "The cosmology large angular scale surveyor (CLASS): 38-GHz detector array of bolometric polarimeters". In: *Millimeter, Submillimeter, and Far-Infrared Detectors and Instrumentation for Astronomy VII*. Vol. 9153. Proc. SPIE. July 2014, 91531J. DOI: 10.1117/12.2056530. arXiv: 1408.4789 [astro-ph.IM].

[5] C. L. Bennett et al. "First-Year Wilkinson Microwave Anisotropy Probe (WMAP) Observations: Foreground Emission". In: ApJS 148 (Sept. 2003), pp. 97–117. DOI: 10.1086/377252. eprint: astro-ph/0302208.

[6] C. L. Bennett et al. "Four-Year COBE DMR Cosmic Microwave Background Observations: Maps and Basic Results". In: ApJ 464 (June 1996), p. L1. DOI: 10.1086/310075. eprint: astro-ph/9601067.

[7] BICEP2/Keck Collaboration et al. "Joint Analysis of BICEP2/Keck Array and Planck Data". In: *Physical Review Letters* 114.10, 101301 (Mar. 2015), p. 101301. DOI: 10.1103/PhysRevLett.114.101301. arXiv: 1502.00612.

[8] Max Born and Emil Wolf. *Principles of optics: electromagnetic theory of propagation, interference and diffraction of light*. Elsevier, 2013.

[9] R. R. Caldwell, C. Hirata, and M. Kamionkowski. "Dust-polarization Maps and Interstellar Turbulence". In: ApJ 839, 91 (Apr. 2017), p. 91. DOI: 10.3847/1538-4357/aa679c. arXiv: 1608.08138.

[10] J. R. Eimer. "The Cosmology Large Angular Scale Surveyor (CLASS): In search of the energy scale of inflation". PhD thesis. The Johns Hopkins University, 2013.

[11] J. R. Eimer et al. "The cosmology large angular scale surveyor (CLASS): 40 GHz optical design". In: *Millimeter, Submillimeter, and Far-Infrared Detectors*

and Instrumentation for Astronomy VI. Vol. 8452. Proc. SPIE. Sept. 2012, p. 845220. DOI: 10.1117/12.925464. arXiv: 1211.0041 [astro-ph.IM].

[12] A. Einstein. "Kosmologische Betrachtungen zur allgemeinen Relativitätstheorie". In: *Sitzungsberichte der Königlich Preußischen Akademie der Wissenschaften (Berlin), Seite 142-152.* (1917).

[13] T. Essinger-Hileman. "Probing Inflationary Cosmology: The Atacama B-Mode Search (ABS)". PhD thesis. Princeton University, 2011.

[14] T. Essinger-Hileman et al. "Systematic effects from an ambient-temperature, continuously rotating half-wave plate". In: *Review of Scientific Instruments* 87.9, 094503 (Sept. 2016), p. 094503. DOI: 10.1063/1.4962023. arXiv: 1601.05901 [astro-ph.IM].

[15] D. P. Finkbeiner. "Microwave Interstellar Medium Emission Observed by the Wilkinson Microwave Anisotropy Probe". In: ApJ 614 (Oct. 2004), pp. 186–193. DOI: 10.1086/423482. eprint: astro-ph/0311547.

[16] D. J. Fixsen et al. "The Cosmic Microwave Background Spectrum from the Full COBE FIRAS Data Set". In: ApJ 473 (Dec. 1996), p. 576. DOI: 10.1086/178173. eprint: astro-ph/9605054.

[17] A. Friedmann. "Über die Krümmung des Raumes". In: *Zeitschrift fur Physik* 10 (1922), pp. 377–386. DOI: 10.1007/BF01332580.

[18] J. R. Graham et al. "The Performance and Scientific Rationale for an Infrared Imaging Fourier Transform Spectrograph on a Large Space Telescope". In: PASP 110 (Oct. 1998), pp. 1205–1215. DOI: 10.1086/316237. eprint: astro-ph/9803163.

[19] A. H. Guth. "Inflationary universe: A possible solution to the horizon and flatness problems". In: Phys. Rev. D 23 (Jan. 1981), pp. 347–356. DOI: 10.1103/PhysRevD.23.347.

[20] K. Harrington et al. "The Cosmology Large Angular Scale Surveyor". In: *Millimeter, Submillimeter, and Far-Infrared Detectors and Instrumentation for Astronomy VIII*. Vol. 9914. Proc. SPIE. July 2016, 99141K. DOI: 10.1117/12.2233125. arXiv: 1608.08234 [astro-ph.IM].

[21] G. Hinshaw et al. "Five-Year Wilkinson Microwave Anisotropy Probe Observations: Data Processing, Sky Maps, and Basic Results". In: ApJS 180 (Feb. 2009), pp. 225–245. DOI: 10.1088/0067-0049/180/2/225. arXiv: 0803.0732.

[22] G. Hinshaw et al. "Nine-year Wilkinson Microwave Anisotropy Probe (WMAP) Observations: Cosmological Parameter Results". In: ApJS 208, 19 (Oct. 2013), p. 19. DOI: 10.1088/0067-0049/208/2/19. arXiv: 1212.5226.

[23] W. Hu and M. White. "A CMB polarization primer". In: New A 2 (Oct. 1997), pp. 323–344. DOI: 10.1016/S1384-1076(97)00022-5. eprint: astro-ph/9706147.

[24] E. Hubble. "A Relation between Distance and Radial Velocity among Extra-Galactic Nebulae". In: *Proceedings of the National Academy of Science* 15 (Mar. 1929), pp. 168–173. DOI: 10.1073/pnas.15.3.168.

[25] L. M. Krauss, S. Dodelson, and S. Meyer. "Primordial Gravitational Waves and Cosmology". In: *Science* 328 (May 2010), p. 989. DOI: 10.1126/science.1179541. arXiv: 1004.2504 [astro-ph.CO].

[26] James W. Lamb. "Miscellaneous data on materials for millimetre and submillimetre optics". In: *International Journal of Infrared and Millimeter Waves* 17.12 (1996), pp. 1997–2034. ISSN: 1572-9559. DOI: 10.1007/BF02069487. URL: https://doi.org/10.1007/BF02069487.

[27] A. D. Linde. "A new inflationary universe scenario: A possible solution of the horizon, flatness, homogeneity, isotropy and primordial monopole problems". In: *Physics Letters B* 108 (Feb. 1982), pp. 389–393. DOI: 10.1016/0370-2693(82)91219-9.

[28] J. C. Mather et al. "Measurement of the cosmic microwave background spectrum by the COBE FIRAS instrument". In: ApJ 420 (Jan. 1994), pp. 439–444. DOI: 10.1086/173574.

[29] N. J. Miller et al. "Recovery of Large Angular Scale CMB Polarization for Instruments Employing Variable-delay Polarization Modulators". In: ApJ 818,

151 (Feb. 2016), p. 151. DOI: 10.3847/0004-637X/818/2/151. arXiv: 1509.04628 [astro-ph.IM].

[30] Erik Oberg et al. *Machinery's handbook*. Vol. 200. Industrial Press New York, 2004.

[31] A. A. Penzias and R. W. Wilson. "A Measurement of Excess Antenna Temperature at 4080 Mc/s." In: ApJ 142 (July 1965), pp. 419–421. DOI: 10.1086/148307.

[32] Planck Collaboration et al. "Planck 2015 results. XIII. Cosmological parameters". In: A&A 594, A13 (Sept. 2016), A13. DOI: 10.1051/0004-6361/201525830. arXiv: 1502.01589.

[33] Planck Collaboration et al. "Planck intermediate results. XXX. The angular power spectrum of polarized dust emission at intermediate and high Galactic latitudes". In: A&A 586, A133 (Feb. 2016), A133. DOI: 10.1051/0004-6361/201425034. arXiv: 1409.5738.

[34] A. G. Riess et al. "Observational Evidence from Supernovae for an Accelerating Universe and a Cosmological Constant". In: AJ 116 (Sept. 1998), pp. 1009–1038. DOI: 10.1086/300499. eprint: astro-ph/9805201.

[35] M. Su, T. R. Slatyer, and D. P. Finkbeiner. "Giant Gamma-ray Bubbles from Fermi-LAT: Active Galactic Nucleus Activity or Bipolar Galactic Wind?" In:

ApJ 724 (Dec. 2010), pp. 1044–1082. DOI: 10.1088/0004-637X/724/2/1044. arXiv: 1005.5480 [astro-ph.HE].

[36] K. U-Yen et al. "A Broadband Planar Magic-T Using Microstrip-Slotline Transitions". In: *IEEE Transactions on Microwave Theory Techniques* 56 (Jan. 2008), pp. 172–177. DOI: 10.1109/TMTT.2007.912213.

[37] D. J. Watts et al. "Measuring the Largest Angular Scale CMB B-mode Polarization with Galactic Foregrounds on a Cut Sky". In: ApJ 814, 103 (Dec. 2015), p. 103. DOI: 10.1088/0004-637X/814/2/103. arXiv: 1508.00017.

[38] L. Zeng et al. "A Low Cross-Polarization Smooth-Walled Horn With Improved Bandwidth". In: *IEEE Transactions on Antennas and Propagation* 58.4 (Apr. 2010), pp. 1383–1387. ISSN: 0018-926X. DOI: 10.1109/TAP.2010.2041318.

[39] X.-Z. Zhang et al. "New radio observations of the Moon at L band". In: *Research in Astronomy and Astrophysics* 12 (Sept. 2012), pp. 1297–1312. DOI: 10.1088/1674-4527/12/9/010.

[40] Y. C. Zheng et al. "First microwave map of the Moon with Chang'E-1 data: The role of local time in global imaging". In: Icarus 219 (May 2012), pp. 194–210. DOI: 10.1016/j.icarus.2012.02.017.

Vita

Zhilei Xu received his Sc. B. degree in physics from the University of Science and Technology of China (USTC) in 2011, and enrolled in the Physics Ph.D. program at Johns Hopkins University in 2011. He received the highest honor (Guo Moruo Scholoarship) in 2011 from the USTC. His research focuses on experimental cosmology. As a member of the Cosmology Large Angular Scale Surveyor (CLASS) group, he works with other team members to build a telescope to study the very early universe.

Starting in September 2017, Zhilei will work on the Simons Observatory at the University of Pennsylvania, where he will focus on designing the next-generation telescope to study the universe.